Karlsruhe Series in Photonics & Communications, Vol. 36

Daria Madeleine Kohler

Integrated optical sensors on the Si_3N_4-organic hybrid (SiNOH) platform

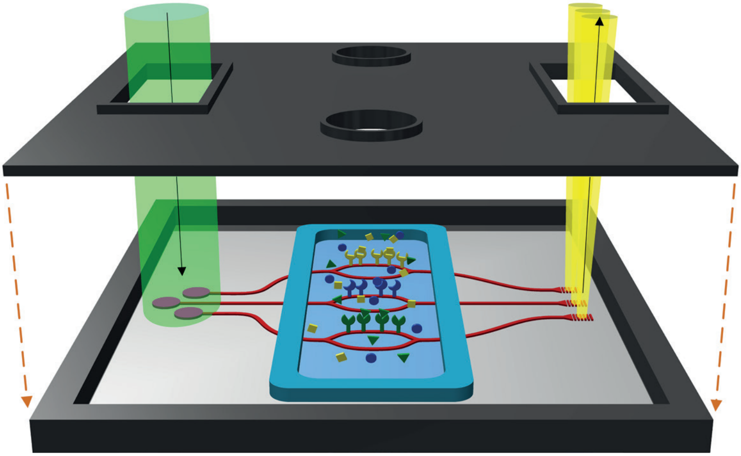

KIT Scientific Publishing

Daria Madeleine Kohler

Integrated optical sensors on the Si_3N_4-organic hybrid (SiNOH) platform

Karlsruhe Series in Photonics & Communications, Vol. 36
Edited by Profs. C. Koos, W. Freude and S. Randel

Karlsruhe Institute of Technology (KIT)
Institute of Photonics and Quantum Electronics (IPQ)
Germany

Integrated optical sensors on the Si_3N_4-organic hybrid (SiNOH) platform

by
Daria Madeleine Kohler

KIT Scientific Publishing

Karlsruher Institut für Technologie
Institut für Photonik und Quantenelektronik

Integrated optical sensors on the
Si_3N_4-organic hybrid (SiNOH) platform

Zur Erlangung des akademischen Grades einer Doktor-Ingenieurin
von der KIT-Fakultät für Elektrotechnik und Informationstechnik des
Karlsruher Instituts für Technologie (KIT) genehmigte Dissertation

von Dipl.-Phys. Daria Madeleine Kohler

Tag der mündlichen Prüfung: 23. März 2022
Hauptreferent: Prof. Dr. Christian Koos
Korreferent: Prof. Dr. Dr. h. c. Wolfgang Freude
Korreferent: Prof. Dr. Andreas Guber

Impressum

Scientific
Publishing

Karlsruher Institut für Technologie (KIT)
KIT Scientific Publishing
Straße am Forum 2
D-76131 Karlsruhe

www.ksp.kit.edu

Print on Demand 2023 – Gedruckt auf FSC-zertifiziertem Papier

ISSN 1865-1100
ISBN 978-3-7315-1228-8
DOI 10.5445/KSP/1000149433

Table of content

Kurzfassung

Gesundheit ist ein unverzichtbares Gut, nach dem wir alle streben, unabhängig von unserer Herkunft, unserem Alter oder unserer gesellschaftlichen Stellung, da sie maßgeblich unsere Lebensqualität beeinflusst. Dieses Gut wird jedoch permanent durch Bakterien, Viren, mutierte Zellen und andere Angreifer attackiert, die sich aggressiv ausbreiten, oder still und heimlich in unseren Körpern überleben, um dann immer wiederzukehren. Die moderne Medizin macht es möglich, viele Krankheiten bereits im Keim zu bekämpfen. Doch dafür sind Methoden der Frühdiagnostik nötig, die Erreger bereits erkennen, bevor sie größeren Schaden an unserem Organismus anrichten können. Während viele Methoden eine aufwändige Bearbeitung der dem Körper entnommenen Proben von mehreren Tagen in einem Zentrallabor erfordert [1], ermöglicht die sogenannte patientennahe Labordiagnostik (engl. point-of-care (POC) diagnostic) eine rasche Diagnose vor Ort [2]. Dadurch ist im Notfall eine schnelle spezifische Behandlung des Patienten im Krankenhaus oder beim Arzt möglich. Zusammen mit einer unkomplizierten Probenentnahme sind mit der POC-Diagnostik kostengünstig Langzeitüberwachungen zu Hause bei Patienten ohne die Anwesenheit von medizinischem Personal möglich, was bei Risikopatienten im Extremfall sogar einen Notfall verhindern kann [3]. Aus technischer Sicht hängen die Leistungsfähigkeit und die Praktikabilität von POC-Ansätzen entscheidend davon ab, ob Biosensoren einfach handhabbar sind, eine hohe Sensitivität aufweisen und sich kostengünstig in großen Stückzahlen herstellen lassen.

In diesem Zusammenhang wurden in den letzten Jahren neue Sensorkonzepte erforscht, die auf Lichtwellenleitern auf integrierten optischen Chips basieren [4]–[8]. Dabei wurden verschiedenste Sensorarchitekturen bei einer Vielzahl von Anwendungen getestet und deren Potential hinsichtlich ihrer hochsensitiven parallelen Detektion von krankheitstypischen Biomarkern in Körperflüssigkeiten unter Beweis gestellt [4], [5]. Ein Problem haben all diese Ansätze jedoch gemeinsam: Das Einkoppeln von Licht in die integrierten photonischen Wellenleiter erfordert mechanisch präzise und in der Handhabung komplexe Systeme, die zu hohen Kosten führen oder die nur von geschultem Personal betrieben werden können [7]. Um dieses Problem zu lösen, werden erste Ansätze verfolgt, bei denen Koppelstrukturen oder Lichtquellen auf ein und demselben Sensorchip integriert werden [4], [9]–[11]; allerdings wurde bislang noch keine Lösungen präsentiert, die eine einfache Handhabung in Kombination mit einer kostengünstigen und serientauglichen Herstellung der Lichtquelle versprechen.

Die vorliegende Arbeit befasst sich mit der Erforschung wellenleiterbasierter Sensorchips, die für die POC-Anwendung außerhalb des Labors geeignet sind. Beim Betreiben der Sensorchips sollte Licht eingesetzt werden, das im Wellenleitermaterial und in dem zu untersuchenden Analyten geringe Propagationsverluste aufweist. Als Ausgangsmaterial für die Wellenleiter wird Siliziumnitrid (Si_3N_4) verwendet [12], [13], das im Gegensatz zum üblicheren Silizium nicht nur im nahinfraroten, sondern auch im sichtbaren Wellenlängenbereich transparent ist und sich daher besonders gut zur Untersuchung biologischer Proben eignet [14]. Damit die Sensitivität von unterschiedlichen Sensoransätzen verglichen werden kann, wird ein mathematisches Modell entwickelt, mit dem Wellenleiter in Abhängigkeit von ihrer Geometrie, der Materialplattform und der Wellenlänge untersucht werden können. Ferner werden Ansätze erforscht, bei denen kostengünstige Laserquellen direkt auf dem Chip integriert werden, so dass präzise und mechanisch anspruchsvolle Kopplungen zu externen Lichtquellen entfallen. In diesem Zusammenhang wurden Bauteile erforscht, die Siliziumnitrid-Wellenleiter mit lichtemittierenden organischen Mantelmaterialien kombinieren. Diese im Folgenden auch als SiNOH-Laser (*engl.* Si_3N_4-organic hybrid-laser) bezeichneten Bauteile lassen sich sehr kostengünstig in großen Stückzahlen herstellen, indem die Wellenleiterstrukturen des Lasers in einem ersten Schritt parallel mit denen des Sensors über standardisierte lithographische Prozesse strukturiert werden. In einem zweiten Schritt werden die Wellenleiterstrukturen, beispielsweise über Druckverfahren, mit organischen Mantelmaterialien kombiniert. Für den Betrieb werden die SiNOH-Laser mit externen Lichtquellen, wie Leuchtdioden oder Laserdioden, optisch gepumpt und das Ausgangssignal der ko-integrierten Sensoren wird mit Hilfe einer technisch einfachen Kamera ausgelesen.

In der vorliegenden Arbeit werden die optimierten Sensoren erfolgreich mit den erforschten SiNOH-Lasern auf einem Chip integriert. Die Funktionalität des Sensorsystems wird anhand der Detektion von Fibrinogen demonstriert. Diese Ansätze werden in den folgenden Kapiteln näher erläutert.

Kapitel 1 gibt eine Übersicht für den Einsatz von wellenleiterbasierten Sensorchips im Gebiet der patientennahen Labordiagnostik, und die Limitierungen derzeitiger Sensorsysteme werden aufgezeigt.

Kapitel 2 gibt eine Einführung in das Design, die Fabrikation und die Funktionsweise von nanophotonischen Bauteilen, die für einen Sensorchip mit integrierter organischer Laserquelle essentiell sind.

In *Kapitel 3* wird ein Sensor charakterisiert, der auf den nanophotonischen Bauteilen, die in Kapitel 2 vorgestellt wurden, basiert. Die funktionelle Oberflächenmodifikation der Sensorwellenleiter wird erläutert, und die für erste Tests eingesetzte Fluidikkammer wird vorgestellt. Die Funktionalität des entwickelten Sensors wird anhand der Detektion von mehreren Konzentrationen von Fibrinogen untersucht.

Kapitel 4 befasst sich mit der Geometrieoptimierung eines Wellenleiterdesigns hinsichtlich hoher Sensitivität für das Anbinden von Biomolekülen und der Anwendbarkeit des Designs für reale Sensoren. Es wird ein mathematisches Modell vorgestellt, mit dem in Kombination mit numerischen Simulationen beliebige Wellenleiter bezüglich ihrer Sensitivität verglichen werden können. Ferner werden die Siliziumplattform in Kombination mit nahinfrarotem Licht und die Siliziumnitridplattform in Kombination mit sichtbarem Licht detailliert für mehrere Wellenleitergeometrien untersucht und diskutiert. Das zugrundeliegende Modell ist allgemein für wellenleiterbasierte Sensoren einsetzbar, sodass Trends und Limitierungen für andere Systeme aufgezeigt werden können.

Kapitel 5 demonstriert und untersucht die Erzeugung von sichtbarem Laserlicht in SiNOH-Wellenleitern, bestehend aus einem Siliziumnitridkern und einer organischen Mantelschicht mit gelöstem Laserfarbstoff. Die Laser werden optisch mit einer externen Lichtquelle mit großem Strahldurchmesser gepumpt, wodurch ein präzises Ausrichten des Chips entfällt. Es werden mehrere Resonatorgeometrien theoretisch und experimentell untersucht und ihr Einsatz in realen Anwendungen diskutiert. Bei den hier vorgestellten SiNOH-Lasern handelt es sich um die ersten organischen Laserquellen, die bisher auf der Siliziumnitridplattform integriert wurden.

In *Kapitel 6* wird ein Sensorsystem vorgestellt, das für die patientennahe Labordiagnostik geeignet ist. Dabei wird der in Kapitel 5 vorgestellten SiNOH-Laser mit dem in Kapitel 2 und 4 entwickelten Sensor auf einem Chip kombiniert. Die Bauteile lassen sich optisch mit einem Laserstrahl mit großem Durchmesser und dementsprechend geringen Justageanforderungen pumpen, während die Ausgangssignale der Sensoren mit einer technisch einfachen Kamera detektiert werden. Die Analytlösung wird in fluidischen Kanälen auf dem Chip geführt. Anhand der Detektion von Fibrinogen mit mehreren Konzentrationen wird das erste Mal die Kombination eines SiNOH-Lasers mit einem wellenleiterbasierten Sensor auf der Siliziumnitridplattform demonstriert.

Kapitel 7 fasst schließlich die Ergebnisse der Arbeit zusammen und bietet einen Ausblick auf die Möglichkeiten, wellenleiterbasierte Sensorsysteme auch für angrenzende Anwendungsgebiete weiterzuentwickeln.

Preface

Health is an indispensable good that we all strive for, regardless of our origin, age or social status, as it has a decisive influence on our quality of life. Unfortunately, this essential good is permanently attacked by, e.g., bacteria, viruses or mutated, aggressively spreading cells, which survive silently after therapy and often unexpectedly start to spread again. Modern medicine makes it possible to nip more and more diseases in the bud. This requires methods to detect such harmful organisms before they can cause any, and often major, damage to our bodies. While many detection methods require several days of time-consuming sample processing in a central laboratory [1], point-of-care (POC) diagnostics enable rapid on-site detection [2]. In case of emergency, such POC diagnosis allows a specific drug treatment of the patient, both in a clinic or in a physician's office. In addition, POC diagnostics can enable a cost-effective long-term monitoring at the patients' home without the presence of medical personnel. This may even prevent an emergency for high-risk patients [3]. On a technological level, the performance and practicability of POC-approaches crucially depends on whether biosensors are easy to handle, whether they show a high sensitivity and whether they can be produced cost-effectively in large quantities.

In this context new sensor concepts have been investigated in recent years that are based on photonic waveguides on integrated optical chips [4]–[8]. The demonstrations of different sensor architectures and their applications combine a highly sensitive parallel detection of a large number of bio-markers in body fluids [4], [5]. Unfortunately, these sensors have one thing in common: the coupling of light to and from the integrated photonic waveguides requires a mechanically precise operation unit that is expensive, that is complex in handling and can only be operated by trained personnel [7]. First approaches to challenge this problem include sensor chips with integrated coupling structures or light sources [4], [9]–[11]. Until today, a promising solution which includes a simple operation unit and a production process that is suitable for cost-effective mass production, is still missing [15].

This work deals with the investigation of a waveguide-based sensor chip, which is suitable for POC-applications outside the laboratory. Typically, silicon is used as waveguide material, but in contrast to silicon nitride, silicon is only transparent in the near infrared wavelength range [12], [13], whereas silicon nitride is also transparent to visible light. Since aqueous biological samples absorb visible light much less than near-infrared light [14], silicon nitride is chosen as the waveguide material. In order to compare the sensitivity of sensors made of different materials, a mathematical model is developed that can be used to investigate waveguides depending on their geometry, platform and operating wavelength. Furthermore, approaches are examined in which cost-effective laser sources are integrated directly on the chip so that precise and mechanically complex alignment to external light sources is not necessary. In this context, components combining silicon nitride waveguides with light emitting organic cladding materials are investigated. These components are called SiNOH laser (Si_3N_4-organic hybrid laser) in the following. The SiNOH lasers can be produced cost-effectively in large quantities, by structuring the waveguides of the laser parallel to those of the sensors using standardized lithographic processes in a first step. In a second step, the waveguide structures are combined with organic cladding materials, which are deposited, e.g., by printing. In operation, the SiNOH lasers are pumped with external light sources, such as LEDs or laser diodes, the signal of the co-integrated sensors are detected by a technically simple camera.

In the present work, the optimized sensors were successfully integrated on a chip together with the investigated SiNOH lasers. The functionality of the sensor system is demonstrated by the detection of fibrinogen. These approaches are explained in more detail in the following chapters.

Chapter 1 gives a general introduction on the application of sensor chips based on photonic waveguides. In particular, the field of POC diagnostics is considered and the limitations of current sensor systems are shown.

Chapter 2 gives an introduction on the design, fabrication and functionality of nanophotonic devices, which are essential for a sensor chip with an integrated organic laser source.

In *Chapter 3* a sensor is presented that is based on the photonic devices that are discussed in Chapter 2. The functional surface modification of the sensor waveguides is explained and the fluidic chamber is introduced. The functionality of the developed sensor is investigated by the detection of several concentrations of fibrinogen.

Chapter 4 deals with the geometry optimization of a waveguide design to obtain a high sensitivity regarding binding of biomolecules and a real-life application of such sensors. A mathematical model is presented with which, in combination with numerical simulations, any waveguide can be compared with respect to its sensitivity. In this chapter, the silicon platform in combination with near-infrared light, and the silicon nitride platform in combination with visible light, are investigated and discussed in detail for several waveguide geometries. This basic model can generally be used for waveguide-based sensors, to identify trends and limitations also for other systems.

Chapter 5 demonstrates and investigates the generation of visible laser light in SiNOH waveguides, consisting of a silicon nitride core and organic cladding layers with dissolved laser dye. The lasers are optically pumped with a large spot of an external light source, which makes a precise alignment of the chip with respect to the laser source unnecessary. Several resonator geometries are investigated both theoretically and experimentally, and their use in real-life applications is discussed. The SiNOH lasers introduced here are the first organic laser sources integrated on the silicon nitride platform up to now.

Chapter 6 deals with a sensor system for laboratory diagnostics which is suitable for application at the patient. The SiNOH laser investigated in Chapter 5 is combined with the sensor developed and discussed in Chapters 2 and 4 on one single chip. The integrated laser is excited by a pump laser beam that is directed at one side of the chip, while the sensor signal is detected by a simple CCD camera. The analyte solution is led in a fluidic chamber on the chip. Based on the detection of fibrinogen with multiple concentrations, the combination of a SiNOH laser with a sensor on the silicon nitride platform was demonstrated for the first time.

Finally, *Chapter 7* summarizes the results of this work and offers an outlook on possibilities to further develop waveguide-based sensor systems for their use in related application areas.

Achievements of the present work

The goal of this thesis is to explore waveguide-based bio-sensor chips that meet the requirements for point-of care applications. For the design of a waveguide-based sensor, a quantitative model is investigated that allows comparing the sensitivity of different waveguides on the silicon and silicon nitride platform, and allows optimizing sensitivity to be achieved under the given measurement conditions. For highly sensitive detection of the phase-shift induced by the binding reactions of the target molecules, an interferometric waveguide structure is integrated on the chip, in which one of the waveguides is covered by a biofunctional layer. The output light intensity can be simply measured by a digital camera. For light coupling to the waveguides of the sensor a new class of on-chip laser sources for visible wavelengths is investigated for the first time. Those laser sources are efficiently co-integrated with the biosensor on the Si_3N_4 platform using low-cost fabrication techniques without any additional lithographic structuring. Finally, the whole sensor system including the integrated laser is evaluated by detection experiments of fibrinogen at multiple concentrations. The viability of the waveguide-based bio-sensor chip is successfully demonstrated.

In the following an overview of the particular achievements is given.

Investigation of a universal sensitivity metric:

With waveguide-based biosensors, target molecules that bind to the surface of the waveguide can be detected by the thereby induced effective refractive index changes. By maximizing the influence of the bound molecules on the effective refractive index of the guided mode, the sensitivity of the sensor can be optimized. A variety of waveguide sensors was presented in the last years but it became increasingly challenging to compare them with respect to sensitivity, as different wavelengths, waveguide geometries and materials and many diverse molecules for detection were employed. In this thesis, a metric is investigated that can be used to compare the sensitivities for different waveguide types and geometries, integration platforms and at different operation wavelengths. The sensitivity metric is calculated and discussed for a variety of waveguide types and geometries for the most common material systems: the silicon nitride platform and the silicon platform. In addition, universal design guidelines for sensor systems are given that allow optimizing sensor waveguides for a given application. This work has been published in Optics Express (OPTICA Publishing Group) [J4].

First time demonstration of Si_3N_4-organic hybrid (SiNOH) lasers:

In biophotonic applications, often aqueous analytes have to be analyzed. Therefore, for waveguide-based bio-sensors, visible light is advantageous for low propagation loss. Silicon nitride (Si_3N_4)-based waveguides fulfill this demand, but the platform is so far limited to passive devices that need to be fed by external light sources. This often requires complicated fiber-chip coupling schemes with stringent alignment tolerances, which makes the system expensive. In this thesis, for the first time, a new class of lasers is investigated that combines Si_3N_4 waveguide cores with light-emitting organic cladding materials, called Si_3N_4-organic hybrid (SiNOH) lasers. The SiNOH lasers are operated by optical pumping from the top with low alignment precision. The functionality of different laser geometries based on ring structures and distributed feedback structures is theoretically investigated and experimentally evaluated. The discussed SiNOH lasers are designed to emit at approximately 600 nm, and the concept can be transferred to a large range of wavelengths in the visible spectrum. The devices can be efficiently integrated on the silicon nitride platform by cost-effective mass production. In this work and for the first time, the SiNOH laser concept is introduced and the successful integration of organic lasers on the silicon nitride platform is demonstrated. These results have been published in Optics Express (OPTICA Publishing Group) [J3].

First time demonstration of bio-sensor chip with integrated SiNOH laser

Based on the first demonstration of the SiNOH lasers, an optical biosensor is co-integrated with a SiNOH laser on the same chip in the next step. The SiNOH laser is pumped from the top. Highly parallel read-out of the optical sensor signals is accomplished with a digital camera. The viability of this approach is evaluated by detecting different concentrations of fibrinogen in phosphate-buffered saline solutions. The results demonstrate for the first time an integrated optical circuit driven by a co-integrated low-cost organic light source. The results have been published in Light: Science & Applications (Nature Publishing Group) [J2].

1 Introduction

There has always been a risk that has preoccupied everyone, regardless of their background or social standing: Diseases can affect any of us, even if we strive for a healthy lifestyle and stay away from harmful environments. During the last decades, society has changed a lot, efficient medicines and therapies have been developed, and already infants are immunized against a variety of diseases. As a result, some diseases have been eradicated or can be treated as a matter of routine. The advance of modern medicine led to the fact that our society has been undergoing a demographic change: people are getting older. All over the globe, life expectation increased by 2.5 years per decade since 1940 [16]. However, with increasing age, other types of diseases, such as cancer, Alzheimer's or Parkinson's disease come to the fore [17]. These are diseases, which either can be hardly cured, or whose progression can be only retarded, and often so only if they are diagnosed at an early stage [18]. This requires methods that detect specific markers before the pathogens cause any major damage to our bodies. These methods imply a high sensitivity and selectivity to the pathogens of interest and a fast result of the analysis, which is at best performed at the point-of-care, i.e., directly during the doctor's visit or as long-term monitoring in the patient's home. When analytic devices are used that come in contact with bodily fluids, cross-contaminations between samples must be avoided. As purifying is not always possible or expensive, it is advantageous if these devices are disposable; the production of high quantities must be cost-efficient.

In recent years, research has been conducted into a new analysis tool that promises precisely these aforementioned properties: sensor chips based on photonic waveguides. A variety of waveguide sensors were demonstrated in the last two decades, based on interferometric structures [6], [19]–[22], or resonant structures , such as ring or disk resonators and grating structures [4], [5], [23]–[29]. Due to the large effective lengths of interaction with the analyte, these sensor structures combine high sensitivity with small device footprint, and are suitable for high-density integration in massively parallel arrays. The detection of many different kinds of viruses, DNA, excosomes, and other small molecules was demonstrated [4]. The sensor performances were improved by varying the sensor geometry [4], [5], [19], the waveguide cross-section [20], [21], [27]–[33], and the read-out units [5], [34]–[36]. In addition, many specific sensor architectures were optimized separately, and it became increasingly challenging to compare them with respect to performance, as different wavelengths, waveguide geometries and materials and the most diverse molecules for detection were employed. In Chapter 4 of this thesis and Ref. [37] a metric is defined that quantifies these influences on the sensitivity so that different waveguide types and geometries, integration platforms and operation wavelengths can be compared.

While the sensitivity of sensors increased immensely, the development of the sensor systems towards point-of-care applications also progressed. There are several approaches to built read-out instruments that are suitable for point-of care applications, mainly sensors based on ring resonators. In 2010, a scanning instrumentation with an array of 32 silicon ring resonators was presented [38]. For each single sensor, the light of a tuneable laser was automatically and sequentially coupled to the input ports formed by grating couplers for each single sensor. In 2012, Genalyte, Inc. started selling automated instruments to the pharmaceutical industry based on his work [39]. Although these instruments are commercially available nowadays, they are mainly used in research laboratories and did not reach surgery or patients' homes. In 2013, an integrated sensor-array chip for multiplexed detection with 128 ring resonators was demonstrated [34]. The light of a powerful tuneable laser was coupled to the chip via a grating coupler and distributed on the chip to the sensors. The sensors are addressed in parallel, but coupling the laser light via a grating coupler requires a complex alignment and therefor a bulky readout unit so that untrained personnel can use the sensor chips. The parallel readout of ring resonators implies a powerful tuneable laser source (10 mW). A laser source with acceptable performance is a rather bulky device, and is therefore in contradiction to the aim of a portable device for POC applications. To solve this challenge, the laser source can be integrated on the chip. In 2019, a sensor array on the silicon nitride platform with a flip-chip-mounted VCSEL emitting at a wavelength of 850 nm [35] was presented. Although this system is very compact, it is questionable if a high-precision assembly of discrete laser dies can comply with the stringent cost limitations of disposable biosensors.

Typically, for the presented sensors, silicon is used as waveguide material, but in contrast to silicon nitride, silicon is only transparent in the near infrared wavelength range, whereas silicon nitride is also transparent to visible light. In biological applications, aqueous analytes are typically examined, such as urine or saliva. The absorption of light is approximately three orders of magnitude smaller at visible wavelengths compared to near-infrared wavelengths [14]. Similarly, absorption in blood samples is low between 600 nm and 1100 nm wavelength, which offers a good compromise between pronounced haemoglobin absorption at shorter wavelengths and strong water absorption at longer wavelengths [40]. Therefore, silicon nitride is chosen as the waveguide material in this work.

On-chip light sources on the silicon nitride platform are examined only rarely so far. For the visible wavelength range, integrated laser sources were presented with perovskites [41], [42] or CdS/CdSe quantum dots [43] as gain media, and were combined with passive silicon nitride waveguides. These approaches require relatively complex manufacturing processes, including material deposition from the gas phase and subsequent lithographic structuring. Both techniques are rather sophisticated and suitable for long-lasting devices, e.g., in the area of optical communications, but they are too lavish for disposable chips used in point of-care diagnostics.

The goal of this thesis is to explore a waveguide-based sensor chip, which is compatible with the requirements of point-of care diagnostics. Silicon nitride is used as waveguide material, and visible light at approximately 600 nm is used for sensor operation to meet the criteria of low absorption in aqueous analyte solutions. A new class of integrated laser source is investigated and adapted for sensor operation. The investigated Si_3N_4-organic hybrid laser (SiNOH) combines an organic gain medium with passive silicon nitride waveguides. Large scale deposition of the gain medium is possible via dispensing, spin coating, or inkjet-printing. The SiNOH laser can be pumped from the top with a laser diode or with light-emitting diodes (LED) without stringent alignment tolerances. In this work, for the first time an organic laser source is integrated on the silicon nitride platform and its performance is investigated. To design the waveguide sensor, a study is performed to obtain a universal metric that allows the comparison of various waveguide platforms and geometries. This study results in design guidelines for sensor waveguides that can be adapted to many applications. In this work, a Mach-Zehnder interferometer is developed as a sensor element that meets the criteria of low propagation loss and high sensitivity in combination with robustness with respect to fabrication inaccuracies. To demonstrate the functionality of the sensor, a waveguide bio-functionalization is developed and applied to detect various concentrations of streptavidin as a proof of concept. For exposure of the sensors to the analyte solution, a microfluidic chamber is designed that allows the continuous exchange of the analyte solution on the sensor waveguides without disturbing the on-chip laser or the light-coupling ports. In a final experiment, the SiNOH laser and the waveguide sensors are combined on the same chip. The SiNOH laser is pumped from free space with a simple focussing lens, whereas the sensor signal is detected with a CCD camera. In a first evaluation step the functionality of this new on-chip sensor system is demonstrated by detecting various concentrations of fibrinogen.

The experimental results in this work demonstrate the versatility of the device concepts, the simple operation principle, and the compatibility with cost-efficient mass production. The demonstrations show the viability of the concept and represent an important milestone in the development efforts towards high-performance practical and low-cost point-of-care systems.

2 Photonic devices, materials and fabrication technology

Nanophotonic waveguide (WG) sensors that are made from silicon or silicon nitride (Si_3N_4) are highly sensitive and open a path towards parallel highly multiplexed detection of a large variety of disease markers in bodily fluids [15]. Most of these sensors exploiting, e.g., ring resonators or Mach-Zehnder-interferometers (MZI), are based on single-mode (SM) WG with transverse dimensions in the sub-micrometer regime. As a consequence, coupling of laser light to these WG is a challenge in its own right, which is currently met by on-chip grating couplers (GC) or by focusing the light on a facet of a WG. However, both options require high-precision sub-µm alignment of the laser beam and of the coupling region. This requires precise mechanical alignment, thereby rendering the underlying read-out systems expensive, sensitive, and difficult to use.

This work aims at exploring concepts of WG-based sensor chips that can be used outside controlled laboratory environments. The basic approach is shown in Figure 2.1(a). A Si_3N_4-organic hybrid (SiNOH) laser is integrated on the sensor chip and optically pumped from the top by an external light source. The emitted light of the SiNOH laser is directly coupled to the SM output WG. The output WG directs the light to a sensor, labeled as MZI in Figure 2.1(a). The WG of the sensor are integrated into a microfluidic chamber for direct contact with the analyte of interest. At the sensor output, the light is radiated upwards via a GC. Eventually the light is captured by a camera for signal detection. Excitation and detection are contactless, avoiding precise alignment between the sensor chip and the pump laser or the camera. This concept should enable simple and easy operation.

The SiNOH laser consists of a Si_3N_4 WG core on a silicon dioxide (SiO_2) layer that serves as the bottom cladding, Figure 2.1(b). Optical gain is provided by an organic top cladding from poly(methyl methacrylate) (PMMA) that is doped with an organic laser dye. The sensor WG relies on the same Si_3N_4 core Figure 2.1(c), but lacks a top cladding such that the surface is in direct contact

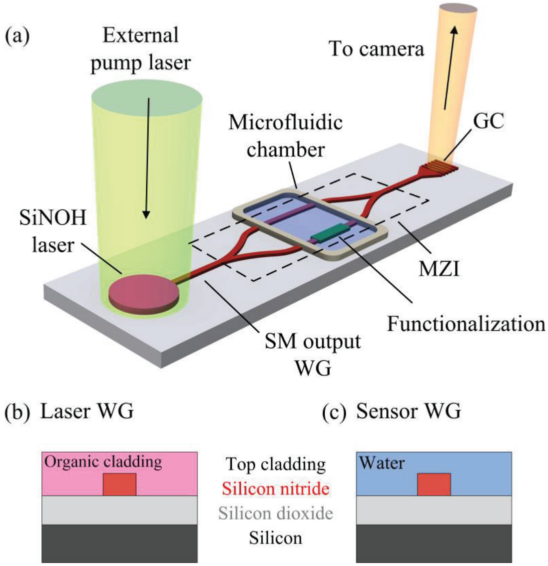

Figure 2.1: Schematic of the integrated sensor chip, consisting of a SiNOH laser and a co-integrated biosensor. **(a)** The SiNOH laser is optically pumped from the top by an external pump laser. The emitted light of the SiNOH laser is directly coupled to the SM output WG and guided to the sensor, illustrated here as an MZI. The WG of the sensor are integrated into a microfluidic chamber to get in direct contact with the analyte of interest. At the sensor output, the light is radiated upwards via a GC, where the light is captured by a camera for signal detection. **(b)**,**(c)** The laser and the sensor WG consist of a Si_3N_4 WG core on a SiO_2 bottom cladding that is supported by a silicon handle wafer. **(b)** The top cladding of the laser WG consists of an organic cladding, whereas the top cladding of the sensor WG consists of the aqueous analyte solution **(c)**.

with the aqueous analyte solutions, e.g., saliva or urine, inside the fluidic chamber. As a consequence, the core of the laser WG is patterned along with the sensor WG core, and an additional lithography step is not required. The organic top cladding of the SiNOH laser can be subsequently dispensed or printed locally. For specific detection of target analytes, the surface is modified by attaching suitable molecules, to which the target molecules can bind. This surface modification is called functionalization.

This chapter deals with the basic devices and materials used to form the integrated sensor chip. The structuring process of the Si_3N_4 WG and nanophotonic devices in general is described in Section 2.1. Optical parameters of the strip WG that form the lasers and sensors are discussed in Section 2.3, where also the design and characterization of GC is shown. The investigation of Mach-Zehnder interferometers is discussed in Section 2.4.

2.1 Fabrication of nanophotonic waveguides and devices

A fabrication process for nanophotonic structures is not only influenced by the material system of the chip, but also by the form and feature sizes of the final devices, the quality and composition of the used chemicals, and the available specific infrastructure. The whole fabrication process of the WG chips described here was developed and carried out at the Institute of Microstructure Technology (IMT) at Karlsruhe Institute of Technology (KIT). The qualitative fabrication process and a short discussion of the usability and quality of different electron beam resists are presented in the following paragraphs. A detailed protocol of the fabrication process can be found in Appendix A.

The used wafers (Active Business Company GmbH, Munich) consist of a stoichiometric 200 nm-thick Si_3N_4 layer that was deposited via low-pressure chemical vapor deposition (LPCVD) on a 2 µm-thick amorphous SiO_2 layer. The SiO_2 layer was deposited by chemical vapor deposition (CVD) and is mechanically supported by a silicon layer of 500 µm thickness, Figure 2.2(a). The SiO_2 layer acts as a lower cladding for the structured WG. Before the structuring, the wafer is diced into chips of $(2\times2)\ \mathrm{cm}^2$ size. To this end, the surface of the wafer is covered with a protective polymer that is removed after dicing by spray cleaning.

In the first step the WG cores are structured on the chips, Figure 2.2(a)-(d). To this end, the negative-tone resist ARN.7520.12 (Allresist GmbH, Strausberg) is spin-coated on the surface of the chip and subsequently exposed to an electron beam, according to the desired layout, Figure 2.2(b), Appendix A.1. All unexposed areas of the resist are removed by spray developing (AR 300-47, Allresist GmbH, Strausberg), and the remaining exposed parts are used as an etch mask according to the layout, Figure 2.2(c). The etch mask is transferred to the Si_3N_4 layer with reactive ion etching, Figure 2.2(d), Appendix A.2. Residual resist is removed with an oxygen plasma.

In a second step, the upper cladding is deposited, Appendix A.3. First, the negative-tone electron beam resist mr-X2-P2-XP (micro resist technology GmbH, Ulm) is spin-coated and exposed by electron-beam lithography, Figure 2.2(e). Development in a beaker is used to remove the cladding on parts of the WG, Figure 2.2(f), and the subsequent curing with ultraviolet (UV) light provides an enhanced chemical stability, Figure 2.2(g). In the resulting cladding openings, functional layers are deposited on the WG cores. For the laser parts, the gain medium is dispensed or spin coated on the chip. For the

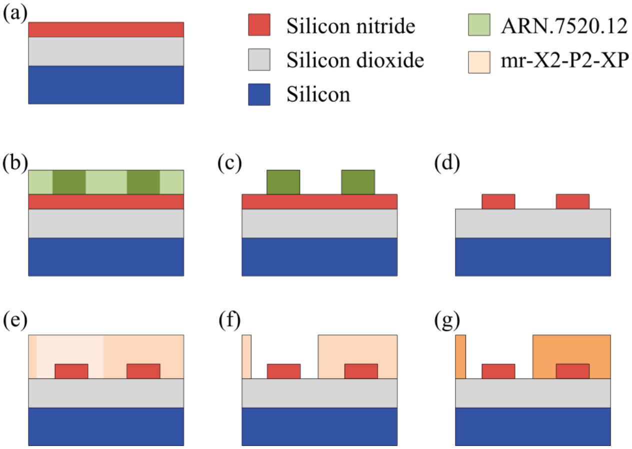

Figure 2.2: Fabrication of the Si_3N_4 WG. **(a)** The Si_3N_4 layer (red) is on top of a SiO_2 layer (grey) that is supported by a thick Si layer (blue). **(b)** To structure the Si_3N_4 layer a resist is spin coated on top of the chip (light green) and exposed by electron-beam lithography (dark green). **(c)** The resist is developed and an etch mask according to the layout remains on top of the Si_3N_4. **(d)** The etch mask is transferred to the Si_3N_4 layer with reactive ion etching, and the residual resist is removed with an oxygen plasma. **(e)** The top cladding of the WG is formed by a layer of the negative resist mr-X2-P2-XP (light ochre) which is then exposed by electron-beam lithography (dark ochre). **(f)** The unexposed regions of the second resist are removed to open the cladding for functional modifications or application of dye-doped polymers in the gain section of SiNOH lasers. **(g)** The resist is cured with UV light to provide a good chemical stability (orange).

sensors, either the chip has to be incubated, or solution-based dispensing is used to immobilize functional layers.

For the structuring of Si_3N_3 WG, three different negative-tone electron-beam resists have been examined to form the etch mask. The properties of all resists are discussed in the following paragraphs.

ARN.7520.12 (Allresist GmbH, Strausberg) is an organic negative-tone resist that has a high resolution of 28 nm for structuring with electron beam lithography [44]. Residual resist is removed with an oxygen plasma, or with acetone after etching. The electron-beam exposure uses a relatively high dose of approximately $1500\,\mu C/cm^2$. In Figure 2.3(a), scanning electron microscope images of structured ARN are shown. The surface appears smooth, and the sidewalls of the lines are steep (cannot be seen in figure Figure 2.3(a)). In the magnified image on the right-hand side the surface structuring of cross-linked resist can be seen.

ma-N 2403 (micro resist technology GmbH, Ulm) is an organic negative-tone resist that has a high resolution of 50 nm [45]. Residual resist can be removed with an oxygen plasma, or with acetone after etching. The electron-beam exposure is done with a relatively low dose of $220\mu C/cm^2$. In Figure 2.3(b), scanning electron microscope images of an ma-N structure are shown. The sidewalls are steep (cannot be seen in figure Figure 2.3(b)). On the surface and

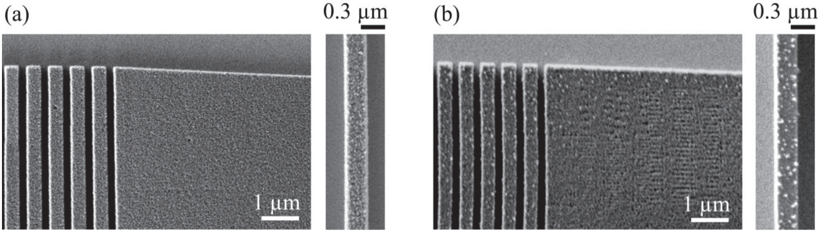

Figure 2.3: Scanning electron microscope images of structured electron beam resists. **(a)** ARN.7520.12. The surface appears smooth and the sidewalls are steep. In the magnified image on the right-hand side the structure of the cross-linked resist can be seen. **(b)** ma-N 2403. Agglomerates appear on the edges of large structures, left-hand side picture, and on the whole surface of small structures, right-hand side picture. In the middle of large structures, no agglomerates are visible.

at the sidewalls, small agglomerates with $(10...50)\,\text{nm}$ diameter are visible. In the center of large structures, left-hand side picture in Figure 2.3(b), no agglomerates are visible; however, the edges and the complete surface of small structures are covered with these agglomerates, right-hand side picture of Figure 2.3(b). Further investigations showed that the density of these agglomerates depends on the electron-beam properties, defined by beam parameters, e.g., dose and beam diameter. It was not possible to find a set of beam-parameters for the desired structures without agglomerates. A transfer of the agglomerates to the Si_3N_4 during etching can be expected.

XR-1541 (HSQ-6%, EM Resist Ltd, Prestbury) is a negative-tone resist with a very high resolution of 10 nm [46]. The molecular structure of cross-linked HSQ is similar to SiO_2. After etching, residual HSQ can be removed with hydrofluoric acid (HF). The etch rate of SiO_2 in HF is 26 times larger compared to the etch rate of Si_3N_4 [47]. It should be mentioned that the SiO_2 bottom substrate is etched in parallel to HSQ, hence there might be undercutting of Si_3N_4 structures. After electron beam exposure with a dose of $1000\,\mu\text{C}/\text{cm}^2$, the resist surface is smooth and the sidewalls are steep. The thickness of spin coated HSQ is limited to approximately 230 nm [46]. Selectivity during the Si_3N_4 etch process is low; experiments show that the mask is completely stripped before a relatively thin layer of 200 nm of Si_3N_4 is etched. Therefore HSQ is not suitable for structuring of Si_3N_4 WG.

2.2 Optical properties of strip waveguides

The basis of the sensors and SiNOH lasers examined in this work are strip WG. For both, sensors and lasers, single-mode operation and large overlap of the WG mode with the top cladding are essential for optimized performance. During sensing experiments, changing analytes or binding of molecules to the surface of the WG core change the refractive index of the top cladding and the propagation constant of the guided mode. The larger the parts of the mode that are guided in the top cladding, the larger is the change of the propagation constant and the associated phase shift that is obtained for a given refractive index change in the environment of the WG. Depending on the geometry of the WG, more than one light mode (fundamental mode) can be guided. These higher order modes show different overlaps with the cladding material, and thus different phase shifts for the same index change in the cladding. As a result, read-out is more complex because the modes must be filtered. Single-mode operation is hence preferred. In SiNOH WG, gain is provided in the top cladding due to stimulated emission. The larger the overlap of the light mode with the top cladding is, the more gain can be provided. For the sensor chips discussed here, the light of the SiNOH laser is guided directly to the single-mode sensor WG, therefore operation of the laser in the fundamental transverse mode of the underlying WG is preferred.

The following Subsection 2.2.1 discusses the optical properties of sensor and SiNOH WG. In particular, the effective refractive index, the number of guided modes and the overlap with the top cladding are investigated. Subsection 2.2.2 discusses the SiNOH WG and in particular the gain.

2.2.1 Passive sensor and SiNOH waveguides

The propagation of a plane wave with vacuum wavelength λ in a homogeneous medium with refractive index n is defined by the propagation constant $\beta = nk_0$, with vacuum propagation constant $k_0 = 2\pi/\lambda$ [48]. In a dielectric WG, the light is guided by a high refractive index core which is clad by a low refractive index medium. In this work, mainly strip WG with Si_3N_4 core and SiO_2 bottom cladding are used, Figure 2.4(a). The height of the WG

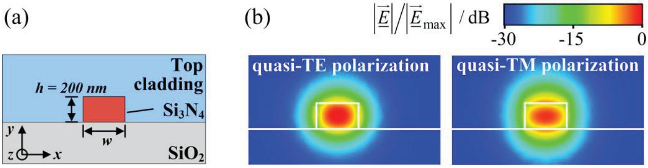

Figure 2.4: Waveguide geometry, materials and mode simulations. **(a)** The strip WG consists of a WG core from Si_3N_4, a bottom cladding of SiO_2 and a top cladding, which is either water (sensor WG) or PMMA (SiNOH WG). The WG core has a fixed height of $h = 200$ nm and a variable width w. **(b)** Simulated normalized electric field magnitudes are exemplarily shown for both the fundamental quasi-TE polarized mode (left-hand side) and the fundamental quasi-TM polarized mode (right-hand side). The width of the simulated WG amounts to 300 nm. For both modes, large parts of the electric field are guided in the WG core. Smaller parts are also guided in the cladding regions.

core is defined by the layer thickness of the initial Si_3N_4 layer, i.e., $h = 200\,\mathrm{nm}$. The WG width w can be chosen freely and is only limited by the technical constrains of the lithography process. The mode field distribution was simulated for different WG widths. Figure 2.4(b) shows normalized electric field magnitudes of the fundamental quasi-transverse electric (quasi-TE) polarized mode, left-hand side, and of the fundamental quasi-transverse magnetic (quasi-TM) polarized mode, right-hand side. A mode is called quasi-TE, if the dominant part of the mode is TE-polarized and is named quasi-TM, if the dominant part of the field is TM-polarized. All simulations were performed with the commercial available software package Computer Simulation Technology Studio Suite (CST Studio Suite, SIMULIA). Port modes were calculated with the frequency-domain solver and a tetrahedral mesh. For the laser WG, the top cladding consists of PMMA doped with a laser dye. For the simulations, a pure PMMA cladding is assumed. For the sensor WG, the top cladding consists of an aqueous analyte solution. For the simulations, pure water is assumed. Table 2.1 lists all used materials, their refractive indices n and their group refractive indices $n_\mathrm{g} = n - \lambda\, \mathrm{d}n/\mathrm{d}\lambda$ [48] at room temperature and for a wavelength of $\lambda = 600\,\mathrm{nm}$. Large parts of the electric field are guided in the WG core for both polarizations. Nevertheless, smaller parts of the electric field are also guided in the cladding regions. For the quasi-TE mode, larger parts are guided near the sidewalls of the WG core, whereas for quasi-TM polarized modes larger parts are guided close to the top and the bottom of the WG core.

The field distributions of the light wave in all WG parts determine the WG propagation constant β which can be expressed by the effective refractive index $n_\mathrm{e} = \beta/k_0$. Figure 2.5 shows simulated effective refractive indices for WG with PMMA top cladding $n_\mathrm{PMMA} = 1.49$, Figure 2.5 (a), and with water

Table 2.1: Refractive indices n and group refractive indices n_g of all used WG materials at wavelength $\lambda = 600$ nm.

Material	$n(\lambda = 600\ \mathrm{nm})$	$n_\mathrm{g}(\lambda = 600\ \mathrm{nm})$
Si_3N_4	2.02 [49]	2.1 [49]
SiO_2	1.46 [50]	1.48 [50]
H_2O	1.33 [51]	1.35 [51]
PMMA	1.49 [52]	1.52 [52]

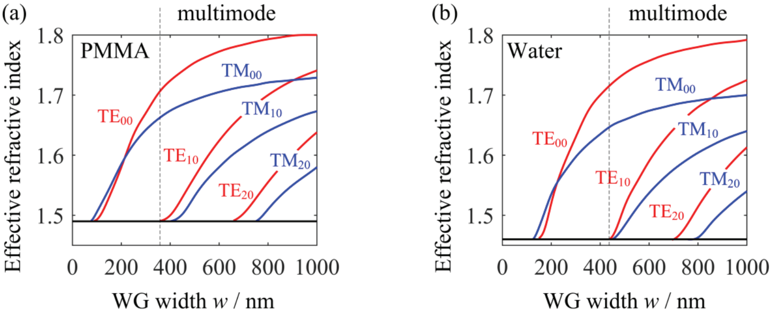

Figure 2.5: Simulated width-dependence of the effective refractive index n_e for the Si_3N_4 WG with water **(a)** or PMMA **(b)** as the top cladding. The WG height amounts to $h = 200$ nm. Effective refractive indices are depicted for quasi-TE polarization, red lines, and quasi-TM polarization, blue lines. The fundamental modes are called TE_{00} and TM_{00}. In addition, for each polarization the next two higher order modes are shown: TE_{10}, TE_{20} and TM_{10}, TM_{20}. **(a)** PMMA as a top cladding. The black horizontal line at the bottom marks the refractive index of PMMA. If the WG width is too small, the mode is mainly guided in PMMA and the light is eventually lost. For all modes the effective refractive index increases for larger WG widths. For the same WG cross section and the same mode-order quasi-TE modes have a larger n_e than quasi-TM modes. Only for narrow WG cores TE_{00} shows a smaller n_e than TM_{00}. The increase is larger for quasi-TE polarized modes compared to quasi-TM polarized modes. For WG widths smaller than 350 nm the WG is single-moded. For WG widths larger than 350 nm also higher order modes can be guided. **(b)** Water as a top cladding. The black horizontal line marks the refractive index of the silicon dioxide bottom cladding that is larger than the water top cladding ($n_{H_2O} = 1.33$). The fundamental quasi-TM mode is guided for smaller WG widths than the fundamental quasi-TE mode. For WG width larger than 450 nm not only the fundamental modes can be guided but also higher order modes.

top cladding $n_{H_2O} = 1.33$, Figure 2.5(b), for different WG widths. Quasi-TE modes are depicted by red lines and quasi-TM modes with blue lines. Different orders of modes are marked by TE_{mn} and TM_{nm}. The subscripts n and m are positive integers and represent the number of mode zero-crossings of the dominant transverse field component along the WG width and the WG height, respectively. For each polarization the fundamental mode TE_{00} and TM_{00} and the next two higher order modes TE_{10}, TE_{20} and TM_{10}, TM_{20} are shown.

For all modes, n_e increases for larger WG widths w, as larger parts of the modes are confined to the WG core. Therefore, n_e converges to the refractive index of Si_3N_4. Top and bottom cladding have often different refractive indices. The smaller the WG core, the larger the part of the mode that is guided in the cladding part that has the larger refractive index. For the SiNOH WG this applies to the top cladding made from PMMA, for sensor WG this applies to the bottom cladding consisting of silicon dioxide, Table 2.1. The black horizontal line marks the refractive index of the part of the cladding with larger refractive index, respectively. Towards smaller WG widths, the mode is guided until the effective refractive index eventually reaches the highest refractive index of the cladding region. For even smaller w the mode cannot be guided in the WG; the mode is cut off for the given frequency. The number of modes that can be guided in the WG depends on the wavelength, the geometry and the difference of the refractive index between core and cladding. Here, only w is varied. For the PMMA top cladding, the WG becomes multimoded for widths larger than 350 nm, whereas for the water top cladding, the WG becomes multimoded for widths larger than 450 nm.

For the PMMA top cladding and narrow WG cores with $w < 200\,\mathrm{nm}$, n_e of TE_{00} is smaller than n_e of TM_{00}. For larger WG cores this trend is inverted. This can be explained by the WG geometry. The WG core has a fixed height of $h = 200\,\mathrm{nm}$. At the intersection point of the curves the WG core has a squared cross-section, and both, quasi-TE and quasi-TM polarized modes, are confined approximately equally. For smaller w the quasi-TM polarized mode is stronger confined to the core, whereas for larger w quasi-TE polarized modes are confined stronger. For the water top cladding, this intersection point is slightly shifted to larger WG cores. The cladding asymmetry of water and SiO_2 for the WG is larger compared to the cladding asymmetry of the SiNOH WG (PMMA and SiO_2), shifting the intersection point to $w = 250\,\mathrm{nm}$.

For both, the sensor and laser WG, the part of the mode that is guided in the top cladding is of special interest. For the sensor WG, the aqueous analyte is to be examined, and a large overlap of the light mode with the cladding leads to large phase shifts. For the laser WG, a large confinement in the cladding, and therefore large optical gain, in combination with low propagation loss leads to low lasing thresholds ([48], Chapter 15). The modes can be described with a complex vectorial electric mode field $\mathbf{E}(\omega,\mathbf{r})$ and a magnetic mode field $\mathbf{H}(\omega,\mathbf{r})$ that depend on the angular frequency ω and the position vector $\mathbf{r}$. If loss is neglected, the cross-sectional power of a guided mode is constant along the propagation direction. The overlap of the mode with a partial volume V_i related to a unit cell with total volume V can be described by the confinement factor. The confinement factor has values between 0 and 1. Here, the material in the partial volume has a constant refractive index n_i and a constant associated group index $n_{\mathrm{g},i} = n_i + \omega\,\partial n_i / \partial\omega$. The confinement factor represents the ratio of the mode energy in a partial volume V_i related to the energy in the total volume V of a unit cell with cross sectional area A and length a [53]:

$$\Gamma_i^{(\mathrm{conf})} = \frac{\iint_{A_i} n_i n_{\mathrm{g},i} |\mathbf{E}|^2 \,\mathrm{d}V}{\iint_{A} n n_\mathrm{g} |\mathbf{E}|^2 \,\mathrm{d}V} = \frac{W_i}{W}. \tag{2.1}$$

For WG that are invariant along the propagation direction, e.g., strip WG, the volume element is $\mathrm{d}V = a\,\mathrm{d}A$.

Figure 2.6 shows the simulated $\Gamma_{\text{Top cladding}}^{(\mathrm{conf})}$ that is the fraction of the mode confined to the top cladding, partial volume $V_i = V_{\text{Top Cladding}}$. The confinement factor was simulated for different WG widths w with a fixed WG height of $h = 200$ nm and materials as shown in Figure 2.4(a). Red dashed lines show $\Gamma_{\text{Top cladding}}^{(\mathrm{conf})}$ for the fundamental quasi-TE mode TE_{00}, blue dashed lines for the fundamental quasi-TM mode TM_{00}. Figure 2.6(a) shows the simulated results for PMMA as a top cladding, and Figure 2.6(b) for water as a top cladding.

For laser WG (PMMA top cladding), $\Gamma_{\text{Top cladding}}^{(\mathrm{conf})}$ decreases with larger w. For smaller w the mode is weakly guided and most parts are confined to the top cladding exhibiting a larger refractive index than the bottom cladding. The wider the WG, the larger the confinement to the WG core, and the smaller the overlap with PMMA. For $w < 200\,\mathrm{nm}$, TE_{00} is stronger confined to the cladding than TM_{00}, whereas for larger w this trend is inverted. Again, this can be explained by the geometry of the WG core. In high and narrow WG cores, TM_{00} is stronger confined to the WG core, whereas in wide WG cores the situation is the other way around.

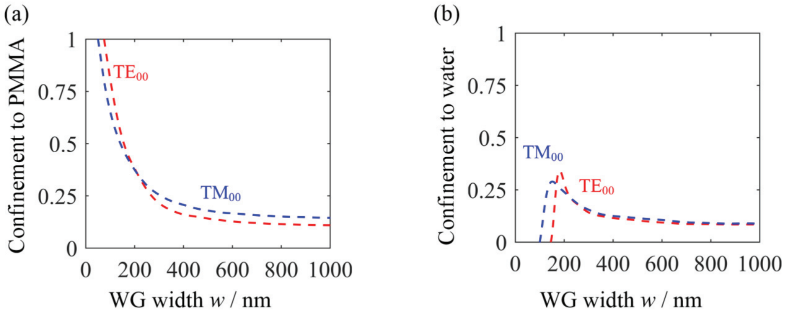

Figure 2.6: Simulated $\Gamma^{\text{(conf)}}_{\text{Top cladding}}$ for different WG widths. Red dashed lines show values for the fundamental quasi-TE mode TE_{00}, blue dashed lines for the fundamental quasi-TM mode TM_{00}. **(a)** PMMA as top cladding. For both polarizations, $\Gamma^{\text{(conf)}}_{\text{Top cladding}}$ decreases for wider WG, as the mode becomes more confined to the WG core. For small WG widths, larger fractions of the mode are guided in the top cladding with larger refractive index ($n_{\text{PMMA}} = 1.49$) compared to that of the bottom cladding ($n_{\text{SiO}_2} = 1.46$). **(b)** Water as top cladding. For both polarizations $\Gamma^{\text{(conf)}}_{\text{Top cladding}}$ shows a maximum. For larger *w*, large parts of the mode are confined to the WG core. For smaller *w*, large parts of the mode are confined to the bottom cladding that has a larger refractive index than water $n_{\text{H}_2\text{O}} = 1.33$.

For sensor WG (water as top cladding) $\Gamma^{\text{(conf)}}_{\text{Top cladding}}$ also decreases for larger *w*, but the trend for small *w* is different. The refractive index of the bottom cladding is much larger than that of water. Hence, $\Gamma^{\text{(conf)}}_{\text{Top cladding}}$ vanishes for water cladding and small *w*, for which the mode is strongly confined to the bottom cladding. For both polarizations a maximum for $\Gamma^{\text{(conf)}}_{\text{Top cladding}}$ is found. For TE_{00} the maximum is located at $w = 190\,\text{nm}$ and for TM_{00} the maximum is located at $w = 160\,\text{nm}$. The maximum $\Gamma^{\text{(conf)}}_{\text{Top cladding}}$ for TE_{00} is slightly larger than for TM_{00}. For WG widths $w > 250\,\text{nm}$, $\Gamma^{\text{(conf)}}_{\text{Top cladding}}$ shows almost the same values for TE_{00} and TM_{00}.

2.2.2 Si_3N_4-organic hybrid waveguides

A Si_3N_4-organic hybrid (SiNOH) WG is formed by a Si_3N_4 WG core with SiO_2 as the bottom cladding and an organic medium as the top cladding. The organic medium consists of a polymer with an embedded laser dye and serves as the gain medium. The resonator is formed by the SiNOH WG and can have various geometries, e.g., a ring or a distributed-feedback grating. Figure 2.7(a) shows the cross section of a strip WG along with the simulated electric field magnitudes $|\mathbf{E}|$ of the fundamental quasi-TE and quasi-TM mode. Simulations were performed with the frequency-domain solver of CST Studio Suite. When the gain medium is pumped, the laser dyes are excited. Near the WG core, parts of the electric field are located in the organic gain medium. The effective modal gain g (unit cm^{-1}) of the laser WG results from the stimulated emission in these regions. The larger the field amplitudes in the organic gain medium are, the more gain the mode experiences. Figure 2.6(a) shows the confinement factor, Equation (2.1), of a WG in the organic gain medium for a strip WG with height $h = 200\,\text{nm}$ and varying width w. The smaller the width, the larger the confinement factor and thus the larger the effective modal gain is. Note that the net power gain G of a resonator with round-trip length $2L$ also depends on the loss coefficient α (unit cm^{-1}), $G = \exp\left[(g-\alpha)2L\right]$ [54]. A larger effective modal gain does not necessarily mean a larger net power gain.

Molecular structure of Pyrromethene 597 For the SiNOH lasers, PMMA is used as an organic cladding. The gain is provided by the organic laser dye PM597 (Pyrromethene 597, Radiant Dyes Laser & Accessories GmbH, Wermelskirchen) which is dissolved in PMMA with a concentration of $25\,\mu\text{mol/g}$. Figure 2.7(b) shows the molecular structure of PM597. Pyrromethene 597 consists mostly of carbon and hydrogen atoms. Carbon has six electrons that can be described by s and p orbitals. In the ground state, the $1s$ orbital is occupied by two electrons, the $2s$ orbital is also fully occupied by

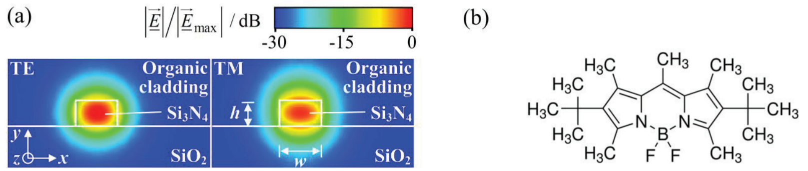

Figure 2.7: Properties of SiNOH WG. **(a)** Cross section of a strip WG with width w and height h along with simulated electric field magnitudes $|\mathbf{E}|$ of the fundamental quasi-TE and quasi-TM mode. Large parts of the electric field propagate in the organic cladding material. If the gain medium is pumped, these parts can cause stimulated emission. **(b)** Structural formula of the laser dye PM597. Double bonds in the ring structures indicate delocalized π-electrons.

two electrons, and two (out of three) *p* orbitals are occupied with one electron each. This results in the ground state configuration $1s^2 2s^2 2p^2$ [55]. When a carbon atom connects to other atoms via four single bonds, a process called hybridization mixes one 2s and three 2p orbitals together to make four equivalent sp^3 hybrid orbitals in a tetrahedral arrangement around the carbon atom, called σ bonds [56]. In the ring structures of PM597, carbon atoms bind also via double bonds to their neighbors, Figure 2.7(b). In doing so, only two *p* orbitals undergo hybridization with the 2*s* orbital resulting in three sp^2 orbitals and one $2p^2$ orbital. A double bond is formed by one sp^2 orbital and by one $2p^2$ orbital of the carbon atom that connect with similar orbitals of another molecule forming a strong σ bond and a weaker π bond [57]. The ring structures in PM597 show alternating double and single bonds that are called π-conjugated. This system allows the π-electrons to be delocalized over the whole conjugated segment, e.g., the π-electrons do not belong to a single bond but to the whole π-conjugated system.

Absorption and emission of light. The ring structures in PM597 show many alternating weaker π bonds and strong σ bonds. The delocalized electrons in the π-conjugated system allow the molecule to form different molecular orbitals that have different energy states. These energy states are close to each other. As more molecular orbitals are formed, the energy gap ΔW between the highest occupied molecular orbital (HOMO) and the lowest unoccupied molecular orbital (LUMO) becomes smaller. The molecule can absorb and emit photons by transiting between these orbitals. Typical energy gaps ΔW between HOMO and LUMO for organic dyes result in photons in the wavelength range between the near infrared and the near ultraviolet [56].

The molecular orbitals of such π-conjugated systems can be translated into different electronic energy states. The energy states split into various vibrational states. In the electronic ground state S_0 (HOMO) of the organic laser dye, all valence electrons are paired (reverse spins) with a total spin $s = 1/2 - 1/2 = 0$. When a photon is absorbed, a valence electron can transit to a higher electronic state S_1 (LUMO), its pairing partner remains in the former state. For relaxation, there are various possibilities.

A Jablonski diagram illustrates transitions of the valence electron between various energy states, Figure 2.8. The horizontal axis shows the spin multiplicity $2s+1$ of the molecule; electronic states with multiplicity 1 are called singlet states; electronic states with multiplicity 3 are called triplet states. On the vertical axis the energy of the molecule is shown. Electronic states S_0, S_1 and T_1 are split into several vibrational states (black lines). The vibrational ground state for each electronic state is indicated with a thick black line. Higher order vibrational states are indicated with thinner black lines. Note that only the first excited electronic states are shown in Figure 2.8. There are excited states at larger energies $S_{2,3,...}$ and $T_{2,3,...}$ that are not relevant for the basic absorption and emission mechanisms discussed here. Transitions between the different states are indicated with arrows. Blue arrows are used for photon absorption, green arrows for radiative relaxations, called emissions. Magenta-colored dashed arrows indicate non-radiative transitions.

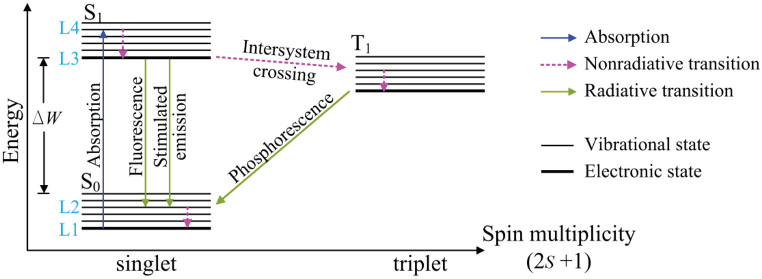

Figure 2.8: Jablonski diagram for organic laser dyes. Energy states are depicted for different spin multiplicities. Only the fundamental singlet S_0 and the first excited singlet S_1 and triplet T_1 electronic states are shown. Vibrational levels are shown as narrow black lines, the fundamental vibrational levels are shown as thick black lines. For laser operation, the laser dye is pumped from the S_0 ground state (L1) to a short-lived (fs-range) vibrational level of the S_1 state (L4), blue arrow. Relaxation to the long-lived (ns-range) ground level is fast and non-radiative, magenta dashed arrow (L3). The relaxation from L3 to a short-lived vibrational level (L2) occurs ideally by stimulated emission, green arrow. As L4 and L2 are short-lived they can be seen as non-occupied during laser operation and the laser dye behaves like a four-level gain medium. Stimulated emission competes with spontaneous emission, green arrow, and nonradiative transitions, e.g., intersystem crossings, magenta dashed arrow. For an intersystem crossing, the molecule transits to a state with different multiplicity. From the S_1 state to the triplet state T_1 the spin of the exited electron flips. Therefore, the transition to the S_0 state is spin forbidden. Triplet states are long-lived, and the emission of a photon during relaxation to the S_0 state is known as phosphorescence, green arrow.

In the ground state, all valence electrons are paired and the spin multiplicity is 1, hence the ground state S_0 is described as a singlet state. If a photon with energy $W_{\mathrm{ph}} > \Delta W$ is absorbed, a molecule in the ground state S_0 might transit to a vibrational state of the excited singlet state S_1, Figure 2.8., blue arrow. The lifetime of higher vibrational states lies in the fs-range ([56] Chapter 1) and the molecule relaxes to the vibrational ground state of the electronic S_1 state, magenta dashed arrow. The lowest level of the S_1 state is a long-lived level in the ns-range ([56] Chapter 1). From there the molecule relaxes to a vibrational level of the S_0 state, either by radiating a photon, a process called fluorescence, green arrow, or by transferring the energy via non-radiative mechanisms to its environment, not shown in Figure 2.8. This vibrational level has a very short lifetime in the fs-range, and the molecule relaxes to the ground state, magenta dashed arrow. Before the molecule relaxes from the S_1 level to the S_0 level, also stimulated emission can occur, green arrow. A photon that is, e.g., trapped in a laser resonator, can induce the emission of another photon with same energy, while the molecule relaxes to the S_0 state. Therefore, organic laser dyes behave like four-level gain media, [56], Chapter 1. Pumping occurs between the long-lived energy level L1 and the short-lived energy level L4, magenta in Figure 2.8, whereas laser emission occurs between the long-lived energy level L3 and the short-lived energy level L2. As L4 and L2 are short-lived, they can be seen as non-occupied during laser operation. Therefore, a population inversion occurs easily between level 3 and 2, if the laser dyes are pumped, [48] Chapter 14.

Transitions between the respective states take place with different probabilities. The more the orbital of the target state overlaps with the orbital of the starting state, the more likely is the transition. This probability can be specified with wavelength (energy)-dependent transition cross sections of the dye molecule. Before photon absorption, the dye molecule is in the electronic ground state. The associated absorption cross section of PM597 in PMMA is shown in Figure 2.9, green curve. The maximum of the absorption cross section is at a wavelength of 523 nm. At this wavelength a transition is most likely and, therefore, optical pumping of the gain medium is most efficient.

The same considerations hold for the emission transition. In this case, a mechanism according to fluorescence may occur, for which the starting state

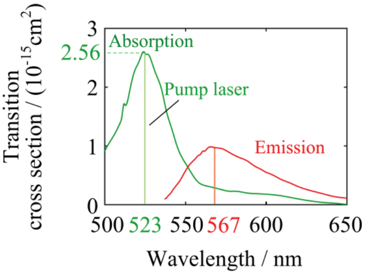

Figure 2.9: Transition cross section of PM597 in PMMA. The maximum of the absorption cross section (green curve) is at shorter wavelengths than the maximum of the emission cross-section (red curve). Some energy of the absorbed photon is transferred to the environment of the molecule when the molecule transits from higher excited vibrational states to the ground state of the electronic states. For high pump efficiencies the SiNOH laser is pumped near the absorption maximum, green line (σ_a (532 nm) = $2.56 \cdot 10^{-15}$ cm^2).

is the vibrational ground state of the first excited electronic state. The emission cross sections are related to the probabilities for transitions in distinct vibrational states of the electronic ground state, Figure 2.9, red curve. The maximum cross section is found at a wavelength of 565 nm, shifted to longer wavelengths compared to the maximum of the absorption cross section. This can be explained by the Stokes shift: Nonradiative transitions occur within the excited S_1 level and the ground state S_0, Figure 2.8, magenta dashed arrows, [58] Chapter 1. During this process, energy is transferred to the molecule's environment. When the photon transits between the electronic states, it has less energy compared to the photon that was absorbed before. The maximum of the emission cross section is smaller than that of the absorption cross section. This can be explained by nonradiative transitions from the excited S_1 level to the S_0 level.

For the SiNOH laser, emission at large emission cross sections is expected. At all wavelengths with absorption and emission cross sections larger than zero, reabsorption of emitted photons is possible. These photons cannot contribute to stimulated emission. In addition, the wavelength dependent net power gain of the laser resonator also depends on loss. The WG geometry or the laser resonator might suppress certain transverse or longitudinal WG modes.

So far, only transitions between singlet states and states with the same multiplicity were considered. For such transitions the spin of the excited electron remains anti-parallel and is quasi-paired with the spin of the remaining electron in the ground state. Transitions from the excited singlet state S_1 to the triplet state T_1 compete with fluorescence and stimulated emission. This so-called intersystem crossing occurs when flipping the spin of the excited electron and therefore uncoupling it from the electron in the ground state. During this mechanism, the multiplicity is changed and equals 3 for triplet states. The intersystem crossing from the T_1 state to the S_0 state is called phosphorescence, which requires a second spin flip and is therefore spin-forbidden, [58] Chapter 1. This leads to a rather long lifetime of the T_1 state in the µs-range [59]. During this duration, the ground state of the laser dye is depleted and cannot contribute to laser emission. The probability for an intersystem crossing from the excited singlet state S_1 to the triplet state T_1 is rather low for PM597 [60]. The probability is strongly influenced by the environment, e.g., by temperature [61] or medium composition [62].

Photodegradation. Generally, the lifetime of an organic laser dye is limited by photodegradation [59]. In excited states, laser dyes can absorb photons and can easily undergo irreversible chemical reactions with the environment which can prohibit light emission. Especially in the long-lived triplet states the probability of such reactions is increased [63].

A major factor that causes photodegradation is the reaction of laser dyes with singlet oxygen [62]. If a dye molecule undergoes an intersystem crossing, it can interact with oxygen that occurs naturally in the paramagnetic triplet state, and singlet oxygen is formed. In a second step, this singlet oxygen can react with dye molecules in the ground state and degrade the molecules [62]. The probability of intersystem crossings is increased by the presence of oxygen [62]. In addition, with higher pump intensities, also higher singlet states are excited. For each transition, there is a possibility that the molecule undergoes an intersystem crossing to one of the excited triplet molecules. The higher the pump intensity is, the more molecules are trapped in the long lived triplet states, and the more singlet oxygen is formed [63], leading to a stronger degradation.

2.3 Grating couplers

To couple light to and from the chip, grating couplers (GC) can be used, which diffract light coming from the top into an on-chip WG or from an on-chip WG to an out-of-plane direction. Typically, laser light is first coupled into a fiber, and the end face of the fiber is positioned on top of the GC. In both cases, µm-precise alignment is needed to achieve high coupling efficiency. The efficiency of this coupling is mainly dictated by the effective refractive index perturbation through the grating. Figure 2.10(a) shows a top-view schematic of a GC. At the beginning (or the end) of a WG, a periodic grating is etched into the Si_3N_4. The grating consists of alternating lands and grooves. The geometry can be described by the grating period a, the gap width d and the fill factor $\mathrm{FF} = (a-d)/a$. After the grating, the WG is tapered from the grating width to the final WG width. The laser light (vacuum wavelength λ) emitted from the fiber end-face propagates through the cladding medium with refractive index n_1, black arrow, Figure 2.10(b), and reaches the grating with an angle of incidence θ, measured with the cladding material respect to the surface-normal direction. In the cladding medium the light has a propagation constant $\beta_1 = n_1 k_0 = n_1 2\pi/\lambda$, with vacuum propagation constant k_0. Inside the WG with effective refractive index n_e, the light propagates in z-direction with propagation constant $\beta = n_\mathrm{e} k_0 = n_\mathrm{e} 2\pi/\lambda$. The laser light from

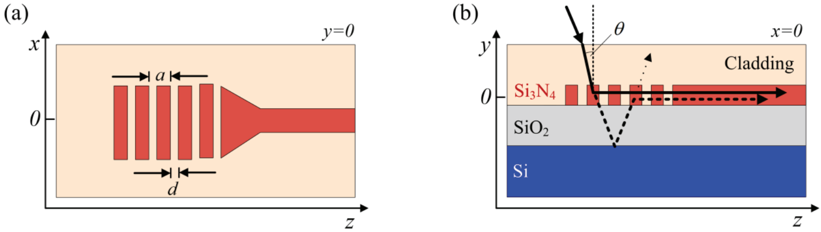

Figure 2.10: Sketch and beam paths of a GC. **(a)** Sketch of a GC at cross section $y = 0$. The geometry can be described by the grating period a and the gap width d. **(b)** Sketch of the GC at cross section $x = 0$. The incident beam, black solid line, is scattered by the grating into the WG. Parts of the beam are transmitted to the SiO_2 layer and reflected at the interface between SiO_2 and Si, dashed black line. Parts of the transmitted beam are afterwards scattered by the grating into the WG.

the fiber shall be coupled to this WG. Therefore, the component of the propagation constant along the *z*-direction can be expressed as $\beta_{1,z} = n_1 k_0 \sin(\theta)$. Together with the wavenumber of the grating $K = 2\pi/a$ the following phase matching condition results,

$$\begin{aligned} n_1 k_0 \sin(\theta) &= n_e k_0 + mK, \\ a &= \frac{m\lambda}{n_1 \sin(\theta) - n_\mathrm{e}}. \end{aligned} \tag{2.2}$$

The integer *m* is called diffraction order and Equation (2.2) is only fulfilled, for negative *m*. In a first step, coupling from the fiber to the WG with an incident angle of $\theta = 0$ is considered. Due to symmetry, light is coupled in both directions of the grating, along *z* and –*z* direction. Therefore, *θ* larger than 0° are preferred.

Due to reciprocity, Equation (2.2) holds for both, coupling light from the fiber to the WG and from the WG to the fiber. For efficient coupling to and from the WG, the period *a* has to be chosen in a way that only one diffraction order *m* fulfils Equation (2.2) for exciting guided modes in the WG. This can be understood by considering the inverse propagation direction. Light travels along the WG and is radiated from the GC to the fiber. If *a* is chosen to be large, more than one combination of *θ* and *m* exist that fulfil Equation (2.2). The power of the WG mode is distributed among all diffraction orders *m* to the cladding. Note that Equation (2.2) also holds for radiation to the substrate. If *a* is chosen to be small, with $(\beta - k_1)/2 < K \leq \beta$, Equation (2.2) only holds for $m = -1$ and only one beam of light is radiated to the cladding. Using a first-order grating with $m = -1$ and the target incident angle of $\theta = 10°$, 600 nm wavelength, $n_1 = 1.5$ and $n_\mathrm{e} = 1.75$, the period is calculated to $a = 403\,\mathrm{nm}$, Equation (2.2).

For high coupling efficiency, also the thickness of the bottom SiO_2 layer has to be adapted to the desired wavelength. The light beam originating from the fiber illuminates the grating and is scattered into the WG, Figure 2.10(b), solid black line. Parts of the beam are transmitted to the SiO_2 layer and reflected at the interface between SiO_2 and Si, dashed black line. Parts of this beam are then scattered at the grating into the WG and interfere with the directly scattered beam, solid line. Depending on the thickness of the SiO_2 layer, the phase relation between the directly scattered beam and the reflected beam changes and wavelength dependent constructive and destructive interference occurs [64]. Considering white light and a small mode field diameter of less than 10 µm after the fiber, we expect a Gaussian spectral distribution of the light in the WG [65]. This Gaussian transmission spectrum is superimposed by the periodic interference pattern which is induced by the directly scattered and the reflected beam.

For experimental optimization of the GC geometry, the period a, fill factor FF, incident angle θ and the thickness of SiO_2 were varied. The transmission efficiency was measured with an in-coupling GC and an identically designed out-coupling GC, connected through a single-mode strip WG of 2 mm length, Figure 2.11(a). The measurement results were normalized to a back-to-back measurement, in which the fiber from the laser was directly coupled to the spectrometer. Therefore, the measured efficiencies include the losses of the in-coupling and out-coupling fibers leading to the sample, of the two identically GC, and of the strip WG in-between.

Figure 2.11(b) shows the normalized (previous section) coupling efficiency for quasi-TE polarized modes of GC with periods of $a = (390...420)\,\mathrm{nm}$ for a fill factor of FF = 80%, an incident angle of $\theta = 10°$ and a SiO_2 thickness of $d_{\mathrm{SiO_2}} = 4\,\mu\mathrm{m}$. For larger periods a, a shift of the transmission spectrum from shorter towards longer wavelengths is observed. This trend can be confirmed by Equation (2.2), with $a \sim \lambda$. For $\lambda = 650\,\mathrm{nm}$ a distinct drop in efficiency can be found for all spectra, identifying a minimum of the periodic interference pattern of the scattered and the reflected beam. To minimize the influence of the interference between reflected and scattered beams, a lower thickness of $d_{\mathrm{SiO_2}} = 2\,\mu\mathrm{m}$ was chosen in a subsequent design. From experimental characterization of these structures, we found a maximized transmission efficiency for a FF of 65%, a period of $a = 390\,\mathrm{nm}$ and an incident angle of $\theta = 8°$ for quasi-TE polarized modes. Figure 2.11(c) shows the normalized transmission efficiency η for five pairs of GC with optimized geometry, colored lines. No destructive interference from directly scattered and reflected beam can be observed. The efficiency for two subsequent GC amounts to $-17.5\,\mathrm{dB}$. The efficiency per GC is calculated to $\eta_{\mathrm{dB,GC}} = (\text{-}8.8 \pm 0.2)$. The area marked with an orange dashed square is

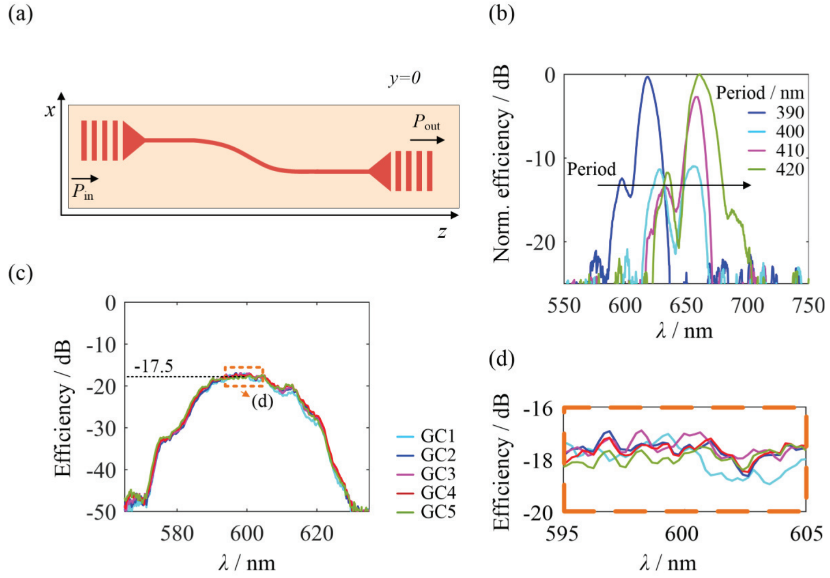

Figure 2.11: Experimental optimization of GC. **(a)** Sketch of the characterized device. An in-coupling GC and an out-coupling GC are connected through a single-mode strip WG. **(b)** Normalized efficiency of GC with a SiO_2 thickness of 4000 µm and different periods $a = (390\ldots420)$ nm. The maximum efficiency shifts with larger periods to longer wavelengths. At $\lambda = 650$ nm a clear drop in efficiency can be seen for all periods. At this wavelength the transmitted beam, dashed line in Figure 2.10(b), interferes destructively with the initial beam, solid line. **(c)** Efficiency for five optimized GC with a SiO_2 thickness of 2000 µm. The efficiency was measured with two GC for in and out coupling, Subfigure **(a)** and normalized to the incident power of the laser. **(d)** Enlarged section of efficiency at $\lambda = 600$ nm of Subfigure **(c)**. The efficiency of five GC varies only slightly, which shows a good reproducibility of the fabrication process.

magnified in Figure 2.11(d) for the target wavelength of $\lambda = 600\,\text{nm}$. For the five different GC pairs with the same geometry, colored lines, only small variations in efficiency can be seen, indicating the good reproducibility of the fabricated GC.

The benefit of the presented GC is the simple fabrication with only one lithography step that can be performed in parallel with WG fabrication at the price of moderate coupling efficiencies. Larger coupling efficiencies for Si_3N_4

GC were shown in combination with more sophisticated fabrication technologies. The coupling efficiency can be described as the product of directionality and mode matching between fiber mode and the mode that is refracted from the GC. The directionality describes the part of the WG mode that is diffracted towards the fiber [66]. Larger directionalities can, e.g., be achieved by including a reflective bottom layer below the SiO_2 substrate. For Si_3N_4 WG, visible light ($\lambda = 660\,\mathrm{nm}$) and quasi-TE polarized modes, up to $-2.4\,\mathrm{dB}$ efficiency was shown for GC with reflective bottom layers from AlCu/TiN, and SiO_2 for the top and bottom cladding (between grating and reflective layer) [67]. Without a reflective layer, these GC setups exhibit coupling efficiencies of $-4.2\,\mathrm{dB}$ [67]. For near infrared wavelengths ($\lambda = 880\,\mathrm{nm}$), coupling efficiencies of $-6.5\,\mathrm{dB}$ [68] were found for shallow edged GC. While these modifications in the GC design lead to higher efficiencies, the manufacturing requires more complex processes, compared to the GC design here presented. Specifically the manufacturing processes include complex material deposition and additional lithographic structuring steps, contradicting the simple design approach that is advantageous for disposable point-of-care sensors.

2.4 Multimode interference couplers

Nanophotonic WG sensors can be used to detect target molecules in aqueous solutions. During sensing experiments, changing analytes or binding of molecules to the surface of the WG core change the refractive index of the top cladding and the phase of the light. This phase shift $\Delta\phi$ can be recorded using interferometric structures. A Mach-Zehnder interferometer (MZI) splits light into a reference arm and a sensing arm. In contrast to the reference arm, the sensing arm is in contact with the analyte. Binding molecules change the phase of the light after the interaction length l from ϕ_0 to $\phi = \phi_0 + \Delta\phi$. The light is combined again with $P \sim 2 + 2\cos(\Delta\phi)$. Due to interference with the light from the reference arm, phase shifts $\Delta\phi$ in the sensing arm can be detected.

For splitting and combining, multimode interference couplers (MMI) can be used. The working principle of MMI is based on self-imaging, first suggested by Bryngdahl in 1973 [69] for a slab WG and then explained in more detail by Ulrich [70]. The central part of the MMI is a WG that is designed to support several lateral modes, typically more than three, while only the fundamental vertical mode can propagate. In this case, an input field reproduces itself in propagation direction in single and multiple images at periodic interval lengths [71]. Figure 2.12 shows two different MMI that can be used as combiners or splitters: A 2 × 2 MMI, Figure 2.12(a), and a 3 × 3 MMI, Figure 2.12(b). Single-mode WG are usually used as in- and outputs. These WG are placed at specific positions x_{in} and x_{out} along the width w at the beginning and the

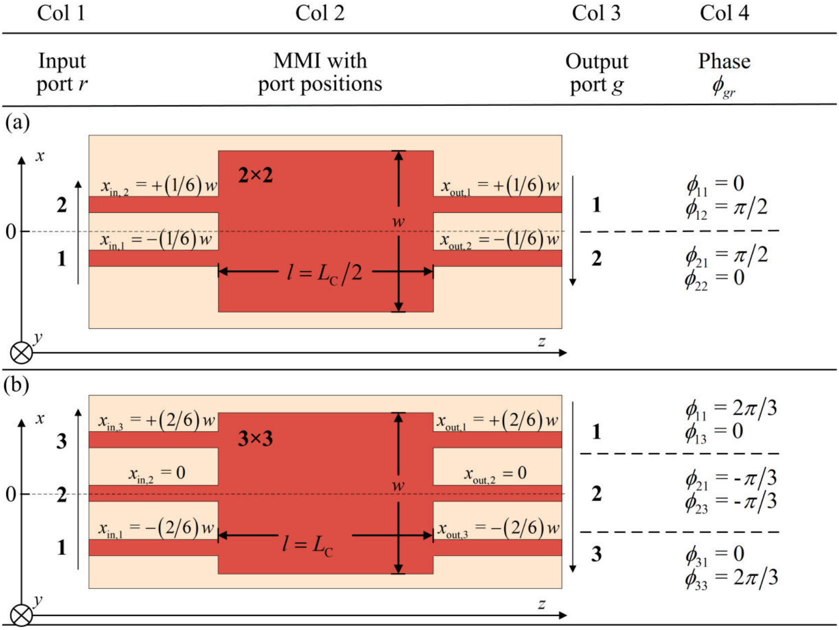

Figure 2.12 Two different MMI couplers with geometrical parameters and phase relations. Labeling and phase calculations follow Ref. [73]. The input ports r are labeled in the first column (bottom-up) and their positions are marked with $x_{\text{in},r}$ in column 2. The output ports s are labeled in column 3 (top-down) and their positions along the x-axis are marked with $x_{\text{out},g}$ in column 3. Column 2 shows sketches of the MM with length l and width w of the multimoded region. Column 4 lists phase shifts ϕ_{gr} between input ports r and output ports g. **(a)** 2 × 2 MMI combiner or splitter. **(b)** 3 × 3 MMI combiner or splitter.

ending of the multimode section, Figure 2.12. The input ports $r = 1, 2, 3, \ldots$ are labeled bottom-up and their positions are marked with $x_{\mathrm{in},r}$. The output ports $g = 1, 2, 3, \ldots$ are labeled top-down and their positions are marked with $x_{\mathrm{out},g}$.

For a given input field, the power distribution and the phase relations between the output fields of the MMI are explained in more detail in the following sections.

Self-imaging An arbitrary input mode field $\underline{E}(x,y,0)=\hat{\underline{E}}(x,y)\exp\left[\mathrm{j}(\omega t-\phi_0)\right]$ with field amplitude $\hat{\underline{E}}$, angular frequency ω, and phase $\phi_0=\beta_0 z$ with propagation constant β_0 is fed to an arbitrary position x to the multimoded section at position $z=0$. In the multimoded section the field is expanded into m guided modes $\underline{E}_\nu$ with mode numbers $\nu=0,1,2,\ldots m$, propagation constants β_ν, vacuum wavelength λ and mode excitation coefficients a_ν. At any position z in the multimoded section the eigenmodes superimpose:

$$\underline{E}(x,y,z)=\sum_\nu a_\nu \underline{E}_\nu(x,y)\exp(-\mathrm{j}\beta_\nu z) \tag{2.3}$$

For a step-index WG and strong guiding the cladding fields can be neglected. Thus, the effective width of the multimoded section equals approximately the geometric width w and the effective refractive index equals approximately the one of the WG core n_1. The propagation constants β_ν and $\Delta\beta_{0\nu}=\beta_0-\beta_\nu$ can be approximated by [71], [72]

$$\beta_\nu=\frac{2\pi n_1}{\lambda}-\frac{(\nu+1)^2\pi\lambda}{4n_1 w^2} \tag{2.4}$$

The coupling length L_{C} between the two lowest-order modes is [72]

$$L_C = \frac{\pi}{\beta_0 - \beta_1} = \frac{\nu(\nu+2)\pi}{3(\beta_0 - \beta_\nu)} = \frac{4n_1 w^2}{3\lambda} \tag{2.5}$$

With Equation(2.4), Equation (2.5), and Equation (2.5) the field in the multimoded section can be written as [71]

$$\begin{aligned} \underline{E}(x,y,z) &= \sum_\nu a_\nu \underline{E}_\nu(x,y)\exp\left(-\mathrm{j}\beta_0 z + \mathrm{j}(\beta_0 - \beta_\nu)z\right) \\ &= \sum_\nu a_\nu \underline{E}_\nu(x,y)\exp\left(-\mathrm{j}\beta_0 z + \mathrm{j}\frac{\nu(\nu+2)\pi}{3L_C}z\right) \end{aligned}. \tag{2.6}$$

For the following considerations it is useful to distinguish between odd and even mode numbers ν:

$$\nu(\nu+2) = \begin{cases} \text{even}, & \text{for } \nu = \text{even} \\ \text{odd}, & \text{for } \nu = \text{odd} \end{cases}, \tag{2.7}$$

and

$$\underline{E}_\nu(-x,y) = \begin{cases} \underline{E}_\nu(x,y), & \text{for } \nu = \text{even} \\ -\underline{E}_\nu(x,y), & \text{for } \nu = \text{odd} \end{cases}. \tag{2.8}$$

From Equation (2.4), it can be seen that for $z = 3mL_C$ with $m = 1,2,3,\ldots$ a direct single image of the input field occurs. If m is even, $\mathrm{j}(\beta_0 - \beta_\nu)3mL_C$ is a multiple of 2π and all modes interfere with the same relative phase compared to the input modes. Therefore, a field distribution that is exactly the same as the input field can be found. Figure 2.13 shows how the initial field evolves in propagation direction z. After $z = 6L_C$ an image of the input field occurs. If m is odd and $z = 3L_C$ the even modes are in phase but the odd modes are in antiphase and $\mathrm{j}(\beta_0 - \beta_\nu)6L_C$ is a multiple of $j\pi$. For the mode fields $-\underline{E}_\nu(x,y) = \underline{E}_\nu(-x,y)$ holds for odd ν and $\underline{E}_\nu(x,y) = \underline{E}_\nu(-x,y)$ for

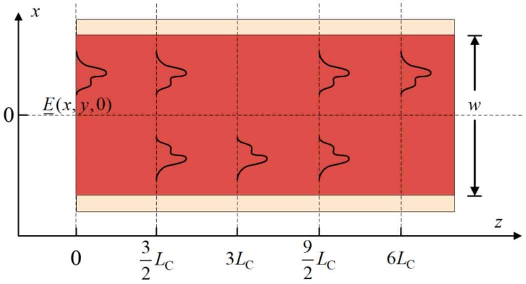

Figure 2.13 General evolution of an input field $\underline{E}(x, y, 0)$ in a multimoded WG section. At $z = 3L_C$ an image of the input field occurs that is mirrored about the symmetry plane $z = 0$. At $z = 6L_C$ a direct image of the input field occurs.

even ν. As a consequence, the image of the input field is mirrored about the symmetry plane at $x = 0$ of the multimoded section at $z = 3L_C$, Figure 2.13.

In a similar way it can be shown that two images occur at $z = (3/2)L_C$ and at $z = 9/2\, L_C$ [71], one image is exactly an image of the incident field, whereas the other one is mirrored about $x = 0$ and delayed by $\pi/2$ with respect to the first one, Figure 2.13. More generally, it can be shown that $N = 1, 2, \ldots$ images of the input field can be found at

$$l = \frac{3mL_C}{N}, \tag{2.9}$$

where N and m have no common divisor. All these images show equal field amplitudes $\hat{\underline{E}}/\sqrt{N}$ [71].

For splitters and couplers usually short devices are preferred. In general, short devices are found for $m = 1$. For special positions of the input port, only selected even or odd modes are excited in the multimoded section, and as a result, the length of the multimoded section can be reduced [71]. Single-moded WG are usually used as in- and output ports, Figure 2.12. For input ports at $x_{\text{in},1} = -(1/6)w$ and $x_{\text{in},2} = (1/6)w$, N-fold images occur at distances that are three times shorter than for the general case [71], [73]:

$$l = \frac{L_{\mathrm{C}}}{N} \tag{2.10}$$

In Figure 2.12, second column, sketches of a 2 ×2 MMI and a 3 × 3 MMI are shown in Rows 1 and 2. As excitation, usually a symmetric fundamental mode of a single-mode WG is chosen. The port positions are chosen to yield the shortest possible device lengths l to $l = L_{\mathrm{C}}/2$ for the 2 ×2 MMI and $l = L_{\mathrm{C}}$ for 3 × 3 MMI, according to Equation (2.10) and Equation (2.9) with $m = 1$.

Phase relations Multiple images of the input field occur at special z-positions according to Equation (2.9). The phases of the images depend on the position of the input field in x-direction, $x_{\mathrm{in},r}$ Figure 2.12, and on the position $x_{\mathrm{out},g}$ of the image. As input field, we assume that a symmetric fundamental mode field is fed by the input WG to the multimoded section and the image is out-coupled by the output WG. The various input and output ports are marked with $r,g = 1, 2, 3, \ldots$ in Figure 2.12. Note that the input WG r are labeled bottom-up and the output WG g are labeled top-down, according the definitions in Ref. [73]. The phase relation ϕ_{gr} between an input port r and an output port g can be calculated as follows, apart from a constant phase [73]:

$$\begin{aligned} \phi_{gr} &= \pi + \frac{\pi}{4N}(g - r)(2N - g + r) && \text{for } r + g \text{ even,} \\ \phi_{gr} &= \frac{\pi}{4N}(r + g - 1)(2N - r - g + 1) && \text{for } r + g \text{ odd.} \end{aligned} \tag{2.11}$$

Figure 2.12, column 4 lists calculated phase relations for the depicted MMI.

For the design of MMI, the width and length of the multimoded section and the single-mode input and output WG were first simulated with CST Studio Suite and the devices were then fabricated, see Subsection 2.1. In a next step, 2 × 2 MMI with fixed width $w = 6$ µm and different lengths were combined to Mach-Zehnder interferometers (MZI) by connecting the output ports of a first MMI to the input ports of a second MMI via a single-mode WG, Figure 2.14(a). Light is coupled into GC, P_{in} Figure 2.14(a), and is then distributed to two arms by the first 2 × 2 MMI, then again combined by the second 2 × 2 MMI and coupled from the MZI through two output ports $P_{\mathrm{out},1}$ and $P_{\mathrm{out},1}$. The fields from the two arms are superimposed in the second MMI. The two arms show a difference in length of $\Delta l = 80\ \mu\text{m}$. At the input at the second MMI, this results in a phase imbalance between the fields $\underline{E}_1$ and $\underline{E}_2$ of $\Delta\phi = k_0 n_e \Delta l \approx 1400\,\text{rad}$ for 600 nm wavelength in the two arms. Single-mode WG with connected GC serve as in- and out-coupling ports of the MZI. The out-coupled powers for port 1 and 2 are

$$\begin{aligned} P_{\text{out},1} &\sim 2 + 2\cos\left(\frac{\pi}{2} + \Delta\phi\right), \\ P_{\text{out},2} &\sim 2 + 2\cos\left(-\frac{\pi}{2} + \Delta\phi\right). \end{aligned} \tag{2.12}$$

For characterizing the devices, light from a white-light source (SuperK, NKT Photonics, Birkerød) was coupled to the input port P_{in}. The transmitted light was coupled from the output ports $P_{\text{out},1}$ and $P_{\text{out},2}$ to a spectrometer sequentially.

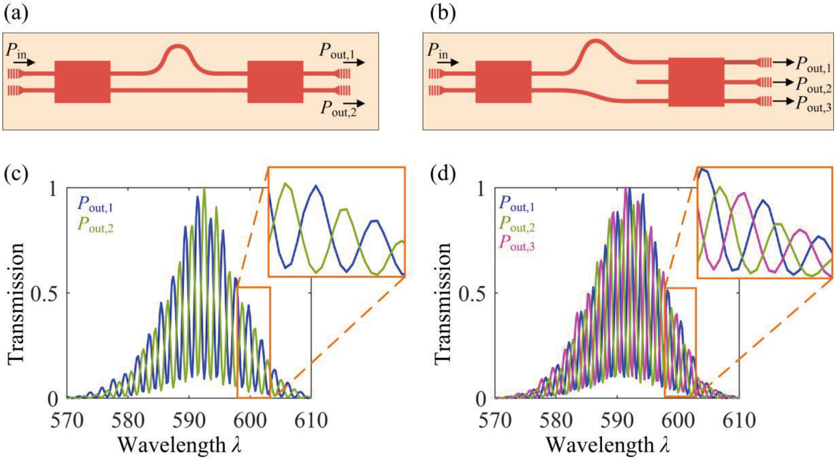

Figure 2.14: Characterization of 2×2 and 2×3 MMI. **(a),(b)** Schematics of the fabricated MZI with 2×2 splitters and 2×2 combiner **(a)** or 3×3 combiner **(b)**. **(c),(d)** Transmitted powers are detected at all output ports $P_{\text{out},1}$, $P_{\text{out},2}$, (and $P_{\text{out},3}$) sequentially. The maximum of the Gaussian envelope of the whole transmitted spectral powers is equal for all ports, showing an equal distribution of the in-coupled light to all ports. The emitted powers are shifted by π **(c)** and by $2\pi/3$ **(d)** to each other, in good agreement with Equation (2.12) and Equation (2.13).

The transmission spectra for the optimized device with length $l = 52$ µm are shown in Figure 2.14(c). The transmission for both output ports was normalized to the maximum spectral output power of $P_{\text{out},2}$ and is shown in Figure 2.14(c). The spectral power $P_{\text{out},1}$ is shown in blue whereas $P_{\text{out},2}$ is shown in green. The Gaussian envelope of the whole transmission spectrum is associated with the transmission spectrum of the GC. The maximum power of this Gaussian envelope is the same for both, $P_{\text{out},1}$ and $P_{\text{out},2}$. The inset in Figure 2.14(c) shows a magnification of the transmitted power near a wavelength of $\lambda = 600\,\text{nm}$. The spectral oscillations of the transmitted powers $P_{\text{out},1}$ and $P_{\text{out},2}$ are shifted with respect to each other by one half of the spectral period, in good agreement with Equation (2.12).

For the characterization of the 3 × 3 MMI, the second MMI in Figure 2.14(a) was exchanged by a 3 × 3 MMI, Figure 2.14 (c). In Table **2.2**, second column, the length l and the width w of the optimized 3 × 3 MMI for $\lambda = 600\text{ nm}$ are listed. The fields from both arms are superimposed and the output powers at the output ports are calculated to

$$\begin{aligned} P_{\text{out},1} &\sim 2 + 2\cos\left(\frac{2\pi}{3} + \Delta\phi\right), \\ P_{\text{out},2} &\sim 2 + 2\cos\left(\Delta\phi\right), \\ P_{\text{out},3} &\sim 2 + 2\cos\left(-\frac{2\pi}{3} + \Delta\phi\right). \end{aligned} \tag{2.13}$$

The Gaussian envelope of the spectral output power has the same maximal power for $P_{\text{out},1}$, $P_{\text{out},2}$ and $P_{\text{out},3}$. An enlargement near a wavelength of $\lambda = 600$ nm is shown in the inset of Figure 2.14(d). The spectral oscillations of the transmitted powers $P_{\text{out},1}$, $P_{\text{out},2}$ and $P_{\text{out},3}$ are shifted with respect to each other by one third of the spectral period, in good agreement with Equation (2.13).

Geometrical parameters for optimized MMI and wavelengths of $\lambda = 600$ nm and $\lambda = 636$ nm are listed in In Table **2.2**.

Table 2.2: Geometrical parameters of different MMI.

	Wavelength λ / nm	Length l / µm	Width w / µm
2 × 2	600	52	5
3 × 3	600	152.5	6
2 × 2	636	48	5
3 × 3	636	139	6

3 Functionalization of waveguide sensors and detecting streptavidin

Streptavidin is a protein that is obtained from the bacterium Streptomyces avidinii. The bond between biotin, also called vitamin B_7, and streptavidin is one of the strongest non-covalent bonds in nature [74]. The binding between streptavidin and biotin is often used as a model for sensors, and also for setting up a surface functionalization. In this chapter, a WG sensor chip is presented and tested for the detection of various concentrations of streptavidin. Light is coupled to and from the chip with GC that were explained in Section 2.3. For the sensor element itself, a MZI is used that is based on the MMI shown in Section 2.4. The architecture and the functionality of the sensor chip are shown in the following Section 3.1. For the specific detection of streptavidin, the WG must be functionalized. Therefore, the WG surface is modified and biotin is immobilized at the WG surface. Streptavidin has four functional groups, also called binding sites that specifically bind one biotin molecule each. The investigated surface functionalization is explained in detail in Section 3.2. For binding experiments, the chip is placed in a fluidic chamber to direct the analyte solution towards the sensor WG. The fluidic chamber is designed such that the input and output GC are accessible for excitation and readout. The fluidic chamber and the readout setup are described in Section 3.3. Finally, the performance and the results of experiments are discussed in Section 3.4.

3.1 Sensor chip for streptavidin detection

In a sensing WG, a mode that travels along the WG in z-direction can be driven by a monochromatic source with angular frequency ω. For the WG mode with effective refractive index n_e we assume a normalized transverse electric field $\underline{E} = \hat{\underline{E}} \exp\left[\mathrm{j}\left(\omega t - \phi\right)\right]$ with complex amplitude $\hat{\underline{E}}$ and phase $\phi = \beta z = k_0 n_\mathrm{e} z$, with propagation constant β and vacuum propagation constant $k_0 = \omega / c$. When biomolecules attach to the WG surface, the effective refractive index n_e of the mode is changed by Δn_e, and therefore the phase is changed to $\phi_S = \phi + \Delta\phi = k_0 \left(n_e + \Delta n_e\right) z$. This phase change can be detected by interfering the output light of the sensing WG with the light obtained from a reference WG, and by detecting the associated phase difference. To do so, the light must be first split to propagate in two arms, the sensing and the reference arm, and then combined again. The measured signal depends on the phase difference $\Delta\phi$ between the light of the sensing and the reference arm. Mach-Zehnder interferometers for sensing can be established with different combiners as shown in Figure 2.12. The phase difference $\Delta\phi$ can be reconstructed from the measured two or three powers from the output ports.

For biosensors, the application of an MZI was first shown by Heideman et al. in 1992 [75]. Since then, MZI were extensively investigated [15], and sensitivities of up to $\Delta\phi_S = 1730 \times 2\pi/\text{RIU}$ for solutions with different refractive indices have been reported [76]. The unit of the phase shift $\Delta\phi$ is rad, and $\Delta\phi_S$ gives the shift of the phase per (dimensionless) index change $\Delta n_e = 1$. To emphasize this dependence the dimensionless refractive index unit (RIU) is introduced.

Mach-Zehnder interferometers are robust with respect to mechanical stress and temperature fluctuations as they are self-referencing: As long as sensing and reference arm are similar in material and geometry, they will be both affected in the same way. The resulting phase shifts in both arms will be equal and have no impact on the measurement results, which depend on the phase difference $\Delta\phi$ between reference and sensing arm. For biosensor applications 2 × 1 MMI, 2 × 2 MMI, and 3 × 3 MMI are used as combiners. In addition to the previously mentioned general advantage of self-referencing of MZI, 2 × 2 MMI and 3 × 3 MMI also allow the correction of power fluctuations in the laser source. At each time and for each phase shift, the total power of all output ports is constant for a fixed input power. Power fluctuations affect all output ports equally and can be calibrated.

3 × 3 MMI have more advantages compared to 2 × 2 MMI combiners: The phase shift between sensing and reference arm $\Delta\phi$ can be directly reconstructed from the three power levels measured at the three output ports, respectively, without any phase ambiguities within the 2π-interval. Furthermore, the sensitivity is independent of the MZI operating point.

Fabrication inaccuracies and temperature changes can cause amplitude and phase errors of the MMI. These errors can be also corrected by digital signal processing with the help of a so-called Clarke transform as explained below. In the following, the sensor concept and the advantages of a 3 × 3 MMI as a combiner are described in more detail.

A schematic of the sensor is shown in Figure 3.1(a). The underlying MZI is formed by a 2 × 2 MMI (MMI$_2$) as a splitter and a 3 × 3 (MMI$_3$) as a combiner. The light is coupled via a GC to a WG and guided to one input port of MMI$_2$. The MMI$_2$ splits the incoming light equally to the sensing arm, (electric field $\underline{E}_S$) and the reference arm (electric field $\underline{E}_R$), see Figure 3.1(a). Both arms contain coiled-up spiral WG, which are arranged close to each other to avoid different environmental influences on the sensing and on the reference arm. After propagating through the two MZI arms, the two optical signals are fed to the lower and the upper input ports of MMI$_3$, where they are superimposed with different phase relations, see Figure 2.12(b). The three output signals P_1, P_2 and P_3 are coupled from the chip by a GC array, Figure 3.1(a). All parts of the WG have a top cladding, except for the spiral-shaped parts of the sensing and of the reference arm, where the top cladding is locally removed. Via these openings, the sensing arm is exposed to the analyte (light

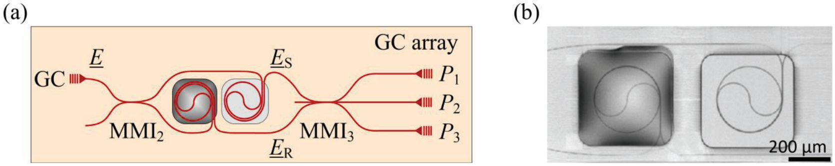

Figure 3.1: Mach-Zehnder interferometer as a sensor. **(a)** Schematic of MZI. The MZI is formed by a 2 × 2 MMI (MMI$_2$) splitter and a 3 × 3 MMI (MMI$_3$) combiner. The light with field $\underline{E}$ is coupled to one input port of a MMI$_2$ by a GC. The MMI$_2$ splits the light equally to the sensing arm ($\underline{E}_S$) and the reference arm ($\underline{E}_R$). Both arms are coiled-up to compact spirals. The fields of the two arms are input to the lower and upper ports of the MMI$_3$, where they are superimposed in a way that the fields of neighboring output ports are phase-shifted by $2\pi/3$ (120°). The three output signals are coupled from the chip by a GC array. All parts of the WG are clad, only at the spiral shaped WG the cladding is opened. **(b)** Microscope image of spiral section of the MZI. The sensing arm is exposed to the analyte (light grey), whereas the reference arm is covered with an index-matched glue (dark grey).

grey), whereas the reference arm is covered with glue that is index-matched to water (dark grey), Figure 3.1(a) and Figure 3.1(b).

The splitter at the input (MMI_2) is designed as a 2 × 2 MMI, such that the field in the sensing arm experiences a $\pi/2$ phase shift with respect to the field in the reference arm, Figure 2.12(a). After traveling along the sensing and the reference arm with equal geometrical lengths l, both the fields exhibit the phase $\phi = \beta L$. If molecules attach to the surface of the sensing WG, the field in the sensing arm experiences an additional phase shift of $\Delta\phi = \Delta\beta L$. The following fields are thus fed into the input ports of the MMI_3:

$$\begin{aligned} \underline{E}_S &= \frac{\underline{E}}{\sqrt{2}} e^{\mathrm{j}\left(\omega t + \frac{\pi}{2} - \phi - \Delta\phi\right)}, \\ \underline{E}_R &= \frac{\underline{E}}{\sqrt{2}} e^{\mathrm{j}(\omega t - \phi)}. \end{aligned} \tag{3.1}$$

The fields from the sensing and the reference arm are combined in three output ports with the phase relations given in Figure 2.12(b), [77]

$$\begin{aligned} P_1 &= \frac{1}{3}\left|\underline{E}_\mathrm{R} + \underline{E}_\mathrm{S} + \exp\left(+\mathrm{j}\frac{2\pi}{3}\right)\right|^2, \\ P_2 &= \frac{1}{3}\left|\underline{E}_\mathrm{R} + \underline{E}_\mathrm{S}\right|^2, \\ P_3 &= \frac{1}{3}\left|\underline{E}_\mathrm{R} + \underline{E}_\mathrm{S} + \exp\left(-\mathrm{j}\frac{2\pi}{3}\right)\right|^2. \end{aligned} \tag{3.2}$$

The emitted sensor signals are radiated to a camera via GC and the camera signals are analog-to-digital converted. To extract the phase shift $\Delta\phi$ from the measured powers, it is useful to first calculate the so-called Clarke field, a complex valued auxiliary quantity from which the phase difference can be directly extracted. For this, the signals are Clarke transformed, leading to a complex correlation function (Clarke “field”) $\underline{s}$ [77], [78]:

$$\begin{aligned} \underline{s} &= \underline{s}_{\mathrm{r}} + \mathrm{j}\underline{s}_{\mathrm{i}} \\ &= 2P_2 - \left(P_3 + P_1\right) + \mathrm{j}\sqrt{3}\left(P_3 - P_1\right) \\ &= 2\underline{E}_{\mathrm{S}}\underline{E}_{\mathrm{R}}^{*} = |\hat{\underline{E}}|^2\, \mathrm{e}^{\mathrm{j}(\Delta\phi - \pi/2)}. \end{aligned} \tag{3.3}$$

For a continuous variation of the phase shift in a binding experiment, $\Delta\phi$ can be extracted from the measured data by unwrapping the Clarke phase $\arg\left(\underline{s}\right)$,

$$\Delta\phi_{\mathrm{sig}} = \Delta\phi - \pi/2 = \mathrm{unwrap}\left(\arg\left(\underline{s}\right)\right) \tag{3.4}$$

In the complex plane, $\underline{s}$ describes a circle with radius $\left|\underline{s}\right| = |\hat{\underline{E}}|^2$ in case of a monotonously increasing phase difference $\Delta\phi$. The sensitivity of a sensor can be calculated by the change of the detected (and digitally processed) signal with the phase shift. For the sensor discussed here, the sensitivity $S_{3\times 3} = \left|\mathrm{d}\underline{s}/\mathrm{d}\Delta\phi\right| = |\hat{\underline{E}}|^2 = \left|\underline{s}\right|$ is constant for all $\Delta\phi$. Due to fabrication imperfections or temperature fluctuations, the phase relation between the three output ports of real sensor devices can deviate from $2\pi/3$. In addition, the GC efficiency of the ports might differ from each other. These effects lead to an ellipsoidal deformation of the locus of $\underline{s}$ in the complex plane and to a shift of the center of the circular locus away from the origin of the complex plane [77]. This error can be corrected by fitting an ellipse to the measurement data and by back transforming this ellipse to a circle that is centered about the origin [77], [78].

3.2 Functionalization strategy

In this application, the MZI sensor structure is to be tested and a surface functionalization for the specific detection of target molecules is to be developed. As a test, streptavidin shall be detected as the target molecule of the sensor. Therefore, streptavidin must bind specifically to the WG surface of the MZI's sensing arm. If target molecules bind to the surface of a sensing WG, the phase in the WG shifts. At the output ports of the sensor a binding curve can be detected, monitoring the phase shift and therefore the amount of bound molecules as a function of time. The form of such a binding curve strongly depends on the interaction strength between target molecule and WG surface. For point-of-care applications, the concentration of a target molecule in a complex solution is of great interest. Therefore, the surface of the WG must be modified to specifically increase the amount of bound target molecules while avoiding binding interaction with other molecules present in the same solution. One possible way is to use another compound, a capture molecule, exhibiting a high binding affinity towards the target molecule. This second compound must be immobilized on the WG surface. In the case of streptavidin, biotin is often used as capture molecule.

A surface functionalization for detecting streptavidin is described in detail in the following paragraphs, a detailed protocol can be found in Appendix B. A schematic of the surface functionalization is shown in Figure 3.2. First, on the Si_3N_4 surface (red), silane molecules (green) are bound. To establish a chemical connection between inorganic, silicon-containing surfaces (such as Si, SiO_2 and Si_3N_4) and organic compounds, silane-compounds can be used [79]. Organosilanes are derivatives of silanes, which consist of silicon and hydrogen. Such organosilanes can contain reactive groups that bind to inorganic surfaces. In addition, the same organosilane can carry reactive groups that bind to organic molecules, thereby acting as a linker between inorganic and organic compounds. Because of these two different binding

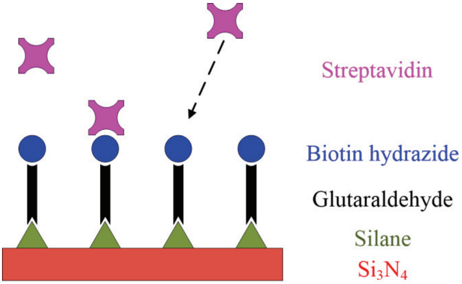

Figure 3.2: Surface functionalization of Si_3N_4. On the Si_3N_4 surface (red) silane molecules (green) are bound in a first step. The bi-functional linker glutaraldehyde (black) is then bound to the silane molecules, followed by biotin hydrazide (blue) attaching to glutaraldehyde. For the sensor demonstration streptavidin with different concentrations is bound to the immobilized biotin hydrazide.

sites, such organosilanes are called bifunctional. In Figure 3.3(a), the structure of aminopropyl(diethoxy)methylsilane (APDEMS) is shown. Because of the amino-group (red), APDEMS is a member of aminosilanes [80]. The amino group can bind to organic molecules. The two ethoxy groups (blue) are split from the silane by hydrolysis in aqueous solutions and hydroxyl (OH)-groups are bound to the silicon atom instead. The thereby formed reactive hydroxyl-groups can bind to hydroxyl-groups on the Si_3N_4 surface via hydrogen bounds. To establish a Si_3N_4 surface with sufficient hydroxyl groups, the Si_3N_4 is treated with oxygen plasma whereby hydroxyl groups are formed. Heating induces a condensation reaction and the silane is covalently bound to the surface [81]. In this reaction, water is released, and Si binds to the Si_3N_4 surface with an oxygen atom in-between. APDEMS has two ethoxy groups. Therefore, it can bind simultaneously to the Si_3N_4 surface and to other APDEMS molecules, thereby forming a polymer matrix [82].

In the next step, glutaraldehyde, black, Figure 3.2, is bound to the amino group (red) of the organosilane. The structure is shown in Figure 3.3(b). With a carbon chain of three ($-CH_2-$) elements, glutaraldehyde is a rather short cross-linker and offers thin functionalization layers. On both ends of the

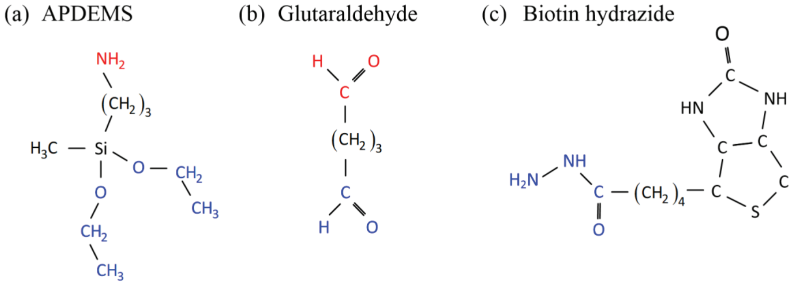

Figure 3.3: Structural formula of compounds used for surface functionalization. **(a)** Aminopropyl(diethoxy)methylsilan (APDEMS) has two binding sites. One side (blue) can be hydrolysed. Afterwards the remaining molecule can bind to Si_3N_4. On the other side an amino group (red) provides a binding site for organic compounds. **(b)** Glutaraldehyde is a cross linker with a chain of three carbon atoms and aldehyde groups on the terminal C-atoms (blue and red). **(c)** For covalent binding to aldehyde groups, biotin hydrazide is used. This derivate of biotin caries a hydrazide group at the carboxylic acid group of biotin (blue).

carbon chain, an aldehyde group (red and blue) can be found. One aldehyde group binds to the amino group of the silane forming an imino group [83], by binding C to N via a double bond.

Finally, biotin hydrazide, Figure 3.2, is bound to glutaraldehyde. Biotin itself cannot bind directly to the aldehyde group of glutaraldehyde. Therefore, a hydrazide group is introduced to the carboxyl group of biotin, and the resulting derivate is called biotin hydrazide. The structure of biotin hydrazide is shown in Figure 3.3(c). The terminal amino group of the hydrazide group (blue) binds to the amino group (red) of the glutaraldehyde and forms a hydrazon bond [84], establishing a double bond between the C-atom of the former aldehyde-group and the terminal N-atom of the hydrazide group.

Biotin hydrazide serves as capture molecule to specifically bind streptavidin to the sensor surface. For more specific applications of the sensor, such as cancer marker detection, this functionalization can be extended with streptavidin and a biotinylated antibody that specifically binds the cancer marker. Antibodies are proteins that are produced in vertebrates as part of the immune system. It is possible to bind a biotin molecule to one end of the antibody without blocking its functionality. This biotinylated antibody can be bound to a streptavidin molecule.

Successful functionalization of the sensor material can be proved by binding fluorescence-labeled streptavidin to biotin hydrazide. For testing the functionalization, a chip with unstructured Si_3N_4 layer is first cleaned using an oxygen plasma. For transportation of the sample to the wet bench, the freshly formed OH-groups are stabilized by incubating the chip in water. The water is removed by nitrogen blowing and heating the chip to 180°C. The silane solution is dispensed on the hot chip and incubated for 5 min at room temperature. The chip is then spun on a spincoater for removing residual silane solution. Heating to 180°C accelerates formation of covalent bonds between the organosilane and Si_3N_4. Rinsing the chip shortly in an ethanol bath removes excess silane molecules. Afterwards, the chip is successively incubated in glutaraldehyde, biotin hydrazide and fluorescence-labeled streptavidin solution. A detailed protocol can be found in Appendix B. Figure

3.4 shows a fluorescence image of a functionalized plane Si_3N_4 surface. The immobilized streptavidin is labeled with the organic dye Cyanine 3 (Cy3) having an absorption maximum at $\lambda_a = 550\,\text{nm}$ and an emission maximum at $\lambda_e = 570\,\text{nm}$. In the middle of the image a dark scratch can be seen that represents a reference signal for the non-functionalized surface. The emission, and hence the functionalization, is homogeneous apart from smaller (lighter) defects. These defects possibly originate from surface contaminations of the Si_3N_4 layer. For example, these could be particles that originate from breaking the wafers into small chips. The regions at the top side and at the left lower corner of the picture are slightly darker compared to the rest of the area, which is caused by an spatially non-uniform illumination of the sample.

3.3 Demonstration setup

For binding experiments, a sensor chip is fabricated according to Section 3.1. The sensor WG is functionalized in such a way that biotin is immobilized to the WG surface, Section 3.2. For the experiment, the analyte needs to be brought in contact with the sensor WG. To this end, the sensor chip is positioned in a fluidic chamber, Figure 3.5(a), which consists of a brass plate

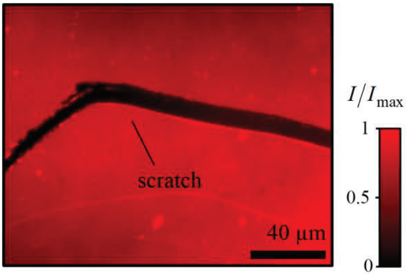

Figure 3.4: Fluorescence image of a plane Si_3N_4 layer that is functionalized with streptavidin. The streptavidin is fluorescence-labelled with Cy3, that emits in the red wavelength range and that absorbs in the green wavelength range. The functionalization layer is scratched (black line) to show a not functionalized area as reference. The lower fluorescence signal on the top and the left bottom corner are due to a spatially non-uniform illumination in the microscope. The functionalization is homogeneous, apart from smaller defects.

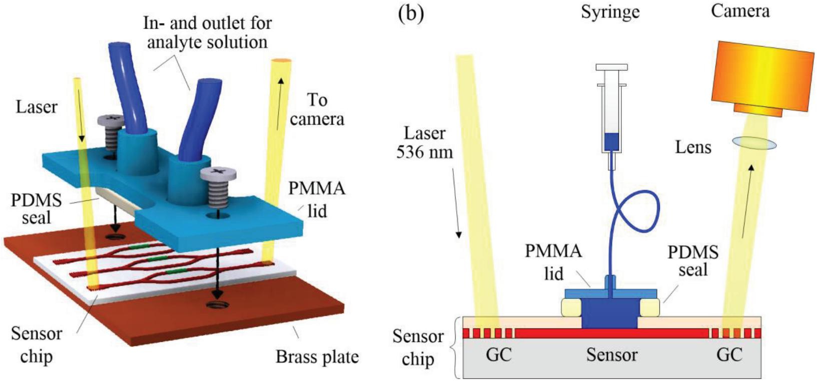

Figure 3.5: Demonstration setup. **(a)** The light of a fiber-coupled laser exposes a GC that feeds a single-mode WG, which guides the light to the sensor. The sensor signal is coupled from the chip by a GC and focussed on a CCD camera by a lens (not shown). The liquid analyte is pumped by a syringe through the fluidics chamber that is formed by the chip surface and a PMMA lid with a PDMS seal in between. The volumetric flow rate is 0.6 ml s^{-1}. **(b)** Fluidic chamber. The chip is positioned on a brass plate and the PMMA lid with the PDMS seal is screwed to the brass plate in such a way, that only the WG sensor is covered, while all GC are freely accessible.

for thermal conductivity, and a PMMA lid with a polydimenthylsiloxan PDMS seal. After placing the chip between the brass plate and the PDMS seal, the PMMA lid is screwed onto the brass plate. Thereby, a fluidic chamber is formed between the chip surface and the PMMA lid with the PDMS seal in-between, where only the sensor itself is covered by the fluidic chamber. The GC, which are used for coupling light to and from the on-chip WG, are not covered. On top of the PMMA seal is an inlet and an outlet for the liquid analyte solution. The analyte is pumped through the chamber by a motor-controlled syringe. The volumetric flow rate is 0.6 ml s^{-1}.

A schematic of the read-out system is illustrated in Figure 3.5(b). The light of a fiber-coupled laser (continuous wave, 635 nm, Velocity TLB-6700, Newport) is coupled to the input GC on the chip. The GC feeds a single-mode WG which guides the light to the sensor. The sensor output signal is coupled from the chip by a second GC. A lens focuses the light on a CCD camera. For signal processing, 40×30 pixel per output GC are repeatedly exposed for

100 ms. The liquid analyte is pumped by a motor-driven syringe through the fluidic. A Peltier element for temperature control is placed beneath the brass plate.

3.4 Detecting streptavidin

With the sensor system, the detection of six different concentrations of streptavidin, solved in phosphate-buffered saline solution (PBS), is tested. First, the fluidic chamber is flushed with PBS that serves as a reference solution, Figure 3.6(a). Second, streptavidin solutions with different concentrations $C_{1\ldots6} = (25\ldots500)\,\mathrm{n\,mol/L}$ are sequentially pumped through the fluidic chamber. Binding of streptavidin to the WG surface leads to a concentration dependent equilibrium between bound and unbound streptavidin. If this equilibrium is disturbed, e.g., by a change of concentration, after a certain time (response time of the sensor) a new equilibrium is achieved. After each streptavidin solution, the chamber is flushed with PBS, to remove unbound streptavidin from the WG surface. During this process, the powers P_1, P_2, P_3, that are transmitted through the three output GC, are continuously detected. For data analysis, the sum of the intensity values of a region on the camera sensor for each GC is recorded. The background of the sensor signals of the three output GC is subtracted, then the signals are normalized to the total signal power $P = P_1 + P_2 + P_3$ for each point in time. Finally each signal is normalized to its maximum signal power that was detected during the whole experiment.

Figure 3.6(b) and Figure 3.6(c) show exemplarily the transmitted powers P_1, P_2 and P_3 and the transformed and calibrated Clarke field, Equation (3.3), for the binding curve of streptavidin in PBS with a concentration of $C_3 = 50\ \mathrm{n\,mol/L}$. First, the chamber is flushed with PBS, orange. Then, the streptavidin solution is pumped through the chamber. Finally, the chamber is flushed with PBS again. When streptavidin molecules bind to the WG surface, the power changes at all output ports. During the flushing with PBS at the

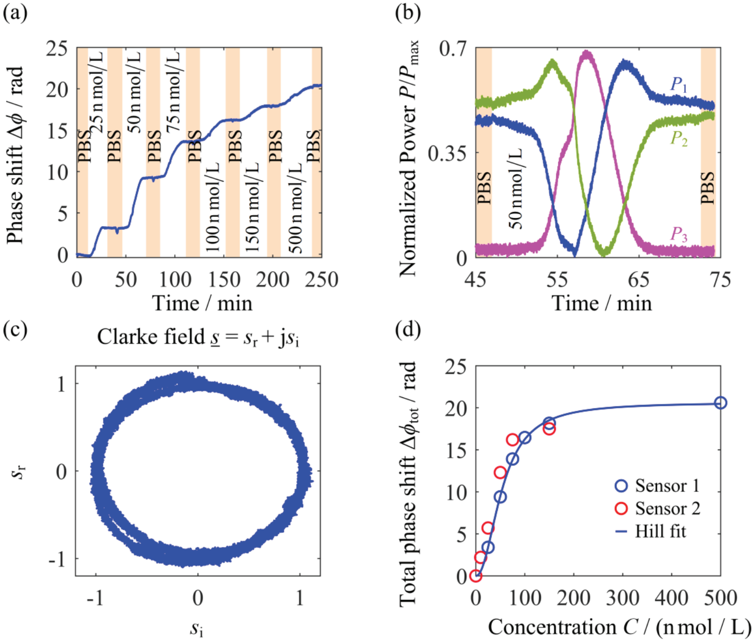

Figure 3.6: Data evaluation and results for the detection of streptavidin. **(a)** Binding curve for six concentrations of streptavidin in PBS (blue). The unwrapped phase shifts with each concentration of streptavidin, and it saturates to a level that is specific for the equilibrium for each concentration. Between filling the chamber with the solutions having different concentrations of streptavidin, the chamber is flushed with PBS (yellow). During PBS injection, the phase is constant. **(b)** Transmitted signals for the binding curve of streptavidin in PBS with $C_3 = 50\,\mathrm{nMol}$. The 3 × 3 MMI induces a phase difference of 120° for the fields at the three output ports and therefore also shifts the signals $P_{1,2,3}$. While streptavidin solution is pumped through the chamber, the phase for all three ports shifts. When the streptavidin molecules bound to the WG surface are in equilibrium with the streptavidin molecules in solution, the phase stops shifting. Flushing with PBS removes unbound streptavidin molecules. **(c)** Calibrated Clarke field, Equation (3.3). The three output signals $P_{1,2,3}$, see Subfigure (a), are transformed to a Clarke field and transformed to a unit circle in the complex $\underline{s}$-plane. **(d)** The total phase shift for each concentration is found by comparing the PBS level after binding equilibrium for each concentration with the PBS level during the first minutes (blue circles). A Hill curve, Equation (3.5), is fit to the data points (blue line). The sensor starts saturating for concentrations larger than $150\ \mathrm{n\,mol/L}$. An experiment with another similar sensor shows slightly different total phase shifts (red).

beginning no phase shift is detected. The signals in Figure 3.6(b) are Clarke-transformed according to Equation (3.3) and calibrated to a unit circle in the complex $\underline{s}$-plane. The resulting corrected Clarke field is plotted in the complex $\underline{s}$-plane in Figure 3.6(c). For the whole time series the complex-valued Clarke field is calculated and the phase is unwrapped, Equation (3.4), see Figure 3.6(a). The phase shifts with each injection of streptavidin solution, and saturates to a level that is specific for the equilibrium for each concentration. During PBS flushing the phase is constant. The small dips during the flushing are caused by pressure changes during the change of syringes, Figure 3.5(a). Flushing with PBS shows no significant drop in the phase shift, therefore no dissociation can be found for the measured time periods. This can be explained by the rather low dissociation constant that is expected for the biotin-streptavidin complex, rendering the strong bond irreversible. Dissociation constants for the binding between biotin and streptavidin are in the range of $K_\mathrm{d} \approx 10^{-14}\,\mathrm{mol/L}$ [85].

The total phase shift $\Delta\phi_\mathrm{tot}$ for each concentration is found by comparing the phase after streptavidin injections with the phase inside the first minutes of the whole experiment during flushing the chamber with PBS. Figure 3.6(d) shows the total phase shift for each concentration C (blue circles). The total phase shift $\Delta\phi_\mathrm{tot}$ linearly depends on concentrations between $25\,\mu\mathrm{mol/L}$ and $75\,\mu\mathrm{mol/L}$. At larger concentrations ($C > 100\ \mathrm{nmol/L}$) only small changes of the phase can be seen for increasing concentrations. The total phase shift saturates for large concentrations at $\Delta\phi_\mathrm{tot,max} = 20.5\,\mathrm{rad}$. This saturation is caused by the limited available binding sites on the WG surface. When all binding sites of the immobilized biotin molecules are occupied, no further molecules can bind, and no further phase shift can be detected for increasing concentrations of streptavidin.

The trend of the total phase shift as a function of concentration follows a so-called Hill curve. A Hill curve describes the binding dynamic between macro molecules: An important property of macromolecules with more than one similar molecular subunit is that the binding affinity can change with the concentration of already bound molecules. This behavior is called cooperativity. The Hill coefficient n describes the cooperativity of the binding mechanism. If $n > 1$, the cooperativity is positive. The binding affinity is low for low analyte concentrations but increases with increasing analyte concentrations. If $n < 1$, the cooperativity is negative. Then, the binding affinity is large for low analyte concentrations and decreases for increasing concentrations [86].

With the dissociation constant K_d, the concentration C, the Hill coefficient n and the saturation phase shift $\Delta\phi_\mathrm{tot,max}$, the total phase shift can be described by the Hill curve [87]:

$$\Delta\phi_\mathrm{tot} = \frac{\Delta\phi_\mathrm{tot,max}}{1 + \frac{K_\mathrm{d}}{C^n}} \tag{3.5}$$

For the experimental data shown, the Hill fit shows a slightly sigmoidal trend that indicates a positive cooperativity. The Hill coefficient amounts to $n = 2.2 \pm 0.2$. The dissociation constant is calculated to be $K_\mathrm{d} = 4 \times 10^{-15} \pm 5.23 \times 10^{-16}\,\mathrm{mol/L}$ and is therefore smaller (stronger binding) than in Ref. [85] with $K_\mathrm{d} \approx 10^{-14}\,\mathrm{mol/L}$.

To test the reproducibility of the functionalization, the experiment was repeated with a fresh sensor chip. The resulting total shifts are plotted in Figure 3.6(d), red circles. The phase shifts differ slightly from the shifts of the first experiment (blue data points) but show a similar trend. A possible reason for this variance could be that the silanization step during the functionalization procedure is sensitive towards environmental conditions, which were not entirely controlled. Slightly changing environmental conditions, e.g., temperature or humidity, can cause changes of the thickness of the silane layer. For a more reproducible surface functionalization must be performed in a controlled atmosphere, e.g., a climate chamber.

4 Surface sensing with integrated optical waveguides

This chapter discusses the surface sensitivity of silicon and silicon nitride waveguides. It defines a sensitivity metric that can be used to broadly compare the surface sensitivity for arbitrary waveguide geometries, materials and wavelengths. Note that two authors contributed equally to this publication. The initial ansatz and scope as well as the concluding evaluation, interpretation and discussion were performed jointly by all authors. For the development of the methods and results, the focus of the author of this thesis was on the simulations while the focus of Johannes Milvich was on the analytical mathematical model. All authors contributed to the preparation of the manuscript. This chapter is taken from [J4] which is published in Optics Express. In order to fit the structure and layout of this document, it was adapted accordingly.

[start of paper [J4]]

Surface sensing with integrated optical waveguides: a design guideline

Optics Express, Vol. 26, No. 16, 326159 (2018)
DOI: 10.1364/OE.26.019885

Johannes Milvich,[1,2†] Daria Kohler,[1,3†] Wolfgang Freude,[1] and Christian Koos,[1,3]

[1.] Karlsruhe Institute of Technology, Institute of Photonics and Quantum Electronics, 76131 Karlsruhe, Germany
[2.] Robert Bosch GmbH, Robert-Bosch-Campus 1, 71272 Renningen, Germany

[3.] Karlsruhe Institute of Technology, Institute of Microstructure Technology
76344 Eggenstein-Leopoldshafen, Germany
† These authors contributed equally to the work

Waveguide-based biochemical sensors exploit detection of target molecules that bind specifically to a functionalized waveguide surface. For optimum sensitivity, the waveguide should be designed to mediate maximum influence of the surface layer on the effective refractive index of the guided mode. In this paper, we define a surface sensitivity metric which quantifies this impact and which allows to broadly compare different waveguide types and integration platforms. Focusing on silicon nitride and silicon-on-insulator (SOI) as the most common material systems, we systematically analyze and optimize a variety of waveguide types, comprising simple strips, slot and double slot structures, as well as sub-wavelength gratings (SWG). Comparing the highest achievable surface sensitivities, we provide universal design guidelines and physically interpret the observed trends and limitations. Our findings allow to select the appropriate WG platform and to optimize sensitivity for a given measurement task.

4.1 Introduction

Waveguide-based optical sensors are used in a variety of applications such as label-free detection of chemical or biological analytes that specifically bind to functionalized waveguide (WG) surfaces [6], [8], [20], [21], [23], [24], [30], [34], [88], [89]. Such sensors exhibit large potential for miniaturization and cost-efficient mass production, utilizing established photonic integration platforms such as silicon or silicon nitride. Sensor schemes are most commonly based on interferometers, e.g., in Mach-Zehnder and Young configuration [6], [20]–[22], [24], or on resonant devices, such as ring, disk and Bragg resonators [8], [20], [23]–[26], [30], [89]–[91], [27], [28], [31], which can be further enhanced by exploiting the Vernier effect [29]. Enabling large effective interaction lengths with the analyte, these sensor structures combine high sensitivity with small device footprint and lend themselves to high-density integration into massively parallel arrays.

The sensor principle relies on an optical WG, guiding a mode which significantly extends into the cladding medium that surrounds the WG core. The interaction between the optical mode field and the varying surface layer properties alters the effective refractive index by Δn_e and thus the optical phase shift accumulated during propagation. The strength of this effect is expressed by the so-called surface sensitivity, which, in combination with the effective-index sensitivity from the phase measurement of the underlying resonator or interferometer, determines the overall sensitivity. Proper optimization of the WG towards high surface sensitivities is hence key for realizing high-performance sensors.

Over the last years, various approaches for optimizing special types of WG were published, both for surface sensing [20], [21], [27]–[33], and for detection of bulk refractive index changes in the WG cladding (homogeneous sensing) [8], [23], [24], [30], [89], [90], [22], [25]–[29], [31]–[33], [91], [92], [93] However, these investigations are often limited to specific WG types and geometries on certain material platforms, such as silicon [8], [20], [23], [24], [89], [90], [28], [32], [93] silicon nitride (Si_3N_4) [20]–[22], [31], [92] and polymers [22], [32]. It is hence impossible to broadly compare the highest achievable surface sensitivities across different WG types and integration platforms. Moreover, most sensitivity analyses consider only a specific type of surface layer with prescribed refractive index.

In this paper, we define a universal surface sensitivity which is broadly applicable to layers of different thicknesses and refractive indices. Focusing on Si_3N_4 and Si as the most common integration platforms, we systematically analyze a wide variety of WG types, comprising simple strip WG, slot and double slot WG, as well as sub-wavelength grating (SWG) WG. For each of these WG types, we identify the optimum geometry for both TE and TM polarization, and we compare the highest achievable surface sensitivities, taking into account implementation limitations that are associated with state-of-the art fabrication technologies. The focus of our analysis is on WG types that can be reliably mass-produced by optical lithography and single-etch structuring of WG on solid substrate layers. Note that even higher sensitivities can be achieved by more sophisticated WG concepts comprising ultra-small features [94] or suspended WG sections [95]. These schemes, however, require dedicated fabrication processes which are not yet accessible through scalable foundry processes. Exploiting the scalability of Maxwell's equations with respect to refractive index and geometry, we derive and physically explain general trends and design rules to corroborate the numerical results. Our findings can be used as design guidelines to select the appropriate WG platform and to optimize sensitivity for a given measurement task.

4.2 Scope

4.2.1 Basic sensing principle: Wave propagation and effective refractive index

For illustrating the basic sensing principle, we regard homogeneous sensing with a waveguide core embedded in an infinitely extended cladding medium. First, we define a few quantities: The propagation of monochromatic plane waves with vacuum wavelength λ in a homogenous medium is determined by the propagation constant $\beta = nk_0$ (refractive index n, vacuum propagation constant $k_0 = 2\pi/\lambda$). Dielectric WG consist of a high-refractive index core (n_{core}) and a low-refractive index cladding medium (n_{M}). For integrated optical WG made from silicon or silicon nitride, the core is usually supported by a buried oxide layer (BOX, bottom cladding) with refractive index n_{BOX}. The evanescent parts of the WG mode, which are essential for the sensing process, extend into the cladding region. The actual field distribution in the various materials determines the WG propagation constant β, which can be expressed by an effective refractive index $n_{\mathrm{e}} = \beta/k_0$. If the refractive index of the WG cladding changes, β and hence n_{e} are modified, which impacts the phase shift $\varphi = -\beta L = -n_{\mathrm{e}} k_0 L$ accumulated over a propagation length L. Due to the large optical frequencies, a change of n_{e} is measured with high accuracy. For a given WG length L, the measured phase shift can be referred to a change Δn_{e} of the effective index, which finally allows to sense a change of the cladding index. The larger Δn_{e} becomes for a certain cladding index change, the more sensitive the device becomes.

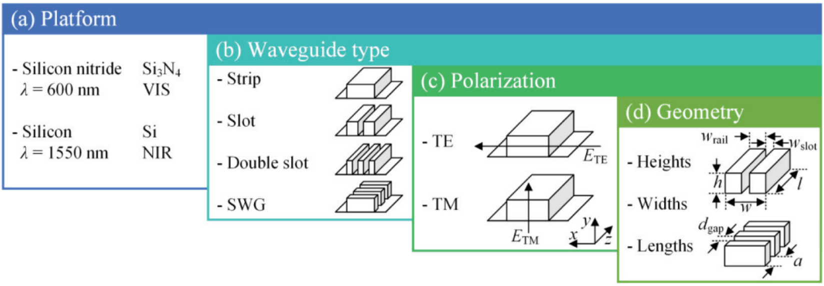

Figure 4.1: Essential design elements for maximizing surface sensitivity. For each combination of **(a)** material platform, **(b)** WG type and **(c)** polarization, the optimum **(d)** geometry can be determined, observing reasonable technological constraints.

4.2.2 Parameters for WG-based sensing

Numerous parameters determine how sensitive Δn_e reacts on a cladding index change Δn_M. Figure 4.1 summarizes the essential design elements for a WG: The material platform, the WG type, the polarization, and the WG geometry.

Platform Common integration platforms for optical sensors rely on a layer stack of a silicon (Si) or silicon nitride (Si_3N_4) device layer on a several micrometer thick BOX (SiO_2) as a bottom cladding, mechanically supported by a Si substrate. WG are structured in the device layer, and the BOX thickness is chosen to avoid leakage into the high-refractive index silicon substrate as well as to optimize grating coupler efficiency.

While Si WG are operated in the near infrared (NIR), Si_3N_4 WG are suitable for operation across the whole visible (VIS) and NIR spectrum. As the target media for biosensors are usually provided in the form of aqueous solutions, sensor operation at VIS wavelengths is much less impaired by water absorption than in the NIR. However, a large wavelength allows relaxed WG fabrication accuracies, and reduces scattering loss due to WG roughness. In this paper, we thus consider Si WG operated at NIR telecom wavelengths around 1550 nm, where low-cost laser sources are readily available, as well as Si_3N_4 WG operated at 600 nm as an example of low-wavelength sensors, Figure 4.1(a).

Waveguide type For both integration platforms, we study four typical WG types, denoted as strip, slot, double slot and subwavelength grating (SWG) WG, Figure 4.1(b). The last three types require significantly smaller feature sizes than the strip WG and thus lead to more challenging fabrication processes. We concentrate on single-mode WG, combining stable operation with high surface sensitivity.

Polarization We study the fundamental mode of both (quasi-)TE and (quasi-) TM polarization, Figure 4.1(c). The term (quasi-)TE refers to the case where the dominant transverse electric field component is oriented parallel to the substrate. Similarly, (quasi-)TM denotes a configuration in which the dominant transverse magnetic field component is parallel to the substrate. For the TE polarization, an enhancement of the electric field E_x exists at the WG sidewalls because the normal component $D_x = \varepsilon_0 n^2(x) E_x(x)$ of the displacement must be continuous, while for TM polarization this field enhancement is to be seen at the top and at the bottom WG surfaces.

Geometry For all combinations of platform, WG type and polarization, we study the impact of the WG geometry in terms of height, width, and length (SWG only) of WG features, Figure 4.1(d). Three standard device layer heights h of 220 nm, 250 nm and 340 nm are considered for Si WG structured on silicon-on-insulator (SOI) wafers. Wafers for structuring Si_3N_4 WG are available with a maximum Si_3N_4 thickness of several hundred nanometers, if stoichiometric growth is important, and we therefore consider typical WG heights h of 200 nm, 300 nm and 400 nm. For all WG types, we vary the overall width w in steps of 10 nm. For slot and double-slot WG, we additionally vary the slot width w_{slot} in four steps. For SWG WG, we vary the period a and the spacing d_{gap} between the WG elements, which can also be quantified by the fill factor $\text{FF} = (a - d_{\text{gap}})/a$. We chose a minimum feature size of $80\,\text{nm}$ to meet commercial technological conditions.

In the following, we define the surface sensitivity as a quantitative metric and maximize it by varying the various WG parameters. Given a certain sensor application, this data set allows to find the optimum design for a WG-based sensor.

4.3 Methods

4.3.1 Sensitivity of waveguide surfaces with respect to attached molecules

In WG-based sensing, two basic approaches are commonly used, which are compared in Figure 4.2. For so-called homogeneous sensing, a bare WG core is exposed to a typically aqueous homogeneous target medium with refractive index n_M, Figure 4.2(a). For surface sensing, a WG core is functionalized such that target molecules from an aqueous solution can bind to the core forming a surface layer with effective thickness t_{SL} and refractive index n_{SL}, Figure 4.2(b).

For homogeneous sensing, a change in n_M causes a change Δn_e of the effective index. This change is the stronger the more the mode optical field extends into the target medium. Homogeneous sensing is usually unspecific,

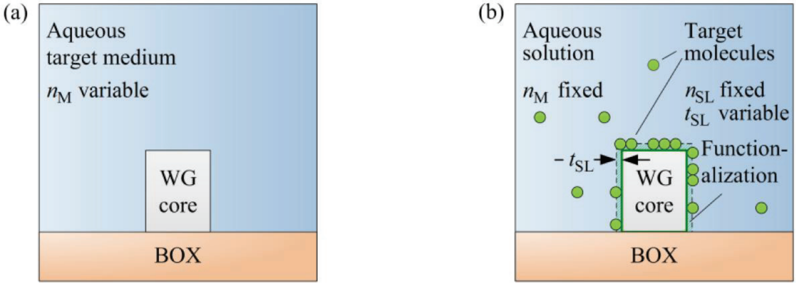

Figure 4.2: Plain and functionalized strip WG on a buried silicon oxide (BOX) layer. **(a)** Homogeneous sensing. The aqueous target medium with refractive index n_M forms the homogeneous cladding of the WG core. A variation of n_M leads to a change in the effective refractive index of a guided mode. **(b)** Surface sensing. The refractive index n_M of the aqueous cladding solution remains constant. Target objects such as molecules, cells, vesicles or other corpuscules attach to the WG core, often mediated by a specific surface functionalization. The effect on the wave propagation is modelled with a surface layer (SL) having a refractive index n_{SL} and an effective layer thickness t_{SL}. The effective layer thickness takes into account the size of the target objects as well as the ratio of occupied binding sites.

i.e., Δn_e cannot be traced back to a specific substance in the target medium if it is unknown which constituent is actually changing.

For surface sensing, the refractive index n_M of the aqueous solution remains essentially fixed, while the molecules, bound to the surface layer, influence the optical mode. By functionalizing the WG surface with dedicated capture agents, surface sensing can be used for specific detection of certain target analytes. The change Δn_e is the stronger, the more the optical field is concentrated within the surface layer. The definition of an effective layer thickness t_SL accounts for a possibly inhomogeneous distribution of target molecules within the surface layer. With biological samples this effective thickness is in the nanometer range, and n_SL is typically around 1.5.

For the remainder of this paper, we concentrate on surface sensing, offering a wide variety of applications. We are hence interested in the detailed influence of the surface layer on the electric and magnetic field distribution.

Figure 4.3 and Figure 4.4 show the simulated electric field magnitudes of the fundamental quasi-TE mode of strip, slot and double slot WG, and for subwavelength grating WG, respectively. Details on the simulation parameters can be found in Section 4.7. White contours mark the surface layer where molecules bind, leading to a change of the local refractive index.

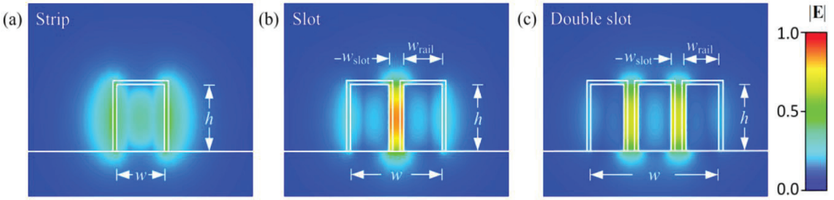

Figure 4.3: Simulated electric field magnitudes of the fundamental quasi-TE mode in different WG geometries with height h and total width w. White contours mark the surface layer on the WG core. The larger the field strength in this region is, the larger the surface sensitivity becomes. The surface layer is disregarded for the field calculation. **(a)** Strip WG. The surface layer experiences only moderate field strengths. **(b)** Slot WG. A large field strength is located in the surface layers of the slot. **(c)** Double slot WG. The field strength in each of the two slots is smaller than for a single slot, but the relevant surface layer area has doubled.

A higher field concentration in these regions increases the surface sensitivity. While in a typical strip WG, Figure 4.3(a), a large portion of the power is located inside the WG core, slot and double slot WG concentrate the power between the rails, Figure 4.3(b) and Figure 4.3(c). This means that the surface layer experiences higher field strengths in slotted WG, leading to a larger Δn_e compared to a strip WG. SWG WG are composed of a multitude of individual WG elements, thus increasing the surface layer area per unit length of the WG. Figure 4.4(a) shows a section of a SWG WG with three periods along the propagation axis (pink arrow). For determining the surface sensitivity, a 3D elementary cell has to be simulated using periodic boundary conditions in the axial direction [96]. The three coloured planes mark the cross sections where the field distributions of Figure 4.4(b)-(d) are plotted. In Figure 4.4(c), high field strengths (red regions) are located at the vertical edges of the blocks.

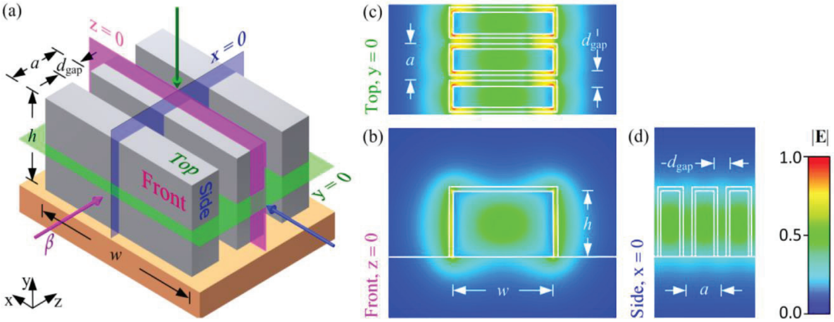

Figure 4.4: Section of a subwavelength grating (SWG) WG and simulated electric field magnitudes of the fundamental quasi-TE mode. Compared to a strip WG, the surface layer area per unit length of the WG is increased. **(a)** Schematic of a SWG WG with width w, height h, period a and gap size d_gap. The pink arrow marks the direction of propagation. Specific cross-sections $z = 0$, $y = 0$, $x = 0$ are indicated with colored planes. Front, Top and Side mark the associated views. **(b)-(d)** Electric field magnitudes. White contours mark the surface layers on the WG core, which are disregarded for the field calculation. The larger the field strength in this region and the larger the surface, the bigger the surface sensitivity becomes. **(b)** Front view at $z = 0$. The surface layer experiences only moderate field strengths. **(c)** Top view at $y = 0$. Large field strengths (red areas) occur at the vertical edges of the blocks. **(d)** Side view at $x = 0$. Moderate field strengths are found at surfaces $z = \mathrm{const.}$

4.3.2 Surface sensitivity and field perturbation approach

In the following, we define the surface sensitivity $S^{(\mathrm{surf})}$ as a quality metric for quantifying which WG design leads to the potentially highest overall sensor sensitivity. In order to obtain $S^{(\mathrm{surf})}$ for a specific WG with a specific surface layer, a full simulation of the WG with and without the surface layer would be required. This would include various combinations of surface layer properties like layer refractive index n_{SL} and layer thickness t_{SL} and thus requires a multitude of high-resolution simulations to resolve the surface layer with a thickness in the range of a few nanometers. Exploring the whole parameter space as discussed in Section 2 and Figure 4.2 would hence be a time-consuming and probably unrealistic endeavour.

To overcome this problem we use a perturbation approach. To this end, we perform a single finite-element method (FEM) simulation of a bare WG for each WG geometry, store the resulting fields and compute the influence of an additional surface layer using a field interaction factor. This technique is only valid for small perturbations, i.e., the modal field does not change significantly with the surface layer, and hence the effective refractive index n_{e} changes only slightly, too. In our case, binding events of molecules change the refractive index of a surface layer of thickness t_{SL} from n_{M} to n_{SL}, where n_{SL} is the refractive index of the attached molecules and n_{M} denotes the background refractive index of the solution. The conditions for the perturbation approach hold, if either the thickness is small – then the refractive index change n_{SL}-n_{M} can be larger – or if n_{SL}-n_{M} is small, in which case t_{SL} can be larger.

We will first consider the general case of a z-variant SWG WG. According to Equation (4.14) and Equation (4.15) in Section 4.9, the local perturbation in the surface layer can be translated into a change $\Delta n_e^{(\mathrm{surf})}$ of the effective refractive index via the field interaction factor $\Gamma_{\mathrm{SL}}\left(t_{\mathrm{SL}}\right)$,

$$\Delta n_{\mathrm{e}}^{(\mathrm{surf})} = \left(n_{\mathrm{SL}} - n_{\mathrm{M}}\right)\Gamma_{\mathrm{SL}},$$
$$\Gamma_{\mathrm{SL}}(t_{\mathrm{SL}}) = \frac{1}{Z_0} \frac{\frac{1}{\mathrm{a}} n_{\mathrm{M}} \iiint\limits_{V_{\mathrm{SL}}} |\mathbf{E}|^2 \, \mathrm{d}V}{\iint \mathrm{Re}(\mathbf{E} \times \mathbf{H}^*) \cdot \mathbf{e}_{\mathrm{z}} \mathrm{d}A} = \frac{c}{n_{\mathrm{g,SL}}} \frac{W_{\mathrm{SL}}}{P}. \tag{4.1}$$

Note that the field interaction factor $\Gamma_{\mathrm{SL}}\left(t_{\mathrm{SL}}\right)$ in Equation (4.1) is different from the intensity-related field confinement factor $\Gamma_i^{(\mathrm{conf})} = W_{\mathrm{SL}}/W$, because it describes also slow-light propagation, see Equation (4.10). For computing $\Gamma_{\mathrm{SL}}(t_{\mathrm{SL}})$, we simulate the fields of a unit cell for a bare SWG WG without surface layers, and integrate $|\mathbf{E}|^2$ over the fictitious surface layer volume V_{SL} within that unit cell of length a. The result is proportional to the electric energy W_{SL} in the surface layer per unit cell, Equations (4.7) and Equation (4.10) for $i = \mathrm{SL}$, normalized to the cross-sectional power P of Equation (4.5). The integral in the denominator extends over the entire (x,y)-plane.

For z-invariant WG such as strip, slot, or double slot structures, Equation (4.1) can be simplified by exploiting the fact that the integral over $|\mathbf{E}|^2$ is invariant along z. Simplifying the volume integral in the numerator, we obtain

$$\Gamma_{\mathrm{SL}}(t_{\mathrm{SL}}) = \frac{1}{Z_0} \frac{n_{\mathrm{M}} \iint\limits_{A_{\mathrm{SL}}} |\mathbf{E}|^2 \mathrm{d}A}{\iint \mathrm{Re}(\mathbf{E} \times \mathbf{H}^*) \cdot \mathbf{e}_{\mathrm{z}} \mathrm{d}A} \tag{4.2}$$

for the special case of z-invariant WG. We use Equation (4.2) to analyze $\Gamma_{\mathrm{SL}}(t_{\mathrm{SL}})$ for a set of widely different silicon strip WG geometries, operated in quasi-TE polarization, see in Figure 4.5(a) “Perturbation”. As a comparison, we extract the numerically exact values $\Gamma_{\mathrm{SL}}^{(\mathrm{sim})}(t_{\mathrm{SL}}) = \Delta n_{\mathrm{e}}^{(\mathrm{surf,\,sim})} \big/ \left(n_{\mathrm{SL}} - n_{\mathrm{M}}\right)$ from $\Delta n_{\mathrm{e}}^{(\mathrm{surf,\,sim})}$ obtained by FEM simulations of quasi-TE fields that include the actual surface layers, and plot them in Figure 4.5(a) with a dashed line “Simulation”. The agreement is very good except for large surface layer thicknesses t_{SL} on narrow and high WG. In this case the majority of the field is contained within the surface layers, violating the assumption of a small field

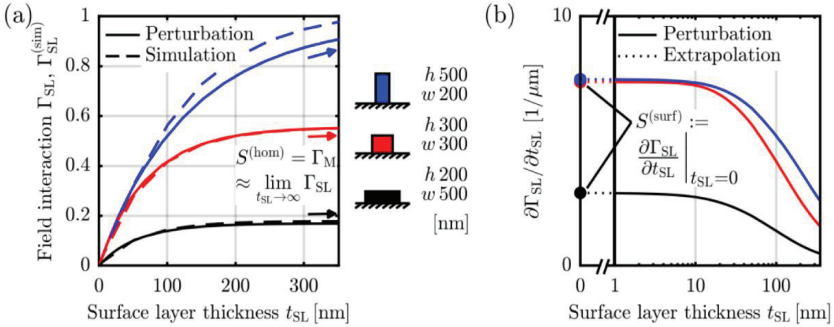

Figure 4.5: Validation of perturbation model and definition of surface sensitivity $S^{(surf)}$ for a set of widely different silicon strip WG geometries propagating quasi-TE fields, see legend. **(a)** Field interaction factor Γ_{SL} in surface layer of thickness t_{SL}. For each geometry, we compare Γ_{SL} computed with a perturbation approach (based on a single FEM simulation without a surface layer) with $\Gamma_{SL}^{(sim)}$ obtained from numerically exact calculations (FEM simulations with different surface layers). For small t_{SL} the agreement is very good. For large t_{SL} (marked by →) and $n_{SL} \approx n_M$, the field interaction factor Γ_{SL} approaches Γ_M and thus the homogeneous sensitivity $S^{(hom)}$. **(b)** The surface sensitivity $S^{(surf)} = \partial\Gamma_{SL}/\partial t_{SL}\big|_{t_{SL}\to\infty}$ allows an easy comparison of different WG, irrespective of the actual surface layer properties.

perturbation. The electric field outside the core decays approximately exponentially. For a penetration depth much larger than t_{SL}, the decay of the field magnitude and of the power within the surface layer can be approximated by a linear function. As a consequence, Γ_{SL} in Figure 4.5(a) exhibits a region where it depends linearly on t_{SL}.

We now want to define a sensing sensitivity which is – in the framework of the perturbation approach – independent of the surface layer thickness. This can be achieved by looking at the derivative $\partial\left(\Delta n_e^{(surf)}\right)/\partial t_{SL}$ at $t_{SL} = 0$. Because n_{SL} influences the result, we define the surface sensitivity as the derivative of the field interaction factor with respect to the surface layer thickness,

$$\begin{aligned}\Delta n_{\mathrm{e}}^{(\mathrm{surf})} &= \left(n_{\mathrm{SL}} - n_{\mathrm{M}}\right) S^{(\mathrm{surf})}, \\ \Delta t_{\mathrm{SL}} &= \left(n_{\mathrm{SL}} - n_{\mathrm{M}}\right) S^{(\mathrm{surf})} t_{\mathrm{SL}}, \\ S^{(\mathrm{surf})} &= \left.\frac{\partial \Gamma_{\mathrm{SL}}}{\partial t_{\mathrm{SL}}}\right|_{t_{\mathrm{SL}}=0}.\end{aligned} \tag{4.3}$$

Within the framework of the perturbation approach, the surface sensitivity $S^{(\mathrm{surf})}$ is independent of both the thickness and the refractive index of the surface layer, thus providing a universal guideline for a sensor design. To confirm this, we calculate the derivatives $\partial\Gamma_{\mathrm{SL}}/\partial t_{\mathrm{SL}}$ for the same WG types as used in Figure 4.5(a), and plot them semi-logarithmically in Figure 4.5(b) in a range $t_{\mathrm{SL}} = (1\ldots350)\,\mathrm{nm}$. We see that $\partial\Gamma_{\mathrm{SL}}/\partial t_{\mathrm{SL}}$ is constant for very small $\Delta\varepsilon(\mathbf{r}) = \varepsilon_0 \cdot \Delta\varepsilon_r(\mathbf{r})$, owing to the approximately linear dependence of Γ_{SL} on t_{SL} in this region. We extrapolate the curve to $t_{\mathrm{SL}} = 0$, where the computation fails due to the finite spatial discretization. In Figure 4.5(b) these extrapolated values are marked with filled circles and denoted by $S^{(\mathrm{surf})}$, see Equation Equation (4.2) and Equation (4.3). Note that a WG design for best homogeneous sensitivity $S^{(\mathrm{hom})} = \Gamma_{\mathrm{M}} \approx \lim_{t_{\mathrm{SL}}\to\infty} \Gamma_{\mathrm{SL}}$ is not necessarily optimum when it comes to surface sensing, see Equation (4.16) in Section 4.9 for rigorous definition of $S^{(\mathrm{hom})}$. This can be inferred by comparing $S^{(\mathrm{hom})}$ of the two top strip WG in Figure 4.5(a) (blue and red arrows) to the corresponding $S^{(\mathrm{surf})}$ of the same WG in Figure 4.5(b) (blue and red dots at $t_{\mathrm{SL}} = 0$): A larger homogeneous sensitivity does not lead to a difference in surface sensitivity. In sensing applications, the desired measurement quantity is the effective surface layer thickness t_{SL}. From a measurement of Δn_{e} and for known bulk refractive indices n_{SL} and $\Delta n(\mathbf{r}) << n(\mathbf{r})$, t_{SL} can be inferred from Equation (4.3). A proper choice of the WG then maximizes $S^{(\mathrm{surf})}$ and therefore the measurement sensitivity for t_{SL}.

4.4 Results

We extract the surface sensitivity $S^{(\mathrm{surf})}$ according to Section 3.2 for all kinds of WG outlined in Section 2.2. For each TE- or TM-operated WG core in

Si_3N_4 or alternatively in Si, a few typical values of heights h, slot widths w_{slot}, periods a and fill factors FF are considered. For each combination of these parameters, the total WG width w (see Figure 4.3) is then optimized to obtain optimum surface sensitivity $S_{\text{opt}}^{(\text{surf})}$. To this end, the WG width is swept with a step size of 10 nm. The range of w was chosen to maintain single-mode operation and to avoid substrate leakage for a BOX thickness of $2\,\mu\text{m}$. The following WG surface sensitivity analysis relates to Si_3N_4 cores operated in the VIS (Section 4.1) as well as to Si cores operated in the NIR (Section 4.2).

4.4.1 Silicon nitride - VIS

For Si_3N_4 strip WG operated at a vacuum wavelength of 600 nm, Figure 4.6(a) displays the surface sensitivity $S^{(\text{surf})}$ as a function of the WG width w for three different WG heights h and for both polarizations. Surface sensitivity generally benefits from large electric field strengths in the region of the surface layer as indicated in Figure 4.3. Within their single-mode range, each WG shows a maximum $S_{\text{opt}}^{(\text{surf})}$ at a distinct width w_{opt}, marked by ● for TE and by ▲ for TM. Any deviation from this optimum width w_{opt} reduces the interaction factor of the mode field with the surface layers, e.g., by concentrating the modal field to the WG core in the case of large w, or by spreading the mode field over a wider cladding region for small w. In the second case, a large portion of the modal field propagates in the BOX, where it cannot contribute to sensing. In Figure 4.6(b), the extracted w_{opt} (green, left vertical axis) and the corresponding $S_{\text{opt}}^{(\text{surf})}$ (magenta, right vertical axis) are plotted as a function of the WG height h. The largest $S_{\text{opt}}^{(\text{surf})}$ are found for large h and small w for both polarizations, with TE operation being more sensitive than TM operation. In the TE case, the two sides of the WG exploit the field enhancement, and only a small portion of the mode propagates in the BOX, see Section 5.2 for a more detailed discussion.

We apply the same procedure to TE-operated Si_3N_4 slot and double slot WG and plot the results in Figure 4.7. As for the strip WG, the sensitivity increases for higher WG. Decreasing WG width first leads to increasing sensitivity, which drops again as the width becomes too small and the mode extends far

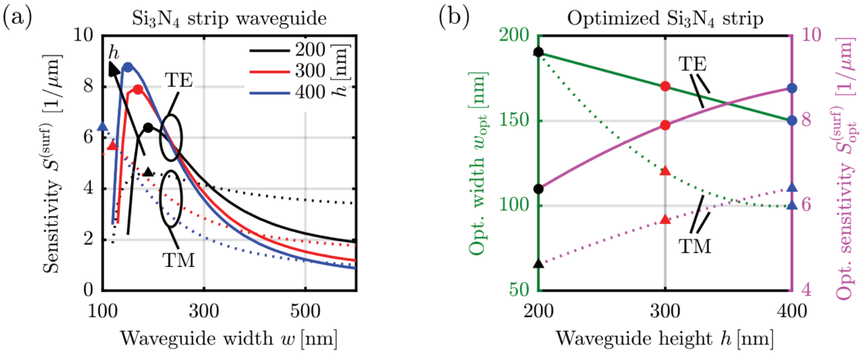

Figure 4.6: Optimization of Si_3N_4 strip WG. **(a)** Surface layer sensitivity $S^{(\mathrm{surf})}$ of Si_3N_4 strip WG for three standard heights h as a function of WG width w in TE and TM operation. For decreasing WG width, the sensitivity first increases to its maximum value and then drops. The drop is caused by the fact that the mode extends far into the cladding or is even lost to the substrate for very small WG widths. The optimum sensitivities $S^{(\mathrm{surf})}_{\mathrm{opt}}$ at the corresponding optimum widths w_{opt} are marked by dots and triangles. **(b)** Comparison of optimum WG width (green, left axis) and optimized surface sensitivity (magenta, right axis) as a function of WG height. High and narrow WG (blue markers) are most sensitive.

into the cladding, Figure 4.7(a). Smaller slot widths increase the field strength in the slot, Figure 4.7(b). This, together with the growth of the total core surface as compared to a strip WG, increases $S^{(\mathrm{surf})}$. The slot WG behaves like two strip WG if $w_{\mathrm{slot}} \gg w_{\mathrm{rail}}$. In this case, each of the strips carries half the power of the slot WG and both the optimum rail width and the optimum sensitivity converge to those of a single optimum strip WG, see top light green line (∞) and light magenta line (∞) in Figure 4.7(b). The double slot WG behaves like three separate strip WG if $w_{\mathrm{slot}} \gg w_{\mathrm{rail}}$. In this case, each strip carries one third of the power of the slot WG. As before, both the optimum rail width and the optimum sensitivity converge to those of a single optimum strip WG, see top light green line (∞) and light magenta line (∞) in Figure 4.7(c) and in Figure 4.7(d).

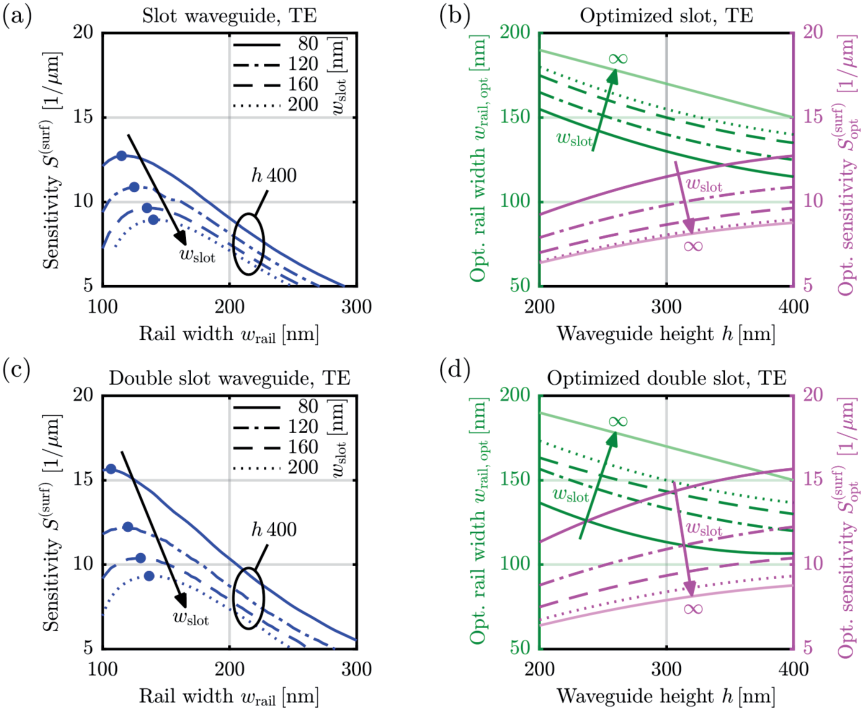

Figure 4.7: Optimization of Si strip, slot and double slot WG. **(a)** Surface layer sensitivity $S^{(\mathrm{surf})}$ for Si strip WG with three standard heights h as a function of WG width w in TE and TM operation. For decreasing WG width, the sensitivity first increases to its maximum value and then drops. The drop is caused by the fact that the mode extends far into the cladding or is even lost to the substrate for very small WG widths. The optimum sensitivities $S_{\mathrm{opt}}^{(\mathrm{surf})}$ at the corresponding optimum widths w_{opt} are marked by dots and triangles in (a) and compared in **(b)**. For TE polarization, high and narrow WG yield the best results. For TM, no pronounced sensitivity gain is observed for higher WG. **(c),(d)** Optimized geometries for slot and double slot Si WG. The sensitivity increases for smaller slot widths and higher WG, the fabrication of which is limited by technological constraints. The light solid lines indicate the limits for $w_{\mathrm{slot}} \to \infty$ (light green and light magenta), which correspond to the case of individual strip WG as shown in **(b)**. Compared to Si_3N_4, operated in the VIS, the Si rails, operated in the NIR, are typically 100 nm wider while the sensitivity is slightly larger.

4.4.2 Silicon - NIR

For silicon WG operated in the NIR at $\lambda = 1550\,\mathrm{nm}$, we apply the same technique as described in Section 4.1 for extracting the optimized widths $\mathbf{E}(t,\mathbf{r}) = \mathbf{E}(\mathbf{r})e^{\mathrm{j}\omega t}$ and sensitivities $S_{\mathrm{opt}}^{(\mathrm{surf})}$. In Figure 4.8(a) we display the surface sensitivity $S^{(\mathrm{surf})}$ of a strip WG with different heights h and polarizations as a function of the strip width w. As for Si_3N_4 strip WG, Figure 4.8(a), we see a sensitivity maximum within the range of single-mode operation. The TE sensitivity exhibits a pronounced maximum when varying the WG width, whereas the maximum of the TM sensitivity is much less pronounced, Figure 4.8(a).

We extract the optimum sensitivity and find that, similar to Si_3N_4, the TE sensitivity can be optimized by choosing a high WG with a narrow width, while the optimum TM sensitivity depends only weakly on the WG height, Figure 4.8(b). This is in contrast to the findings for the Si_3N_4WG, Figure 4.6(a) and Figure 4.6(b). We attribute this to the fact that the refractive index of Si is significantly larger than that of Si_3N_4 and hence the asymmetry introduced by the underlying BOX is less significant for the case of Si WG. Consequently, for the WG heights h under consideration and for small w, the TM modal field does not extend into the BOX as strongly as for the Si_3N_4 WG. Regarding Si slot and double slot WG, Figure 4.8(c) and Figure 4.8(d), the trends for optimum WG parameters are similar to those of Si_3N_4 WG, Figure 4.7, and thus the same conclusions as in Section 4.1 can be drawn.

For achieving better sensitivities, completely different WG structures in form of sub-wavelength gratings (SWG) were proposed [26], [33], [89], see Figure 4.4. For a systematic comparison to strip and slot WG, we calculate and optimize the surface sensitivities of SWG WG, see Figure 4.9. Figure 4.9(a), left y-axis, shows the results obtained from two exemplary families of TE-operated SWG, which share the same period a, but differ in height h, and feature three different fill factors (50%, 60%, 70%, differing in opacity). For the smaller WG height ($h = 220\,\mathrm{nm}$, black lines) the sensitivity does not depend strongly on the WG width. Strip and slotted WG show a fast decrease of sensitivity for widths larger than w_{opt}, since the fields become smaller at the

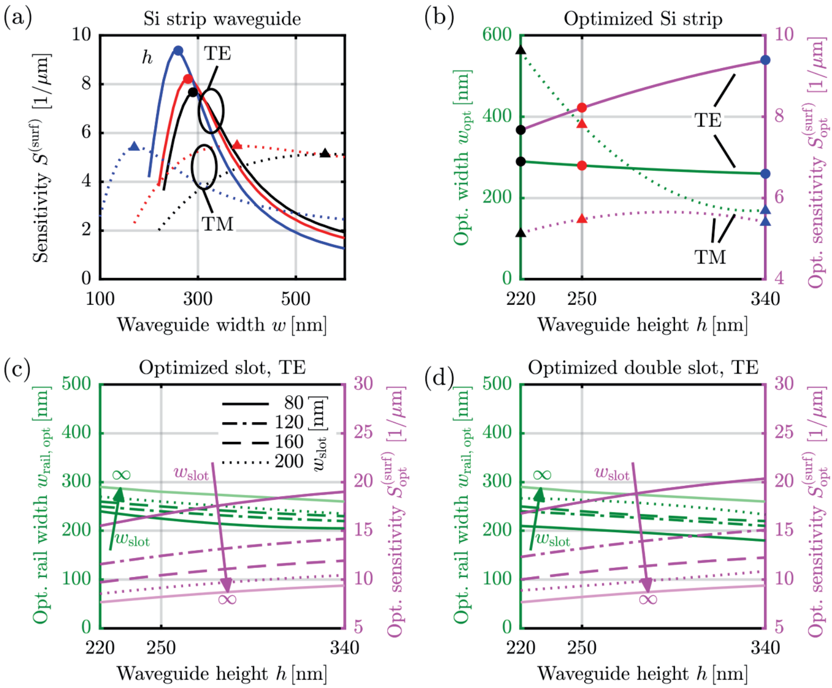

Figure 4.8: Optimization of Si strip, slot and double slot WG. **(a)** Surface layer sensitivity $S^{(\mathrm{surf})}$ for Si strip WG with three standard heights h as a function of WG width w in TE and TM operation. For decreasing WG width, the sensitivity first increases to its maximum value and then drops. The drop is caused by the fact that the mode extends far into the cladding or is even lost to the substrate for very small WG widths. The optimum sensitivities $S^{(\mathrm{surf})}_{\mathrm{opt}}$ at the corresponding optimum widths w_{opt} are marked by dots and triangles in **(a)** and compared in **(b)**. For TE polarization, high and narrow WG yield the best results. For TM, no pronounced sensitivity gain is observed for higher WG. **(c),(d)** Optimized geometries for slot and double slot Si WG. The sensitivity increases for smaller slot widths and higher WG, the fabrication of which is limited by technological constraints. The light solid lines indicate the limits for $w_{\mathrm{slot}} \rightarrow \infty$ (light green and light magenta), which correspond to the case of individual strip WG as shown in **(b)**. Compared to Si_3N_4, operated in the VIS, the Si rails, operated in the NIR, are typically 100 nm wider while the sensitivity is slightly larger.

sensitive side walls and upper surfaces and are more confined to the core. This effect is less pronounced in the SWG WG, since the sensitive surface in

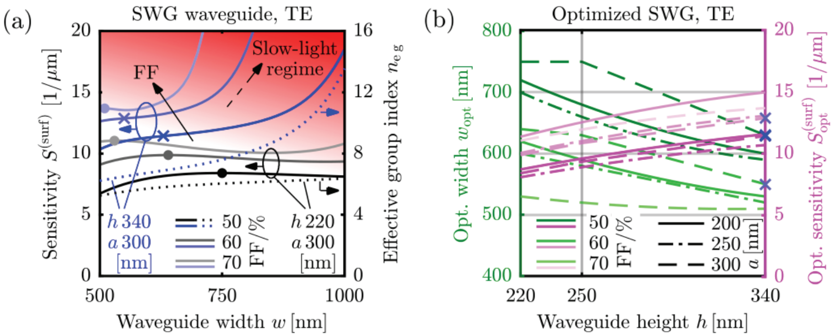

Figure 4.9: Optimization of Si sub-wavelength grating (SWG) WG. **(a)** Sensitivity of two SWG WG families with different heights, but common period $a = 300$ nm as a function of WG width w for varying fill factors FF. Black lines with various shadings stand for a WG height of $h = 220$ nm. In this case, the sensitivity does not change significantly with w. For higher SWG WG ($h = 300$ nm, blue lines), the sensitivity traces do not exhibit an optimum before entering into the so-called slow-light regime, where the sensitivity is dominated by a largely increased effective group index n_{eg} (dotted lines for two different heights for FF = 50%). For these traces, we choose the inflection points (blue crosses) to define reasonable sensor designs that are not subject to the impairments associated with slow-light operation. Note that this does not represent an optimum in a strict mathematical sense. **(b)** Overview of optimized SWG WG sensitivities and geometries outside the slow-light regime for different heights, periods, and fill factors. As a trend, the sensitivity increases for high WG and small gap size $d_{\text{gap}} = a\,(1 - \text{FF})$. Sensitivities obtained from inflection points at the transition to slow-light operation are again marked by blue crosses. Note that the traces for FF = 70% and $a = 200$ nm or $a = 250$ nm do not appear in the plot since the associated gap sizes are below the minimum feature size of 80 nm.

between the individual blocks are still experiencing high field strengths. The maximum sensitivity shifts to smaller w, when the FF increases. This is to be expected: If the FF becomes larger, the effective refractive index increases and the modal field is stronger confined to the SWG "core". For a sufficient influence of the analyte, the field must then extend into the SWG "cladding", which is achieved by decreasing the WG width.

Interestingly, for higher SWG WG ($h = 340\,\text{nm}$, blue lines), no optimum sensitivity within the observed range of w is found. Instead, the sensitivity increases strongly for larger FF and wider WG. This increase is caused by a decrease of the group velocity: Larger FF and increased w lead to an increase of the Bragg wavelength associated with the SWG structure. Once the Bragg wavelength comes close to the operation wavelength of the sensor, the device enters the so-called slow-light regime [96], which is characterized by a greatly reduced group velocity and a greatly increased effective group index n_{eg}.

This leads to strong interaction of the guided mode with the surface layer and hence to a sharp increase of the sensitivity even though the field confinement $\Gamma_i^{(\mathrm{conf})}$ of the surface layer does not significantly increase, see Section 4.9, Equation (4.7). Note, however, that operation in the slow-light regime strongly increases the detrimental impact of environmental influences and fabrication tolerances [97] on mode propagation. Amongst others, the sensitivity and the optical propagation loss can vary significantly, such that reproducible device properties and hence a reliable sensor read-out are difficult to obtain in practice. This susceptibility to tiny changes can be seen exemplarily for the sensitivity of WG operating in the slow-light regime, Figure 4.9(a), which is why we exclude them from the following discussion. For sensitivity traces entering into the slow-light regime without showing a pronounced maximum in Figure 4.9(a), we choose the inflection points (blue crosses) to define reasonable sensor designs that are not subject to the impairments associated with slow-light operation without being optimum in a strict mathematical sense. Note that there is no distinct transition from “normal” SWG operation to the slow-light regime and that a strict classification is therefore difficult. The choice of the inflection point is motivated by the fact that it marks the width at which the influence of the increased effective group index n_{eg} starts dominating over the impact of the field confinement factor $\Gamma^{(\mathrm{conf})}$, Equation (4.10) in Section 4.9, and dotted lines for two different heights for $\mathrm{FF} = 50\%$, see Figure 4.9(a).

The optimal sensitivities of the SWG WG and those obtained for the transition to the slow-light regime are summarized Figure 4.9(b), indicating again a general sensitivity increase with WG height. Sensitivities obtained from inflection points at the transition to slow-light operation are marked by blue crosses. As a trend, $\mathbf{E}(\mathbf{r})$ increases for small $d_{\mathrm{gap}} = a(1-\mathrm{FF})$.

4.4.3 Comparison of optimized sensitivities

As a summary of the last two subsections, we compare the sensitivities for the Si_3N_4 platform in the VIS ($\lambda = 600$ nm) and for the Si platform in the NIR ($\lambda = 1550$ nm). In Figure 4.10, we display the optimized surface layer sensitivities $S_{\mathrm{opt}}^{(\mathrm{surf})}$ of four WG types (strip, slot, double slot, SWG) with optimized widths w_{opt} and three different heights h for each platform. The left (right) panel shows the results for TE (TM) polarization. Three SWG positions are empty because either the gap size is below the minimum feature size of 80 nm, or because the structures do not support a well-guided WG mode ("poor waveguiding").

Generally, WG operated in TE polarization tend to be more sensitive than their TM-operated counterparts. Taking into account technological constraints such as a minimum feature size, the sensitivity of sophisticated WG designs can be increased by approximately a factor of 2 compared to a simple optimized strip WG. Moreover, slotted WG exhibit higher surface sensitivities than strip and SWG WG. Generally, the silicon platform exhibits higher

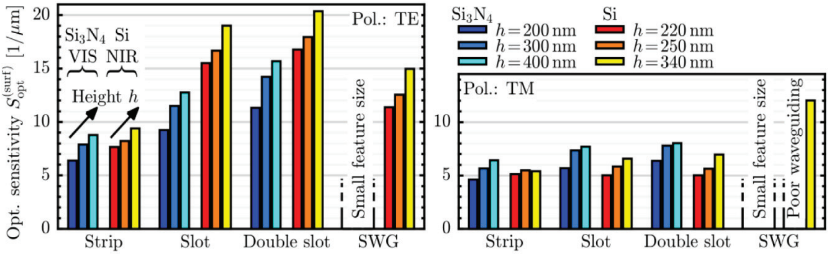

Figure 4.10: Comparison of the optimized sensitivity for the Si_3N_4 platform in the VIS ($\lambda = 600$ nm) and for the Si platform in the NIR ($\lambda = 1550$ nm). We consider four WG types with three standard heights, operated in TE and TM polarization. Sensitivity can be increased by higher WG cores, by using Si rather than Si_3N_4, and by TE-operation instead of TM. The three more advanced WG types (slot, double slot and SWG) offer an enhancement of up to a factor of 2 compared to TE strip WG, coming at the cost of a more complex fabrication process. Some SWG WG are excluded because either the gap size is below 80 nm ("small feature size"), or because the structures do not support a well-guided WG mode ("poor waveguiding"). Typical slot, double slot and SWG WG do not benefit from TM operation.

sensitivities than the silicon nitride platform, which can be attributed to the fact that a higher index contrast leads to a smaller penetration depth into the WG cladding and hence to a stronger interaction with a thin surface layer. Larger WG heights tend to be generally better. For the silicon photonic platform, a sensitivity improvement of a factor of 4 can be achieved by using optimum double slot WG operating in TE polarization instead of non-optimum standard strip WG featuring, e.g., WG dimensions of $w \times h = 450 \times 220\,\mathrm{nm}^2$ for TM operation. A detailed physical explanation of these trends is given in Section 5.2.

4.5 Discussion

For a better understanding of the trends summarized in Figure 4.10, we first discuss in Subsection 4.5.1 the influence of the cladding asymmetry and we introduce universal scaling laws of Maxwell's equations that allow to generalize the findings to other wavelengths and material platforms. Subsequently, Subsection 4.5.2 explains in detail the trends when varying platform, operating wavelength, polarization, and WG geometry. Subsection 4.5.3 discusses our results in view of an overall sensor performance, including the impact of mode loss and analyte delivery as well as a practical instruction on finding global sensitivity optima.

4.5.1 Physical interpretation - Cladding asymmetry and scaling laws

Cladding asymmetry We consider WG cores that are supported by a SiO_2 substrate (BOX) and are surrounded by an aqueous medium. Since the refractive index of SiO_2 is larger than that of water, the cladding of the WG is asymmetric. It is hence impossible to increase the interaction of the guided light with the functionalized surface of the WG core by simply indefinitely reducing the core dimensions. Any attempt to do so will predominantly increase the fraction of the mode fields in the BOX, which do not contribute to sensing, and therefore decrease the fraction in the surface layer, leading to a decrease of surface sensitivity.

Scaling laws According to Section 4.10, Table 4.1, line (1), scaling the geometry of a WG by σ_g while simultaneously scaling the operating frequency by $\sigma_\omega = 1/\sigma_g$ leads to a simple geometrical scaling of the eigenfunctions of the electric and magnetic fields by a factor of σ_g. This effect has no impact on the homogeneous sensitivity, since the relative portion of the mode fields in the cladding medium remains the same. However, the surface sensitivity Equation (4.3) as defined by a derivative with respect to the layer thickness t_{SL} scales by $1/\sigma_g$. *The optimum surface sensitivity of a WG with fixed RI profile hence scales proportionally to frequency and requires an inverse scaling of the geometry*.

Furthermore, scaling the refractive index profile of a WG by σ_n while simultaneously scaling the operating frequency by $\sigma_\omega = 1/\sigma_n$ does not change the distributions of the electric and the magnetic field. Note, however, that the ratio of the electric-field eigenfunction $\mathbf{E}(\mathbf{r})$ and the magnetic field eigenfunction $\mathbf{H}(\mathbf{r})$ must be scaled by a factor of $1/\sigma_n$, see Equation (4.19) and the corresponding discussion. In total, this leaves the sensitivity unchanged, see Section 4.10, Table 4.1, line (2). *The optimum surface sensitivity of a WG with fixed geometry does not change for a scaling of the RI profile along with an inverse scaling of the frequency*.

4.5.2 Trends for increased surface sensitivity

High index-contrast platform The surface sensitivity is maximized by an increased field concentration at the core surface which is in contact with the analyte-delivering aqueous medium. For a given wavelength, the surface sensitivity tends to increase if the refractive index ratio $n_{\mathrm{core}}/n_{\mathrm{M}}$ between core and cladding is increased. This is caused by the fact that the enhancement of surface-normal electric-field components is proportional to the square $(n_{\mathrm{core}}/n_{\mathrm{M}})^2$ of the index ratio. Similarly, the surface sensitivity increases when the refractive index profile is scaled up by a factor of $\sigma_{\mathrm{n}} > 1$ while the geometry is scaled down by $\sigma_{\mathrm{g}} = 1/\sigma_{\mathrm{n}}$ to maintain the same operating frequency, see Section 4.10, Table 4.1, line (4).

Short operating wavelength For a given platform, higher surface sensitivities can be achieved with shorter wavelengths. The geometry of the WG has to be chosen guided by the scaling law in Section 4.10, Table 4.1, line (1). A Si_3N_4 WG operated in the VIS will achieve a higher optimized surface sensitivity than an up-scaled Si_3N_4 WG operated in the NIR. When comparing optimized Si_3N_4 WG operated in the VIS with Si WG in the NIR, we see similar sensitivities, see Figure 4.10. This is due to a combination of scaling the operating frequency along with WG geometry and an increase of the index contrast, which have contrary effects on the surface sensitivity that partially cancel each other. However, optimized WG in the high index-contrast Si platform will be as good as or better than those in the Si_3N_4 platform, as the limitation caused by the cladding asymmetry is more severe for lower core refractive indices.

TE polarization The TE-mode sensitivity generally outperforms that of the TM-mode. For high index-contrast WG as considered in this work, the surface sensitivity is dominated by regions exhibiting a large field enhancement due to field discontinuities at the core-cladding interface. In the case of strip WG and of vertical-slot WG, TE mode operation exploits more of these surfaces showing a field enhancement compared to TM mode operation, where the interface to the bottom oxide cladding (BOX) does not contribute to the sensitivity.

It has to be noted that in typical telecom applications, WG with large widths and small heights are used (e.g. $w \times h = 450 \times 220\,\mathrm{nm}^2$). These established WG geometries are often directly transferred to sensing applications. For these WG and for improper choices of WG widths exceeding 400 nm, the TM-polarized mode may exhibit higher sensitivity than the TE, see Figure 4.8(a). However, under the assumption that the width w is chosen properly, TE-polarized modes exhibit optimized sensitivities. If an application demands Si WG operated with TM polarized light, SWG WG are best, see Figure 4.10.

Enlarged surface Larger core surfaces can generally lead to higher sensitivities. This is exploited by slot, double slot and SWG WG, which introduce additional sensor surfaces compared to strip WG. For slot and double slot WG operated in TE polarization, these additional surfaces lead to an enhancement of the dominant transvers electric-field component and can hence further increase surface sensitivity, see Figure 4.3. For SWG WG, the enhancement at the additional surfaces between the blocks affects the weaker longitudinal electric-field component, Figure 4.4. The sensitivity gain of SWG WG is hence smaller than that of slot and double slot WG and depends only weakly on the polarization.

Narrow waveguides Optimized sensing WG have a narrower core than typical routing WG designed for low-loss light transport. Narrow WG increase the sensitivity for both TE and TM polarization. When narrowing the WG, the sensitive area of the surface layer remains essentially constant for TE polarization, but the surface field strength initially increases. For very small WG widths, the modal field expands into the cladding and the field interaction with the surface layer decreases, hence reducing surface sensitivity. For TM polarization, an additional effect comes into play: When reducing the WG width, the top surface, containing high field strengths due to the field discontinuity, becomes smaller, while the overall field strengths at the core surface become more dominant as the mode expands into the cladding. This interplay leads to a less pronounced optimum with respect to the WG width than for TE polarization, see Figure 4.6(a) and Figure 4.8(a).

High waveguides Higher WG cores outperform thinner WG cores. Higher WG cores reduce the relative portion of the fields located in the BOX (cladding asymmetry). Since this area does not contribute to sensing, less field strength in the BOX leads to larger sensitivities. In addition, and especially for the TE mode, higher WG cores enlarge the sensitive sidewall regions that are subject to field enhancement.

Small slot widths and gap sizes Smaller slot widths and gap sizes generally increase the sensitivity. For slot WG, the sensitivity gain for TE is more pronounced than for TM polarization.

4.5.3 Overall sensor system performance and the impact of mode loss

It is important to note that, when implementing these WG into functional sensors, the overall system performance will also depend on additional aspects that are outside the scope of our current analysis. One of the most important aspects is the propagation loss of the optical mode: Adsorption of target molecules to the WG surface is usually measured by recording the phase shift accumulated over a certain propagation length L. In technical implementations of sensors, the phase measurement accuracy depends on the precision with which amplitudes can be measured in an interference setup. This precision and ultimately the detection limit of the sensor system decreases with increasing propagation losses, which, like the sensitivity, depends on WG platform, type, polarization and geometry. A rigorous system optimization would ideally have to take into account all these effects to account for mutual trade-offs and to find a global optimum of the WG design. This, however, would require a quantitative relationship between the WG geometry and the associated power propagation loss $\exp(\alpha L)$ characterized by the loss constant α, which is impossible to state in a general and reliable manner across different integration platforms.

For finding optima for the overall system sensitivity S_{sys} for a specific sensor implementation, we need to know three dependencies: The surface sensitivity $S^{(\mathrm{surf})}$ as a function of the WG geometry, provided in this paper, the WG loss constant α as a function of the WG geometry, which must be experimentally determined for the specific WG type and technology, and the influence of this loss on the effective-index sensitivity $\mathbf{H}(\mathbf{r}'/\sigma_g), \mathbf{E}(\mathbf{r}'/\sigma_g)$, which translates $\Delta n_{\mathrm{e}}^{(\mathrm{surf})}$ into a measurable output signal, e.g., a current ([6], [23], [98]). If the linewidth of the light source is neglected, the overall system sensitivity can be expressed by the product of the surface sensitivity and the effective-index sensitivity

$$S_{\mathrm{sys}} = S^{(\mathrm{surf})} S_{\mathrm{e}}(\alpha). \tag{4.4}$$

The results presented in this paper can hence serve both as guidelines for identifying and selecting promising WG designs and as quantitative measures to determine the overall system sensitivity S_{sys} once the technology-dependent loss constant α and the architecture-specific relationship $S_{\text{e}}(\alpha)$ are known.

Another aspect that may influence the overall performance of practical sensors is the analyte delivery to the sensor surface. In this context, narrow gaps or other high aspect-ratio voids tend to have less exchange with the surrounding liquid or might even not be accessible to large target objects such as cells or cellular vesicles. In these cases, simple strip WG geometries might exhibit advantages in comparison to more complex concepts featuring narrow strips and slots.

4.6 Summary

We have performed a comparative study of different WG types for application in label-free detection of chemical or biological analytes that specifically bind to functionalized WG surfaces. To this end, we have introduced the so-called surface sensitivity $S^{(\text{surf})}$ as a general quality metric that is broadly applicable to surface layers of different thicknesses and refractive indices. This metric allows to optimize the WG design and to compare the fundamentally achievable sensor performances across different WG types and integration platforms. We specify optimized WG designs along with the corresponding surface sensitivities for the most common WG parameter combinations. We also introduce and explain a computationally efficient recipe for applying the methodology to additional WG types that are not covered by our current study.

The following key findings result from our study: First, sensitivity trends can be explained by the interplay of a cladding asymmetry, the scaling laws of Maxwell's equations and the effect of field enhancement. Second, WG with optimum surface sensitivities are typically high and narrow, are fabricated on high-index contrast platforms and operated in TE polarization. Third, the surface sensitivity of highly sophisticated WG such as slot, double slot or sub-wavelength grating exceeds that of optimized strip WG by a factor of 2, and that of standard telecom strip WG by a factor of 4 if realistic feature size constraints are observed.

4.7 Simulation parameters and mesh considerations

[This section was published as Appendix A of [J4]]

In the following, we describe the relevant parameters used for the simulation, which are performed with CST (Computer Simulation Technology GmbH) Microwave Studio. Modal fields of the WG are calculated in the frequency domain. Simulation boundaries in the cross section are perfectly absorbing. The computational mesh is tetrahedral, and an ultra-fine mesh is required around the WG core to obtain accurate field data within the surface layers. The field interaction factor Γ_{SL} is well-described by a linear approximation for t_{SL} smaller than the penetration depth, see Figure 4.5(a). The surface sensitivity $S^{(\mathrm{surf})}$ can be reliably extracted from the derivative $\partial\Gamma_{\mathrm{SL}}/\partial t_{\mathrm{SL}}$ at $t_{\mathrm{SL}} = 0$ by a linear extrapolation of data within the first 10 nm, see Figure **4.5**(b). We have found that a mesh size of < 3 nm around the WG core region is sufficient. The choice of the mesh size in the cladding region was left to the program. The simulation area had a total size of 4 µm × 4 µm, where the bottom half of the simulation region was occupied by the 2 µm thick BOX. For WG significantly narrower than w_{opt}, the WG mode is not well-confined to the core anymore, and much larger simulation windows are required. These results were omitted from the discussion, but lie at non-practical WG geometries far away from any sensitivity optimum (Figure 4.6). The refractive indices were assumed to be $n_{\mathrm{Si}} = 3.48$, $n_{\mathrm{H_2O}} = 1.33$, $n_{\mathrm{SiO_2}} = 1.44$ for NIR light and $n_{\mathrm{Si_3N_4}} = 2.01$, $n_{\mathrm{H_2O}} = 1.33$, $n_{\mathrm{SiO_2}} = 1.46$ for VIS light.

4.8 TM simulations WG geometries

[This section was published as Appendix B of [J4]]

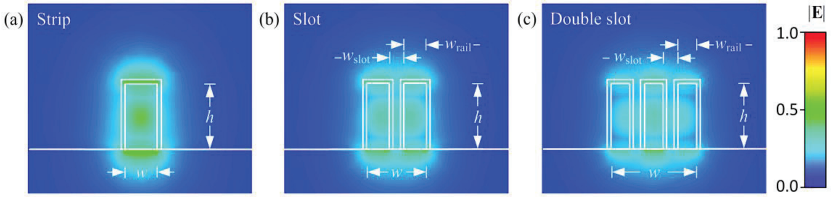

Figure 4.11: Simulated electric field magnitudes of the fundamental quasi-TM mode in different WG types with height h and total width w. White contours mark the surface layer on the WG core, which is disregarded for the field calculation. Surface sensitivity generally benefits from large electric field strengths in the region of the surface layer. **(a)** Strip WG. Large portion of the fields is lost to the non-sensitive interface between core and BOX. **(b),(c)** Slot WG and double slot WG. In contrast to the TE-Mode (Figure 4.3) there is no enhancement of the electrical field in the slot. The surface layer at the top of the core and in the slot experiences only moderate field strengths.

4.9 Propagation and sensitivity in waveguides

[This section was published as Appendix C of [J4]]

In the following discussion we assume a positive time dependence $\exp(\mathrm{j}\omega t)$. The complex vectorial electric mode field $\mathbf{E}(\omega,\mathbf{r})$ and magnetic mode field $\mathbf{H}(\omega,\mathbf{r})$ depend on angular frequency ω and position vector $\mathbf{r}$. We assume dispersive dielectric and non-magnetic materials which could be periodic along z with a period a. The propagation constant is β and the effective refractive index is $n_{\mathrm{e}} = \beta/k_0$, $k_0 = \omega/c$. Within each region, all refractive indices and all other parameters of the material are assumed to be constant. The various regions are denoted by a subscript i.

Cross-sectional power, stored energy, and field confinement factor The cross-sectional power P associated with a guided mode is constant along the propagation direction z (unit vector $\mathbf{e}_z$) if losses are neglected. This is true even if the WG geometry varies periodically in the direction of propagation, as in the case of SWG WG. The cross-sectional power is expressed by the real part of the time-averaged complex Poynting vector in the direction of propagation, integrated over the WG cross-section A with $\mathrm{d}A = \mathrm{d}x\,\mathrm{d}y$,

$$P = \tfrac{1}{2}\iint_A \mathrm{Re}\left(\mathbf{E}\times\mathbf{H}^*\right)\cdot\mathbf{e}_\mathrm{z}\,\mathrm{d}A. \tag{4.5}$$

The time-averaged stored energy per unit length is obtained by an integration of the modal electric and magnetic energy densities over a unit cell volume V [53]. The expression can be simplified with the help of the space-dependent material group index $n_\mathrm{g} = n + \omega\,\partial n/\partial\omega$ and with the identity $\iiint \varepsilon_0\varepsilon_\mathrm{r}\left|\mathbf{E}\right|^2\mathrm{d}V = \iiint \mu_0\mu_\mathrm{r}\left|\mathbf{H}\right|^2\mathrm{d}V$ [53], where, for non-magnetic materials, $\mu_r = 1$. This leads to

$$\begin{aligned} W^{(\mathrm{cell})} &= \frac{1}{a}\iiint_V \frac{1}{4}\left(\frac{\partial}{\partial\omega}\left(\omega\varepsilon_0\varepsilon_\mathrm{r}(\omega)\right)\left|\mathbf{E}\right|^2 + \frac{\partial}{\partial\omega}\left(\omega\mu_0\mu_\mathrm{r}(\omega)\right)\left|\mathbf{H}\right|^2\right)\mathrm{d}V \\ &= \frac{1}{a}\iiint_V \frac{1}{2}\varepsilon_0 n n_\mathrm{g}\left|\mathbf{E}\right|^2\mathrm{d}V. \end{aligned} \tag{4.6}$$

Note that in this relation, $W^{(\mathrm{cell})}$ is a length-related energy density with unit J/m and denotes the ratio of stored energy within a WG section, e.g., a unit cell, and the length of the section, e.g., the unit cell length a. For z-invariant WG, the volume element is simply $\mathrm{d}V = a\,\mathrm{d}A$.

The field confinement factor $\Gamma_i^{(\mathrm{conf})}$ represents the ratio of the mode energy in a partial volume V_i related to the energy in the total volume V of a unit cell,

$$\Gamma_i^{(\mathrm{conf})} = \frac{\iiint_{V_i} n_i n_{\mathrm{g},i}\left|\mathbf{E}\right|^2\mathrm{d}V}{\iiint_V n n_\mathrm{g}\left|\mathbf{E}\right|^2\mathrm{d}V} = \frac{W_i^{\mathrm{cell}}}{W^{\mathrm{cell}}}, \qquad \sum_i \Gamma_i^{(\mathrm{conf})} = 1. \tag{4.7}$$

Inside any partial volume V_i the refractive indices n_i and the associated group refractive index $n_{\mathrm{g,i}}$ are constant.

Variation theorem, effective group index, and field interaction factor The influence of small perturbations on the propagation constant $\Delta\beta$ can be examined by extending a variation theorem [[53], Equation (2.2.73)] for dielectric WG,

$$\Delta\beta = \frac{1}{4aP}\iiint\limits_V \left(\Delta(\omega\varepsilon_0\varepsilon_r)|\mathbf{E}|^2 + \Delta(\omega\mu_0)|\mathbf{H}|^2\right)\mathrm{d}V, \tag{4.8}$$

where $\Delta(\omega\varepsilon_0\varepsilon_r)$ and $\Delta(\omega\mu_0)$ denote the perturbations. If we introduce only a frequency perturbation $\Delta\omega$ at a fixed dielectric profile, we find that the effective group index $n_{\mathrm{eg}} = c\,\mathrm{d}\beta/\mathrm{d}\omega = n_{\mathrm{e}} + \omega\,\mathrm{d}n_{\mathrm{e}}/\mathrm{d}\omega$ is proportional to the ratio of the total energy W per unit cell length, and the power P,

$$n_{\mathrm{eg}} = c\frac{\Delta\beta}{\Delta\omega} = \frac{1}{Z_0}\frac{\frac{1}{a}\iiint\limits_V n n_g |\mathbf{E}|^2\,\mathrm{d}V}{\iint\limits_A \mathrm{Re}\left(\mathbf{E}\times\mathbf{H}^*\right)\cdot \mathrm{e}_z\,\mathrm{d}A} = c\frac{W}{P}. \tag{4.9}$$

Here, $Z_0 = 1/(\varepsilon_0 c)$ is the free-space wave impedance. Combining Equation (4.7) and Equation (4.9) we define the field interaction factor $\Gamma_i = n_{\mathrm{eg}}/n_{\mathrm{g},i}\cdot\Gamma_i^{(\mathrm{conf})}$ of a certain WG region denoted by subscript i,

$$\Gamma_i = \frac{n_{\mathrm{eg}}}{n_{\mathrm{g},i}}\Gamma_i^{(\mathrm{conf})} = \frac{1}{Z_0}\frac{\frac{1}{a}n_i\iiint\limits_{V_i}|\mathbf{E}|^2\,\mathrm{d}V}{\iint\limits_A \mathrm{Re}(\mathbf{E}\times\mathbf{H}^*)\cdot\mathrm{e}_z\,\mathrm{d}A}, \qquad n_{\mathrm{eg}} = \sum_i \Gamma_i n_{\mathrm{g},i}. \tag{4.10}$$

Note that the definition of $\Gamma_i = n_{\mathrm{eg}}/n_{\mathrm{g},i}\cdot\Gamma_i^{(\mathrm{conf})}$ is equivalent to the definition of $\Gamma_i = \Delta n_{\mathrm{e}}/\Delta n_i$ as the ratio of a local refractive index change Δn_i in region i and the associated change Δn_e of the effective modal index n_{e}, see next section. The effective group index can be expressed by a sum of the partial field interaction factors Γ_i multiplied with the respective material group indices. The field interaction factor is determined by the relative mode energy $\Gamma_i^{(\mathrm{conf})}$ in region i and by the time the mode dwells in that region, expressed by the effective modal group index n_{eg}, which can be larger than $n_{g,i}$. This is exploited in slow-light applications. For this case the field interaction factor can become larger than one.

Dielectric profile perturbation and definition of sensitivities If the 3D refractive index profile $n(\mathbf{r})$ with $\mathbf{r}=(x,y,z)$ of a WG is changed by a small amount $\Delta n(\mathbf{r}) << n(\mathbf{r})$, the associated change of the propagation constant $\Delta\beta$ can be calculated with the perturbation approach, Equation (4.8). A small refractive index change $\Delta n(\mathbf{r})$ corresponds to a change $\Delta\varepsilon(\mathbf{r})=\varepsilon_0\cdot\Delta\varepsilon_r(\mathbf{r})$ in electric permeability, where [99]:

$$\Delta\varepsilon_\mathrm{r}(\mathbf{r})=\left(n(\mathbf{r})+\Delta n(\mathbf{r})\right)^2-n^2(\mathbf{r})\approx 2n(\mathbf{r})\Delta n(\mathbf{r}) \tag{4.11}$$

Typical index differences are in the order of $\Delta n=0.1\ldots0.2$, which justifies the approximation in Equation (4.11). For homogeneous sensing, only the refractive index of the aqueous cladding medium (partial volume $i=\mathrm{M}$) in the volume V_M changes by Δn_M, see Figure 4.2(a),

$$\begin{aligned}
\Delta n^{(\mathrm{hom})}&=\begin{cases}\Delta n_\mathrm{M} & \text{inside } V_\mathrm{M}\\ 0 & \text{else}\end{cases},\\
\Delta\varepsilon_\mathrm{r}^{(\mathrm{hom})}&=\begin{cases}2n_\mathrm{M}\Delta n_\mathrm{M} & \text{inside } V_\mathrm{M}\\ 0 & \text{else}\end{cases}.
\end{aligned} \tag{4.12}$$

For surface sensing, we consider a thin surface layer (partial volume $i=\mathrm{SL}$) of refractive index $\Delta n^{(\mathrm{surf})}$ around the WG core, which locally replaces the aqueous medium with refractive index n_M. The refractive index change is confined to and constant within the surface layer volume V_SL of thickness t_SL, see Figure 4.2(b),

$$\begin{aligned}
\Delta n^{(\mathrm{surf})}&=\begin{cases}n_\mathrm{SL}-n_\mathrm{M} & \text{inside } V_\mathrm{SL}\\ 0 & \text{else}\end{cases},\\
\Delta\varepsilon_\mathrm{r}^{(\mathrm{surf})}&=\begin{cases}2n_\mathrm{M}\left(n_\mathrm{SL}-n_\mathrm{M}\right) & \text{inside } V_\mathrm{SL}\\ 0 & \text{else}\end{cases}.
\end{aligned} \tag{4.13}$$

We introduce the perturbations defined by Equation (4.11)-Equations (4.13) at a fixed frequency into the general variation theorem of Equation(4.8). Since the permittivity perturbation is limited to V_{SL} in the case of surface sensing, the change of the propagation constant $\Delta\beta^{(\mathrm{surf})}$ can be expressed as

$$\begin{aligned}\Delta\beta^{(\mathrm{surf})} &= \frac{\omega}{4aP}\iiint_V \varepsilon_0 \Delta\varepsilon_{\mathrm{r}}^{(\mathrm{surf})}(\mathbf{r})|\mathbf{E}|^2\,\mathrm{d}V \\ &= k_0 \frac{1}{Z_0}\frac{\frac{1}{a}n_{\mathrm{M}}\iiint_{V_{\mathrm{SL}}}|\mathbf{E}|^2\,\mathrm{d}V}{\iint_A \mathrm{Re}(\mathbf{E}\times\mathbf{H}^*)\cdot\mathbf{e}_{\mathrm{z}}\,\mathrm{d}A}\Delta n^{(\mathrm{surf})} \\ &= k_0\Gamma_{\mathrm{SL}}\Delta n^{(\mathrm{surf})}.\end{aligned} \tag{4.14}$$

Similarly, for homogeneous sensing, the permittivity perturbation is limited to V_{M}, the change of the propagation constant $\Delta\beta^{(\mathrm{hom})}$ is obtained from Equation (4.14) by replacing the superscript "(surf)" by "(hom)" and by integrating over V_{M} instead of V_{SL}. A direct link between $\Delta\beta$ and the field interaction factor Γ Equation (4.10) is observed. For a sensor it is important how the effective modal index n_e changes with respect to the local refractive index perturbation Δn. For surface (homogeneous) sensing, we have

$$\Delta n_{\mathrm{e}}^{(\mathrm{surf})} = \Gamma_{\mathrm{SL}}\Delta n^{(\mathrm{surf})},\ \Delta n_{\mathrm{e}}^{(\mathrm{hom})} = \Gamma_{\mathrm{M}}\Delta n^{(\mathrm{hom})}. \tag{4.15}$$

For our sensitivity analyses, we calculate the field interaction factors for a WG by numerically calculated mode fields. We directly define the homogeneous sensitivity $S^{(\mathrm{hom})}$ to be identical with the corresponding field interaction factor Γ_{M}, measuring the impact of the refractive index perturbation Δn_{M} within $|\mathbf{E}'(\mathbf{r})|/|\mathbf{H}'(\mathbf{r})| = 1/\sigma_{\mathrm{n}}\cdot|\mathbf{E}(\mathbf{r})|/|\mathbf{H}(\mathbf{r})|$ on the effective modal index n_{e}. We further define the surface sensitivity $S^{(\mathrm{surf})}$ as the derivative of the field interaction factor Γ_{SL} (surface layer volume V_{SL}) with respect to the surface layer thickness t_{SL},

$$S^{(\mathrm{hom})} = \Gamma_\mathrm{M} = \frac{\Delta n_\mathrm{e}^{(\mathrm{hom})}}{\Delta n_\mathrm{M}}\,,$$
$$S^{(\mathrm{surf})} = \left.\frac{\partial \Gamma_\mathrm{SL}}{\partial t_\mathrm{SL}}\right|_{t_\mathrm{SL}=0} = \frac{1}{\left(n_\mathrm{SL} - n_\mathrm{M}\right)} \frac{\partial}{\partial t_\mathrm{SL}} \Delta n_\mathrm{e}^{(\mathrm{surf})}\Big|_{t_\mathrm{SL}=0}. \tag{4.16}$$

4.10 Scaling laws of Maxwell’s equations

[This section was published as Appendix D of [J4]]

We consider dielectric media, which are assumed to be lossless, isotropic, linear and non–magnetic at the (angular) frequencies $\omega = 2\pi f$ of interest. The vacuum speed of light is denoted by c. The (real) relative permittivity $\varepsilon_\mathrm{r}(\mathbf{r})$ is linked to the refractive index n by $\varepsilon_\mathrm{r} = n^2$. Reshaping Maxwell’s equations for harmonic solutions of the form $\mathbf{E}(t,\mathbf{r}) = \mathbf{E}(\mathbf{r})\mathrm{e}^{\mathrm{j}\omega t}$ and $\mathbf{H}(t,\mathbf{r}) = \mathbf{H}(\mathbf{r})\mathrm{e}^{\mathrm{j}\omega t}$, we find the wave equations for the magnetic and electric fields [100],

$$\left(\operatorname{curl} \frac{1}{\varepsilon_\mathrm{r}(\mathbf{r})} \operatorname{curl}\right)\mathbf{H}(\mathbf{r}) = \frac{\omega^2}{c^2}\mathbf{H}(\mathbf{r}),$$
$$\left(\frac{1}{\varepsilon_\mathrm{r}(\mathbf{r})} \operatorname{curl}\operatorname{curl}\right)\mathbf{E}(\mathbf{r}) = \frac{\omega^2}{c^2}\mathbf{E}(\mathbf{r}). \tag{4.17}$$

Equation (4.17), together with boundary conditions, defines an eigenvalue problem, where ω is the angular eigenfrequency and $\mathbf{H}(\mathbf{r})$ and $\mathbf{E}(\mathbf{r})$ are the corresponding eigenfunctions of the wave equations.

Scaling the geometry. If the geometry of the WG is scaled by a factor $\sigma_g > 0$, i.e., $\mathbf{r}' = \mathbf{r}\sigma_g$, $\varepsilon_\mathrm{r}'(\mathbf{r}) = \varepsilon_\mathrm{r}(\mathbf{r}/\sigma_g)$ and $\mathrm{curl}' = \mathrm{curl}/\sigma_g$, the magnetic field equation Equation (4.17) can be expressed as

$$\left(\operatorname{curl}' \frac{1}{\varepsilon'_\mathrm{r}(\mathbf{r}')} \operatorname{curl}'\right)\mathbf{H}\left(\frac{\mathbf{r}'}{\sigma_\mathrm{g}}\right) = \frac{\omega'^2}{c^2}\mathbf{H}\left(\frac{\mathbf{r}'}{\sigma_\mathrm{g}}\right), \ \omega' = \frac{\omega}{\sigma_\mathrm{g}}. \tag{4.18}$$

An equivalent equation holds for the electric field. For the scaled WG, we find the same eigenfunctions $\mathbf{H}(\mathbf{r}'/\sigma_g), \mathbf{E}(\mathbf{r}'/\sigma_g)$ as in Equation (4.17); we only have to scale the argument $\mathbf{r} = \mathbf{r}'/\sigma_g$ together with the associated angular eigenfrequency $\omega' = \omega\sigma_\omega$ with $\sigma_\omega = 1/\sigma_\mathrm{g}$ [101].

Scaling the refractive index. If we know the solutions for a WG with dielectric structure $\varepsilon_\mathrm{r}(\mathbf{r}) = n^2(\mathbf{r})$, and we look for the results of a WG with $\varepsilon_\mathrm{r}'(\mathbf{r}) = n'^2(\mathbf{r})$, where the refractive index is scaled everywhere with a real constant σ_n according to $n'(\mathbf{r}) = n(\mathbf{r})\sigma_\mathrm{n}$ and $\varepsilon_\mathrm{r}'(\mathbf{r}) = \varepsilon(\mathbf{r})\sigma_\mathrm{n}^2$, we find for the magnetic field equation

$$\left(\mathrm{curl}\frac{1}{\varepsilon_\mathrm{r}'(\mathbf{r})}\mathrm{curl}\right)\mathbf{H}(\mathbf{r}) = \frac{\omega'^2}{c^2}\mathbf{H}(\mathbf{r}),\ \omega' = \frac{\omega}{\sigma_\mathrm{n}}. \tag{4.19}$$

The eigenfunctions $\mathbf{H}(\mathbf{r})$ remain unchanged, but the associated angular eigenfrequencies are scaled to $\omega' = \omega\sigma_\omega$ with $\sigma_\omega = 1/\sigma_\mathrm{n}$ [101]. The electric field equation can be formulated equivalently. Note that the relative ratio of the electric-field eigenfunction $\mathbf{E}(\mathbf{r})$ and the magnetic field eigenfunction $\mathbf{H}(\mathbf{r})$ must be scaled by a factor of $1/\sigma_\mathrm{n}$ to still satisfy the Maxwell's curl equations that link the electric to the magnetic field and vice versa, $|\mathbf{E}'(\mathbf{r})|/|\mathbf{H}'(\mathbf{r})| = 1/\sigma_\mathrm{n} \cdot |\mathbf{E}(\mathbf{r})|/|\mathbf{H}(\mathbf{r})|$.

Scaling the geometry and the refractive indices. If we scale both the geometry with σ_g and the refractive indices with σ_n, e.g. $\mathbf{r}' = \mathbf{r}\sigma_\mathrm{g}$, $\varepsilon_\mathrm{r}'(\mathbf{r}) = \varepsilon_\mathrm{r}(\mathbf{r}/\sigma_\mathrm{g}) \cdot \sigma_\mathrm{n}^2$ and $\mathrm{curl}' = \mathrm{curl}/\sigma_\mathrm{g}$, we find for the magnetic field equation

$$\left(\mathrm{curl}'\frac{1}{\varepsilon_\mathrm{r}'(\mathbf{r}')}\mathrm{curl}'\right)\mathbf{H}\left(\frac{\mathbf{r}'}{\sigma}\right) = \frac{\omega'^2}{c^2}\mathbf{H}\left(\frac{\mathbf{r}'}{\sigma}\right),\ \omega' = \frac{\omega}{\sigma_\mathrm{n}\sigma_\mathrm{g}}. \tag{4.20}$$

The eigenfunction $\mathbf{H}(\mathbf{r}'/\sigma)$ remains unchanged with scaled arguments, and the associated angular eigenfrequencies are scaled to $\omega' = \omega\sigma_\omega$ with $\sigma_\omega = 1/(\sigma_\mathrm{n}\sigma_\mathrm{g})$. The electric field equation can be written equivalently. Note that the relative ratio of the electric-field eigenfunction $\mathbf{E}(\mathbf{r})$ and the magnetic field eigenfunction $\mathbf{H}(\mathbf{r})$ must be scaled by a factor of $1/\sigma_\mathrm{n}$ to still satisfy the Maxwell's curl equations that link the electric to the magnetic field and vice versa, $|\mathbf{E}'(\mathbf{r})|/|\mathbf{H}'(\mathbf{r})| = \left(1/\sigma_\mathrm{n}\right)\cdot|\mathbf{E}(\mathbf{r})|/|\mathbf{H}(\mathbf{r})|$.

If the frequency ω remains unchanged, the geometry and the refractive indices must scale inversely with $\sigma_\mathrm{g} = 1/\sigma_\mathrm{n}$, so that the eigenfunction $\mathbf{H}(\mathbf{r}'/\sigma)$ remains unchanged. The relative ratio of the electric-field eigenfunction $\mathbf{E}(\mathbf{r})$ and the magnetic field eigenfunction $\mathbf{H}(\mathbf{r})$ must again be scaled by a factor of $1/\sigma_\mathrm{n}$ to $|\mathbf{E}'(\mathbf{r})|/|\mathbf{H}'(\mathbf{r})| = \left(1/\sigma_\mathrm{n}\right)\cdot|\mathbf{E}(\mathbf{r})|/|\mathbf{H}(\mathbf{r})|$.

Impact on homogeneous and surface sensing. For comparison of Si_3N_4 WG in the VIS and Si WG in the NIR, we are especially interested in the impact of simultaneously scaling the refractive indices, the geometry and the frequency on the homogeneous sensitivity $S^{(\mathrm{hom})} = \Gamma_\mathrm{M}$ and the surface sensitivity $S^{(\mathrm{surf})} = \partial\Gamma_\mathrm{SL}/\partial t_\mathrm{SL}$. The different scaling operations and results are summarized in Table 3.1.

In the case of scaling the geometry and accordingly the frequency with remaining refractive indices, the numerical value of the ratio of the integrals in Γ_SL remains constant, see Equation (4.10), and therefore the homogeneous sensitivity remains unchanged, $S^{(\mathrm{hom})'} = S^{(\mathrm{hom})}$. However, due to the scaled surface layer thickness $t_\mathrm{SL}' = \sigma_g t_\mathrm{SL}$, the surface sensitivity scales according to $S^{(\mathrm{surf})}{}' = \partial\Gamma_\mathrm{SL}/\partial t_\mathrm{SL}' = S^{(\mathrm{surf})}/\sigma_\mathrm{g} = S^{(\mathrm{surf})}\sigma_\omega$, see Table 4.1, line (1).

In the case of scaling the refractive indices and accordingly the frequency with remaining geometry, the numerical value of the ratio of the integrals in Γ_SL remains constant, as the ratio of the eigenfunctions scales with $|\mathbf{E}'(\mathbf{r})|/|\mathbf{H}'(\mathbf{r})| = \left(1/\sigma_\mathrm{n}\right)\cdot|\mathbf{E}(\mathbf{r})|/|\mathbf{H}(\mathbf{r})|$. Therefore the homogeneous and surface sensitivity do not change, see Table 4.1, line (2).

If the geometry and the refractive index of the WG is scaled, the frequency must be scaled accordingly, with $\sigma_\omega = 1/(\sigma_\mathrm{n}\sigma_g)$. Under the premises of the scaled ratio of the eigenfunctions, the numerical value of the ratio of the integrals in Γ_SL remains constant, and therefore $S^{(\mathrm{surf})}$ scales with $1/\sigma_\mathrm{g}$ due to the scaled surface layer thickness $t_\mathrm{SL}' = \sigma_\mathrm{g} t_\mathrm{SL}$, see Table 4.1, line (3).

In the case of scaling the refractive indices with constant frequency, the geometry has to be scaled according to $\sigma_g = 1/\sigma_\omega$ in order to keep the eigenfunctions but with scaled ratio. The homogeneous sensitivity is again not changing, while the surface sensitivity scales with $\sigma_\mathrm{n}\sigma_\omega = 1/\sigma_\mathrm{g}$, see Table 4.1, line (4).

Table 4.1: Impact of scaling the frequency, geometry and refractive index on the homogeneous and surface sensitivities.

Geometry	Refr. Index	Frequency	Scaling law	Hom. sensitivity	Surf. sensitivity	
$\mathbf{r}'$	n'	ω'		$S^{(\mathrm{hom})\prime}$	$S^{(\mathrm{surf})\prime}$	
$\mathbf{r}\sigma_\mathrm{g}$	n	$\omega\sigma_\omega$	$\sigma_\omega = 1/\sigma_\mathrm{g}$	$S^{(\mathrm{hom})}$	$S^{(\mathrm{surf})}/\sigma_\mathrm{g}$	(1)
$\mathbf{r}$	$n\sigma_\mathrm{n}$	$\omega\sigma_\omega$	$\sigma_\omega = 1/\sigma_\mathrm{n}$	$S^{(\mathrm{hom})}$	$S^{(\mathrm{surf})}$	(2)
$\mathbf{r}\sigma_\mathrm{g}$	$n\sigma_\mathrm{n}$	$\omega\sigma_\omega$	$\sigma_\omega = 1/(\sigma_\mathrm{n}\sigma_\mathrm{g})$	$S^{(\mathrm{hom})}$	$S^{(\mathrm{surf})}/\sigma_\mathrm{g}$	(3)
$\mathbf{r}\sigma_\mathrm{g}$	$n\sigma_\mathrm{n}$	ω	$\sigma_\mathrm{g} = 1/\sigma_\mathrm{n}$	$S^{(\mathrm{hom})}$	$S^{(\mathrm{surf})}/\sigma_\mathrm{g}$	(4)

[end of paper [J4]]

5 Lasing in Si_3N_4-organic hybrid (SiNOH) waveguides

This chapter shows the principle of a SiNOH laser and discusses spiral laser resonators and resonators with distributed feedback. This chapter is taken from [J3] which is published in Optics Express. The initial ansatz and scope as well as the concluding evaluation, interpretation and discussion were performed jointly by D. Kohler, C. Koos and W. Freude. D. Kohler developed the SiNOH lasers and conceived the experiments. The experiments were performed by D. Kohler and I. Allegro. D. Kohler and S. F. Wondimu investigated the gain medium. L. Hahn supported the fabrication of the SiNOH lasers, which were designed by D. Kohler. D. Kohler, C. Koos and W. Freude prepared the manuscript. In order to fit the structure and layout of this document, it was adapted accordingly.

[start of paper [J3]]

Lasing in Si_3N_4-organic hybrid (SiNOH) waveguides

Optics Express, Vol. 28, No. 4, 19885-19906 (2020)
DOI: 10.1364/OE.381572

Daria Kohler,[1,2] , Isabel Allegro,[2] Sentayehu Fetene Wondimu,[1,2] Lothar Hahn,[2] Wolfgang Freude,[1] and Christian Koos,[1,3]

[1.] Karlsruhe Institute of Technology, Institute of Photonics and Quantum Electronics, 76131 Karlsruhe, Germany
[2.] Karlsruhe Institute of Technology, Institute of Microstructure Technology 76344 Eggenstein-Leopoldshafen, Germany

Silicon nitride (Si_3N_4) waveguides offer low-loss wave propagation over a wide spectral range including visible wavelengths and lend themselves to photonic integrated circuits for bio-photonic applications. The Si_3N_4 device portfolio, however, is so far limited to passive devices that need to be fed by external light sources. This often requires delicate and costly fiber-chip coupling schemes that are subject to stringent alignment tolerances. In this paper, we present and investigate a class of lasers that combine Si_3N_4 waveguides with light-emitting organic cladding materials in a hybrid approach. These Si_3N_4-organic hybrid (SiNOH) lasers are operated by optical pumping from the top with low alignment precision. We theoretically and experimentally investigate different SiNOH laser concepts based on spiral-shaped ring resonators and distributed feedback (DFB) resonators. While our devices are designed for an emission wavelength of approximately 600 nm, the SiNOH laser concept can be transferred to a large range of wavelengths in the visible spectrum. The devices are amenable to cost-efficient mass production and have the potential to address a wide range of applications in bio-photonics and point-of-care diagnostics.

5.1 Introduction

Integrated sensors based on optical waveguides (WG) have an enormous potential in bio-photonics and in biomedical diagnostics, especially when it comes to multiplexed and highly sensitive detection of a wide variety of target molecules [15], [19]. For bio-photonic applications, operation in the visible wavelength range is particularly interesting due to the low absorption in aqueous solutions, which allows for large interaction lengths in refractive-index sensors [102] enables low-background absorption spectroscopy with large dynamic range [103], or is instrumental to living-cell imaging via WG-based total internal reflection fluorescence (TIRF) microscopy [104]. Specifically, absorption in typical aqueous analytes, such as urine or saliva, is approximately three orders of magnitude smaller at visible (VIS) wavelengths of, e.g., 600 nm than at near-infrared (NIR) wavelengths of, e.g., 1550 nm [14]. Similarly, blood analysis in photonic sensors largely relies on the so-called therapeutic window between 600 nm and 1100 nm which offers a good compromise between pronounced hemoglobin absorption at shorter wavelengths and strong water absorption at longer wavelengths [40].

In this context, silicon nitride (Si_3N_4) has emerged as a highly attractive integration platform for WG-based sensors, offering low-loss propagation over a wide spectral range from VIS to NIR wavelengths [9], [105]–[107]. Silicon nitride WG feature a high refractive-index contrast between the core ($n_{Si_3N_4} = 2.02$ @ $\lambda = 600$ nm [49]) and the silicon dioxide cladding ($n_{SiO_2} = 1.46$ @ $\lambda = 600$ nm [50]) or aqueous analyte ($n_{H_2O} = 1.33$ @ $\lambda = 600$ nm [51]) and are therefore perfectly suited for densely integrated sensor arrays with small footprint and low analyte consumption. Moreover, Si_3N_4-based photonic integrated circuits (PIC) can be efficiently fabricated in large quantities using mature wafer-scale processes that exploit the CMOS technology base and that are accessible through a world-wide ecosystem of photonic foundries [106], [107]. This opens a path towards cost-efficient mass production of highly functional sensor chips for one-time use in point-of-care diagnostics.

However, despite its various advantages, the basic Si_3N_4 integration platform is so far limited to passive building blocks. Silicon nitride PIC hence have to rely either on external light sources that are coupled to the optical sensor chip [102], [108], [109], or on a hybrid integration of light-emitting materials in combination with passive Si_3N_4 WG [15], [110], [111]. Light supplied by external sources requires delicate fiber-chip coupling schemes that are subject to stringent mechanical tolerances, and the associated complexity is prohibitive for low-cost disposable sensors. Moreover, grating couplers, which are the mainstay for fiber-chip coupling in silicon photonics, suffer from low refractive-index contrast when realized on the Si_3N_4 platform. This leads to low grating strength, poor directionality, and low coupling efficiencies [112]. These challenges can be overcome by on-chip light sources. Previous demonstrations of visible-light sources on the Si_3N_4 platform comprise DFB resonators with CdS/CdSe quantum dots [113] as the gain material. Further investigations concentrated on ring and disk resonators that are vertically coupled to Si_3N_4 WG cores and that contain perovskites [41], [42] or CdS/CdSe quantum dots [43] light-as emitting material. However, these approaches require comparatively complex manufacturing processes, including material deposition from the gas phase and subsequent lithographic structuring. For disposable point-of-care sensors, highly scalable low-cost fabrication techniques for light sources would be advantageous.

In this paper we expand on our previous demonstrations [114] of a new class of laser sources that can be efficiently integrated on the Si_3N_4 platform using low-cost fabrication techniques without any additional lithographic structuring. The devices rely on a hybrid approach that combines nanophotonic Si_3N_4 WG cores with dye-doped organic cladding materials which can be optically pumped by an external laser or a light-emitting diode (LED) without any high-precision alignment of the pump spot and without any mechanical contact to the chip. The dye-doped organic cladding can be efficiently deposited on the wafer by spin coating, by local dispensing, or by inkjet printing. An appropriate choice of laser dyes and cavity designs would allow to integrate a multitude Si_3N_4-organic hybrid (SiNOH) lasers with various emission wavelengths across the VIS and NIR spectral ranges on a common substrate. In our work, we develop a theoretical model of SiNOH lasers for spiral-shaped ring resonators and for distributed-feedback (DFB) resonators, and we experimentally demonstrate lasing in both structure types. In combination with simple camera read-out schemes, our concept shows a route towards disposable sensor chips for highly multiplexed detection of a wide range of analytes in point-of-care diagnostics. During the preparation of this manuscript, the concept of SiNOH lasers [54], [114] was independently demonstrated by another group [115], [116] using second-order DFB structures that are amenable to production with relaxed lithography resolution requirements. These experiments prove the viability of the concept and demonstrate its transferability to different photonic integration platforms.

5.2 Si_3N_4-organic hybrid device concept and design considerations

The basic concept of Si_3N_4-organic hybrid (SiNOH) lasers [71] is illustrated in Figure 5.1. The SiNOH lasers are optically pumped from the top by an external light source, see Figure 5.1(a). High-precision alignment of the pump spot is not required, and the scheme lends itself to integration of laser arrays with individually defined emission wavelengths $\lambda_{1 \ldots n}$. The SiNOH laser light is emitted directly into Si_3N_4 single-mode WG and can be efficiently coupled to a subsequent sensor array, here illustrated as Mach-Zehnder

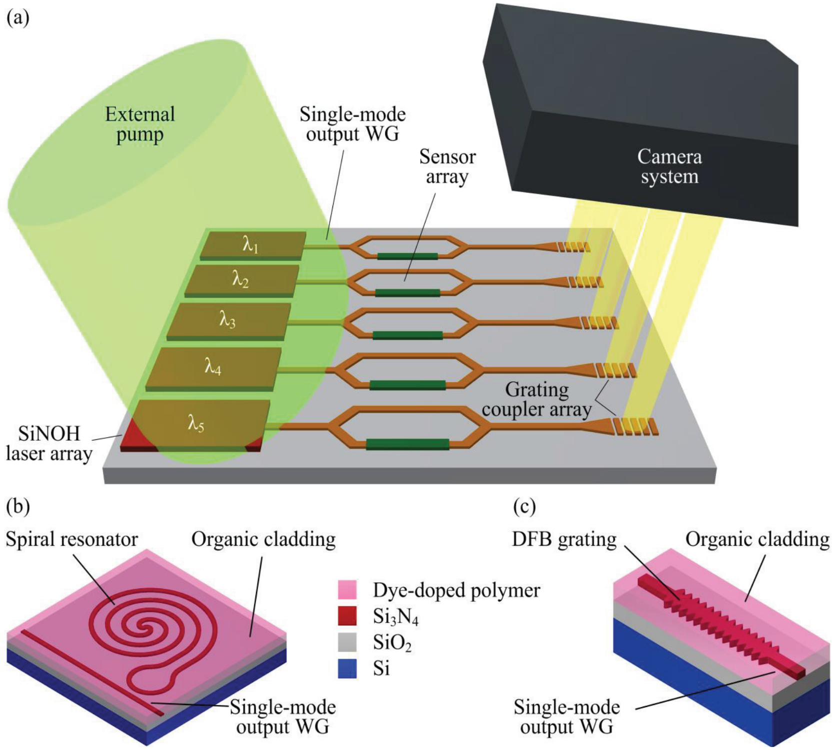

Figure 5.1: Basic concept of integrated Si_3N_4-organic hybrid (SiNOH) lasers. **(a)** SiNOH lasers feeding an array of waveguide-based sensors. The lasers are optically pumped from the top by an external light source illuminating an extended spot, without any need for high-precision mechanical alignment. Laser light is emitted directly into the Si_3N_4 single-mode WG and can hence be efficiently coupled to an array of on-chip sensors, here illustrated as Mach-Zehnder interferometers. The light from the sensor output is radiated to the top by grating couplers and captured by a camera. **(b)** SiNOH laser with spiral-shaped resonator. The active WG consists of a Si_3N_4 core with a dye-doped organic cladding as a gain medium. An appropriate resonator design in combination with a suitable gain medium allows to realize various emission wavelengths $\lambda_{1\ldots n}$ on the same chip. The ring resonator is coiled up into a double spiral and coupled evanescently to a single-mode output WG. **(c)** SiNOH laser with distributed-feedback (DFB) resonator, formed by a strip WG with periodic sidewall corrugations.

interferometers. At the sensor outputs, light is radiated into free space via grating couplers and captured by a camera. This concept allows for contactless excitation and readout of large-scale sensor arrays on technically simple low-cost optical sensor chips.

5.2.1 Device concept

The active SiNOH WG have a Si_3N_4 core on top of a silicon dioxide bottom cladding, see Figure 5.1(b) and Figure 5.1(c). Optical gain is provided by an organic top cladding that is doped with a light-emitting dye. By appropriate choice of the gain medium and of the device design, various emission wavelengths $\lambda_{1\ldots n}$ can be realized on the same chip. These devices can be pumped with a single light source such as an LED. SiNOH lasers of different wavelengths can be realized by either choosing individual gain materials or by combining a single broadband gain material with different resonator designs. On the silicon platform, we have previously demonstrated similar concepts for on-chip lasers emitting in the NIR [117].

In our experiments, we investigate two laser resonator types: A spiral-shaped ring resonator, Figure 5.1(b), and a distributed-feedback (DFB) structure, Figure 5.1(c). The ring resonator is coiled up into a long double spiral and is coupled evanescently to a single-mode output WG, Figure 5.1(b). Compared to the DFB laser, the double spiral covers a much larger chip area and hence offers a better overlap with a moderately focused pump beam that leads to relaxed alignment tolerances. The DFB resonator is formed by a straight strip WG with sidewall corrugations, Figure 5.1(c). The footprint of the DFB resonator is small such that many SiNOH lasers can be pumped simultaneously with one pump beam. The DFB structure supports lasing in basically two longitudinal modes spectrally located at both edges of the Bragg stop-band. Asymmetries or a quarter-wavelength defect reduce the number of lasing modes to one. Pump efficiency, threshold and spectral properties depend strongly on the modal gain and on the loss of the respective laser types - this is discussed in more detail in the following subsections. For the devices shown in this work, we use first-order Bragg gratings with a period of approximately 170 nm, which requires comparatively high lithography resolution. It has recently been demonstrated that SiNOH DFB lasers can also be realized with second-order gratings [115], [116], having grating periods of more than 350 nm. Such structures are amenable to high-throughput mass fabrication using, e.g., 248 nm deep-UV lithography.

5.2.2 Gain and loss in SiNOH WG

The power of the oscillating laser mode depends on the SiNOH WG loss and on the efficiency with which the pump is coupled to the active WG region. Within the resonator, the waves experience a net power gain of $G = \exp\left[\left(g-\alpha\right)2L\right]$ for one round-trip of length $2L$, where g and α denote the effective modal power gain and loss coefficients (unit cm^{-1}) of the laser cavity. In the case of a ring resonator, $2L$ denotes the ring perimeter, while for the case of a DFB laser L represents the geometrical resonator length.

The gain of the laser resonator results from the interaction of the evanescent parts of the WG mode with the dye molecules in the organic top cladding, which are optically excited by the pump light. The simulated electric field magnitudes $|\mathbf{E}|$ of the quasi-TE and quasi-TM modes in the cross-section of a strip WG are shown in Figure 5.2(a) and Figure 5.2(b), respectively. Figure 5.2(d)-2(e) display the field distribution of a DFB mode at the upper and the lower edge of the stop-band. Note that the terms “upper” and “lower” refer to optical frequency or photon energy and not to wavelength.

Gain and loss in ring resonators For ring resonators, the optical loss of the laser cavity is caused by attenuation of the mode when propagating along the ring, and by the power output coupling $|\kappa_\mathrm{r}|^2$ to the bus WG [30]. The net round-trip power gain and the net modal gain at threshold is therefore

$$G = \mathrm{e}^{\left(g_\mathrm{th}-\alpha\right)2L}\left(1-|\kappa_\mathrm{r}|^2\right)=1, \qquad \left(g_\mathrm{th}-\alpha\right)2L = -\ln\left(1-|\kappa_\mathrm{r}|^2\right) \tag{5.1}$$

Gain and loss in DFB resonators For DFB lasers, the resonator mode can be described by two counter-propagating waves. The grating couples these waves with a coupling factor κ. In the following, we assume the coupling factor to be real-valued, $\kappa \in \mathbb{R}$, i.e., the propagating mode only experiences a

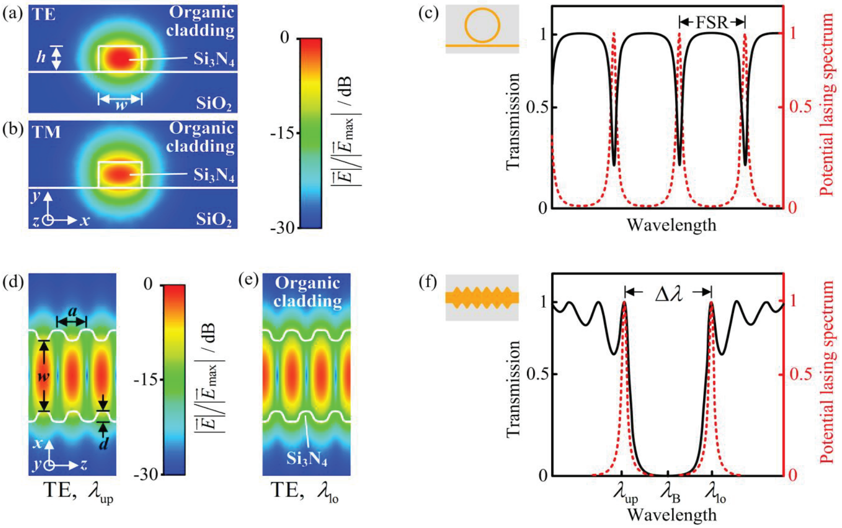

Figure 5.2: Waveguide (WG) and resonator concepts of SiNOH lasers. **(a),(b)** Strip WG used for ring-resonator SiNOH lasers: The graph shows the WG cross section (width *w*, height) along with the simulated electric field magnitudes |**E**| of the fundamental quasi-TE mode **(a)** and the fundamental quasi-TM mode **(b)**. **(c)** Ring-resonator cavity: Schematic power transmission between the input and the output of the straight bus WG (black solid line) as a function of the vacuum wavelength λ. Lasing occurs at the resonances (red dashed line) marked by notches in the transmission. For the devices used in this publication, the ring-resonator WG are coiled up to form spirals, see Figure 5.1(b). **(d),(e)** Distributed-feedback (DFB) structures: Top view of corrugated strip WG (width *w*, height *h*, corrugation period *a*, and corrugation depth *d*), along with the simulated electric field magnitudes |**E**| of the DFB mode at the upper band edge with larger photon energy and short-wavelength resonance λ_{up} **(d)** as well as at the lower band edge with smaller photon energy and long-wavelength resonance λ_{lo} **(e)**. All mode fields are plotted in the plane $y = h/2$. **(f)** DFB resonator: Schematic power transmission between the input and the output of the corrugated section (black solid line) as a function of the vacuum wavelength λ. For a DFB grating without phase shift, lasing occurs at the upper or lower edge of the stop-band (red dashed lines).

periodic perturbation of the refractive index, but not of the modal gain [31]. This assumption is based on the observation that the periodic sidewall corrugation does not affect the penetration depth of the evanescent field into the cladding to a substantial degree. For low gain, $\frac{1}{2}(g-\alpha)\ll\kappa$, the first-order resonances of a DFB laser are at the stop-band edges, and the net modal threshold power gain g_{th} can be approximated by [[118], Equations. (29) and (6)]

$$\left(g_{\text{th}}-\alpha\right)L=2\left(\frac{\pi}{\kappa L}\right)^{2} \tag{5.2}$$

5.2.3 Design considerations

For lasers operated in sensor applications, the important characteristics are the spectrum, the polarization, the threshold, and the output power. These parameters are defined by the resonator, the properties of the laser gain medium, and the pump.

Spectrum and polarization As a gain medium, we use the organic dye Pyrromethene (PM597) dispersed in a poly(methyl methacrylate) (PMMA) matrix, see Figure 5.2(d) for the associated emission and the absorption cross sections. The material offers a predominantly inhomogeneously broadened gain spectrum [119], which allows for simultaneous lasing of multiple longitudinal cavity modes. Note that the spectral characteristics of the modal gain of a SiNOH WG may differ from that of the dye emission cross section due to the wavelength-dependence of the modal overlap with the active cladding. In our devices, we observe lasing mostly around 600 nm, while the emission cross section peaks at around 570 nm. With a ring-shaped laser resonator, the emission spectrum of the organic laser dye is longitudinally filtered according to the comb-shaped eigenmode spectrum, having a free spectral wavelength range $\text{FSR}=\lambda_0^2/(n_{\text{e,g}}L)$ centered at the operating wavelength λ_0, Figure 5.2(c). In addition to the fundamental TE and TM mode, Figure 5.2(b), transverse modes of higher order can propagate if the WG is sufficiently wide ($w\geq 400\,\text{nm}$). For the ring resonator, we find one set of longitudinal modes for each transverse mode in each polarization. The number of lasing modes can be reduced with additional filters, see Section 5.4.2.

For a DFB laser, the analysis of the spectral emission characteristics relies on coupled-mode theory [120]. Assuming a DFB grating period a, the refractive index modulation along the WG can be described by an effective index modulation $n_\mathrm{e}(z) = n_\mathrm{e,av} + \Delta n_\mathrm{e} \sin(2\beta_\mathrm{B} z)$, having an amplitude Δn_e and an average effective refractive index $n_\mathrm{e,av}$. The propagation constant is $\beta_\mathrm{B} = 2\pi n_\mathrm{e,av} / \lambda_\mathrm{B}$ at the Bragg wavelength $\lambda_\mathrm{B} = 2 n_\mathrm{e,av} a$. The coupling strength of the grating for weak coupling can then be approximated given by [120]

$$\kappa = \frac{\pi \, \Delta n_\mathrm{e}}{\lambda_\mathrm{B}} \tag{5.3}$$

A sketch of a transmission spectrum of a DFB structure and its associated stop-band can be seen in Figure 5.2(f), black line. The transmission stop-band is centered at the Bragg wavelength $\lambda_\mathrm{B} = 2 n_\mathrm{e,av} a$, and the bandwidth $\Delta\lambda$ of the stop-band, Figure 5.2(f), for a first-order Bragg grating is given by [120]

$$\Delta\lambda = \frac{\lambda_\mathrm{B}^2}{\pi n_\mathrm{av}} \sqrt{\kappa^2 + \frac{\pi^2}{L^2}} \tag{5.4}$$

Note that, in a DFB laser without any phase shift, laser emission occurs at the stop-band edges, rather than in the center of the stop-band at λ_B, see Figure 5.2(f), red dashed line. If a quarter-wavelength shift is included at the center of the Bragg-grating section, i.e., if a defect is introduced in the periodic structure, the emission wavelength can also be within the stop-band of the DFB structure. As with the ring resonator, we find one set of longitudinal modes for each transverse mode in each polarization.

Laser threshold and output power The independent estimation for the net gain at threshold, Equation (5.1) and Equation (5.2), can only be applied to laser modes in media with inhomogeneously broadened gain spectrum, in which longitudinal modes do not compete for gain. For the organic gain medium used in our devices, the overall gain spectrum is predominantly inhomogeneously broadened, whereas homogeneous broadening only plays a role within very small wavelength ranges [32,33]. Within the ranges of homogeneous broadening, longitudinal modes compete for gain, and the mode with the largest net gain finally starts to oscillate. The more modes are competing, the higher the threshold for the dominant mode becomes. The two lasing modes of DFB lasers without quarter-wavelength shift are separated sufficiently so that no competition occurs. In contrast to that, the modes of ring resonators with large diameters and hence small FSR are subject to gain competition, and the lasing thresholds are therefore higher. Introducing an additional longitudinal mode filter reduces the number of longitudinal modes inside the homogeneous linewidth and decreases the pump threshold. Note that gain competition can also occur for modes of different polarizations, e.g., if TE-polarized and TM-polarized modes have a strong spatial overlap inside the gain medium, Figure 5.2(a) and Figure 5.2(b).

A high differential quantum efficiency η_d of the laser is important for a high output power. This is particularly important for lasers based on organic dyes, for which higher pump powers lead to a faster degradation, e.g., due to photo-oxidation, and thus reduce the lifetime of the device. The ratio of induced emission and total emission, comprising induced and spontaneous emission, is denoted as η_ind. The spontaneous emission depends on the total number of modes inside the emission spectrum of the material and therefore increases with the overall volume of the pumped region. The differential efficiency η_d is obtained by the product of η_ind and the probability that an emitted photon is coupled out of the laser cavity. This probability can be quantified by the total photon lifetime τ_P in the resonator, $\tau_\mathrm{P}^{-1} = \tau_\mathrm{R}^{-1} + \tau_\alpha^{-1}$, including resonator losses $\tau_\alpha^{-1} \propto \alpha$ and outcoupling loss τ_R^{-1}, where τ_R is the lifetime due to outcoupling only. The differential quantum efficiency is then given by [[121], Equation (3.151)]

$$\eta_\mathrm{d} = \eta_\mathrm{ind} \frac{1/\tau_\mathrm{R}}{1/\tau_\mathrm{P}} \tag{5.5}$$

Low propagation loss α requires a low threshold modal gain g, Equation (5.1) and Equation (5.2), and leads to a high quantum efficiency for a given outcoupling, Equation (5.5). Note that the ratio η_ind of induced emission and total emission increases itself with τ_R. As a consequence, the outcoupling has to be optimized for extracting the maximum power from the resonator. A small active volume with a small number of modes, which can accept spontaneous emission, results in a larger η_{ind} than a larger active volume, if the overall emission is the same.

5.3 Device fabrication

The SiNOH laser WG are fabricated with only one lithographical step. The WG cores are structured in a 200 nm thick stochiometric Si_3N_4 layer, which is deposited via low-pressure chemical vapor deposition (LPCVD) on top of a 2 µm thick silicon dioxide layer mechanically supported by a silicon wafer. As etch mask, we use a negative-tone resist structured by electron-beam lithography and spray developing. Dry etching with a mixture of SF_6 and CHF_3 is used to transfer the structure of the mask to the Si_3N_4 layer. An oxygen plasma etching step follows and removes the etch mask. After structuring the WG cores, a 800 nm thick layer of PMMA with dispersed laser dye Pyrromethene 597 (PM597, Radiant Dyes Laser & Accessories GmbH) is globally deposited onto the chips by spin coating to act as an active cladding. For a local deposition the gain material can be dispensed [27] or structured with electron beam or UV lithography [35]. The concentration of the dye within the PMMA matrix material is $25\,\mu\text{mol/g}$ and was optimized previously in investigations of polymer goblet lasers [35].

For characterization, the chips are cleaved on one side to provide access to the facet of the bus WG. Details of fabricated devices are shown in Figure 5.3(a) shows a scanning electron microscopy (SEM) image of the Si_3N_4 WG cores that belong to a spiral laser with ring-resonator mode filter. To improve the pump efficiency, the ring-resonator WG is coiled up densely to form a double spiral WG with a minimal curvature radius of 40 µm in the center. Figure 5.3(b) displays a part of a DFB strip WG with sidewall corrugations. Figure 5.3(c) shows a cross-section of the Si_3N_4 WG core embedded in the dye-doped PMMA cladding.

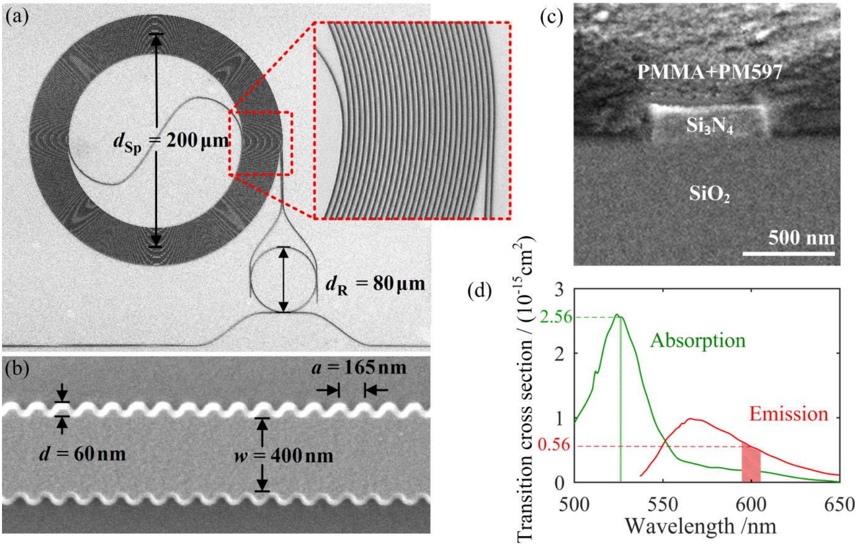

Figure 5.3: SEM images of the Si_3N_4 WG with spectra of the absorption and emission cross sections of the organic dye, dispersed in the PMMA cladding. **(a)** Spiral resonator: To improve the overlap with the pump, the ring resonator WG is coiled up densely to form a double spiral with a minimal curvature radius of 40 µm in the center. **(b)** DFB resonator: Corrugated WG with width *w*, corrugation depth *d*, and period *a*. **(c)** Cross-section of the Si_3N_4 WG core clad with PMMA and Pyrromethene (PM597). **(d)** Emission and absorption cross-sections of PM597 embedded in a PMMA matrix. The material is pumped by a laser, emitting near the absorption maximum of PM597 in PMMA, green line (σ_a (532 nm) = $2.56\cdot10^{-15}$ cm^2). The emission of the SiNOH laser is near 600 nm, red bar (σ_e (600 nm) = $0.56\cdot10^{-15}$ cm^2). The laser emission is redshifted from the wavelength of maximum emission cross section at approximately 570 nm due to re-absorption of emitted photons by dye molecules in the ground state.

For light emission, the structures must be optically pumped. Figure 5.3(d) shows the wavelength-dependent absorption and emission cross sections of PM597 dispersed in PMMA. The pump wavelength is chosen near the absorption maximum, Figure 5.3(d), green vertical line, and the emission of the SiNOH laser appears near 600 nm, indicated by a red bar, red-shifted from the maximum of the emission cross section of the laser dye at approximately 570 nm. This may be explained by the fact that re-absorption of emitted photons through the dye molecules in the ground state is stronger at 570 nm than at 600 nm and by a general concentration-dependence of the emission wavelength of dye lasers [36]. Emission wavelengths of approximately 600 nm have also been observed in other experiments that rely on PM597 as gain material [35,37].

5.4 Characterization and demonstration of lasing

In the following, we first introduce the experimental setup used to investigate our devices. We then discuss the results obtained for spiral and DFB laser. A comparative discussion of the two device types follows in Section 5.5.

5.4.1 Characterization setup

The experimental setup is shown in Figure 5.4. The SiNOH lasers are pumped from the top by a frequency-doubled Nd:YLF pulsed laser (CL523, CrystaLaser) at a wavelength of 523 nm, a pulse duration of 20 ns, and a

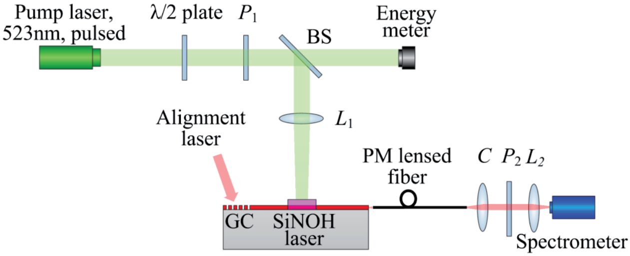

Figure 5.4: Experimental setup for characterizing SiNOH lasers. The devices are pumped via a free-space beam from a pulsed laser which is focused onto the chip by a lens L_1. The energy of the pump pulsed impinging on the SiNOH devices is varied by rotating a half-wave (λ/2) plate with respect to a fixed linear polarizer P_1. A beam splitter BS transmits half of the pump emission to a pulse energy meter. The SiNOH laser emission is coupled from the chip by a lensed polarization-maintaining (PM) fiber. A collimator C and a refocusing lens L_2 are used to couple the light to a spectrometer. A rotatable linear polarizer P_2 can be inserted in the collimated portion of the beam for selecting the proper polarization of the lasing modes. The position of the lensed fiber is adjusted with the help of an auxiliary alignment laser at 635 nm, which is coupled to the bus WG (spiral laser) or to the corrugated WG (DFB laser) through a grating coupler (GC). The same grating coupler is used for measuring the transmission of the DFB structures.

repetition rate of 20 Hz, Figure 5.4. Pulsed operation with a rather low repetition rate was chosen to ensure relaxation of dyes in excited triplet states between subsequent pulses. The lifetime of these triplet states is typically in the microsecond range, thereby preventing operation of dye lasers at high repetition rates or in continuous wave (cw) mode [38,39]. The pulse energy is varied by a half-wave ($\lambda/2$) plate and a subsequent polarizer P_1, and a beam splitter BS is used to transmit half of the pump energy to an energy meter. The pump light is focused on the chip by a lens L_1. The SiNOH laser light is coupled from the chip edge with a polarization-maintaining (PM) lensed fiber. A collimator C and a refocusing lens L_2 are used to couple the emitted light to a spectrometer (Shamrock 500i, Andor, 60 pm resolution, 2 s integration time). An optional rotatable linear polarizer P_2 is inserted between the fiber collimator and the refocusing lens for selecting the proper polarization of the lasing mode. An auxiliary alignment laser and a grating coupler help in actively adjusting the lensed fiber to the output WG of the SiNOH laser. For the DFB structures, we also measure the transmission by coupling the light of a white-light source (SuperK, NKT Photonics) to the chip via the grating coupler and by capturing the transmitted light at the output with the lensed fiber which is connected to the spectrometer.

All experiments reported in the following were conducted at room temperature. However, we expect that SiNOH lasers can be operated at other temperature ranges as well. Previous experiments using also PM597-doped PMMA as a gain material have shown that lasing is still possible at temperatures of 65°C [35]. This should be sufficient for biophotonic experiments, which are usually conducted at room temperature or at body temperatures around 37°C. Cooling organic dyes to below 0 °C can even improve the emission performance [40].

5.4.2 Lasers based on spiral-shaped ring resonators

The ring resonator has a perimeter of $2L = 17.5$ mm and consists of a densely packed double spiral for optimally filling the pump spot area, see Figure 5.5(a) - Figure 5.5(c) for a sketch of the device layout. The pump beam has a

Gaussian profile with a full-width half-maximum spot size of 200 µm. The curvature of the spiral-shaped WG is limited to provide a minimum bending radius of 40 µm, thereby keeping the associated loss sufficiently low. To achieve low propagation loss for the fundamental TE and TM modes, the WG width is chosen to be 500 nm, leading to two guided modes for each polarization at a wavelength of 600 nm. The multimode (MM) sections are indicated by black lines in Figure 5.5(a) Figure 5.5(c). Measuring the transmission of the straight MM WG sections using an undoped PMMA cladding without laser dye, we find a propagation loss of 5 dB/cm. This is much lower than the loss of 7 dB/cm found for narrower, 300 nm-wide single-moded WG with undoped PMMA cladding. We believe that these losses can be further reduced by optimized fabrication processes. To suppress laser oscillation of higher order transverse modes in the MM devices, we use short single-mode WG sections, indicated as orange lines in Figure 5.5(a) - Figure 5.5(c), which are inserted in the center of the spiral and as a loop in the coupling section between spiral and straight bus WG. As a consequence, we find significantly reduced lasing thresholds for lasers with MM WG in the spiral section as compared to their single-mode counterparts – despite the slightly reduced overlap of the guided light with the active cladding in the MM WG. Note that significantly smaller propagation losses could be achieved by optimized fabrication processes, which should allow for further reductions of the lasing threshold.

In a first step of our device characterization, we measure the lasing threshold of the double spiral laser with a simple loop at the outer end of the spiral WG, Figure 5.5(a). In this experiment, the whole spiral WG is pumped with a beam having a Gaussian intensity distribution, see green spot in Figure 5.5(a). This pump spot overlaps only partially with the spiral WG such that much of the pump energy remains unused. Figure 5.5(d) shows the normalized lasing spectrum for a pump pulse energy of 715 nJ, recorded with an integration time of 2 s of the CCD camera in the spectrometer.

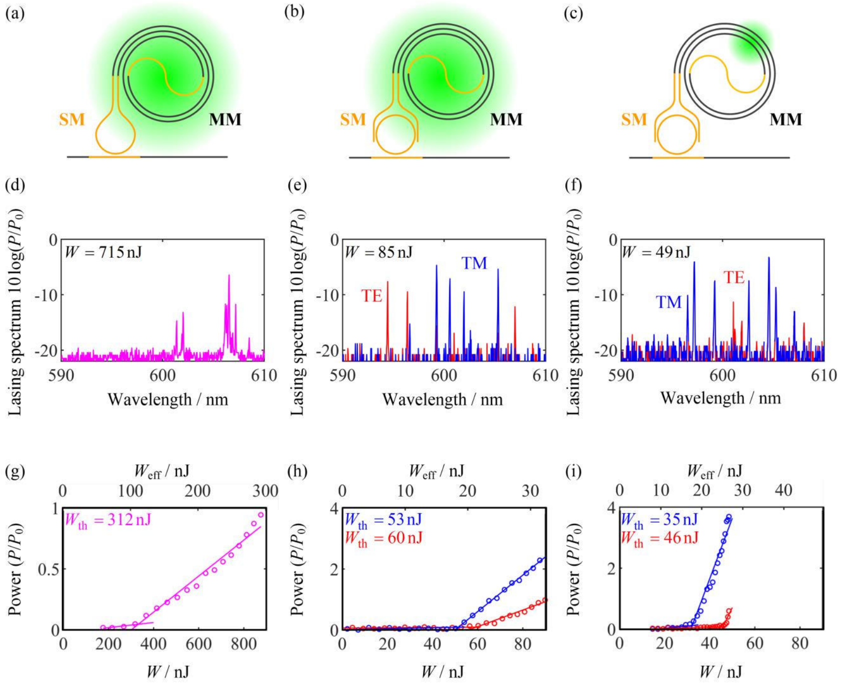

Figure 5.5: Characterization of spiral SiNOH lasers using different mode filters and pump spot sizes. **(a)-(c)** Resonator geometries and pump spots (green). A transverse mode filter (orange) is implemented by tapering down the multimode spiral-shaped resonator WG from 500 nm width to 300 nm for single-mode propagation. **(b),(c)** A ring resonator with a round-trip propagation loss of 1 dB (4 dB /cm, $Q = 5\times10^3$) acts as a longitudinal mode filter at the outer end of the double spiral and reduces the number of lasing modes in the spiral resonator. A pump spot size of the order of the spiral diameter leads to a waste of pump energy that is absorbed outside the overlap region with the spiral WG, see Subfigures **(a),(b)**. Focusing the pump spot to an area with high WG density, Subfigure **(c)**, decreases the threshold. **(d)-(f)** Emission spectra. Since the spectrometer used for recording the emission spectra is not calibrated, we report the output power with respect to a common reference power P_0. Note that the scaling of the vertical axis in Subfigure **(d)** differs from that in Subfigures **(e)** and **(f)**. If a small ring resonator is used as a longitudinal mode filter at the outer end of the double spiral, its FSR determines the lasing lines. **(g)-(i)** Laser output power as a function of the total pump pulse energy W (lower horizontal axis) and of the effective pump pulse energy W_{eff} that is absorbed in the overlap region of the respective pump spot with the spiral WG (upper horizontal axes). The threshold energies W_{th} refer to the total pump pulse energy, i.e., to the lower axes. In Subfigure **(g)**, the scaling of the axes differs from the scaling in Subfigures **(h)** and **(i)**. We find that introducing the additional

ring filter as spectrally selective feedback, Subfigure **(h)**, decreases the pump threshold by a factor of 6 compared to the case without ring filter, Subfigure **(g)**. Using a focused pump spot that leads to an enhanced overlap with the spiral WG, Subfigure **(i)**, we can achieve a further reduction of the threshold by a factor of 1.5 along with an increase of the differential quantum efficiency, to be seen by the steeper slope of the laser characteristic as compared to Subfigure **(h)**.

The FSR of the spiral-shaped ring is estimated to be $\mathrm{FSR}_{\mathrm{Spiral}} = 10$ pm, which corresponds to 8.3 GHz and cannot be resolved by the spectrometer (resolution 60 pm). The recorded spectra are not very stable – lasing occurs only in a small range (590 nm to 610 nm) of the spontaneous emission spectrum of the laser dye, and the center of the lasing spectrum changes from integration interval to integration interval. We attribute this to mode competition, possibly in combination with temperature-induced phase fluctuations of mode patterns in the multi-mode spiral WG. Note that the spectrometer used for recording the emission spectra is not calibrated and indicates only relative power levels P/P_0 with respect to an unknown reference power P_0. This reference power is the same for all measurements reported in the subsequent experiment, such that relative power levels P/P_0 may be compared across different measurements. For quantifying the input/output power characteristics of our devices, we sum up the powers in all spectral lines and depict the calculated normalized output power P/P_0 as a function of the pump pulse energy W, Figure 5.5(g). Despite the unstable lasing spectrum, no significant fluctuation of the total emitted power is observed which supports the idea of mode competition. We find a laser threshold of 312 nJ, corresponding to a pump fluence of approximately $400\,\mu\mathrm{J/cm}^2$ for the area occupied by the spiral WG.

In a next step, we investigate a spiral laser, where the outer ends of the double spiral are optically connected through a small ring resonator, Figure 5.5(b). This ring resonator has a free spectral range of $\mathrm{FSR}_{\mathrm{Ring}} = 660$ pm (540 GHz) and is used as longitudinal mode filter. We again use a Gaussian pump spot covering the entire spiral WG, having the same overlap with the spiral WG as in the previous experiment. Figure 5(e) shows the lasing spectrum for a pump pulse energy of 87 nJ. Lasing occurs for the fundamental TM mode (blue) and for the fundamental TE mode (red). The emission lines are spaced by multiples of $\mathrm{FSR}_{\mathrm{Ring}}$ The spectrum differs greatly from Figure 5.5(d) and is stable from integration interval to integration interval. We attribute this to the fact that the homogeneous linewidth of the dye is comparable to or smaller than $\mathrm{FSR}_{\mathrm{Ring}}$ such that different longitudinal modes do not compete for gain. As a consequence, the pump energy at threshold, Figure 5.5(h), is smaller than for the case of modes competing for gain as in Figure 5.5(a), Figure 5.5(d) and Figure 5.5(h) shows further that TM-polarized lasing modes have lower thresholds (53 nJ) than TE-polarized modes (60 nJ), corresponding to pump fluences of $56\,\mu\mathrm{J}/\mathrm{cm}^2$ (TM) and $65\,\mu\mathrm{J}/\mathrm{cm}^2$ (TE) at the laser-active area of the spiral, respectively. This is attributed to the fact that TM-polarized modes transport a larger fraction (0.2) of cross-sectional power in the gain medium outside the WG core than the TE modes (0.17). In addition, the loss for a TM-polarized mode (high electric field strengths at the smooth upper surface) is smaller than for a TE-polarized mode (high electric field strengths at the rough sidewalls). Moreover, the differential quantum efficiency increases signifycantly when introducing the filter ring resonator. This can be seen by comparing the slopes in Figure 5.5(g) and Figure 5.5(h) (note the different scales on the vertical axes). To understand this result, it is important to note that the power coupling factor between the loop and the straight outcoupling WG in in Figure 5.5(a) is the same as the power coupling factor between the ring and the straight outcoupling WG in in Figure 5.5(b). However, the resonant power enhancement in the filter ring leads to an effective increase of power coupled from the spiral to the straight output WG, thereby causing a significant reduction of the outcoupling photon lifetime τ_{R} of the laser cavity. Since both structures in Figure 5.5(a) and Figure 5.5(b) feature the same propagation losses in the spiral and hence the same photon lifetime τ_{α}, a reduction of τ_{R} leads to an increase of the differential quantum efficiency η_{d}, see Equation (5.5).

The threshold of the spiral laser can be further decreased by increasing the overlap of the pump spot with the spiral WG. One way to achieve this is to focus the pump spot to an area with densely spaced WG, Figure 5.5(c), green spot, such that a larger fraction of pump light is absorbed in the vicinity of the

Si_3N_4 WG. The emission spectrum obtained with the focused pump spot, Figure 5.5(f), shows similar properties as the one obtained by pumping the entire spiral with a large pump spot, Figure 5.5(e). At the same time, the focused pump spot allows to reduce the overall pump pulse energy at the lasing threshold, Figure 5.5(i). Specifically, we obtain a threshold pump pulse energy of 46 nJ and 35 nJ for the TE and the TM mode, respectively, and the corresponding fluences amount to $1095 \mu J / cm^2$ and $980 \mu J / cm^2$. This is a reduction by a factor of 1.5 as compared to the case of the large pump spot, see Figure 5.5(h). For a fair comparison of different pump spot geometries, we define an effective pump pulse energy W_{eff} that is absorbed in the overlap region of the pump spot and the spiral WG, see upper horizontal axes in Figure 5.5(g), Figure 5.5(h), and Figure 5.5(i). The area of the spiral was modeled as a ring with a width of 50 µm and an inner radius of 80 µm for the densely spaced WG regions. The S-shaped bend in the middle of the spiral is neglected since it does not play a significant role.

Comparing Figure 5.5(h) and Figure 5.5(i), we find that the effective pump pulse energy W_{eff} is the same for both cases, and is in accordance with Figure 5.5(d), indicating that the re-absorption in the unpumped regions is small. However, the differential quantum efficiency is larger for the focused pump beam, because the active volume is smaller and η_{ind} is therefore larger, see text after Equation (5.5).

We also estimate the total output power levels that can be achieved with the current devices. To this end, we use a spiral laser according to Figure 5.5(b), and we exchange the spectrometer with the pulse energy meter, see Figure 5.5. For a pump pulse energy of $W = 4 \mu J$, we measure an emitted pulse energy of 80 pJ at the fiber output. This corresponds to an on-chip pulse energy of approximately 1 nJ when accounting for a fiber-chip coupling loss of the order of 9 dB and for an on-chip propagation loss of 2 dB in the 3 mm-long passive WG between the laser and the chip edge. For a pulse duration of approximately 20 ns, this corresponds to a pulse peak power of the order of 50 mW. Clearly, the average power is much lower and amounts to approximately 20 nW for the 20 Hz pulse repetition frequency used in our experiment. We believe that the output power of our SiNOH lasers can be greatly improved by optimized device design, material composition, and fabrication processes. In addition, the average power can be increased by using higher pulse repetition rates – probably in combination with shorter pulse durations to keep the photodegradation low, see Section 5.5.

While the gain spectrum of the dyes in the active organic cladding is predominantly subject to inhomogeneous gain broadening, homogeneous broadening might play a role as well [32,33]. This can also be observed from the emission spectra of the SiNOH spiral lasers: The filter ring in Figure 5.5(b) and Figure 5.5(c) has a free spectral range of FSR = 0.6 nm. When pumping the full ring, Figure 5.5(b), laser emission occurs only for cavity modes that are spaced by at least two FSR, see corresponding spectrum in Figure 5.5(e). On the other hand, when pumping only a part of the ring, Figure 5.5(c), cavity modes spaced by one FSR may oscillate, but exhibit a strong imbalance in emitted power. We attribute both findings to gain competition within a partially homogeneously broadened gain spectrum, where the bandwidth of the homogeneous broadening is of the order of 0.6 nm, corresponding to one FSR.

5.4.3 Distributed-feedback laser

Sidewall corrugations of a WG can couple counter-propagating WG modes and thereby establish a distributed feedback (DFB) resonator, Figure 5.6(a). The DFB structure is defined by its length L, width w, corrugation depth d, and corrugation period a. The number of periods is denoted by m, the feedback strength is κ, Equation (5.3), and the separation of the lowest-order lasing modes is $\Delta\lambda$, Equation (5.4). The active medium of the DFB laser is pumped from the top with an elliptical pump spot that fully illuminates the DFB WG. Figure 5.6(b), black line, shows the typical transmission spectrum of a passive DFB resonator measured by coupling the light of a supercontinuum laser (SuperK Versa, NKT Photonics GmbH) to the GC and by detecting the transmitted light with the spectrometer Figure 5.6. The resolution

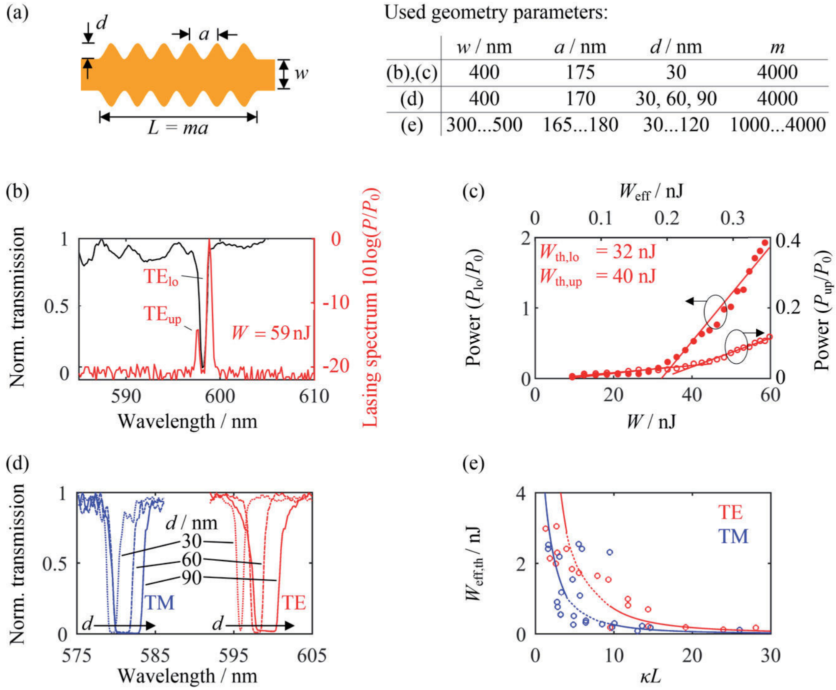

Used geometry parameters:

	w / nm	a / nm	d / nm	m
(b),(c)	400	175	30	4000
(d)	400	170	30, 60, 90	4000
(e)	300...500	165...180	30...120	1000...4000

Figure 5.6: Transmission spectra and threshold characteristics of DFB resonators with various geometries. **(a)** Schematic of a DFB section with length L, corrugation depth d, period a, and width w along with the parameters used in Subfigures 4.6(b)-(e). **(b)** Normalized transmission spectrum of the DFB WG (black line, RWB = 260 pm) and normalized lasing spectrum (red line, RBW = 60 pm) of a DFB laser above threshold. The lasing modes are located at the edges of the stop-band which are blurred in the measured transmission spectrum because of the rather coarse resolution of the spectrometer. The dominant laser mode occurs at the low-frequency stop-band edge TE_{lo}, i.e., at higher wavelengths, whereas the lasing mode at the upper stop-band edge TE_{up} (higher frequency, lower wavelength) has much less power. **(c)** Laser characteristics: The dominant laser mode TE_{lo} at the lower stop-band edge starts lasing for lower pump pulse energies (• $W_{\text{th,lo}} = 32$ nJ, left vertical axis) than the weak mode TE_{up} at the upper stop-band edge (○,$W_{\text{th,up}} = 41$ nJ, right axis). The horizontal upper axis gives effective pump pulse energy W_{eff}, defined by the fraction of the pump pulse energy that is absorbed in the overlap region with the DFB structure. Since the spectrometer used for recording the emission spectra is not calibrated, we report the output power with respect to a common reference power P_0. **(d)** Normalized transmission spectrum of the DFB WG for TE (red lines) and TM polarization (blue lines) for different corrugation depths d. A larger corrugation depth d leads to a larger stop-band width $\Delta\lambda$. For the same corrugation depth d, $\Delta\lambda$ is larger for TM than for TE polarization. **(e)** Threshold pump pulse energies for different coupling

strengths κL for TE and TM polarization. The pump pulse energy W_{eff} refers to the effective pulse energy that is absorbed in the vicinity of the DFB WG structure. The laser threshold decreases for larger κL. For TM polarization, we observe smaller thresholds than for TE polarization. This can be explained by the larger overlap of the TM mode with the gain medium and by the smaller propagation loss compared to the TE mode.

bandwidth (RBW) has been chosen to rather high RBW = 260 pm because the super- continuum source is limited in power spectral density. As a consequence, the transmission maxima expected at the band edges cannot be resolved. The emission spectrum of the pumped resonator is depicted in the same figure by a red line and shows two lasing modes $\mathrm{TE}_{\mathrm{lo}}$ and $\mathrm{TE}_{\mathrm{up}}$ having a spectral distance of $\Delta\lambda = 1.2\,\mathrm{nm}$. The dominant mode occurs at the lower bandgap edge for lower photon energies, $\mathrm{TE}_{\mathrm{lo}}$, whereas the lasing mode $\mathrm{TE}_{\mathrm{up}}$ at the upper high-photon energy bandgap edge is less pronounced. Note that when pumping the laser, the induced gain and the higher temperature lead to a blue shift of the DFB stop-band as compared to the cold resonator. For better visualization, this was compensated by blue-shifting the measured transmission spectrum by 0.2 nm in Figure 5.6(b).

The laser output powers P_{lo} and P_{up} for the two lasing modes in Figure 5.6(b) was measured as a function of the pump pulse energy W, Figure 5.6(c). In the investigated device, the dominant laser mode of Figure 5.6(b), filled red circles, starts lasing for lower pump pulse energies $W_{\mathrm{th,lo}} = 32\,\mathrm{nJ}$ than the less pronounced one with $W_{\mathrm{th,up}} = 41\,\mathrm{nJ}$, open red circles. The differential quantum efficiency according to Equation (5.5) is larger for the $\mathrm{TE}_{\mathrm{lo}}$ mode than for the $\mathrm{TE}_{\mathrm{up}}$ mode. Note that this behavior was not systematic, and that we also observed DFB lasers or pump conditions in which the laser emission at the lower stop-band edge was equal to or stronger than the emission at the upper edge. We attribute this observation to slight imbalances in the net gain of the two modes that may be caused by, e.g., different overlaps with the gain material, by differences in scattering losses due to rough wave WG surfaces, or by frequency-dependent external feedback originating from the remote waveg WG facets. As both modes are amplified, the homogeneous line broadening of the dye must be smaller than the spectral separation of the DFB resonator modes.

Figure 5.6(d) shows transmission spectra for TE (red lines) and TM modes (blue lines) of DFB resonators with different corrugation depths d but otherwise same geometries. The center wavelengths of the stop-bands for TE modes are red-shifted by $16\,\mathrm{nm} \ldots 18\,\mathrm{nm}$ from those of the TM-polarized modes, which is caused by the slightly higher effective index seen by the TE modes as compared to the TM modes. At the same time, we observe a red-shift of the stop-bands for increasing depths d. This red-shift is slightly stronger for the TE-polarized modes than for their TM-polarized counterparts. This can be explained by the following consideration: Changing the corrugation depth does not only change the coupling strength κ, but also the average WG width $w_{\mathrm{e,av}} = w + d/2$. This leads to an increase of the average effective refractive index $n_{\mathrm{e,av}}$ seen by the guided modes, and this increase is stronger for TE polarization than for TM. As a consequence, the center wavelength $\lambda_{\mathrm{B}} = 2n_{\mathrm{e,av}}a$ increases stronger for TE than for TM modes. We also find that the bandwidth $\Delta\lambda$ of the stop-band is slightly larger for TM-polarized modes than for TE polarized modes for the same corrugation depth d, which means that the grating strength is larger for TM modes.

The threshold pump pulse energies measured for devices with different coupling strengths κ and different lengths $L = ma$ are shown in Figure 5.6(e), where TM polarization is indicated by blue circles and TE polarization by red circles. For better comparison of the threshold pump energies we consider again only the effective pump pulse energy $W_{\mathrm{th,eff}}$ that is absorbed in the vicinity of the DFB resonator, i.e., within a rectangular region that comprises the DFB WG and as well as a 600 nm-wide strip to each side of the WG. In this graph, the coupling strength κ was obtained from simulations of homogeneous WG with widths w and $w + d$, which provides the effective-index difference Δn_{e} and the coupling strength κ according to Equation (5.3). For comparing the experimental results to the theory developed in [31], we also plot dashed and solid reference lines in Figure 5.6(e). These lines are obtained by assuming that the gain at threshold is proportional to the associated pump pulse energy, $W_{\mathrm{th,eff}} \propto g_{\mathrm{th}}L$.

In the low-gain regime, i.e., in the right-hand part of the diagram ($g_{\mathrm{th}} \ll \kappa$), we use Equation (5.3). to derive a model function. For simplicity, we assume that the gain at threshold is mainly dictated by the finite feedback of the DFB structure while the impact of the propagation loss α can be neglected, i.e., $\alpha L \ll 2\left(\pi/\kappa L\right)^2$ even in the low-gain regime. This leads to a model function of the form $W_{\mathrm{th,eff}} = C\left(\pi/\kappa L\right)^2$, where the scaling factor C is used as a fit parameter. The associated sections of the reference curves in the right-hand part of Figure 5.6(e) are drawn as solid lines. For the high-gain regime, $g_{\mathrm{th}} \gg \kappa$, Ref. [31] only provides a numerical solution [31, Fig. 8], which we plot into the left-hand part of Figure 5.6(e) as solid lines using the scaling factor C obtained from the low-gain regime. A dashed spline connects the two partial curves.

Even though the measured data points in Figure 5.6(e) are subject to substantial variations, they follow the overall trend obtained from the reference lines. The laser threshold decreases for larger κL, and the threshold is smaller for TM polarization than for TE polarization. This can be explained by the larger overlap of the TM-polarized mode with the gain medium compared to the TE-polarized mode. In addition, the propagation loss is expected to be smaller for TM-polarized modes as large field strengths are located at the smooth upper surface of the WG core, whereas TE-polarized modes interact stronger with the rather rough sidewalls of the WG core. Low thresholds of $W_{\mathrm{th,eff}} < 0.3\,\mathrm{nJ}$ are reached with total coupling strengths $\kappa L > 15$. The pump fluences on the resonator at threshold are $40\,\mu\mathrm{J}/\mathrm{cm}^2 \ldots 60\,\mu\mathrm{J}/\mathrm{cm}^2$. Note that, when designing DFB lasers, decreasing the threshold by increasing κL is only effective to a certain extent. At very large values of κL, the optical feedback is very strong, and the outcoupling rate τ_{R}^{-1} becomes small compared to the overall resonator loss rate τ_{P}^{-1}, thereby reducing the differential quantum efficiency according to Equation (5.5).

To achieve single-mode lasing, DFB lasers with a quarter-wave shift ($\mathrm{DFB}_{\lambda/4}$) at $z = L/2$ were investigated, see Figure 5.7(a). The optical quarter-wave $(\lambda/4)$ shift in the center of the Bragg grating corresponds to a spatial shift of the z-dependent width modulation by half the grating period, i.e., by

$a/2$. This leads to laser emission at the Bragg wavelength λ_B, supported by a lasing mode that is spatially confined to the region of the phase shift and that decays exponentially towards both ends of the grating. Figure 5.7(b), black line, shows the transmission spectrum of a passive $\mathrm{DFB}_{\lambda/4}$ resonator with the parameters given in Figure 5.7(a), which leads to $\kappa L = 3.4$. Also here, the transmission spectrum was measured using a rather high RBW of 260 pm to cope with the limited output power of the super-continuum source.

The emission spectrum of the pumped resonator is depicted in the same figure, red line, recorded with a RBW of 60 pm. From a Lorentzian fit, we calculate the full-width half-maximum of the lasing emission to be FWHM = 230 pm (190 GHz). Although there is no characteristic transmission peak at λ_B in the

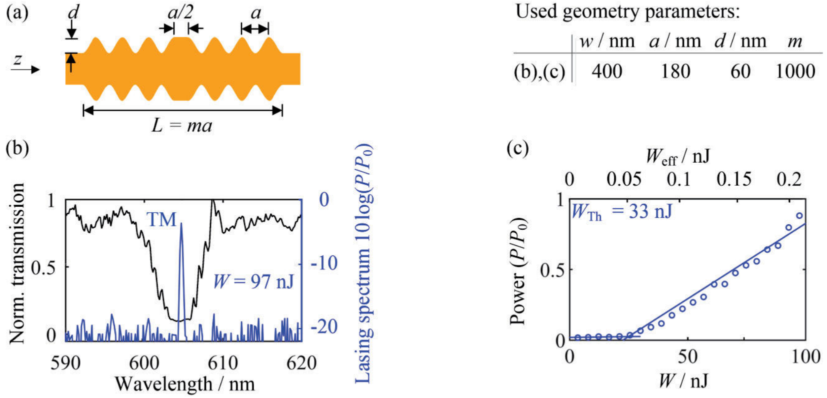

Used geometry parameters:

	w / nm	a / nm	d / nm	m
(b),(c)	400	180	60	1000

Figure 5.7: Transmission spectrum and threshold of a $\mathrm{DFB}_{\lambda/4}$ laser. **(a)** Schematic of a DFB section with quarter-wave (λ/4) shift at $z = L/2$, total length L, corrugation depth d, period a, and width w. The quarter-wave (λ/4) shift corresponds to a geometrical shift by $a/2$ and leads to lasing at the Bragg wavelength. Parameters for Subfigures 4.7(b),(c) are listed in the table on the right. **(b)** Normalized transmission spectrum (black line, RBW = 210 pm) and laser emission (blue line, RBW = 60 pm) for a TM-polarized mode. The lasing mode is located at λ_B in the middle of the stop-band. The expected transmission peak at λ_B cannot be seen, due to a non-negligible background and due to limited spectrometer resolution and low emission power of the whit-light source used for the measurement. **(c)** Laser characteristics: The TM laser mode starts lasing for pump pulse energies $W_\mathrm{th} = 33$ nJ. The horizontal upper axis shows the fraction of the pump pulse energy W_eff that is absorbed in the overlap region with the $\mathrm{DFB}_{\lambda/4}$ structure. The output power is again specified with respect to a common reference power P_0.

middle of the transmission stop-band, a laser mode emerges at λ_B. We attribute the missing transmission peak to the non-negligible background in the transmission measurement and to the limited spectral resolution, which was again dictated by the limited emission power of the white-light source. The laser output power was measured as a function of the overall and the effective pump pulse energy W and W_{eff}, respectively, Figure 5.7(c). The effective pump pulse energy W_{eff} refers again to the pulse energy absorbed in the vicinity of the DFB resonator, i.e., within a rectangular region that comprises the DFG WG and a 600 nm-wide strip to each side of the WG.

We find a threshold of $W_{\text{th}} = 33\,\text{nJ}$ $(W_{\text{th,eff}} = 0.07\,\text{nJ})$, which is comparable to the threshold of the DFB gratings with large κL in Figure 5.6(d). The threshold pump fluence at the resonator is $64\,\mu\text{J}/\text{cm}^2$.

5.5 Comparative discussion

Based on our analysis of the different SiNOH laser concepts we compare the properties that are crucial for applications in bio-sensors. Important requirements are the spectral properties of the emitted light, the on-chip footprint, as well as robustness and tolerance with respect to fabrication inaccuracies. These aspects are discussed in the following section.

Spectral properties of emitted light For the spiral resonators, the number of modes is mainly defined by the FSR of the feedback filter ring, the spectral distribution of the net gain, and the bandwidth of the homogeneous line broadening. In our experiments, we found that lasing occurs within a 15 nm bandwidth centered at approximately 600 nm. The number of modes within the bandwidth can be controlled by the radius of the feedback filter ring. Increasing the FSR to obtain lasing in a single longitudinal mode is not always possible because smaller radii of the feedback ring filter can lead to higher losses due to radiation and therefore to higher thresholds. Moreover, the exact emission wavelength might sensitively depend on the temperature of the feedback ring filter. For spiral lasers, lasing can occur simultaneously in TE and TM polarization.

For the DFB resonator, single-mode emission can be achieved over a large spectral range, limited by the gain spectrum of the dye. By carefully choosing the period of the grating, the polarization can be controlled. In some cases, two modes can be amplified at both boundaries of the stop-band, but usually one mode is dominant. For $\mathrm{DFB}_{\lambda/4}$ lasers, only one mode at the Bragg wavelength oscillates. Similar to the DFB lasers, the mode can be chosen in a large spectral range by varying the period of the grating. For both DFB and $\mathrm{DFB}_{\lambda/4}$ lasers, emission usually occurs in one polarization only.

Device lifetime Generally, the device lifetime of organic lasers is limited by photodegradation of the dyes [38]. However, this did not represent a practical limitation in our experiments – we could test the SiNOH devices for several hours, i.e., with more than 100 000 pump pulses, while still retaining at least 50 % of the initial emission power. These findings are in line with recently published results on similar devices [28] and should permit operation of SiNOH lasers in disposable point-of-care devices. Note that the pump pulse duration used in our experiments amounts to 20 ns and is thus significantly longer than the fluorescence lifetime of the dyes, which is approximately 5 ns [41]. Using shorter pump pulses might hence allow to further improve the device lifetime [38,39].

We also observe an increase of the degradation rate if the pump spot is focused to a smaller area as in the scheme depicted in Figure 5.4(b). This can be explained by considering the photodegradation mechanism in more detail: When photons are absorbed, the dye molecules are transferred from a singlet ground state to a singlet excited state, which has a lifetime in the nanosecond range [42]. With a certain probability, such a singlet excited state can undergo an intersystem crossing to a triplet excited state, which requires another intersystem crossing to relax to the singlet ground state and which thus has a rather long lifetime in the microsecond range [42]. Photodegradation can either directly result from a chemical reaction of excited triplet-state dyes with their molecular environment [43] or can be indirectly caused through generation of highly reactive singlet oxygen molecules during one of the intersystem crossings [44]. Focusing the pump to a smaller cross section has two effects on this mechanism: First, the length of the active WG sections within the pump spot is smaller, such that laser operation requires a higher density of excited single-state dyes to compensate the cavity losses. Second, a higher photon density may also lead to further transitions from the first excited singlet states to higher singlet states, from where the transition to a triplet state is more likely [44]. We believe that a systematic investigation of these effects can lead to additional approaches to increase the device lifetime.

Footprint and overlap with pump spot The larger the overlap of the laser WG with the pump spot, the more energy can be transferred to the SiNOH laser. For spiral lasers, good overlap with a circular pump spot can be achieved and can be further increased by focusing the pump light to an area with densely spaced WG or by using alternative pump spot shapes such as rings. Generally, spiral lasers have larger on-chip footprint than other devices.

For the DFB and the $\mathrm{DFB}_{\lambda/4}$ laser, the overlap with a circular pump spot is much smaller than that for the spiral, but its size may be increased by using, e.g., a cylindrical lens that generates a line-shaped focus. The devices offer small on-chip footprint and lend themselves to integration in arrays which can be excited by one large pump spot.

Robustness and tolerance to fabrication inaccuracies Within the limited set of approximately 50 devices investigated for the current study, we found the reliability of spiral lasers to be higher than that of DFB and $\mathrm{DFB}_{\lambda/4}$ lasers, especially when the devices are coupled to additional on-chip photonic circuits. This could be caused by optical feedback, which might have a higher impact on DFB and $\mathrm{DFB}_{\lambda/4}$ lasers than on spirals, or by a higher sensitivity of the DFB gratings with respect to fabrication inaccuracies. These aspects require further investigation.

5.6 Summary

We demonstrate and investigate hybrid organic dye lasers emitting at 600 nm wavelength that can be monolithically integrated on the silicon nitride (Si_3N_4)

platform. The Si_3N_4-organic hybrid (SiNOH) lasers are operated by optical pumping from the top with relaxed alignment precision of the pump spot with respect to the on-chip structures. SiNOH lasers can be fabricated in a single lithography step by structuring the silicon nitride waveguides together with other devices on the same chip, and by subsequently dispensing or spin coating the organic gain medium on top of the WG cores.

In our proof-of-concept study, we investigate two different laser geometries, spiral-shaped ring resonators and DFB resonators, and compare our experimental findings with theoretical models. All investigated SiNOH lasers offer acceptable threshold fluences of $40\mu J/cm^2 ... 70\mu J/cm^2$ with vast room for further improvement. We also provide a comparative discussion of the different device concepts. To the best of our knowledge, our experiments represent the first demonstration of SiNOH spiral lasers and of SiNOH DFB-lasers with first-order gratings. By using different dyes and by adapting the resonator design, SiNOH lasers should be able to address the entire visible wavelength range. We expect that the versatility of the device concepts, the simple operation principle and the compatibility with cost-efficient mass fabrication will make the SiNOH lasers a highly attractive option for applications in bio-photonics and point-of-care diagnostics.

[end of paper [J3]]

6 Biophotonic sensors with integrated Si_3N_4-organic hybrid (SiNOH) lasers

This chapter shows the first WG-based sensor system that comprises a MZI-based biosensor and a co-integrated SiNOH laser. The functionality is demonstrated by detecting various concentrations of fibrinogen. Furthermore, the sensitivity and operation in point-of-care applications is discussed. The experiments were conceived by D. Kohler., K. Länge., and C. Koos. D. Kohler developed the SiNOH laser and performed the experiments. L. Hahn supported the fabrication of the Si_3N_4 waveguide structures, which were conceived and designed by D. Kohler., J. Milvich., and G. Schindler. A. Hofmann developed the processes for local dispensing of the passivation layers on the reference arm of the sensor. D. Kohler, W. Freude., and C. Koos prepared the manuscript. This chapter is taken from [J2] which is published in Optics Express. In order to fit the structure and layout of this document, it was adapted accordingly.

[start of paper [J2]]

Bio-photonic sensors with integrated Si_3N_4-organic hybrid (SiNOH) lasers for point-of-care diagnostics

Light Sci. Appl. Vol. 10, No. 64 (2021)
DOI: 10.1038/s41377-021-00486-w

Daria Kohler[1,2], Gregor Schindler[2], Lothar Hahn[2], Johannes Milvich[1,4], Andreas Hofmann[3], Kerstin Länge[2], Wolfgang Freude[1] and Christian Koos[1,2,*]

[1] Karlsruhe Institute of Technology, Institute of Photonics and Quantum Electronics, 76131 Karlsruhe, Germany

[2] Karlsruhe Institute of Technology, Institute of Microstructure Technology
76344 Eggenstein-Leopoldshafen, Germany
[3] Karlsruhe Institute of Technology (KIT), Institute for Automation and
Applied Informatics (IAI), Hermann-von-Helmholtz-Platz 1, 76344
Eggenstein-Leopoldshafen, Germany
[4] Robert Bosch GmbH, Robert-Bosch-Campus 1, 71272 Renningen,
Germany

Early and efficient disease diagnosis with low-cost point-of-care devices is gaining importance for personalized medicine and public health protection. Within this context, waveguide-(WG)-based optical biosensors on the silicon nitride (Si_3N_4) platform represent a particularly promising option, offering highly sensitive detection of indicative biomarkers in multiplexed sensor arrays operated by light in the visible wavelength range. However, while passive Si_3N_4-based photonic circuits lend themselves to highly scalable mass production, the integration of low-cost light sources remains a challenge. In this paper, we demonstrate optical biosensors that combine Si_3N_4 sensor circuits with hybrid on-chip organic lasers. These Si_3N_4-organic hybrid (SiNOH) lasers rely on a dye-doped cladding material that are deposited on top of a passive WG and that are optically pumped by an external light source. Fabrication of the devices is simple: The underlying Si_3N_4 WG are structured in a single lithography step, and the organic gain medium is subsequently applied by dispensing, spin-coating, or ink-jet printing processes. A highly parallel read-out of the optical sensor signals is accomplished with a simple camera. In our proof-of-concept experiment, we demonstrate the viability of the approach by detecting different concentrations of fibrinogen in phosphate-buffered saline solutions with a sensor-length (L-)related sensitivity of $S/L = 0.16\,\mathrm{rad}/(\mathrm{nM\,mm})$. To our knowledge, this is the first demonstration of an integrated optical circuit driven by a co-integrated low-cost organic light source. We expect that the versatility of the device concept, the simple operation principle, and the compatibility with cost-efficient mass production will make the concept a highly attractive option for applications in biophotonics and point-of-care diagnostics.

6.1 Introduction

Integrated sensors based on optical waveguides (WG) exhibit an enormous application potential in bio-photonics and medical diagnostics, especially when it comes to multiplexed, highly sensitive detection of a wide variety of target molecules [4], [19]. In bio-photonic applications, the visible (VIS, $\lambda = 400$ nm … 700 nm) and short-wavelength near-infrared (NIR, $\lambda = 700$nm … 1100 nm) spectral ranges are of particular interest [40], offering a low absorption [14] and hence permitting large interaction lengths of the guided light with analytes in mostly aqueous solutions [102], [103]. Within this context, silicon nitride (Si_3N_4) has emerged as a powerful integration platform for WG-based sensor systems [122]. Its advantages are the low propagation loss over the wide spectral range between 400 nm and 2.3 µm [9], [105]–[107] in addition to the high refractive-index contrast between the Si_3N_4 WG core ($n_{\mathrm{Si_3N_4}} = 2.01$ @ $\lambda = 600$ nm [49]) and the silicon dioxide cladding ($n_{\mathrm{SiO_2}} = 1.46$ @ $\lambda = 600$ nm [50]). Moreover, Si_3N_4-based photonic integrated circuits (PICs) can be efficiently fabricated in large quantities using mature wafer-scale processes that offer high yield and are that accessible through a worldwide ecosystem of photonic foundries [9], [105]. This opens a path towards cost-efficient mass production of highly functional sensor chips for one-time use in point-of-care diagnostics.

However, with a few exceptions in the mid-infrared wavelength range [123], biosensors on the Si_3N_4 integration platform remain limited to mainly passive circuits and usually rely on external light sources coupled to the chip [24], [102], [109], [124]. This requires delicate fibre-chip coupling schemes that are subject to stringent mechanical tolerances, which conflicts with the demand for technically simple low-cost sensor systems for point-of-care diagnostics. Cointegration of sensor circuits with on-chip lasers might represent an alternative, but all demonstrations have so far been limited to NIR sources that are first realized on a separate substrate and that are then flip-chip mounted onto passive Si_3N_4 PICs in a dedicated assembly step [35]. This involves serial assembly processes and thus mitigates most of the scalability advantages of highly parallel wafer-level mass fabrication. It is hence uncertain whether high-precision assembly of discrete laser dies could comply with the stringent cost limitations of disposable biosensors.

In this paper, we demonstrate a Si_3N_4 biosensor monolithically co-integrated with a low-cost hybrid laser source operating at visible wavelengths. The laser relies on the concept of Si_3N_4-organic hybrid (SiNOH) integration and combines passive Si_3N_4 WG cores with dye-doped organic cladding materials [54], [114]–[116], [125]. The devices are technically simple and can be efficiently realized by wafer-level printing techniques. SiNOH lasers may either be optically pumped by an external laser or a light-emitting diode (LED) without any high-precision alignment of the pump spot or physical contact with the chip. In a proof-of-concept experiment, we demonstrate the viability of the sensor system by detecting different concentrations of fibrinogen in an aqueous buffer solution. To our knowledge, this is the first demonstration of a Si_3N_4 photonic integrated circuit driven by an on-chip laser source emitting at visible wavelengths.

6.2 Results

6.2.1 Concept

The concept of a Si_3N_4-based biosensor with co-integrated SiNOH lasers is shown in Figure 6.1(a). For robust handling purposes in point-of-care applications, the sensor chip is placed in a cartridge (black) containing windows for optical pumping and readout. The sensor comprises a microfluidic chamber with in- and outlets for the liquid analyte solution. The chamber is formed by the chip surface, the cartridge lid, and an elastic seal (blue) between the chip surface and the lid. The SiNOH lasers are pumped from the top by an external light source with a large spot size such that high-precision alignment of the chip with respect to the pump beam is not needed. The generated laser light is coupled with a Si_3N_4 single-mode WG and guided to an array of on-chip sensors. The output light is radiated through the read-out window by grating couplers and captured by a camera. Optical pumping

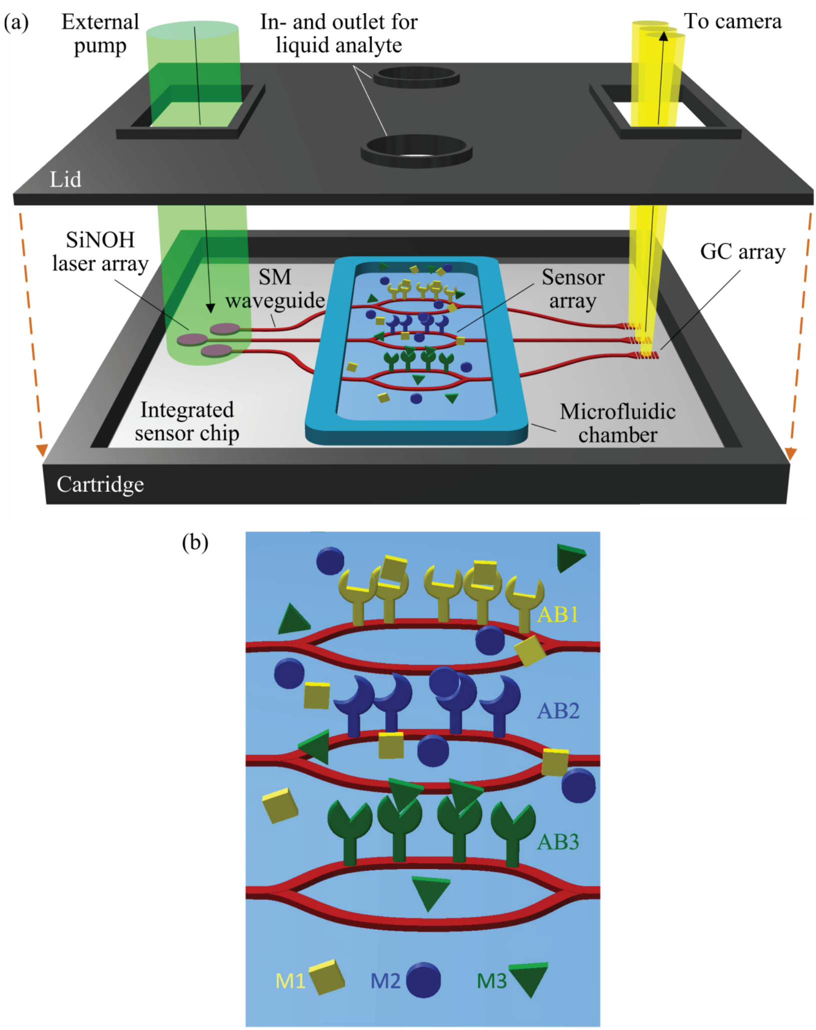

Figure 6.1: Concept of the Si_3N_4-based biosensor with co-integrated lasers. **(a)** The Si_3N_4 chip combines a SiNOH laser array with an array of sensors, illustrated as Mach-Zehnder interferometers (MZI), and is placed in a cartridge (black) containing windows for optical pumping and readout. The sensor comprises a microfluidic chamber with an in- and outlet for the liquid analyte solution, which is formed by the chip surface, the cartridge lid, and an elastic seal (blue) between the chip surface and lid acting as the chamber sidewalls. The

integrated SiNOH lasers are pumped by an external light source with a large pump spot size such that high-precision alignment is not needed. The light originating from the sensor output is radiated from the chip to a read-out camera by grating couplers. **(b)** Simplified schematic of the MZI-based sensor. Each MZI contains one sensing and one reference arm. The sensing arms are functionalized with individual antibodies AB1, AB2, and AB3 that bind specific target molecules M1, M2, and M3, respectively, to the WG surfaces.

and read-out offer the advantage that no physical contact with the chip is required and thus greatly simplifies the handling of the devices – a key aspect in point-of-care applications. Figure 6.1(b) shows a simplified schematic of the sensor section, consisting of three Mach-Zehnder interferometers (MZIs) with one sensing arm and one reference arm each. The sensing arms are functionalized with individual antibodies AB1, AB2, and AB3 that bind specific target molecules M1, M2, and M3, respectively, to the WG surface. The reference arms are not functionalized.

6.2.2 Proof-of-concept system

To demonstrate the viability of the sensor concept shown in Figure 6.1, we realized a proof-of-principle demonstrator that combines an on-chip SiNOH laser with an MZI-based biosensor in a microfluidic chamber. The layout of the underlying Si_3N_4 chip is shown in Figure 6.2(a). The MZI is placed between the SiNOH laser and the grating coupler (GC) array. The laser is sufficiently far from the GC array to avoid any optical cross-talk by stray light originating from the pump laser.

The SiNOH laser relies on a passive Si_3N_4 WG, which is embedded into a light-emitting cladding that can be optically pumped (Inset of Figure 6.2(a)). Details of the SiNOH laser have been presented in an earlier publication [54]. In our experiments, the cladding consisted of 800-nm-thick polymethylmethacrylate (PMMA) doped with an organic dye. This cladding can be deposited via simple wafer-level dispensing or ink-jet printing processes. The SiNOH laser cavity is realized as an open-ended spiral-shaped Si_3N_4 WG with a distance of 1.5 µm between neighbouring turns

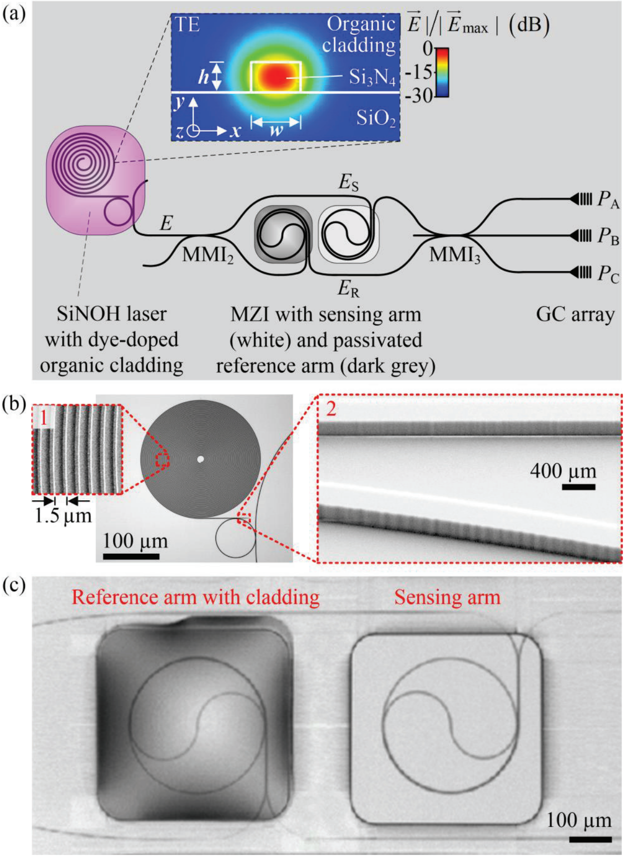

Figure 6.2: Fabricated demonstrator chip, combining a SiNOH laser with an MZI-based biosensor. **(a)** The SiNOH laser cavity is an open-ended spiral WG that is evanescently coupled to a ring resonator, which feeds the input WG of the MZI-based sensor circuit. Resonant coupling of the counter-propagating modes in the ring leads to narrowband frequency-selective back-reflection from the outer end of the spiral. Broadband optical feedback from the inner end of the spiral is provided by reflection from the open WG end at the centre in combination with roughness-induced backscattering along the 20-mm-long spiral WG. The cladding window of the SiNOH laser (magenta) is filled with dye-doped PMMA acting as an organic gain material. The inset shows a typical cross-section (width w and height h) of a SiNOH WG along with the simulated electric field magnitudes $|\mathbf{E}|$ of the fundamental quasi-TE mode. The sensor MZI is formed by a 2×2 MMI splitter (MMI$_2$) and a 3×3 MMI combiner (MMI$_3$), of which only two input ports are used. The

splitter distributes the light originating from the SiNOH laser equally to the two spiral-shaped arms. The sensing arm (white) is exposed to the analyte solution, while the reference arm (dark grey) is passivated by a cover material. The three output signals of MMI_3 are coupled from the chip by a GC array and recorded by a camera (not shown). **(b)** Light-microscopy image of a SiNOH laser cavity without cladding. The spiral is densely coiled up with a 1.5-µm distance between neighbouring WG, see Inset 1. The waveguides are subject to a certain sidewall roughness in the form of vertical grooves, see Inset 2. This roughness may lead to loss and to a resonantly enhanced coupling of the counter propagating modes in the ring resonator. **(c)** Spiral-shaped WG in the MZI arms. For passivation purposes, the reference arm is covered with a low-index glue that is approximately index-matched to the aqueous analyte solution applied to the sensing arm.

(Figure 6.2(b)). The spiral WG is evanescently coupled to a ring resonator, where the resonant coupling of counter-propagating modes leads to frequency-selective optical feedback. The ring resonator also feeds the output WG, thus yielding an MZI-based sensor circuit. The overall footprint of the SiNOH laser amounts to less than $0.3 \times 0.3\ \text{mm}^2$ – much smaller than the microfluidic structures required for the handling of the analyte, which typically extend over several millimetres. Note that the concept of combining passive inorganic WG structures with functional organic cladding materials has previously been exploited in silicon photonic circuits operated in the near-infrared wavelength range. This silicon-organic hybrid (SOH) integration concept lends itself to electro-optic modulators with a record-high efficiency [126] and to low-cost on-chip laser sources [117].

The sensor circuit itself consists of a 2 × 2 multimode interference coupler (MMI_2) that splits the incoming light into the two spiral-shaped arms of the MZI (Figure 6.2(a) and Figure 6.2(c)). The sensing arm (white) is exposed to the analyte, while the reference arm (dark grey) is covered by a protective layer (Figure 6.2(c)). The sensing and reference arms exhibit the same geometrical length, i.e., $L = 1.8$ mm. The output fields of the sensing arm ($\underline{E}_\text{S}$) and the reference arm ($\underline{E}_\text{R}$) are fed to the two input ports of a 3 × 3 MMI (MMI_3). The three output signals propagate to a GC array, which radiates the light to the top. The MMI and GC are designed for operation under quasi-TE polarization, for which the horizontal component (x-component) of the optical mode field dominates (please refer to the inset of Figure 6.2(a)).

6.2.3 On-chip SiNOH laser

The SiNOH laser design is slightly different from that of the devices presented in our former publications [54], [114] (Section 5.4.2). Specifically, we found that due to the high gain provided by the dye-doped organic cladding material, lasing was possible even for cavities with fairly low Q-factors. We exploit this fact by replacing the closed spiral cavity used in Ref. [54] (Section 5.4.2) with an open spiral, which does not require a large S-turn at the centre and hence allows us to greatly increase the overlap with the Gaussian pump spot. This becomes more obvious when comparing the area fill factor of the open SiNOH laser spiral shown in Figure 6.2(b) to the sensor spirals in the MZI arms shown in Figure 6.2(c). The open laser spiral is densely coiled with a distance of 1.5 µm between the neighbouring WG and fills a circular area with a 100-µm radius. It is pumped with a Gaussian spot (green) exhibiting a full-width half-maximum of 160 µm. The slightly multimoded (MM) spiral WG reveals a width of 500 nm that is tapered down to 300 nm to allow single-mode coupling to a ring resonator with a radius of 40 µm and a free spectral range of $\mathrm{FSR} = 0.66\,\mathrm{nm}$ (540 GHz). To avoid gain competition between the various lasing modes, the FSR was deliberately chosen to slightly exceed the bandwidth of the homogeneous gain broadening that was previously estimated to be on the order of 0.6 nm [54] (Chapter 5). It should be noted that the FSR must not be chosen unnecessarily large to ensure that all dye molecules emit into a spectrally sufficiently close lasing mode. This leads to polychromatic laser emission – a feature that must be considered when designing the sensor coupled to the SiNOH laser. Within the ring, resonantly enhanced coupling of the counter-propagating modes leads to single-mode frequency-selective reflection of light back into the spiral. This coupling arises from the surface roughness of the WG ring (as shown in Figure 6.2(b)). Moreover, broadband optical feedback is provided from the inner end of the spiral through reflection from the open WG end at the centre, possibly in combination with the roughness-induced backscattering along the 18-mm-long spiral WG. We also measured the propagation loss of the Si_3N_4 WG in the SiNOH cavity, which, for an undoped PMMA cladding, amounted to approximately $5\,\mathrm{dB/cm}$ for the 500-nm-wide multimode spiral WG and to approximately $7\,\mathrm{dB/cm}$ for the narrower 300-nm-wide single-mode WG. A more detailed discussion of the optical feedback in the SiNOH laser cavity has been provided in Supplementary Note 1.

In the first step, we characterize the SiNOH lasers without attached biosensors, see Figure 6.3. Figure 6.3(a) shows the associated test structure with two output grating couplers GC1 and GC2. The device is optically pumped by a frequency-doubled Nd:YLF pulsed laser (CL523, CrystaLaser, Reno, USA) with an emission wavelength of 523 nm, a pulse duration of 20 ns, and a repetition rate of 20 Hz. Within the single-mode (SM) ring resonator, the clockwise-propagating mode is predominantly excited, but it also experiences resonantly enhanced coupling to the counter-clockwise-propagating mode because of structural imperfections such as sidewall, see Inset 2 of Figure 6.3(b). This is confirmed by comparing the output power found at GC1 and GC2, see Figure 6.3(b). The top row shows the colour-coded intensity distribution of the light radiated from GC1 and GC2 as recorded by a camera. The bottom row shows cross-sectional intensity plots along the main axes of the grating couplers, i.e., at $x = 0$. The emission from GC2 is approximately three times as high as the emission from GC1, indicating that the clockwise-propagation mode is predominantly excited but experiences substantial coupling to its clockwise-propagating counterpart.

For a further investigation, we captured the light from GC2 with a single-mode fibre and connected it to a spectrometer with a resolution bandwidth of 60 pm and an integration time of 2 s. Figure 6.3(c) shows the emission spectrum at a pump-pulse energy of $W = 93$ nJ. The spectrum is normalized to the highest peak and shows three dominant quasi-TE-polarized lines within the recorded spectral range of 10 nm. The peak power of the emitted laser pulse is on the order of 100 mW, which is twice as high as that of previously demonstrated SiNOH lasers [54] (Section 5.4.2). This improvement was achieved by using open-spiral cavities, which do not require a large S-turn at the centre and thus provide a better overlap with the pump spot than their closed-spiral counterparts used in our previous demonstration. The normalized average output power $P/P_{\max}$ vs. the pump-pulse energy W is

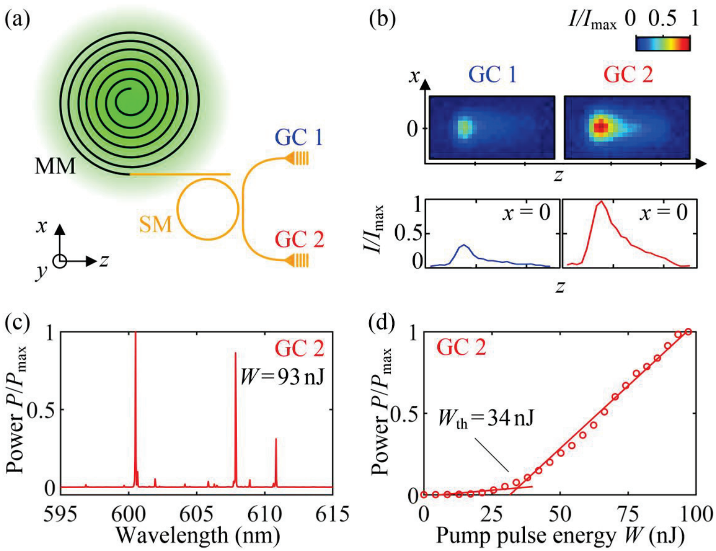

Figure 6.3: Characterization of SiNOH laser. **(a)** SiNOH laser geometry: A multimode WG (MM, black, $w = 500$ nm) embedded in the gain medium is coiled into a spiral with an outer diameter of 200 µm. The arrangement offers a large overlap of the spiral WG with the Gaussian pump spot exhibiting a full-width half-maximum of 160 µm (green). The MM WG is tapered down to a single-mode (SM) WG subject to $w = 300$ nm (orange), which is evanescently coupled to a SM ring resonator ($Q = 5\times10^3$). The ring resonator is coupled to the SM output WG that guides the light to GC 1 and GC 2, which are both optimized for quasi-TE polarization. **(b)** Colour-coded intensity of the SiNOH laser light emitted from GC 1 and GC 2 (upper row) along with a cross-section of the emission profile along the line of $x = 0$ (bottom row). The emission from the GC is recorded by a CCD camera (three-fold magnification) and normalized to the maximum detected power intensity I_{max} measured at GC 2. By comparing these plots, we find that the clockwise-propagating power in the ring is three times as high as the counter-clockwise-propagating power, which provides feedback into the pumped spiral. **(c)** Normalized emission spectrum of the SiNOH laser recorded under quasi-TE-polarization at GC 2 (resolution bandwidth: 60 pm; integration time: 2 s). Three dominant lasing modes are shown. **(d)** Normalized laser output power as a function of the pump pulse energy W. We find a lasing threshold of $W_{th} = 34$ nJ.

shown in Figure 6.3(d). At each pump-pulse energy level, the output power is measured by integrating the spectrum, as shown in Figure 6.3(c), over all wavelengths. We find a clear lasing threshold with a threshold pump-pulse energy of $W_{\mathrm{th}} = 34$ nJ. We also investigated the output power emitted from GC1 as a function of the pump-pulse energy, observing that the lasing threshold is essentially the same as that extracted from GC2, see Appendix C, Figure C.2. This confirms the notion that the emission at GC1 results from resonant coupling of counter-propagating modes in the ring. By investigating the output spectra of GC2 for different pump-pulse energies, we find that the three lasing modes exhibit distinct thresholds with no indication of gain competition, see Appendix C, Figure C.1. Further details on the SiNOH spiral laser and the emission characteristics are contained in Supplementary Note 1.

6.2.4 MZI-based sensors and polychromatic laser sources

MZI-based sensors offer the general advantage that they are robust with respect to mechanical stress and temperature fluctuations, in particular when the sensing and reference arm rely on WG which feature identical or very similar cross-sections and which are placed in close vicinity to each other. Temperature fluctuations in the chip will then affect both MZI arms in the same way, without any impact on the measurement result, which only depends on the phase difference at the output of the two arms. In general, 2 × 1 MMI, 2 × 2 MMI or 3 × 3 MMI may be used as power combiners in MZI-based biosensors. MZI based on 2 × 2 MMI and 3 × 3 MMI allow for correction of laser-power fluctuations, which affects all output signals equally. This is in contrast to structures involving 2 × 1 MMI, for which a phase shift in the sensor arm is indistinguishable from a power fluctuation in the light source. Compared to 2 × 2 MMI, 3 × 3 MMI offers several additional sensing advantages. First, the difference $\Delta\phi$ of the phase shifts in the two MZI arms can be directly reconstructed from the power levels P_{A}, P_{B}, and P_{C} measured at the three output ports A, B, and C, respectively, without any phase ambiguities within the usual 2π-interval. Second, appropriate signal processing allows achieving a sensitivity that is independent of the MZI operating point. Moreover, fabrication inaccuracies and temperature influences causing amplitude and phase errors of the MMI can be corrected by digital signal processing (DSP). In the following paragraphs, these advantages are explained in more detail.

As discussed in the previous section, polychromatic emission is a distinct feature of SiNOH lasers that is closely related to the gain medium. This aspect must be considered when describing the interplay of the light source with the sensor. In the following, we assume a polychromatic source with M spectral lines with optical angular frequencies ω_m ($m = 1, 2, \ldots, M$) and complex amplitudes $\hat{\underline{E}}_m$, see Supplementary Note 3 for additional details. We represent the optical power of each spectral line by the squared magnitude of the respective complex field amplitude $\hat{\underline{E}}_m$, and the total power is given as the sum of the powers of the individual components, $P_{\text{source}} = \sum_{m=1}^{M} \left|\hat{\underline{E}}_m\right|^2$, see Appendix C.2.2, Equation (C.7). Within the Si_3N_4 MZI WG, we assume propagation along the z-direction with propagation constant β_m. The resulting fields associated with an individual spectral component are hence represented by $\underline{E}_m = \hat{\underline{E}}_m \exp\left[\mathrm{j}\left(\omega_m t - \beta_m z\right)\right]$, with z being the propagation distance along the WG, and the overall complex field is the superposition of $\underline{E} = \sum_{m=1}^{M} \underline{E}_m$. The physical electric field is obtained by calculating the real part, i.e., $E(\mathbf{r}, t) = \text{Re}\left[\underline{E}(\mathbf{r}, t)\right]$.

At the input of the MZI, the electric field is split by the 2 × 2 MMI into equal portions in the sensing and reference WG, Appendix C.2 for a detailed mathematical description of the MZI operated by monochromatic and polychromatic sources, respectively. Splitting of the field in the 2 × 2 MMI leads to a phase shift of $-\pi/2$ in the field in the reference arm with respect to the field in the sensing arm. For simplicity, we assume that the reference and measurement arms exhibit equal geometrical lengths L. The effective index of the reference arm is denoted as $n_{\text{e,R}}$ and is assumed to remain constant during the sensing experiments since the reference arm is completely embedded into a passivation layer to isolate the Si_3N_4-based WG from the analyte. Regarding the sensing arm, the effective index in the absence of any analyte molecules is denoted as $n_{\text{e,S}}$. If the sensor is exposed to the analyte, adsorption of target molecules leads to a change $\Delta n_{\text{e,S}}$ in the effective refractive index. At the input of the 3 × 3 MMI combiner, the electric field $\underline{E}_{\text{R}}$ in the reference arm can thus be written as

$$\begin{aligned}
\underline{E}_{\mathrm{R}} &= \sum_{m=1}^{M} \frac{\hat{\underline{E}}_m}{\sqrt{2}}\, \mathrm{e}^{\mathrm{j}\left(\omega_m t+\phi_{\mathrm{R},m}-\pi/2\right)}, \\
\phi_{\mathrm{R},m} &= -\beta_{\mathrm{R},m} L = -k_{0,m} n_{\mathrm{e,R},m} L, \qquad k_{0,m} = \omega_m / c\,.
\end{aligned} \tag{6.1}$$

The electric field $\underline{E}_{\mathrm{S}}$ in the sensing arm is

$$\begin{aligned}
\underline{E}_{\mathrm{S}} &= \sum_{m=1}^{M} \frac{\hat{\underline{E}}_m}{\sqrt{2}}\, \mathrm{e}^{\mathrm{j}\left(\omega_m t+\phi_{\mathrm{S},m}+\Delta\phi_{\mathrm{S},m}\right)}, \\
\phi_{\mathrm{S},m} &= -\beta_{\mathrm{S},m} L = -k_{0,m} n_{\mathrm{e,S},m} L, \\
\Delta\phi_{\mathrm{S},m} &= -\Delta\beta_{\mathrm{S},m} L = -k_{0,m} \Delta n_{\mathrm{e,S},m} L\,.
\end{aligned} \tag{6.2}$$

The 3 × 3 MMI combiner at the output of the MZI leads to a superposition of the fields $\underline{E}_{\mathrm{S}}$ and $\underline{E}_{\mathrm{R}}$ with realtive phase shifts of $2\pi/3$, 0, and $-2\pi/3$ at the ports A, B, and C, respectively [73]. The associated output powers P_{A}, P_{B} and P_{C}, respectively, are detected at the respective GCs, Figure 6.2(a), analogue-to-digital converted, and numerically processed by applying a Clarke transform, see Appendix C.2.2 for a more detailed mathematical description. This leads to a correlation function, which we refer to as the Clarke field $\underline{s}_{\mathrm{poly}}$ [77], [78],

$$\begin{aligned}
\underline{s}_{\mathrm{poly}} &= \underline{s}_{\mathrm{r}} + \mathrm{j}\,\underline{s}_{\mathrm{i}} = 2\left\langle \underline{E}_{\mathrm{S}} \underline{E}_{\mathrm{R}}^{*} \right\rangle_T \\
&= \sum_{m=1}^{M} \left[\left| \hat{\underline{E}}_m \right|^2 \mathrm{e}^{\mathrm{j}\left[\Delta\phi_{\mathrm{S},m}+\pi/2+\left(\phi_{\mathrm{S},m}-\phi_{\mathrm{R},m}\right)\right]} \right] \\
&= 2P_{\mathrm{B}} - \left(P_{\mathrm{C}} + P_{\mathrm{A}}\right) + \mathrm{j}\sqrt{3}\left(P_{\mathrm{C}} - P_{\mathrm{A}}\right).
\end{aligned} \tag{6.3}$$

For a monochromatic light source ($M = 1$), as shown in Figure 6.4, Equation (6.3) can be simplified, see Supplementary Note 2,

$$\begin{aligned}
\underline{s}_{\mathrm{mono}} &= \underline{s}_{\mathrm{r}} + \mathrm{j}\,\underline{s}_{\mathrm{i}} = 2\underline{E}_{\mathrm{S}} \underline{E}_{\mathrm{R}}^{*} = \left| \hat{\underline{E}} \right|^2 \mathrm{e}^{\mathrm{j}\left[\Delta\phi_{\mathrm{S}}+\pi/2+\left(\phi_{\mathrm{S}}-\phi_{\mathrm{R}}\right)\right]}, \\
\left| \underline{s}_{\mathrm{mono}} \right| &= \left| \hat{\underline{E}} \right|^2 = P_{\mathrm{source}}.
\end{aligned} \tag{6.4}$$

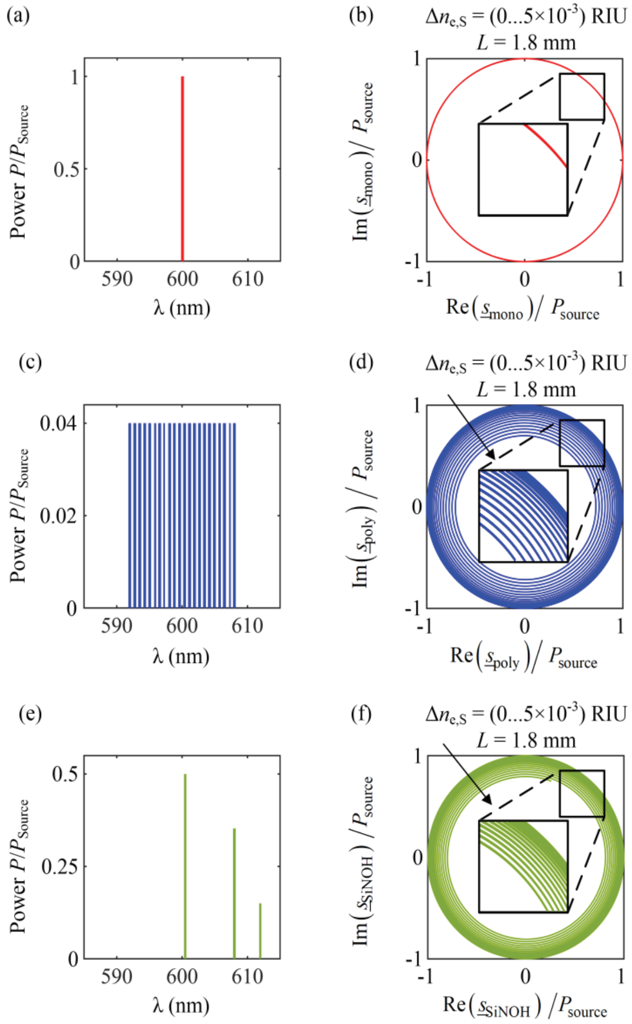

Figure 6.4: Calculated complex Clarke fields $|\mathbf{E}|$ of an MZI with 3×3 MMI combiner at the output for different light sources. **(a),(c),(e)** Normalized emission spectrum for a monochromatic laser line, Subfigure **(a)**, for a polychromatic laser with equally spaced lines of equal powers, Subfigure **(c)**, and for a SiNOH laser with three monochromatic lasing lines located at different wavelengths and exhibiting different powers, Subfigure **(e)**.

(b),(d),(f) Clarke fields $\underline{s}$ calculated from the three output powers of the 3×3 MMI according to Equation (6.3) and plotted in the complex $\underline{s}$-plane. The geometrical lengths of the sensing and reference arms amount to $L = 1.8$ mm, and the effective refractive index difference $\Delta n_{\mathrm{e,S}}$ varies between 0 and 5×10^{-3} RIU. We assume a wavelength of 600 nm. **(b)** For the monochromatic laser, Subfigure (a), $\underline{s}_{\mathrm{mono}}$ describes a circle with radius $\left|\underline{s}_{\mathrm{mono}}\right| = P_{\mathrm{Source}}$, centred at the origin. **(d)** For the polychromatic laser, Subfigure **(c)**, the magnitude $\left|s_{\mathrm{poly}}\right|$ decreases with increasing $\Delta n_{\mathrm{e,S}}$, and $\left|s_{\mathrm{poly}}\right|$ describes a spiral. **(f)** For the SiNOH laser described in Figure 3.3, the magnitude $\left|\underline{s}_{\mathrm{SiNOH}}\right|$ decreases with increasing $\Delta n_{\mathrm{e,S}}$, as shown in Subfigure **(f)**, but the decrease is smaller than for the case of $\left|\underline{s}_{\mathrm{poly}}\right|$. In real experiments, non-ideal MMI and GC could lead to an elliptical deformation of the otherwise circular or spiral-shaped locus of the corresponding Clarke field $\underline{s}$ in the complex plane. This can be compensated by transforming the ellipse back into a circle with a unity radius [77], [78].

Note that we have assumed a lossless sensor circuit to simplify our analysis. In case of a lossy device, the power P_{Source} in Equation (6.4) has to be accordingly reduced, but this does not have any consequences for the subsequent considerations. In the monochromatic case, the phase shift between the sensing and reference arms can be determined from the total phase $\Delta\phi$ of the complex Clarke field according to Equation (5.4),

$$\begin{aligned}\Delta\phi &= \Delta\phi_{\mathrm{S}} + \pi/2 + \left(\phi_{\mathrm{S}} - \phi_{\mathrm{R}}\right) \\ &= -\frac{\omega}{c}\left[\Delta n_{\mathrm{e,S}} + \left(n_{\mathrm{e,S}} - n_{\mathrm{e,R}}\right)\right]L + \pi/2 .\end{aligned} \tag{6.5}$$

The phase $\Delta\phi$ hence changes with $\Delta n_{\mathrm{e,S}}$. For a sufficiently slow continuous variation in the phase shift during a binding experiment, $\Delta\phi$ can be extracted from the measured data by unwrapping the Clarke phase $\arg\left(\underline{s}_{\mathrm{mono}}\right)$,

$$\Delta\phi = \mathrm{unwrap}\left(\arg\left(\underline{s}_{\mathrm{mono}}\right)\right) \tag{6.6}$$

For polychromatic light sources, we find that a relationship similar to Equation (6.6) can be adopted to extract the phase shift $\Delta\phi$ from the associated Clarke field $\underline{s}_{\mathrm{poly}}$, provided that the maximum frequency span of the source is smaller than the free spectral range of the generally unbalanced MZI, see Appendix C.2.2 for details,

$$\left|\omega_m - \omega_0\right| \ll \frac{c}{\Delta n_{\mathrm{e,g}} L} \quad \forall\, m, \quad \Delta n_{\mathrm{e,g}} = \Delta n_{\mathrm{e,g,S}} + \left(n_{\mathrm{e,g,S}} - n_{\mathrm{e,g,R}}\right) \tag{6.7}$$

where the centre frequency ω_0 is given by the average of all emission frequencies ω_m, and $\omega_0 = \sum_{m=1}^{M} \omega_m \big/ M$.

The sensor sensitivity is defined by the magnitude of the derivative of the complex Clarke field $\underline{s}$ with respect to the phase shift $\Delta\phi$:

$$S_{\mathrm{Clarke}} = \left|\frac{\mathrm{d}\,\underline{s}}{\mathrm{d}\,\Delta\phi}\right| = \left|\underline{s}\right|, \qquad \underline{s} \in \left\{\underline{s}_{\mathrm{mono}}, \underline{s}_{\mathrm{poly}}\right\} \tag{6.8}$$

For an ideal MZI operated by a monochromatic laser, the sensitivity remains constant for all phase shifts $\Delta\phi$, $S_{\mathrm{Clarke}} = \left|\mathrm{d}\,\underline{s}_{\mathrm{mono}} / \mathrm{d}\,\Delta\phi\right| = \left|\hat{\underline{E}}\right|^2$, and $\underline{s}_{\mathrm{mono}}$ describes a circle with radius $\left|\underline{s}_{\mathrm{mono}}\right| = \left|\hat{\underline{E}}\right|^2 = P_{\mathrm{source}}$ in the complex $\underline{s}$-plane when changing $\Delta n_{\mathrm{e,S}}$ and $\Delta\phi$, as shown in Figure 6.4(a) and Figure 6.4(b), respectively. In contrast to this, real devices are subject to fabrication imperfections and temperature fluctuations, leading to deviations of the relative shifts at the three optical output ports of the 3 × 3 MMI from the ideal value of $2\pi/3$. In addition, the GC efficiencies of the three output ports might differ from each other. These effects lead to an elliptical deformation of the locus of $\underline{s}$ in the complex plane and to a shift of the centre away from the origin $\underline{s} = 0$ [77]. This error is generally corrected by fitting an ellipse to measured data and by transforming this ellipse back to a circle with a unity radius centred at the origin [77], [78]. In the following analysis, we assume that this correction has been performed, and we thus consider the case of an ideal sensor circuit.

While the amplitude of the Clarke field $\left|\underline{s}_{\mathrm{mono}}\right|$ for a monochromatic laser line remains constant with increasing $\Delta n_{\mathrm{e,S}}$, the amplitude of the Clarke field $\left|\underline{s}_{\mathrm{poly}}\right|$ for polychromatic lines may depend on $\Delta n_{\mathrm{e,S}} \approx \Delta n_{\mathrm{e,g,S}}$, see Appendix C.2.2, Equation (C.9). For simplicity, we assume a light source with $M \gg 1$ equidistant laser lines within a maximum spectral range $\Delta\omega_{\max}$, all exhibiting equal field amplitudes $\hat{\underline{E}}_m = \hat{\underline{E}}$, as shown in Figure 6.4(c). In this case, an approximation is possible; please refer to Appendix C.2.2, Equation (C.20),

$$\begin{aligned}\left|\underline{s}_{\text{poly}}\right| = 2\left|\underline{E}_{\text{S}}\underline{E}_{\text{R}}^{*}\right| = \left|\hat{\underline{E}}\right|^{2} M \frac{\sin\left(\dfrac{\Delta n_{\text{e,g}}L}{2c}\Delta\omega_{\max}\right)}{\dfrac{\Delta n_{\text{e,g}}L}{2c}\Delta\omega_{\max}} \\ = P_{\text{source}} \frac{\sin\left(\dfrac{\Delta n_{\text{e,g}}L}{2c}\Delta\omega_{\max}\right)}{\dfrac{\Delta n_{\text{e,g}}L}{2c}\Delta\omega_{\max}}.\end{aligned} \tag{6.9}$$

Equation (6.9) indicates that the magnitude $\left|\underline{s}_{\text{poly}}\right|$ and hence the sensitivity $S_{\text{Clarke}} = \left|\underline{s}_{\text{poly}}\right|$ decrease with increasing $\Delta n_{\text{e,g}}$, especially for large sensor arm lengths L. Figure 6.4(d) shows the Clarke field $\underline{s}_{\text{poly}}$ in the complex $\underline{s}$-plane for $M = 25$ monochromatic equidistant laser lines centred at 600 nm, which are separated by an $\text{FSR} = 0.66\,\text{nm}$ (540 GHz) and exhibit equal powers, see Figure 6.4(c). The geometrical length of the MZI arms amounts to $L = 1.8$ mm, and the effective group refractive index $\Delta n_{\text{e,g,S}}$ varies between 0 and $5\times10^{-3}\,\text{RIU}$, leading to a phase shift $\Delta\phi$ between 0 and 100 rad.

We also perform a sensitivity analysis using the specific spectral characteristics measured for our SiNOH lasers. For these devices, we expect a lasing spectrum with several monochromatic lines exhibiting different powers within a maximal spectral range of $\Delta\omega_{\max} = 2\pi\times10\,\text{THz}$ $(\Delta\lambda = 15\,\text{nm})$ [54] (Section 5.4.2). As an example, Figure 6.3(c) shows the spectrum of three dominant lines in the spectral range of $\Delta\lambda \approx 10\,\text{nm}$, which is approximated by three monochromatic lines in Figure 6.4(e). The electric fields are calculated by using Equation (C.8) and Equation (C.9) in Appendix C.2.2. Equation (C.3) in Appendix C.2.1 and Equation (C.10) in Appendix C.2.2 can then be used to calculate the corresponding complex Clarke field $\underline{s}_{\text{SiNOH}}$. Compared to $\left|\underline{s}_{\text{poly}}\right|$, Figure 6.4(d), the magnitude $\left|\underline{s}_{\text{SiNOH}}\right|$ of the Clarke field decreases less with increasing $\Delta n_{\text{e},g}$, as shown in Figure 6.4(f), and the same is true for the sensitivity.

In the experiment described in the next section, we adopt an MZI with a sensor arm length of $L = 1.8\,\mathrm{mm}$. For a worst-case estimate of the sensitivity degradation, we assume a polychromatic source as in Figure 6.4(c) and Equation (6.9) with equidistant spectral lines spread over a spectral range of 15 nm. This leads to a minimum amplitude of the Clarke field $\left|\underline{s}_{\mathrm{poly}}\right| = 0.85\left|\underline{s}_{\mathrm{mono}}\right|$, i.e., a maximum degradation of the sensitivity of 15%. We hence conclude that for mm-scale sensor lengths, the polychromatic emission of SiNOH lasers should not lead to a notable degradation of the sensor performance.

6.2.5 Experimental sensor-system demonstration

To demonstrate the viability of sensor systems based on SiNOH light sources, we perform a proof-of-concept experiment, see Figure 6.5 for the associated setup. Pump light generated by a frequency-doubled Nd:YLF pulsed laser (CL523, CrystaLaser) with an emission wavelength of 523 nm, a pulse duration of 20 ns, and a repetition rate of 20 Hz is focused on the SiNOH laser by a lens L_1. The pulse energy is varied by a half-wave ($\lambda/2$) and a subsequent polarizer P. The SiNOH laser is coupled to an on-chip WG that guides the light to the MZI-based interferometric sensor, which contains a 3 × 3 MMI at the output, see Figure 6.2(a). At the output of the MMI, the light is radiated to the top by an array of GCs. A long-pass filter F suppresses any stray light from the pump laser, and a subsequent lens L_2 focuses the light on a CCD camera (Stingray, Allied Vision) with a 3-fold magnification. Images are continuously recorded at an exposure time of $T = 2$ s. The intensity radiated by each GC is detected by summing the grey-scale values of a 30 × 40-pixel area around the corresponding intensity maximum of the camera. In the sensing experiment, the liquid analyte solution is pumped by a syringe through the fluidic chamber, which is formed by the chip surface and the PMMA lid with a PDMS seal in between. To attain a constant volumetric flow rate, the syringe is emptied using a stepper motor. In the subsequent sensing experiments, the SiNOH laser is driven with a pump pulse energy of $W = 500\,\mathrm{nJ}$. The sensor arm has a length of $L = 1.8\,\mathrm{mm}$.

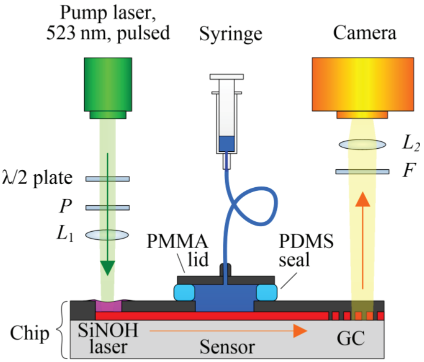

Figure 6.5: Schematic of the experimental setup. The SiNOH laser is pumped with a free-space beam from a pulsed laser, which is focused by lens L_1. The pulse energy is varied by rotating a half-wave ($\lambda/2$) plate with respect to a fixed linear polarizer P. The SiNOH laser is coupled to an on-chip WG (red) that guides the light to the interferometric sensor, please refer to Figure 6.2(a) for a top view of the sensor chip. At the sensor output, light is radiated to an approximately surface-normal direction of the chip by a GC array. A long-pass filter F is used to suppress any stray light from the pump laser. A subsequent lens L_2 focuses the light on a CCD camera. The liquid analyte is pumped by a syringe through the fluidic chamber that is formed by the chip surface and the PMMA lid with a PDMS seal in between. The volumetric flow rate is $0.6\,\mathrm{mL/s}$.

For the proof-of-concept demonstration, we detected the adsorption of fibrinogen onto the surface of the Si_3N_4 WG. This rather simple binding experiment allows us to investigate the performance of the sensor system without any impairment caused by complex media or complicated binding mechanisms. For our experiment, we prepared mixtures of four different concentrations (17 nM, 52 nM, 87 nM, and 121 nM) of fibrinogen in phosphate-buffered saline solution (PBS). We then pumped these solutions sequentially through the fluidic chamber at a volumetric flow rate of $0.6\,\mathrm{mL/s}$, starting with the lowest concentration of 17 nM and ending with the highest concentration of 121 nM. Figure 6.6(a) shows the measured binding curve (green line), i.e., the detected phase shift $\Delta\phi$ as a function of time. The white areas mark the periods during which the different fibrinogen solutions were pumped through the chamber. At the beginning of the experiment and after

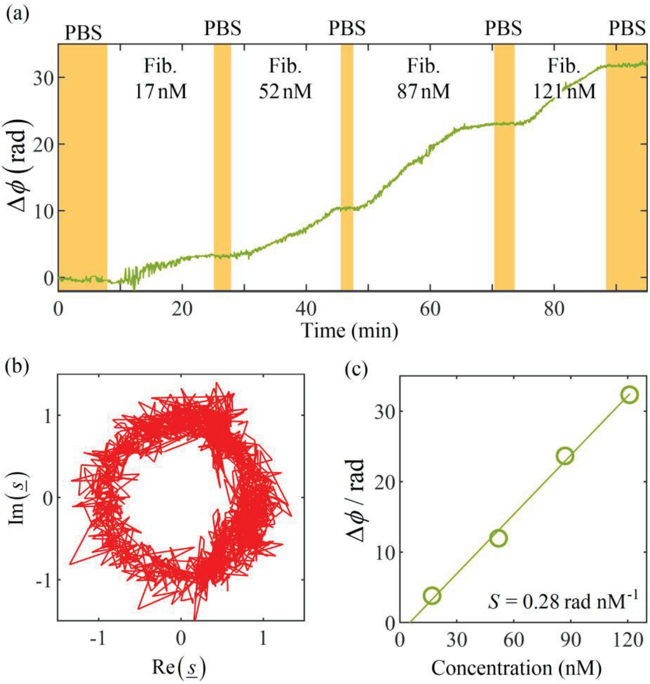

Figure 6.6: Demonstration of a sensor with SiNOH lasers as light sources, used for detection of fibrinogen dissolved in a phosphate-buffered saline (PBS) solution. **(a)** Binding curve, indicating the measured phase shift $\underline{s}$ as a function of time. During the time intervals marked in white, PBS solutions with fibrinogen concentrations of 17 nM, 52 nM, 87 nM, and 121 nM are injected into the fluidic chamber. After each injection of a certain solution, pure PBS is used to flush the chamber during the time intervals indicated in yellow. For each concentration, the phase converges to a constant value when binding equilibrium is reached. **(b)** Locus-corrected complex Clarke field $\underline{s}$ for the various detection times in the complex $\underline{s}$-plane. More details of the locus correction are provided in Appendix C.3. **(c)** Phase shift $\Delta\phi$ vs. fibrinogen concentration: The phase shift for each concentration is calculated from the average phase measured during the subsequent PBS flushing period. As a reference $\Delta\phi = 0$ for the phase shift, we use the average phase measured during an initial PBS flushing period (marked in yellow) in the first eight minutes of the experiment. The phase shift $\Delta\phi$ increases linearly with the concentration, leading to a sensitivity of $S = 0.28\,\mathrm{rad/nM}$.

each fibrinogen injection, the chamber was flushed with PBS for several minutes, as indicated by the yellow areas in Figure 6.6(a). PBS flushing removed any unbound molecules from the WG surface.

Before calculating the Clarke fields, the raw power levels emitted from the different GCs were extracted from the recorded images by summing the grey-scale values of the respective 30 × 40 pixel areas as described above. To extract the phase shift $\Delta\phi$, we first removed the background offset of the three signals such that the resulting power levels $\tilde{P}_\mathrm{A}$, $\tilde{P}_\mathrm{B}$ and $\tilde{P}_\mathrm{C}$ were zero for destructive interference at ports A, B, and C, respectively. In the next step, the three port powers are normalized to the total power $\tilde{P} = \tilde{P}_\mathrm{A} + \tilde{P}_\mathrm{B} + \tilde{P}_\mathrm{C}$ measured at the respective time instant,

$$P_\mathrm{X} = \frac{\tilde{P}_\mathrm{X}}{\tilde{P}_\mathrm{A} + \tilde{P}_\mathrm{B} + \tilde{P}_\mathrm{C}}, \quad X \in \{A, B, C\} \tag{6.10}$$

The normalized dimensionless power quantities P_A, P_B, and P_C are then used to calculate the Clarke field according to Equation (6.3). Note that the power normalization according to Equation (6.10) removes the impact of laser-power fluctuations, which affect the numerator and the denominator in the same way. The phase shift, which is calculated from the normalized power quantities according to Equation (6.3), should thus be robust with respect to laser intensity noise. The Clarke field obtained from Equation (6.3) is then corrected by fitting a centred ellipse, see Section 3C, which is then transformed to a unity-radius circle [77], [78]. Figure 6.6(b) shows the locus-corrected Clarke field $\underline{s}$ for the various detection times in the complex $\underline{s}$-plane. To extract the binding curve, we calculate the phase shift $\Delta\phi$ by unwrapping the time-dependent phase of the Clarke field $\underline{s}$ in analogy to Equation (6.6). Figure 6.6(a) shows the phase shifts measured over the duration of the experiment. Note that for the MZI-based sensors used in this experiment, the MMI couplers were already optimized for uniform power splitting ratios and phase shifts, such that the impact of the locus correction is rather small, see Appendix C.3 for a more detailed discussion. It should also be noted that the temporal evolution of the binding curve shown in Figure 6.6(a) is dictated by the binding dynamics of the fibrinogen to the WG surface, in particular by the mobility of the target molecules in the analyte solution and by the binding affinity to the sensor surface, while camera-based acquisition system would have allowed to track much faster changes in the phase shift.

We further investigated the sensitivity of our sensor. As a reference, we use the average phase shift measured during the first eight minutes of the experiment, in which the sensor is exposed to the PBS only. This reference phase is subtracted from all subsequently measured phase values. At each concentration, the flow of fibrinogen solution is maintained until equilibrium is reached, indicated by a steady value of the phase shift. Our observation of an equilibrium is in line with previous experiments of the concentration-dependent binding of fibrinogen onto silicon-nitride surfaces [127]. Note that the fibrinogen remains on the WG surface, even when flushing the chamber with the PBS. This observation cannot be explained by the rather simple binding model according to Langmuir [128] but is in line with the experimental observations in Ref. [127]. We attribute this phenomenon to the high adsorption affinity of fibrinogen to the surface of the Si_3N_4 WG. Figure **6.6**(c) shows the average phase shifts measured during PBS flushing after each fibrinogen injection interval as a function of the fibrinogen concentration. From the linear increase of the phase shift $\Delta\phi$ with increasing concentration ΔC, we calculate a sensitivity of $S = 0.28\,\mathrm{rad/nM}$. For the 1.8-mm-long sensor arm, this leads to a length-related sensitivity of $S/L = \Delta\phi/(L\,\Delta C) = 0.16\,\mathrm{rad}/(\mathrm{mm\,nM})$. Based on the standard deviation $\sigma_{\Delta\phi} = 0.2\,\mathrm{rad}$ of the binding curve when the sensor is exposed to the PBS only, Appendix C.3, we calculate the limit of detection to be $\mathrm{LoD} = 3\sigma_{\Delta\phi}/S = 2.14\,\mathrm{nM}$.

To our knowledge, our experiments represent the first demonstration of a WG-based sensor circuit on the Si_3N_4 platform driven by an on-chip laser source emitting at visible wavelengths. Previously demonstrated Si_3N_4-based sensor circuits with co-integrated light sources were either limited to mid-infrared wavelengths emitted by epitaxially grown quantum cascade lasers [123] or relied on external light sources such as vertical-cavity surface-emitting lasers (VCSELs) that emit at near-infrared wavelengths and that are flip-chip mounted to the underlying Si_3N_4 substrate [35]. In comparison to these approaches, the SiNOH concept stands out due to its amenability to highly scalable mass fabrication by wafer-level printing of organic dye materials onto passive Si_3N_4 photonic integrated circuits.

6.3 Discussion

We demonstrate an integrated sensor system with on-chip SiNOH lasers on the Si_3N_4 platform. The sensor is operated by optically pumping the SiNOH lasers from the top with relaxed alignment precision and by detecting the sensor signal with a CCD camera. The whole chip can be fabricated in a single lithography step, and the gain medium of the SiNOH laser can be easily deposited by wafer-level dispensing or printing processes. In a proof-of-concept demonstration, we used this sensor system to detect different concentrations of fibrinogen dissolved in a phosphate-buffered saline solution (PBS). We determined a sensor-length-related sensitivity of $S = 0.16\,\mathrm{rad}/(\mathrm{nM\,mm})$.

To our knowledge, this is the first demonstration of an integrated optical circuit driven by a co-integrated low-cost organic light source. We expect that the versatility of the device concept, the simple operating principle, and the compatibility with cost-efficient mass fabrication will make integrated sensors containing SiNOH lasers a highly attraequctive option for applications in biophotonics and point-of-care diagnostics.

Sensitivity limitations and improvements

In the fibrinogen sensing experiment presented in this work, we estimate a detection limit of $\mathrm{LoD} = 2.14\,\mathrm{nM}$. Note, however, that this concentration-related detection limit is largely dictated by the specific binding experiment, in particular by the molecular mass of the analyte and by its binding affinity to the WG surface, such that a comparison to other sensing experiments is difficult. To benchmark the sensitivity of our sensor system with respect to the state of the art, we also estimate the limit of detection for homogeneous sensing $\mathrm{LoD}_{\mathrm{hom}}$, i.e., for detection of a global refractive-index change in the liquid cladding that homogenously covers the sensor WG. To this end, we first calculate the length-related sensitivity of our Si_3N_4 WG for such homogeneous sensing experiments, which amounts to $S_{\mathrm{hom}}/L = 1450\,\mathrm{rad}/(\mathrm{RIU\;mm})$. While this value compares well to the value of $1620\,\mathrm{rad}/(\mathrm{RIU\;mm})$ reported in other sensing experiments with Si_3N_4 waveguides [129], further improvements can be achieved by using advanced designs of the sensor WG, exploiting, e.g., slot structures or subwavelength gratings (SWG) [37], [130] (Chapter 4). Using again the standard deviation of the phase measurement, $\sigma_{\Delta\phi} = 0.2\,\mathrm{rad}$, we determine a limit of detection of $\mathrm{LoD}_{\mathrm{hom}} = 2.29\times10^{-4}\,\mathrm{RIU}$, which may now be compared to that of other demonstrations of WG-based sensors. For meaningful benchmarking, we focus our comparison on experiments that also rely on Si_3N_4-based MZI sensors operated at visible wavelengths up to approximately 850 nm. In this wavelength range, there are several reports on actual sensing experiments [127], [129], [131], [132], among which Ref. [132] reports a detection limit of $\mathrm{LoD}_{\mathrm{hom}} = 7\times10^{-6}\,\mathrm{RIU}$. This is 30-fold better than our result. Note, however, that this detection limit was achieved with a sensing WG of length $L = 15$ mm, which is more than eight-fold larger than the 1.8-mm length applied in our example. In addition, the experiment reported in Ref. [132] relied on a benchtop-type helium-neon (HeNe) laser with a typical output power in the milliwatt range. This is more than four orders of magnitude higher than the average power of 40 nW estimated for our SiNOH lasers based on the 100-mW on-chip pulse peak power and a duty cycle of 4×10^{-7}. There is hence much room for further improvement of the limit of detection, e.g., by increasing the pulse repetition frequency and hence the output power of the SiNOH laser, see subsequent section. In addition, further improvements of the sensor are possible, by mitigating, e.g., the impact of thermal drift by using reference and sensor WG that are perfectly matched with respect to their thermal characteristics. Note that the propagation losses of our current Si_3N_4 WG are still comparatively high, ranging from $5\,\mathrm{dB/cm}$ to $7\,\mathrm{dB/cm}$, depending on the WG width. Low propagation losses ranging from

$0.5\,\mathrm{dB/cm}$ to $2.5\,\mathrm{dB/cm}$, as reported for comparable WG [9], could lead to further improvements in the performance of both the laser and the sensor. Based on these estimations, we believe that the performance of visible-wavelength SiNOH-driven MZI sensors could be enhanced to match that of benchtop-type laboratory systems.

Towards compact portable sensor systems for point-of-care applications
An essential part of the sensor system that requires further elaboration for technically viable point-of-care operation is the pump source. Our current demonstration relies on a bulky benchtop-type Nd:YLF laser, emitting pulses with an energy of 500 nJ at a rather low repetition rate of 20 Hz. The pulse length amounts to 20 ns, leading to a low duty cycle of 4×10^{-7} and an accordingly low average output power, which requires a long integration interval of 2 s for the readout camera. In a point-of-care system, this bulky solid-state laser may be replaced by a compact high-power laser diode, emitting at 520 nm with a CW output power of, e.g., 900 mW [133], [134]. Under pulsed operation, these diodes could provide pump pulse energies typically ranging from 120 nJ to 130 nJ, which is still above the lasing threshold from 30 nJ to 40 nJ of the current devices. Moreover, the repetition rates can be greatly increased to, e.g., to 1 kHz, such that the system could be operated at approximately 10 times higher optical powers and hence greatly improved signal-to-noise power ratios (SNRs). Note that a repetition rate of 1 kHz is still low enough to allow for relaxation of excited triplet-state dye molecules with typical lifetimes on the order of tens of microseconds [59], [135] between subsequent pulses. It should also be noted that the design of the laser cavity and the pumping scheme could be further optimized, thereby offering even higher output powers and lower thresholds, which might eventually be compatible with pump-power levels offered by light-emitting diodes (LEDs). On the receiver side, signal readout and data analysis may rely on compact highly sensitive cameras for visible wavelengths and on compact powerful processors, both of which are readily available on the market.

Regarding the degradation of the laser dye, the current lifetime of at least two hours permits extended measurements even at high power levels. In the case of slow binding processes, the sensor does not have to be continuously operated as was done in our current experiment but may be periodically turned on and off to further increase the lifetime. This operation mode also leads to reduced power consumption and might allow for battery operation of the entire sensor system. Moreover, the lifetime of organic laser dyes may be greatly improved by hermetic encapsulation layers [59], possibly in combination with oxygen quenchers [136].

Another important aspect is the sample preparation and functionalization of the WG surface to enable specific binding of target molecules. Ideally, the system could be operated without any additional sample pretreatment. Massively parallel detection through an array of differently functionalized devices in combination with advanced data analysis might help to improve the specificity of the sensor. Detection of target molecules without pretreatment has, e.g., been demonstrated with saliva [137] and urine [138]. For complex analyte solutions such as blood, where pretreatment is hitherto unavoidable, compact equipment for point-of-care applications such as portable centrifuges has been demonstrated [139] and commercialized [140] in recent years.

Summary

We demonstrate an integrated sensor system with on-chip SiNOH lasers on the Si_3N_4 platform. The sensor is operated by optically pumping the SiNOH lasers from the top with relaxed alignment precision and by detecting the sensor signal with a CCD camera. The whole chip can be fabricated in a single lithography step, and the gain medium of the SiNOH laser can be easily deposited by wafer-level dispensing or printing processes. In a proof-of-concept demonstration, we used this sensor system to detect different concentrations of fibrinogen dissolved in a phosphate-buffered saline solution (PBS). We determined a sensor-length-related sensitivity of $S = 0.16\,\mathrm{rad}/(\mathrm{nM\ mm})$.

To our knowledge, this is the first demonstration of an integrated optical circuit driven by a co-integrated low-cost organic light source. We expect that the versatility of the device concept, the simple operating principle, and the compatibility with cost-efficient mass fabrication will make integrated sensors containing SiNOH lasers a highly attractive option for applications in biophotonics and point-of-care diagnostics.

6.4 Materials and Methods

Fabrication of the Si_3N_4 waveguides and SiNOH lasers

The Si_3N_4 WG of both the SiNOH laser and sensor circuit are jointly fabricated in a single lithographic step. The WG cores are structured in a 200-nm-thick Si_3N_4 layer on top of a 2-µm-thick silicon dioxide layer mechanically supported by a silicon wafer. A negative-tone resist structured via electron-beam lithography and spray development is used as a mask for dry etching of the Si_3N_4 layer with a mixture of SF_6 and CHF_3. An oxygen plasma etching step is applied to remove the etch mask. After structuring the WG cores, a negative-tone photoresist mrX (mr-X2-P2-XP, Micro Resist Technology, Berlin, Germany) is spin coated and exposed by e-beam lithography to act as a cladding that covers the optical WG except for the laser cavity and the arms of the MZI. To form the light-emitting cladding, laser dye PM597 (Pyrromethene 597, Radiant Dyes Laser & Accessories GmbH, Wermelskirchen, Germany) is dissolved in PMMA at a concentration of $25 \mu\mathrm{mol/g}$ and then deposited onto the laser WG (Figure 6.2(a), the magenta-coloured region). In a final step, the reference WG of the MZI is passivated by covering it with glue (MyPolymer MY-136, Ness Ziona, Israel), which is approximately index-matched to water, see Figure 6.2(c). Phosphate-buffered saline solution (PBS) is used as a solvent for the analyte in the sensing arm.

[end of paper [J2]]

7 Summary and outlook

7.1 Summary

Waveguide based sensor chips are expected to become an essential part of modern medical diagnostics. The operation of the sensor chips in compact and portable readout devices in combination with cost-effective mass production will be essential to application of such devices in powerful point-of-care diagnostic system for patients. In this work, a new approach for waveguide-based biosensors is presented that combines a robust geometrically optimized sensor for label-free detection of molecules with an optically pumped, low-cost on-chip laser source. The concept investigated by numerical modeling, and the viability of the underlying concept is verified by proof-of concept experiments. The main results of the work include the following aspects:

Definition of a universal sensitivity metric and design of a robust sensor: A metric for surface sensitivity has been defined that allows a comprehensive comparison of different waveguide types, operation wavelengths and integration platforms. For the silicon nitride platform and visible light, and for the silicon platform and near infrared light, the metric was calculated and discussed for a variety of waveguide types and geometries. General findings were discussed and a guideline for designing a waveguide sensor for different approaches was given. Based on these findings, a sensor waveguide was designed that meets the criteria for robust fabrication, high sensitivity, and compatibility with a broadband laser source.

First demonstration of Si_3N_4-organic hybrid (SiNOH) lasers: A new class of on-chip laser sources has been introduced that can be efficiently integrated on the silicon nitride platform by low-cost mass production. These S_3N_4-organic hybrid (SiNOH) lasers are optically pumped from the top without stringent alignment requirements. Lasing has been demonstrated for various resonator geometries based on ring structures and distributed feedback structures at approximately 600 nm wavelengths. All SiNOH lasers showed threshold fluences of $40\mu\mathrm{J}/\mathrm{cm}^2 \ldots 70\mu\mathrm{J}/\mathrm{cm}^2$, with vast room for further improvement.

First demonstration of a bio sensorchip with integrated SiNOH laser: The first silicon nitride photonic integrated circuit is demonstrated that is driven by an on-chip laser source emitting in the visible wavelength range. A spiral SiNOH laser was combined with a Mach-Zehnder interferometer on the same chip. The SiNOH laser was pumped with a large laser spot without the need of a precise alignment, while the sensor signal was detected with a CCD camera. For analyte delivery, a fluidic chamber was developed that covers the chip, but provides access to the SiNOH lasers and the signal output ports. The functionality of the sensor concept was demonstrated by detecting various concentrations of fibrinogen.

7.2 Outlook

The experiments presented in this work are mainly proof-of-concept demonstrations, and further investigations are needed to advance the concepts to a level that allows for application in real point-of-care systems. This also includes steps towards medically relevant applications and studies, which are indispensable to launch real-life applications. Furthermore, the different studies can be adapted to explore new areas of applications, e.g. in the field of gas sensing or the combination of the SiNOH laser with other photonic devices.

Sensor: For larger laser powers, the sensor sensitivity can be further improved by increasing the sensor length. In addition, depending on the fabrication technology, the waveguide geometry can be optimized for higher sensitivity, e.g., by exploiting slot waveguides or subwavelength grating structures. A first approach for surface functionalization is presented in this work. For use in complex media, e.g., blood, saliva, serum or urine, the functionalization needs to be further modified to bind target molecules on the one hand, and to prevent the binding of other molecules in the analyte solution on the other hand.

SiNOH laser: This work focuses mainly on the resonator geometry of the SiNOH lasers. Further work could include the variation of the gain medium, e.g., to shift the emission wavelengths or to make the gain medium more heat resistant. Reduced propagation loss due to improved patterning techniques for underlying waveguides could increase laser performance and enable pumping of the lasers with incoherent light sources, such as light-emitting diodes (LED). The SiNOH-laser concept can also be adapted for longer laser lifetimes.

Integrated sensor system: Further investigations should aim at expanding the system for multiplexed sensing in complex media, e.g., blood, saliva, serum or urine. To this end, local functionalization of different sensors on the same chip should be established to enable parallel detection of different target molecules. Furthermore, the application of the sensor system is not limited to the detection of biomolecules. By replacing the surface functionalization with a gas sensitive cover layer, gas mixtures can be analyzed in a similar way. A holistic mathematical model for waveguide-based sensor systems has been developed in parallel to the activities related to this thesis [141].

Appendices

A Silicon nitride waveguide fabrication

A.1 Etch mask

Resist deposition

- Adhesion promoter: Ti Prime (Microchemicals GmbH)
  Water removal: Hotplate, 180°C, 5 min
  Deposition: Spin coater, 1500 rpm/s, 3000 rpm, 60 s, open lid
  Binding: Hotplate, 120°C, 2 min
- Electron beam resist: AR-N 7520.12 (340 nm, Allresist GmbH)
  Deposition: Spin coater, 1000 rpm/s, 1500 rpm, 60 s, closed lid
  Solvent removal: Hotplate, 85°C, 1 min
- Conductive top layer: Espacer 300HX02 (Showa Denko K. K.)
  Deposition: Spin coater, 1500 rpm/s, 1500 rpm, 60 s, open lid

Electron beam exposure

- Dose: 1600 μC/cm^2
- Proximity effect correction
- Beam step size: 5 nm

Development

- Remove Espacer: Spray developer, water, 120 s
- Development: Spray developer, AR 300-47 (Allresist GmbH), 50 s
- Stop development: Spray developer, water, 60 s

A.2 Dry etching

Conditioning

- 20 min with etch recipe

Etching

- Reactive ion etching
- Temperature: 20°C, Pressure: 5 mT

- RF: 50 W, ICP: 1500 W
- Gases: CHF3 (40 sccm), SF6 (7 sccm)
- Etch time: 50 s (260 nm/min)

Mask removal

- Oxygen plasma, 100 W, 10 min

A.3 Cladding layer

Resist deposition

- Electron beam resist: mr-X2-P2-XP: (2 µm, micro resist technology GmbH)
  Deposition: Spin coater, 1000 rpm/s, 1000 rpm, 60 s, open lid
  Solvent removal: Hotplate, 90°C, 5 min

Electron beam exposure

- Dose: 12 µC/cm2
- Beam step size: 100 nm

Development

- Development: beaker, PGMEA, 3min
- Stop development: beaker, isopropanol, 3min

UV flood exposure

- 86%, 5 min

B Surface functionalization

Silanization

- O2-plasma: 30 min, 100 W
- Transport in water
- Nitrogen blow
- Water removal: hotplate, 180°C, 5 min
- Incubation: 90 µl APDEMS, 2 ml Ethanol, 120 µl Ethanol, 30 min
- Spincoating: 600 rpm, 500 rpm/s, 60 s
- Hotplate: 180°C, 2 min
- Washing: ethanol, 2 min
- Hotplate: 180°C, 2 min

Cross-linker

- Incubation: 25 µl glutaraldehyde in 1975 µl PBS, 2h
- 3 × Washing: 1 ml PBS, 2 min

Biotin hydrazide

- Incubation: 0.6 mg biotin hydrazide, 200 µl DMSO, 3800µl PBS, 24 h
- 3 × Washing: 1 mL PBS, 2 min

C Details on Si_3N_4-organic hybrid lasers and on Mach-Zehnder interferometer-based sensors

C.1 Further details on the SiNOH laser

[This section was published as Supplementary information Note 1 of [J2]]

The concept of our SiNOH lasers has been discussed in Chapter **5**. In this section, we provide further details of the SiNOH spiral laser with open spiral, as reported in Section 6.2.3, focusing on its operating principle, its characterization, and the interpretation of the results.

In Section 6.2.3, we state that broadband optical feedback is provided from the inner end of the spiral by reflection from the open waveguide (WG) end in the center, possibly in combination with roughness-induced backscattering, whereas coupling of light between neighboring windings of the WG spiral does not play a significant role. This notion is based on numerical investigations of the device. Since a simulation of the full spiral would require prohibitive computational resources, we simplified the structure and checked the coupling between two straight WG with the same dimensions (width $w = 500$ nm, height $h = 200$ nm) and spacing (1.5 µm) as the spiral WG. We determined the propagation constant β_s of the symmetric and the antisymmetric modes β_a and calculated the coupling length by $\Lambda = \pi / \left|\beta_\mathrm{s} - \beta_\mathrm{a}\right|$. In this definition, Λ denotes the propagation length after which the power is completely transferred from one WG to the other. For the fundamental quasi-TE and the fundamental quasi-TM modes, Λ is more than 7 m, and we can therefore exclude that coupling of fundamental modes between neighboring windings of the spiral plays a significant role. We repeated the simulation for the next higher-order TE and TM modes, leading to $\Lambda = 20$ mm for quasi-TE and $\Lambda = 5$ mm for quasi-TM polarization. This is comparable to the length of the spiral, which amounts to 18 mm, such that coupling between higher-order modes might occur. Still, we expect that there will be no significant impact on the lasing performance, since the multimode Si_3N_4 WG in the spiral is tapered down to a single-mode WG towards the ring resonator at the output. This taper will strip all higher-order modes such that they will not see any relevant feedback at this side of the resonator. In addition, coupling of higher-order modes in the WG towards the center of the spiral would still be in the forward direction and should thus not lead to enhanced feedback. Note that we use an open spiral in our experiments, rather than a coiled-up loop, where coupling of parallel WG could indeed lead to a frequency-selective feedback to the backward direction, see Section 5.4.2.

Based on these results, we expect that optical feedback from the spiral will be predominantly caused by scattering at the rough WG sidewalls, and by reflection from the open inner end of the spiral WG. This feedback will be rather broadband – potentially with some frequency variations due to Anderson localization [142]. In contrast to this, roughness-induced backward scattering in the single-mode ring-resonator is resonantly enhanced by constructive interference of light that scattered back in subsequent round-trips of the ring, thereby building up a counter-propagating resonant mode. This build-up will only end when an equilibrium state is reached, in which the net power loss from the forward-propagation resonator mode to the outside of the resonator and to its backward-propagating counterpart is exactly compensated by the power coupled in from the outside. Due to this resonant enhancement of backscattering, the feedback of the ring is spectrally narrowband and concentrated to the discrete ring resonances. This effect, which has also been reported for other Si_3N_4 ring resonators [143], can be nicely observed by investigating the power emission from GC 1 and GC 2 in Figure 6.3 of Section 6.2.3.

According to this model, a spiral WG without a ring resonator should also be able to lase, but the threshold should increase strongly, and the emission should not be concentrated to discrete resonance frequencies that are defined by the ring in our current device. We investigated this aspect experimentally by measuring the lasing characteristics of a spiral that is not coupled to a ring resonator. Instead, the straight orange-colored WG portion in Figure 6.3(a) of Section 6.2.3 is directly routed to the chip edge, where we would expect broadband Fresnel reflection at the facet with a rather low power reflection factor of a few percent. For this spiral, we found rather high threshold pump energies in the range of 2...5 µJ – much higher than the 30…40 nJ found for the devices in 6.2.3 – along with an unstable spectrum that changes continuously on a time scale of a few seconds. We attribute these variations to thermal drift on the chip, which strongly impacts the emission frequencies associated with Anderson localization. Note that the drastic increase in pump threshold for the device without ring resonator cannot be explained by the reduced feedback alone, but may also result from strong gain competition due to the absence of a frequency-selective feedback. This is in good agreement with previous observations from SiNOH lasers, see Section 5.4.2 and Section 4.2 in Ref. [54].

Regarding the fabrication of SiNOH structures, one important aspect is the potential formation of voids or air bubbles in the organic gain medium. We have explored this aspect in the context of our previous publication, where we investigated cross sections of cleaved SiNOH WG, see, e.g., Figure 6.3(b) of Ref. [54] (Section 5.4.2). In these investigations, we did not find any indication of voids or air bubbles. This is in good agreement with our experience from silicon-organic hybrid (SOH) devices [144], where void formation was never observed, even when cladding slot WG with slot widths of the order of 100 nm [144]. We also measured the propagation loss of the Si_3N_4 WG in the SiNOH cavity, which, for an un-doped PMMA cladding, amounts to approximately 5 dB/cm for the 500 nm-wide multi-mode spiral WG and to around 7 dB/cm found for narrower 300 nm-wide single-mode WG. We attribute these losses to rough WG sidewalls, see Inset 2 of Figure **6.2**(b) of Section 6.2.2, which may arise from discrete writing patterns of the electron-beam lithography system used for defining the WG. This roughness may also be the origin of resonantly enhanced scattering-induced coupling of light between counter propagating modes in the reflector ring.

We also performed investigations of the SiNOH-laser emission characteristics. Specifically, we simultaneously measured the input-output-power characteristics for the two grating couplers GC1 and GC2, see Figure C.2. We found that the power of the "forward" or clockwise propagating mode in the small ring, probed through GC2, was three times as strong as the power of the "backward" or counter-clockwise propagating mode, probed through GC1, while the threshold observed from the two outputs is essentially the same. This

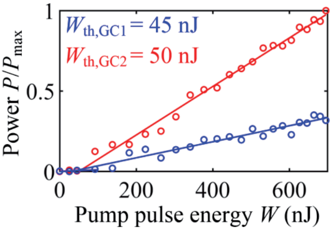

Figure C.1: Laser characteristics extracted from clockwise and counter-clockwise propagating modes in the reflector ring, see Figure 6.3(a) of Section 6.2.3. Normalized laser output powers probed from the counter-clockwise propagating mode through GC 1, blue, and from the clockwise-propagating mode through GC 2, red, both as function of the pump-pulse energy W. We find essentially the same lasing thresholds, thereby confirming the notion that that the clockwise and the counter-clockwise propagating modes in the reflector ring resonator are resonantly coupled to each other.

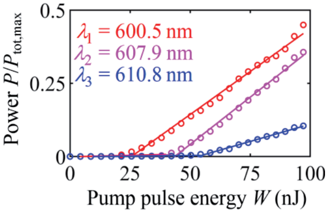

Figure C.2: Lasing characteristics of different spectral modes. Normalized laser output power of the three dominant laser lines shown in Figure 6.3(c) of Subsection 6.2.3 as functions of the pump-pulse energy W. We find lasing thresholds W_{th} of 25 nJ, 43 nJ, and 52 nJ with no indicating of gain competition. This is consistent with the fact that we chose the FSR of the reflector ring slightly larger than the bandwidth of homogeneous line broadening, that was measured in a previous publication.

supports the notion that the emission at GC1 results from resonant coupling of counter-propagating modes in the ring. We also investigated the spectrum taken from GC 2 in more detail and extracted the lasing thresholds from the three separate modes individually, Figure C.1. We find that the modes exhibit distinct thresholds with no indication of gain competition. This is ensured by the fact that we chose the FSR of the reflector ring slightly larger than the bandwidth of homogeneous line broadening, that was measured in Subsection 5.4.2.

C.2 MZI and different laser sources

C.2.1 Monochromatic sources

[This section was published as Supplementary information Note 2 of [J2]]

For the analysis of monochromatic laser sources, we assume excitation of the sensor at an angular frequency ω and a normalized electric field $\underline{E} = \hat{\underline{E}} \exp\left[\mathrm{j}\left(\omega t - \beta z \right) \right]$ having a complex amplitude $\hat{\underline{E}}$ and a propagation constant β in the z-direction. We represent the optical power as the squared magnitude of the electric field, $P_{\text{source}} = \left| \hat{\underline{E}} \right|^2$. The electric field is split by the 2 × 2 MMI into equal portions in the sensing and the reference WG, whereby the field in the reference arm is phase-shifted by $-\pi/2$ with respect to the field in the sensing arm. Reference and sensing arms have equal geometrical arm lengths L. Because the reference arm is optically isolated from the analyte by a thick passivation layer, its refractive index $n_{\text{e,R}}$ is constant during sensing experiments. With the vacuum speed of light c, the field $\underline{E}_{\text{R}}$ at the end of the reference arm and the associated phase shift ϕ_{R} can be written as

$$\begin{aligned} \underline{E}_{\text{R}} &= \frac{\hat{\underline{E}}}{\sqrt{2}} \exp\left[\mathrm{j}\left(\omega t + \phi_{\text{R}} - \pi / 2 \right) \right], \\ \phi_{\text{R}} &= -\beta_{\text{R}} L = -k_0 n_{\text{e,R}} L, \qquad k_0 = \omega / c. \end{aligned} \tag{C.1}$$

In the sensing arm, the effective refractive index $n_{\mathrm{e,S}}$ is changed by $\Delta n_{\mathrm{e,S}}$ when molecules attach to the WG surface. This leads to an additional phase shift of $\Delta\phi_{\mathrm{S}}$ compared to the phase ϕ_{S} without attached molecules,

$$\begin{aligned}
\underline{E}_{\mathrm{S}} &= \frac{\hat{E}}{\sqrt{2}} \exp\left[\mathrm{j}\left(\omega t + \phi_{\mathrm{S}} + \Delta\phi_{\mathrm{S}}\right)\right], \\
\phi_{\mathrm{S}} &= -\beta_{\mathrm{S}} L = -k_0 n_{\mathrm{e,S}} L\,, \\
\Delta\phi_{\mathrm{S}} &= -\Delta\beta_{\mathrm{S}} L = -k_0 \Delta n_{\mathrm{e,S}} L\,.
\end{aligned} \tag{C.2}$$

Combination of the fields by the 3 × 3 MMI leads to a superposition of $\underline{E}_{\mathrm{R}}$ and $\underline{E}_{\mathrm{S}}$, where the field contributions from the sensing arm at the three MMI output ports are phase-shifted by $2\pi/3$ (120°) [73],

$$\begin{aligned}
P_{\mathrm{A}} &= \left(\frac{1}{3}\right)\left|\underline{E}_{\mathrm{R}} + \underline{E}_{\mathrm{S}} \exp\left(+\mathrm{j}\frac{2\pi}{3}\right)\right|^2, \\
P_{\mathrm{B}} &= \left(\frac{1}{3}\right)\left|\underline{E}_{\mathrm{R}} + \underline{E}_{\mathrm{S}}\right|^2, \\
P_{\mathrm{C}} &= \left(\frac{1}{3}\right)\left|\underline{E}_{\mathrm{R}} + \underline{E}_{\mathrm{S}} \exp\left(-\mathrm{j}\frac{2\pi}{3}\right)\right|^2.
\end{aligned} \tag{C.3}$$

The three output powers are detected, analog-to-digital converted, and numerically processed by applying a Clarke transform. For a monochromatic light source, this leads to a complex correlation function (Clarke “field”) $\underline{s}_{\mathrm{mono}}$ [77], [78],

$$\begin{aligned}
\underline{s}_{\mathrm{mono}} &= \underline{s}_{\mathrm{r}} + \mathrm{j}\,\underline{s}_{\mathrm{i}} \\
&= 2\underline{E}_{\mathrm{S}}\underline{E}_{\mathrm{R}}^{*} = \left|\hat{\underline{E}}\right|^2 \mathrm{e}^{\mathrm{j}\left[\Delta\phi_{\mathrm{S}} + \pi/2 + \left(\phi_{\mathrm{S}} - \phi_{\mathrm{R}}\right)\right]} \\
&= 2P_{\mathrm{B}} - \left(P_{\mathrm{C}} + P_{\mathrm{A}}\right) + \mathrm{j}\sqrt{3}\left(P_{\mathrm{C}} - P_{\mathrm{A}}\right), \\
\left|\underline{s}_{\mathrm{mono}}\right| &= \left|\hat{\underline{E}}\right|^2 = P_{\mathrm{source}}.
\end{aligned} \tag{C.4}$$

When changing $n_{\mathrm{e,S}}$, the Clarke field s_{mono} describes a circle with radius $\left|\underline{s}_{\mathrm{mono}}\right| = \left|\hat{\underline{E}}\right|^2$ in the complex plane. The phase shift $\Delta\phi$ changes with $\Delta n_{\mathrm{e,S}}$ and is found by unwrapping the Clarke phase $\arg\left(\underline{s}_{\mathrm{mono}}\right)$,

$$\begin{aligned}\Delta\phi(\omega) &= \Delta\phi_{\mathrm{S}} + \pi/2 + (\phi_{\mathrm{S}} - \phi_{\mathrm{R}}) \\ &= \mathrm{unwrap}\left(\arg\left(\underline{s}_{\mathrm{mono}}\right)\right)\end{aligned} \tag{C.5}$$

For all values $\Delta\phi_{\mathrm{S}}$ and therefore for all index changes $\Delta n_{\mathrm{e,S}}$, the sensitivity S_{Clarke} is constant and corresponds to $|\underline{s}_{\mathrm{mono}}|$,

$$S_{\mathrm{Clarke}} = \left|\frac{\mathrm{d}\,\underline{s}_{\mathrm{mono}}}{\mathrm{d}\Delta\phi_{\mathrm{S}}}\right| = |\underline{s}_{\mathrm{mono}}| = \left|\hat{\underline{E}}\right|^2 \tag{C.6}$$

C.2.2 Polychromatic sources

[This section was published as Supplementary information Note 3 of [J2]]

To better reflect the experimental situation of an MZI-based sensor driven by a SiNOH laser, we also investigate the sensor behavior for a polychromatic source with $m = 1, 2, \ldots, M$ lines at angular frequencies ω_m and real constant amplitudes $\hat{\underline{E}}_m$. Each line is represented by an expression of the form $\underline{E}_m = \hat{\underline{E}}_m \exp[\mathrm{j}(\omega_m t - \beta_m z)]$. The field at the input of MMI$_2$, Figure 5.2(a) of the main manuscript, is then $\underline{E} = \sum_{m=1}^{M} \underline{E}_m$. The total power as measured with a photodetector results from an average over the observation time *T*, which is large compared to the oscillation period of any two lines in the spectrum, $T \gg 2\pi/|\omega_m - \omega_n|$ for $m \neq n$. We again represent the optical power of the source as the sum of the squared electric-field magnitudes of the various components,

$$\begin{aligned}P_{\mathrm{source}} &= \left\langle |E|^2 \right\rangle_T = \left\langle \sum_{m=1,n=1}^{M} \underline{E}_m \underline{E}_n^* \right\rangle_T \\ &= \left\langle \sum_{m=1,n=1}^{M} \hat{\underline{E}}_m \hat{\underline{E}}_n \exp\left[\mathrm{j}(\omega_m - \omega_n)t - \mathrm{j}(\beta_m - \beta_n)z\right] \right\rangle_T \\ &= \sum_{m=1}^{M} \left|\hat{\underline{E}}_m\right|^2\end{aligned} \tag{C.7}$$

In these relations, $\langle\cdot\rangle_T$ indicates a time average over time T. For the analysis of the sensor behavior, we first consider the reference arm. After propagating through the geometrical reference arm length L, the spectral components of the field are phase shifted by $\phi_{\mathrm{R},m}$, and the total field at the end of the reference arm amounts to

$$\begin{aligned}
\underline{E}_{\mathrm{R}} &= \sum_{m=1}^{M} \frac{\hat{\underline{E}}_m}{\sqrt{2}} \exp\left[\mathrm{j}\left(\omega_m t + \phi_{\mathrm{R},m} - \pi/2\right)\right], \\
\phi_{\mathrm{R},m} &= -\beta_{\mathrm{R},m} L = -k_{0,m} n_{\mathrm{e,R},m} L, \qquad k_{0,m} = \omega_m / c\,.
\end{aligned} \tag{C.8}$$

For the sensing arm, we assume the same geometrical length L. In addition, we account for the changes of the effective refractive indices $n_{\mathrm{e,S},m}$ by $\Delta n_{\mathrm{e,S},m}$, which are caused by adsorption of molecules to the WG surface. This leads to an additional phase shift $\Delta\phi_{\mathrm{S},m}$, such that the total field at the end of the sensing arm can be written as

$$\begin{aligned}
\underline{E}_{\mathrm{S}} &= \sum_{m=1}^{M} \frac{\hat{\underline{E}}_m}{\sqrt{2}} \exp\left[\mathrm{j}\left(\omega_m t + \phi_{\mathrm{S},m} + \Delta\phi_{\mathrm{S},m}\right)\right], \\
\phi_{\mathrm{S},m} &= -\beta_{\mathrm{S},m} L = -k_{0,m} n_{\mathrm{e,S,m}} L, \\
\Delta\phi_{\mathrm{S},m} &= -\Delta\beta_{\mathrm{S},m} L = -k_{0,m} \Delta n_{\mathrm{e,S},m} L\,.
\end{aligned} \tag{C.9}$$

At the output ports of the 3 × 3 MMI, the fields from the reference arm, Equation (C.8), and from the sensing arm, Equation (C.9), are combined in analogy to Equation (C.3). The measured output powers P_{A}, P_{B} and P_{C} result from an average in analogy to Equation (C.7). Using Equation (C.4), we can derive the Clarke field for a polychromatic source,

$$\begin{aligned}
\underline{s}_{\mathrm{poly}} &= \underline{s}_{\mathrm{r}} + \mathrm{j}\,\underline{s}_{\mathrm{i}} \\
&= 2\left\langle \underline{E}_{\mathrm{S}} \underline{E}_{\mathrm{R}}^{*} \right\rangle_T = \sum_{m=1}^{M} \left(\left| \hat{\underline{E}}_m \right|^2 \mathrm{e}^{\mathrm{j}\left[\Delta\phi_{\mathrm{S},m} + \pi/2 + \left(\phi_{\mathrm{S},m} - \phi_{\mathrm{R},m}\right)\right]} \right) \\
&= \sum_{m=1}^{M} \left(\left| \hat{\underline{E}}_m \right|^2 \mathrm{e}^{\mathrm{j}\Delta\phi(\omega_m)} \right) \\
&= 2P_{\mathrm{B}} - \left(P_{\mathrm{C}} + P_{\mathrm{A}}\right) + \mathrm{j}\sqrt{3}\left(P_{\mathrm{C}} - P_{\mathrm{A}}\right),
\end{aligned} \tag{C.10}$$

where the phase differences $\Delta\phi(\omega_m)$ of the various spectral components in the sensor and the reference arm depend on the respective frequency ω_m,

$$\begin{aligned}\Delta\phi(\omega_m) &= \Delta\phi_{\mathrm{S},m} + \pi/2 + \left(\phi_{\mathrm{S},m} - \phi_{\mathrm{R},m}\right) \\ &= -\frac{\omega_m}{c}\left[\Delta n_{\mathrm{e,S},m} + \left(n_{\mathrm{e,S},m} - n_{\mathrm{e,R},m}\right)\right]L + \frac{\pi}{2}.\end{aligned} \tag{C.11}$$

We expand the function $\Delta\phi(\omega)$ of Equation (C.11) in a Taylor series around a center frequency ω_0 and keep only the linear term,

$$\begin{aligned}&\Delta\phi(\omega) \approx \Delta\phi_0^{(0)} + \Delta\phi_0^{(1)}(\omega - \omega_0), \\ &\Delta\phi_0^{(0)} = \Delta\phi(\omega_0), \quad \Delta\phi_0^{(1)} = \left.\frac{\mathrm{d}\left(\Delta\phi(\omega)\right)}{\mathrm{d}\omega}\right|_{\omega=\omega_0}.\end{aligned} \tag{C.12}$$

As a center frequency ω_0, we choose the average of all emission frequencies $\omega_{m=1\ldots M}$, of the polychromatic light source,

$$\omega_0 = \frac{1}{M}\sum_{m=1}^{M}\omega_m \tag{C.13}$$

The derivative $\Delta\phi_0^{(1)}$ in Equation (C.12) can be expressed by the group refractive index $n_\mathrm{g}(\omega) = n + \omega_0 \left(\mathrm{d}n/\mathrm{d}\omega\right)\big|_{\omega=\omega_0}$ at the center frequency ω_0. With the group refractive index $n_\mathrm{e,g,S}$ and $n_\mathrm{e,g,R}$ of the sample and the reference arm, respectively, and the change $\Delta n_\mathrm{e,g,S}$ of the group-refractive index due to adsorption of molecules to the surface of the sensor arm, $\Delta\phi_0^{(1)}$ can be written as

$$\Delta\phi_0^{(1)} = -\left[\Delta n_\mathrm{e,g,S} + \left(n_\mathrm{e,g,S} - n_\mathrm{e,g,R}\right)\right]\frac{L}{c} = -\Delta n_\mathrm{e,g}\frac{L}{c} \tag{C.14}$$

The quantity $\Delta n_\mathrm{e,g}$ is the group refractive index difference between the sensor and the reference arm in the presence of an analyte. Substituting $\Delta\phi(\omega_m) \approx \Delta\phi_0^{(0)} + \Delta\phi_0^{(1)}(\omega_m - \omega_0)$ in Equation (C.10), we can re-write the Clarke field for the polychromatic light source,

$$\begin{aligned} \underline{s}_{\text{poly}} &= \underline{s}_{\text{r}} + \text{j}\,\underline{s}_{\text{i}} = 2\left\langle \underline{E}_{\text{S}} \underline{E}_{\text{R}}^{*} \right\rangle_{T} \\ &= \text{e}^{\,\text{j}\Delta\phi_0^{(0)}} \sum_{m=1}^{M} \left| \hat{\underline{E}}_m \right|^2 \text{e}^{\,\text{j}\Delta\phi_0^{(1)}(\omega_m - \omega_0)} \\ &= \text{e}^{\,\text{j}\Delta\phi(\omega_0)} \sum_{m=1}^{M} \left| \hat{\underline{E}}_m \right|^2 \text{e}^{-\text{j}\Delta n_{\text{e,g}}(\omega_m - \omega_0) L/c} . \end{aligned} \tag{C.15}$$

Equation (C.14) can be simplified if $\Delta n_{\text{e,g}} \left|\omega_m - \omega_0\right| L/c \ll 1$ holds, i.e., if the frequency offset $\left|\omega_m - \omega_0\right|$ of the laser lines is significantly smaller than the free spectral range $c/\left(\Delta n_{\text{e,g}} L\right)$ of the unbalanced MZI. We assume that the interferometer is well balanced, $n_{\text{e,g,S}} \approx n_{\text{e,g,R}}$, and that analyte-induced change $\Delta n_{\text{e,g,S}}$ of the group refractive index is small, thus leading to a large free spectral range. In this case, the exponential in the sum of Equation (C.15) is approximately one, and the phase of $\underline{s}_{\text{poly}}$ is determined by $\Delta\phi_0^{(0)}$ only, i.e., the (narrowband) polychromatic source behaves as if it was monochromatic. In this case, Equation (C.15) can then be re-written as

$$\begin{aligned} \underline{s}_{\text{poly}} &= \underline{s}_{\text{r}} + \text{j}\,\underline{s}_{\text{i}} = 2\left\langle \underline{E}_{\text{S}} \underline{E}_{\text{R}}^{*} \right\rangle_{T} \\ &= \text{e}^{\,\text{j}\Delta\phi(\omega_0)} \sum_{m=1}^{M} \left| \hat{\underline{E}}_m \right|^2 \\ &= P_{\text{source}}\, \text{e}^{\,\text{j}\Delta\phi(\omega_0)} . \end{aligned} \tag{C.16}$$

The phase change can be found by unwrapping s_{poly} as in Equation (C.5),

$$\begin{aligned} \Delta\phi(\omega_0) &= \Delta\phi_{\text{S},0} + \pi/2 + \left(\phi_{\text{S},0} - \phi_{\text{R},0}\right) \\ &= \text{unwrap}\left(\arg\left(\underline{s}_{\text{poly}}\right)\right). \end{aligned} \tag{C.17}$$

For a (wideband) polychromatic source, the condition $\Delta n_{\text{e,g}} \left|\omega_m - \omega_0\right| L/c \ll 1$ is not fulfilled, and the magnitude $\left|\underline{s}_{\text{poly}}\right|$ of the Clarke field depends on the amplitudes and on the frequency span of the monochromatic lines,

$$\begin{aligned}\left|\underline{s}_{\text{poly}}\right|^2 &= 4\left|\underline{E}_{\text{S}}\underline{E}_{\text{R}}^*\right|^2 \\ &= \sum_{m=1,n=1}^{M}\left|\underline{\hat{E}}_m\right|^2\left|\underline{\hat{E}}_n\right|^2 \mathrm{e}^{\mathrm{j}\Delta n_{\text{e,g}}\left(\omega_m-\omega_n\right)\frac{L}{c}} \\ &= \sum_{m=1}^{M}\left|\underline{\hat{E}}_m\right|^4+\sum_{m=2}^{M}\sum_{n=1}^{m-1}\left|\underline{\hat{E}}_m\right|^2\left|\underline{\hat{E}}_n\right|^2 2\cos\left(\Delta n_{\text{e,g}}\left(\omega_m-\omega_n\right)\frac{L}{c}\right).\end{aligned} \tag{C.18}$$

This in contrast to the case of a monochromatic laser line, for which the magnitude $\left|\underline{s}_{\text{mono}}\right|$ of the Clarke field is constant with increasing $\Delta\phi$, Equation (C.4) and Equation (C.5). Equation (C.18) can be simplified by assuming $M \gg 1$ equidistant laser lines in a maximum spectral range $\Delta\omega_{\max}$, and by postulating approximately equal field amplitudes $\underline{\hat{E}}_m \approx \underline{\hat{E}}$. The phase change differences $\Delta n_{\text{e,g}}\left(\omega_m-\omega_n\right)L/c$ can then be written as

$$\Delta n_{\text{e,g}}\left(\omega_m-\omega_n\right)L/c = \Delta n_{\text{e,g}}\frac{\Delta\omega_{\max}}{M}\left(m-n\right)L/c \tag{C.19}$$

When evaluating the sums in Equation (C.18), we neglect $M\left|\underline{\hat{E}}\right|^4$ compared to $M^2\left|\underline{\hat{E}}\right|^4$ and replace the sums by integrals, $\sum_{m=2}^{M}\sum_{n=1}^{m-1}\left(\cdot\right)=\int_{m=0}^{M}\int_{0}^{m}\left(\cdot\right)\mathrm{d}m\,\mathrm{d}n$. This leads to

$$\begin{aligned}\left|\underline{s}_{\text{poly}}\right|^2 &= \left|\underline{\hat{E}}\right|^4\int_{m=0}^{M}\int_{n=0}^{m}2\cos\left(\frac{\Delta n_{\text{e,g}}\Delta\omega_{\max}L}{M\,c}\left(m-n\right)\right)\mathrm{d}n\,\mathrm{d}m \\ &= \left|\underline{\hat{E}}\right|^4 M^2\frac{\sin^2\left(\frac{\Delta n_{\text{e,g}}L}{2c}\Delta\omega_{\max}\right)}{\left(\frac{\Delta n_{\text{e,g}}L}{2c}\Delta\omega_{\max}\right)^2} \\ &= P_{\text{source}}^2\frac{\sin^2\left(\frac{\Delta n_{\text{e,g}}L}{2c}\Delta\omega_{\max}\right)}{\left(\frac{\Delta n_{\text{e,g}}L}{2c}\Delta\omega_{\max}\right)^2}.\end{aligned} \tag{C.20}$$

Equation (C.20) illustrates that the magnitude $\left|\underline{s}_{\mathrm{poly}}\right|$ decreases for increasing $\Delta n_{\mathrm{e,g}}$ and therefore for increasing $\Delta n_{\mathrm{e,g,S}}$. For $\Delta\omega_{\max} \to 0$, the result for one monochromatic line is reproduced, Equation (C.4).

C.3 3 × 3 MMI, Clarke field transformation and resolution

[This section was published as Supplementary information Note 4 of [J2]]

In our experiments, we rely on MZI with 3 × 3 MMI as power combiners at the output. A key advantage of this approach is that phase ambiguities within a 2π-interval can be avoided. This is possible due to the detection of three sensor signals that have a fixed phase difference of 2π/3 (120°) with respect to each other. The transformation of these signals to a Clarke field leads to a locus in form of a circle in the complex plane, where the position on the curve is well defined within a phase shift $\Delta\phi$ of 2π, see Equation (C.4) and Equation (C.15). In contrast to that, MZI with 2 × 2 MMI only deliver two perfectly complementary signals at the output. In these devices, any phase difference $\Delta\phi$ leads to exactly the same output powers as its 2π -complement $2\pi - \Delta\phi$. As a consequence, unambiguous phase extraction is possible only within intervals of π.

To illustrate the locus-correction of the complex Clarke field $\underline{s}$ used in Chapter 6, we compare the temporal evolution of the raw, i.e., uncorrected Clarke field to its locus-corrected counterpart, Figure C.3(a). The underlying data was extracted from the binding experiment of 121 nM fibrinogen in phosphate-buffered saline solution (PBS), see right-hand part of the binding curve in Figure 6.6(a) of Subsection 6.2.5. In our experiments, the MMI couplers were already optimized for uniform power splitting ratios and phase shifts, such that the impact of the locus correction is rather small. As a consequence, the binding curves extracted from the corrected and the uncorrected data are essentially identical, see Figure C.3(b). The appreciable fluctuations of the Clarke fields in our measurements originate from rather low signal-to-noise power ratios (SNR) of the recorded signals. This can be improved by higher output powers of the SiNOH lasers, which can be achieved by using higher pulse repetition frequencies, see Section “Towards compact portable sensor systems for point-of-care applications” in Section 6.3. For the current sensor implementation, we quantify the variations of the phase shift extracted while flushing the sensor with PBS, leading to a standard deviation of $\sigma_{\Delta\phi} = 0.2\,\text{rad}$.

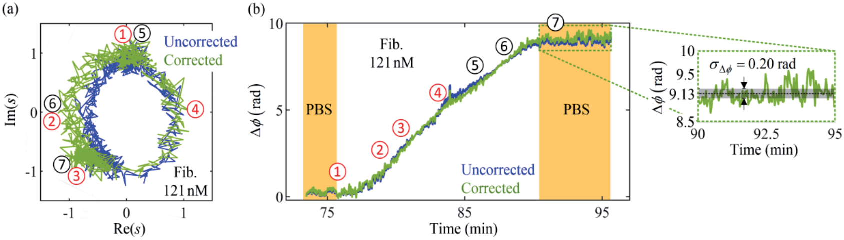

Figure C.3: Exemplary Clarke-field correction and binding curve. **(a)** Evolution of the uncorrected (blue) and locus-corrected (green) Clarke field s in the complex $\underline{s}$-plane for the binding experiment of 121 nM fibrinogen, see right-hand part of the binding curve in Figure 6.6(a) of Subsection 6.2.5. **(b)** Measured phase shift as a function of time for the uncorrected (blue) and the corrected (green) binding curve. The encircled numbers in red and black mark subsequent phases as they are indicated in Subfigure C.3**(a)**. Inset: Magnified portion of the corrected data (green) that were detected during flushing the sensor with phosphate buffered saline solution (PBS). The standard deviation of the binding curve amounts to $\sigma_{\Delta\phi} = 0.20$ rad.

D Bibliography

[1] D. Issadore and R. M. Westervelt, *Point-of-Care Diagnostics on a Chip*. Springer-Verlag Berlin Heidelberg, 2013.

[2] P. B. Luppa and R. J. Hrsg, *POCT - Patientennahe Labordiagnostik*. 2017.

[3] K. Baryeh, S. Takalkar, M. Lund, and G. Liu, *Introduction to Medical Biosensors for Point of Care Applications*. Elsevier Ltd, 2017.

[4] E. Luan, H. Shoman, D. M. Ratner, K. C. Cheung, and L. Chrostowski, "Silicon Photonic Biosensors Using Label-Free Detection," *Sensors (Switzerland)*, vol. 18, no. 10, pp. 1–42, 2018.

[5] P. Steglich, M. Hülsemann, B. Dietzel, and A. Mai, "Optical Biosensors Based on Silicon-on-Insulator Ring Resonators: A Review," *Molecules*, vol. 24, no. 3, pp. 1–16, 2019.

[6] P. Kozma, F. Kehl, E. Ehrentreich-förster, C. Stamm, and F. F. Bier, "Integrated Planar Optical Waveguide Interferometer Biosensors : A Comparative Review," *Biosens. Bioelectron.*, vol. 58, pp. 287–307, 2014.

[7] A. F. Gavela, D. G. García, J. C. Ramirez, and L. M. Lechuga, "Last Advances in Silicon-Based Optical Biosensors," *Sensors (Switzerland)*, vol. 16, no. 3, pp. 1–15, 2016.

[8] L. Chrostowski *et al.*, "Silicon Photonic Resonator Sensors and Devices," *Proc. SPIE*, vol. 8236, p. 823620, 2012.

[9] D. J. Blumenthal, R. Heideman, D. Geuzebroek, A. Leinse, and C. Roeloffzen, "Silicon Nitride in Silicon Photonics," *Proc. IEEE*, vol. 106, no. 12, pp. 2209–2231, 2018.

[10] Z. Wang *et al.*, "Novel Light Source Integration Approaches for Silicon Photonics," *Laser Photonics Rev.*, vol. 11, no. 4, pp. 1–21, 2017.

[11] R. Bo, H. Yan, and L. Yanan, "Research Progress of III-V Laser Bonding to Si," *J. Semicond.*, vol. 37, no. 12, pp. 1–12, 2016.

[12] LioniX International BV, "LioniX International," 2021. [Online]. Available: https://www.lionix-international.com/.

[13] LIGENTEC S. A., "LIGENTEC," 2021. [Online]. Available: https://www.ligentec.com/.

[14] K. F. Palmer and D. Williams, "Optical Properties of Water in the Near Infrared.," *J Opt Soc Am*, vol. 64, no. 8, pp. 1107–1110, 1974.

[15] E. Luan, H. Shoman, D. M. Ratner, K. C. Cheung, and L. Chrostowski, "Silicon Photonic Biosensors Using Label-Free Detection," *Sensors (Switzerland)*, vol. 18, no. 10, pp. 1–42, 2018.

[16] T. Schilling, "Bundeszentrale Für Politische Ildung, Demografischer-Wandel," 2020. [Online]. Available: https://www.bpb.de/politik/innenpolitik/demografischer-wandel/.

[17] D. K. Zoufal, "Bundesministerium Für Gesundheit (BMG), Krankheiten, Kopf Und Nerven," 2020. [Online]. Available: https://gesund.bund.de/themen/kopf-und-nerven.

[18] WHO Headquarters in Geneva, "World Health Organization, Promoting Cancer Early Diagnosis," 2020. [Online]. Available: https://www.who.int/activities/promoting-cancer-early-diagnosis.

[19] E. Makarona, P. Petrou, S. Kakabakos, K. Misiakos, and I. Raptis, "Point-of-Need Bioanalytics Based on Planar Optical Interferometry," *Biotechnol. Adv.*, vol. 34, no. 3, pp.

209–233, 2016.

[20] A. Densmore *et al.*, “Sensitive Label-Free Biomolecular Detection Using Thin Silicon Waveguides,” *Adv. Opt. Technol.*, vol. 2008, p. 725967, 2008.

[21] B. Sepulveda *et al.*, “Optical Biosensor Microsystems Based on the Integration of Highly Sensitive Mach – Zehnder Interferometer Devices,” *J. Opt. A*, vol. 8, pp. 561–566, 2006.

[22] A. Densmore *et al.*, “A Silicon-on-Insulator Photonic Wire Based Evanescent Field Sensor,” *IEEE Photonics Technol. Lett.*, vol. 18, no. 23, pp. 2520–2522, 2006.

[23] S. Schmidt *et al.*, “Improving the Performance of Silicon Photonic Rings, Disks, and Bragg Gratings for Use in Label-Free Biosensing,” in *Proceedings of SPI*, 2014, no. 9166, p. 91660M.

[24] V. M. N. Passaro, B. Troia, P. Bari, and F. De Leonardis, “World’ s Largest Science , Technology & Medicine Open Access Book Publisher Chemical Sensors Based on Photonic Structures,” in *Advances in Chemical Sensors*, W. Wang, Ed. In Tech, 2012, pp. 89–120.

[25] A. Kargar and C.-Y. Chao, “Design and Optimization of Waveguide Sensitivity in Slot Microring Sensors,” *J. Opt. Soc. Am. A*, vol. 28, no. 4, p. 596, 2011.

[26] L. Huang *et al.*, “Improving the Detection Limit for On-Chip Photonic Sensors Based on Subwavelength Grating Racetrack Resonators,” *Opt. Express*, vol. 25, no. 9, p. 10527, 2017.

[27] H. Sun, A. Chen, and L. R. Dalton, “Enhanced Evanescent Confinement in Multiple-Slot Waveguides and Its Application in Biochemical Sensing,” *IEEE Photonics J.*, vol. 1, no. 1, pp. 48–57, 2009.

[28] I. Khodadad, N. Clarke, M. Khorasaninejad, D. Henneke, and S. S. Saini, “Optimization of Multiple-Slot Waveguides for Biochemical Sensing,” *Appl. Opt.*, vol. 53, no. 23, p. 5169, 2014.

[29] T. Claes, W. Bogaerts, and P. Bienstman, “Experimental Characterization of a Silicon Photonic Biosensor Consisting of Two Cascaded Ring Resonators Based on the Vernier-Effect and Introduction of a Curve Fitting Method for an Improved Detection Limit,” *Opt. Express*, vol. 18, no. 22, p. 22747, 2010.

[30] H. Yan *et al.*, “Unique Surface Sensing Property and Enhanced Sensitivity in Microring Resonator Biosensors Based on Subwavelength Grating Waveguides,” *Opt. Express*, vol. 24, no. 26, p. 29724, 2016.

[31] C. A. Barrios, “Analysis and Modeling of a Silicon Nitride Slot-Waveguide Microring Resonator Biochemical Sensor,” *Proc. SPIE*, vol. 7356, p. 735605, 2009.

[32] F. Dell’Olio and V. M. N. Passaro, “Optical Sensing by Optimized Silicon Slot Waveguides,” *Opt. Express*, vol. 15, no. 8, pp. 4977–4993, 2007.

[33] J. G. Wangüemert-Pérez *et al.*, “Evanescent Field Waveguide Sensing with Subwavelength Grating Structures in Silicon-on-Insulator,” *Opt. Lett.*, vol. 39, no. 15, p. 4442, 2014.

[34] S. Janz *et al.*, *Silicon Photonic Wire Waveguide Sensors*. Springer, 2009.

[35] D. H. Geuzebroek, G. Besselink, E. Schreuder, F. Falke, A. Leinse, and R. Heideman, “Silicon-Nitride Biophotonic Sensing Platform,” *Proc. SPIE*, vol. 1092117, p. 42, 2019.

[36] C. Xiong *et al.*, “Silicon Photonic Integrated Circuit for On-Chip Spectroscopic Gas Sensing,” *Proc. SPIE*, vol. 10923, p. 15, 2019.

[37] J. Milvich, D. Kohler, W. Freude, and C. Koos, “Surface Sensing with Integrated Optical Waveguides: A Design Guideline,” *Opt. Express*, vol. 26, no. 16, p. 19885, 2018.

[38] M. Iqbal *et al.*, “Label-Free Biosensor Arrays Based on Silicon Ring Resonators and High-

Speed Optical Scanning Instrumentation," *IEEE J. Sel. Top. Quantum Electron.*, vol. 16, no. 3, pp. 654–661, 2010.

[39] Genalyte, "Genalyte," 2021. [Online]. Available: https://www.genalyte.com/.

[40] H. W. Lim and N. A. Soter, *Clinical Photomedicine*. New York: Marcel Dekker, inc, 1993.

[41] P. J. Cegielski *et al.*, "Integrated Perovskite Lasers on Silicon Nitride Waveguide Platform by Cost-Effective High Throughput Fabrication," *Opt. Express*, vol. 25, no. 12, pp. 4624–4629, 2017.

[42] P. J. Cegielski *et al.*, "Monolithically Integrated Perovskite Semiconductor Lasers on Silicon Photonic Chips by Scalable Top-Down Fabrication," *Nano Lett.*, vol. 18, no. 11, pp. 6915–6923, 2018.

[43] W. Xie *et al.*, "On-Chip Integrated Quantum-Dot–Silicon-Nitride Microdisk Lasers," *Adv. Mater.*, vol. 29, no. 16, pp. 2–7, 2017.

[44] Allresist GmbH, "AR-N 7500, 7520," 2020. [Online].
Available: http://www.allresist.de/ebeamresists-ar-n7500_7520/.

[45] Micro resist technology GmbH, "Ma-N 2400 and Mr-EBL 6000 - Negative Tone Photoresists," 2000. [Online]. Available: https://www.microresist.de/produkt/ma-n-2400-series/.

[46] EM Resist Ltd, "H-SiOx (HSQ) – Negative Tone Electron Beam Resist," 2020. [Online]. Available: http://www.emresist.com/hsq-resist/.

[47] K. R. Williams, S. Member, K. Gupta, S. Member, and M. Wasilik, "Etch Rates for Micromachining Processing — Part II," vol. 12, no. 6, pp. 761–778, 2003.

[48] B. E. A. Saleh and M. C. Teich, *Fundamentals of Photonics*, 2nd ed. Wiley, 2012.

[49] H. R. Philipp, "Optical Properties of Silicon Nitride," *J. Electrochem. Soc.*, vol. 120, no. 2, p. 295, 1973.

[50] I. H. Malitson, "Interspecimen Comparison of the Refractive Index of Fused Silica," *J. Opt. Soc. Am.*, vol. 55, no. 10, p. 1205, 1965.

[51] M. Daimon and A. Masumura, "Measurement of the Refractive Index of Distilled Water from the Near-Infrared Region to the Ultraviolet Region," *Appl. Opt.*, vol. 46, no. 18, pp. 3811–3820, 2007.

[52] G. B. Eadie, M. I. B. Rindza, R. I. A. F. Lynn, A. R. Osenberg, and J. A. S. S. Hirk, "Refractive Index Measurements of Poly (Methyl Methacrylate) (PMMA) from 0.4 - 1.6 μM," vol. 54, no. 31, pp. 139–143, 2015.

[53] H. Kogelnik, "Theory of Dielectric Waveguides," in *Integrated Optics*, Berlin Heidelberg, 1975, pp. 13–81.

[54] D. Kohler, I. Allegro, S. F. Wondimu, L. Hahn, W. Freude, and C. Koos, "Lasing in Si_3N_4-Organic Hybrid (SiNOH) Waveguides," *arXiv* 1909.00020 [physics,optics], 2019.

[55] F. A. Carey and R. J. Sundberg, *Advances in Organic Chemistry, Part A: Structure and Mechanism*, 4th ed. Kluwer Academic, Plenum Publisher, 2000.

[56] S. L. M. Anni, *Organic Lasers, Fundamentals, Developments, and Applications*. Singapore: Pan Stanford Publishing Pte. Ltd., 2018.

[57] F. P. Schäfer, *Dye Lasers*. Berlin Heidelberg: Springer, 1973.

[58] J. R. Lakowicz, *Principles of Fluorescence Spectroscopy*, 3rd ed. New York: Springer Science and Business Media, LLC, 2006.

[59] S. Chénais and S. Forget, “Recent Advances in Solid-State Organic Lasers,” *Polym. Int.*, vol. 61, no. 3, pp. 390–406, 2012.

[60] T. Susdorf *et al.*, “Photophysical Characterization of Pyrromethene 597 Laser Dye in Silicon-Containing Organic Matrices,” *Appl. Phys. B Lasers Opt.*, vol. 86, no. 3, pp. 537–545, 2007.

[61] J. R. Lakowicz, *Principles of Fluorescence Spectroscopy*, 3rd ed. Singapore: Springer Science+Business Media, LLC, 2006.

[62] G. Gupta, W. H. Steier, Y. Liao, J. Luo, L. R. Dalton, and A. K. Y. Jen, “Modeling Photobleaching of Optical Chromophores: Light-Intensity Effects in Precise Trimming of Integrated Polymer Devices,” *J. Phys. Chem. C*, vol. 112, no. 21, pp. 8051–8060, 2008.

[63] J. B. Pawley, *Handbook of Biological Confocal Microscopy*. New York: Springer Science+Business Media, LLC, 2006.

[64] H. Zhang, C. Li, X. Tu, X. Luo, M. Yu, and P. G. Q. Lo, “High Efficiency Silicon Nitride Grating Coupler,” *Appl. Phys. A Mater. Sci. Process.*, vol. 115, no. 1, pp. 79–82, 2014.

[65] M. Passoni, D. Gerace, L. Carroll, and L. C. Andreani, “Grating Couplers in Silicon-on-Insulator: The Role of Photonic Guided Resonances on Lineshape and Bandwidth,” *Appl. Phys. Lett.*, vol. 110, no. 4, pp. 8–13, 2017.

[66] L. Cheng, S. Mao, Z. Li, Y. Han, and H. Y. Fu, “Grating Couplers on Silicon Photonics: Design Principles, Emerging Trends and Practical Issues,” *Micromachines*, vol. 11, no. 7, 2020.

[67] S. Romero-García, F. Merget, F. Zhong, H. Finkelstein, and J. Witzens, “Visible Wavelength Silicon Nitride Focusing Grating Coupler with AlCu/TiN Reflector,” *Opt. Lett.*, vol. 38, no. 14, p. 2521, 2013.

[68] A. Z. Subramanian, S. Selvaraja, P. Verheyen, A. Dhakal, K. Komorowska, and R. Baets, “Near-Infrared Grating Couplers for Silicon Nitride Photonic Wires,” *IEEE Photonics Technol. Lett.*, vol. 24, no. 19, pp. 1700–1703, 2012.

[69] O. Bryngdahl, “Image Formation Using Self-Imaging Techniques.,” *J Opt Soc Am*, vol. 63, no. 4, pp. 416–419, 1973.

[70] R. Ulrich, “Light-Propagation and Imaging in Planar Optical Waveguides,” *Nouv. Rev. d’Optique*, vol. 6, no. 5, pp. 253–262, 1975.

[71] L. B. Soldano and E. C. M. Pennings, “Optical Multi-Mode Interference Devices Based on Self-Imaging: Principles and Applications,” *J. Light. Technol.*, vol. 13, no. 4, pp. 615–627, 1995.

[72] M. Blahut and A. Opilski, “Multimode Interference Structures-New Way of Passive Elements Technology for Photonics,” *Opto-Electronics Rev.*, vol. 9, no. 3, pp. 293–300, 2001.

[73] M. Bachmann, P. A. Besse, and H. Melchior, “General Self-Imaging Properties,” *Appl. Opt.*, vol. 33, no. 18, pp. 3905–3911, 1994.

[74] C. E. Chivers, A. L. Koner, E. D. Lowe, and M. Howarth, “How the Biotin-Streptavidin Interaction Was Made Even Stronger: Investigation via Crystallography and a Chimaeric Tetramer,” *Biochem. J.*, vol. 435, no. 1, pp. 55–63, 2011.

[75] R. G. Heideman, R. P. H. Kooyman, and J. Greve, “Performance of a Highly Sensitive Optical Waveguide Mach-Zehnder Interferometer Immunosensor,” *Sensors Actuators B. Chem.*, vol. 10, no. 3, pp. 209–217, 1993.

[76] X. Tu *et al.*, “Thermal Independent Silicon-Nitride Slot Waveguide Biosensor with High

Sensitivity," *Opt. Express*, vol. 20, no. 3, p. 2640, 2012.

[77] R. Halir, L. Vivien, X. Le Roux, D. X. Xu, and P. Cheben, "Direct and Sensitive Phase Readout for Integrated Waveguide Sensors," *IEEE Photonics J.*, vol. 5, no. 4, 2013.

[78] P. J. Reyes-Iglesias, I. Molina-Fernández, A. Moscoso-Mártir, and A. Ortega-Moñux, "High-Performance Monolithically Integrated 120° Downconverter with Relaxed Hardware Constraints," *Opt. Express*, vol. 20, no. 5, p. 5725, 2012.

[79] M. Antoniou, D. Tsounidi, P. S. Petrou, K. G. Beltsios, and S. E. Kakabakos, "Functionalization of Silicon Dioxide and Silicon Nitride Surfaces with Aminosilanes for Optical Biosensing Applications," *Med. Devices Sensors*, vol. 3, no. 5, pp. 1–11, 2020.

[80] M. Zhu, M. Z. Lerum, and W. Chen, "How to Prepare Reproducible, Homogeneous, and Hydrolytically Stable Aminosilane-Derived Layers on Silica," *Langmuir*, vol. 28, no. 1, pp. 416–423, 2012.

[81] G. T. Hermanson, *Bioconjugate Techniques*, 3rd ed. Oxford: Elsevier Inc., 2013.

[82] E. A. Smith and W. Chen, "How to Prevent the Loss of Surface Functionality Derived from Aminosilanes," *Langmuir*, vol. 24, no. 21, pp. 12405–12409, 2008.

[83] N. S. K. Gunda, M. Singh, L. Norman, K. Kaur, and S. K. Mitra, "Optimization and Characterization of Biomolecule Immobilization on Silicon Substrates Using (3-Aminopropyl)Triethoxysilane (APTES) and Glutaraldehyde Linker," *Appl. Surf. Sci.*, vol. 305, pp. 522–530, 2014.

[84] T. Ganguly, B. B. Kasten, D. K. Buar, L. R. MacGillivray, C. E. Berkman, and P. D. Benny, "The Hydrazide/Hydrazone Click Reaction as a Biomolecule Labeling Strategy for M(CO)3 (M = Re, 99mTc) Radiopharmaceuticals," *Chem. Commun.*, vol. 47, no. 48, pp. 12846–12848, 2011.

[85] C. M. Dundas, D. Demonte, and S. Park, "Streptavidin-Biotin Technology: Improvements and Innovations in Chemical and Biological Applications," *Appl. Microbiol. Biotechnol.*, vol. 97, no. 21, pp. 9343–9353, 2013.

[86] D. I. Cattoni, O. Chara, S. B. Kaufman, and F. L. G. Flecha, "Cooperativity in Binding Processes: New Insights from Phenomenological Modeling," *PLoS One*, vol. 10, no. 12, pp. 1–14, 2015.

[87] J. N. Weiss, "The Hill Equation Revisited: Uses and Misuses," *FASEB J.*, vol. 11, no. 11, pp. 835–841, 1997.

[88] Y. Wang, J. Flueckiger, C. Lin, and L. Chrostowski, "Universal Grating Coupler Design," *Proc. SPIE*, vol. 8915, p. 7, 2013.

[89] J. Flueckiger *et al.*, "Sub-Wavelength Grating for Enhanced Ring Resonator Biosensor," *Opt. Express*, vol. 24, no. 14, p. 15672, 2016.

[90] X. Wang *et al.*, "A Silicon Photonic Biosensor Using Phase-Shifted Bragg Gratings in Slot Waveguide," *J. Biophotonics*, vol. 6, no. 10, pp. 821–828, 2013.

[91] S. T. Fard *et al.*, "Performance of Ultra-Thin SOI-Based Resonators for Sensing Applications," *Opt. Express*, vol. 22, no. 12, pp. 9499–9506, 2014.

[92] A. Dhakal *et al.*, "Efficiency of Evanescent Excitation and Collection of Spontaneous Raman Scattering near High Index Contrast Channel Waveguides," *Opt. Express*, vol. 23, no. 21, p. 27391, 2015.

[93] D. X. Xu *et al.*, "Silicon Photonic Integration Platform-Have We Found the Sweet Spot?," *IEEE J. Sel. Top. Quantum Electron.*, vol. 20, no. 4, 2014.

[94] M. G. Scullion, T. F. Krauss, and A. Di Falco, “Slotted Photonic Crystal Sensors,” *Sensors (Switzerland)*, vol. 13, no. 3, pp. 3675–3710, 2013.

[95] J. Hu and D. Dai, “Cascaded-Ring Optical Sensor with Enhanced Sensitivity by Using Suspended Si-Nanowires,” *IEEE Photonics Technol. Lett.*, vol. 23, no. 13, pp. 842–844, 2011.

[96] R. Halir *et al.*, “Waveguide Sub-Wavelength Structures: A Review of Principles and Applications,” *Laser Photonics Rev.*, vol. 9, no. 1, pp. 25–49, 2015.

[97] S. Hughes, L. Ramunno, J. F. Young, and J. E. Sipe, “Extrinsic Optical Scattering Loss in Photonic Crystal Waveguides: Role of Fabrication Disorder and Photon Group Velocity,” *Phys. Rev. Lett.*, vol. 94, no. 3, pp. 1–4, 2005.

[98] W. Bogaerts *et al.*, “Silicon Microring Resonators,” *Laser Photonics Rev.*, vol. 6, no. 1, pp. 47–73, 2012.

[99] C. Koos, *Nanophotonic Devices for Linear and Nonlinear Optical Signal Processing*. Karlsruhe: Universitätsverlag Karlsruhe, 2007.

[100] J.-M. Brosi, “Slow-Light Photonic Crystal Devices for High-Speed Optical Signal Processing,” *Quantum Electron.*, vol. 4, p. 192, 2008.

[101] J. D. Joannopoulos, G. S. Johnson, J. N. Winn, and R. D. Meade, *Photonic Crystals, Molding the Flow of Light*. New Jersey: Princeton University Press, 2008.

[102] P. Muellner, E. Melnik, G. Koppitsch, J. Kraft, F. Schrank, and R. Hainberger, “CMOS-Compatible Si3N4 Waveguides for Optical Biosensing,” *Procedia Eng.*, vol. 120, no. September, pp. 578–581, 2015.

[103] A. Z. Subramanian *et al.*, “Silicon and Silicon Nitride Photonic Circuits for Spectroscopic Sensing On-a-Chip [Invited],” *Photonics Res.*, vol. 3, no. 5, p. B47, 2015.

[104] J.-C. Tinguely, Ø. I. Helle, and B. S. Ahluwalia, “Silicon Nitride Waveguide Platform for Fluorescence Microscopy of Living Cells,” *Opt. Express*, vol. 25, no. 22, p. 27678, 2017.

[105] P. Muñoz *et al.*, “Silicon Nitride Photonic Integration Platforms for Visible, near-Infrared and Mid-Infrared Applications,” *Sensors (Switzerland)*, vol. 17, no. 9, pp. 1–25, 2017.

[106] T. A. Huffman, G. M. Brodnik, C. Pinho, S. Gundavarapu, D. Baney, and D. J. Blumenthal, “Integrated Resonators in an Ultralow Loss Si_3N_4/SiO_2 Platform for Multifunction Applications,” *IEEE J. Sel. Top. Quantum Electron.*, vol. 24, no. 4, 2018.

[107] W. D. Sacher *et al.*, “Monolithically Integrated Multilayer Silicon Nitride-on-Silicon Waveguide Platforms for 3-D Photonic Circuits and Devices,” *Proc. IEEE*, vol. 106, no. 12, pp. 2232–2245, 2018.

[108] J. Wang, Z. Yao, and A. W. Poon, “Integrated Optofluidic Label-Free Biosensors Using a Silicon-Nitride-Based Coupled-Resonator Optical Waveguide,” *Integr. Opt. Devices, Mater. Technol. XX*, vol. 9750, no. September, p. 975014, 2016.

[109] T. Taniguchi *et al.*, “Detection of Antibody-Antigen Reaction by Silicon Nitride Slot-Ring Biosensors Using Protein G,” *Opt. Commun.*, vol. 365, pp. 16–23, 2016.

[110] J. T. Bovington, M. J. R. Heck, and J. E. Bowers, “Heterogeneous Lasers and Coupling to Si_3N_4 near 1060 Nm,” *Opt. Lett.*, vol. 39, no. 20, p. 6017, 2014.

[111] M. Belt and D. J. Blumenthal, “Erbium-Doped Waveguide DBR and DFB Laser Arrays Integrated within an Ultra-Low-Loss Si_3N_4 Platform,” *Opt. Express*, vol. 22, no. 9, p. 10655, 2014.

[112] Y. Chen *et al.*, “Experimental Demonstration of an Apodized-Imaging Chip-Fiber Grating

Coupler for Si_3N_4 Waveguides," *Opt. Lett.*, vol. 42, no. 18, p. 3566, 2017.

[113] Y. Zhu *et al.*, "On-Chip Single-Mode Distributed Feedback Colloidal Quantum Dot Laser under Nanosecond Pumping," *ACS Photonics*, vol. 4, no. 10, pp. 2446–2452, 2017.

[114] D. Kohler *et al.*, "Lasing in Si_3N_4-Organic Hybrid (SiNOH) Spiral Resonators," in *Conference on Lasers and Electro-Optics, OSA Technical Digest (online)(Optica Publishing Group, 2018)*, 2018, vol. 144108, no. i, pp. 2–5.

[115] F. Vogelbacher *et al.*, "Integrated Silicon Nitride Organic Hybrid DFB Laser with Inkjet Printed Gain Medium," *Opt. Express*, vol. 27, no. 20, p. 29350, 2019.

[116] F. Vogelbacher *et al.*, "Slot-Waveguide Silicon Nitride Organic Hybrid Distributed Feedback Laser," *Sci. Rep.*, vol. 9, no. 1, pp. 1–9, 2019.

[117] D. Korn *et al.*, "Lasing in Silicon-Organic Hybrid Waveguides," *Nat. Commun.*, vol. 7, pp. 1–9, 2016.

[118] A. Yariv, "Critical Coupling and Its Control in Optical Waveguide-Ring Resonator Systems," *IEEE Photonics Technol. Lett.*, vol. 14, no. 4, pp. 483–485, 2002.

[119] M. V. Bondar, O. V. Przhonska, and Y. A. Tikhonov, "Inhomogeneous Broadening of Organic Dyes in Polymeric Media: Nonlinear Transmission Spectra and Photochemical Kinetics," *J. Phys. Chem.*, vol. 96, no. 26, pp. 10831–10837, 1992.

[120] H. Kogelnik and C. V. Shank, "Coupled-Wave Theory of Distributed Feedback Lasers," *J. Appl. Phys.*, vol. 43, no. 5, pp. 2327–2335, 1972.

[121] G. Grau and W. Freude, *Optische Nachrichtentechnik, Eine Einführung*. Springer, 1986.

[122] M. A. G. Porcel *et al.*, "[INVITED] Silicon Nitride Photonic Integration for Visible Light Applications," *Opt. Laser Technol.*, vol. 112, pp. 299–306, 2019.

[123] B. Schwarz *et al.*, "Monolithically Integrated Mid-Infrared Lab-on-a-Chip Using Plasmonics and Quantum Cascade Structures," *Nat. Commun.*, vol. 5, no. May, pp. 1–7, 2014.

[124] E. Chatzianagnostou *et al.*, "High-Sensitivity Plasmo-Photonic Interferometric Sensors on a Chip," *Proc. SPIE*, no. February, p. 65, 2020.

[125] F. Vogelbacher *et al.*, "A Coupled-Spiral Silicon Nitride Organic-Hybrid Laser," *IEEE Photonics Technol. Lett.*, vol. 32, no. 10, pp. 561–564, 2020.

[126] C. Kieninger *et al.*, "Ultra-High Electro-Optic Activity Demonstrated in a Silicon-Organic Hybrid (SOH) Modulator," *Optica*, vol. 5, no. 6, 2017.

[127] Y. M. Shirshov *et al.*, "Analysis of the Response of Planar Polarization Interferometer to Molecular Layer Formation: Fibrinogen Adsorption on Silicon Nitride Surface," *Biosens. Bioelectron.*, vol. 16, no. 6, pp. 381–390, 2001.

[128] H. M. Haake, A. Schütz, and G. Gauglitz, "Label-Free Detection of Biomolecular Interaction by Optical Sensors," *Fresenius. J. Anal. Chem.*, vol. 366, no. 6–7, pp. 576–585, 2000.

[129] E. Melnik *et al.*, "Surface Modification of Integrated Optical MZI Sensor Arrays Using Inkjet Printing Technology," *Procedia Eng.*, vol. 168, pp. 337–340, 2016.

[130] J. G. Wangüemert-Pérez *et al.*, "[Invited] Subwavelength Structures for Silicon Photonics Biosensing," *Opt. Laser Technol.*, vol. 109, pp. 437–448, 2019.

[131] M. S. Murib, D. Martens, and P. Bienstman, "Label-Free Real-Time Optical Monitoring of DNA Hybridization Using SiN Mach–Zehnder Interferometer-Based Integrated Biosensing Platform," *J. Biomed. Opt.*, vol. 23, no. 12, p. 1, 2018.

[132] F. Prieto *et al.*, "An Integrated Optical Interferometric Nanodevice Based on Silicon

Technology for Biosensor Applications," *Nanotechnology*, vol. 14, no. 8, pp. 907–912, 2003.

[133] Thorlabs GmbH, "Thorlabs: Visible Laser Diodes: Center Wavelengths from 404 Nm to 690 Nm," 2020. [Online]. Available: https://www.thorlabs.com/newgrouppage9.cfm?objectgroup_id=7.

[134] NaKu Technology Co. Ltd, "CivilLaser: 520nm 1200mW High Power Green Laser Dot Line Cross Laser Diode Module," 2020. [Online]. Available: https://www.civillaser.com/index.php?main_page=product_info&products_id=1038.

[135] S. Series and O. Sciences, *Organic Solid- State Lasers*, 3rd ed. Heidelberg: Springer, 2013.

[136] M. Ahmad, T. A. King, D. K. Ko, B. Heon Cha, and J. Lee, "Photostability of Lasers Based on Pyrromethene 567 in Liquid and Solid-State Host Media," *Opt. Commun.*, vol. 203, no. 3–6, pp. 327–334, 2002.

[137] I. A. Estrada *et al.*, "Multiplex Detection of Pathogen Biomarkers in Human Blood, Serum, and Saliva Using Silicon Photonic Microring Resonators," *Adv. Glob. Heal. through Sens. Technol. 2015*, vol. 9490, no. May 2015, p. 94900E, 2015.

[138] D. Martens *et al.*, "A Low-Cost Integrated Biosensing Platform Based on SiN Nanophotonics for Biomarker Detection in Urine," *Anal. Methods*, vol. 10, no. 25, pp. 3066–3073, 2018.

[139] S. Vemulapati and D. Erickson, "H.E.R.M.E.S: Rapid Blood-Plasma Separation at the Point-of-Need," *Lab Chip*, vol. 18, no. 21, pp. 3285–3292, 2018.

[140] S. Vemulapati and T. Eveleth, "Hermes Life Science, Sample Prep, Simplified," 2020. [Online]. Available: https://www.hermeslifesciences.com/.

[141] J. Milvich, D. Kohler, W. Freude, and C. Koos, "Integrated Phase-Sensitive Photonic Sensors: A System Design Tutorial," *Adv. Opt. Photonics*, vol. 13, no. 3, p. 584, 2021.

[142] P. W. Anderson, "Absence of Diffusion in Certain Random Lattices," *Phys. Rev.*, vol. 109, no. 5, pp. 1492–1505, 1958.

[143] A. S. Raja *et al.*, "Electrically Pumped Photonic Integrated Soliton Microcomb," *Nat. Commun.*, vol. 10, no. 1, pp. 1–8, 2019.

[144] S. Koeber *et al.*, "Femtojoule Electro-Optic Modulation Using a Silicon-Organic Hybrid Device," *Light Sci. Appl.*, vol. 4, no. 2, 2015.

E Glossary

E.1 List of abbreviations

POC	Point-of-care
Si_3N_4	Siliconnitride
SiNOH	Si_3N_4-organic hybrid
LED	Light-emitting diode
WG	Waveguide
MZI	Mach-Zehnder interferometer
SM	single-mode
GC	Grating coupler
SiO	Silicon dioxide
PMMA	Poly(methyl methacrylate)
LPCVD	Low-pressure chemical vapor deposition
CVD	Chemical vapor deposition
UV	Ultraviolet
HF	Hydrofluoric acid
Quasi-TE	Quasi-transverse electric
MMI	Multimode interference coupler
Quasi-TM	Quasi-transverse magnetic
HOMO	Highest occupied molecular orbital

LUMO	Lowest occupied molecular orbital
RUI	Refractive index unit
APDEMS	Aminopropyl(diethoxy)methylsilane
OH	Hydroxyl
PBS	Phosphate-buffered saline solution
SOI	Silicon-on-insulator
SWG	Sub-wavelength grating
BOX	Buried oxide layer
NIR	Near infrared
VIS	Visible
FEM	Finite-element method
DFB	Distributed Feedback
TIRF	Total internal reflection fluorescence
PIC	Photonic integrated circuit
SEM	Scanning electron microscope
cw	Continuous wave
PM	Polarization-maintaining
MM	Multimode
RBW	Resolution bandwidth
SOH	Silicon-organic hybrid
DSP	Digital signal processing
VCSEL	Vertical-cavity surface-emitting laser

SNR	Signal-to-noise power ratio

E.2 Symbols

Greek symbols

α	Loss constant
β	Propagation constant
ε_0	Permittivity
ε_r	Relative permittivity
$\Gamma_i^{(\mathrm{conf})}$	Confinement factor of volume *i*
Γ_i	Field interaction factor of volume *i*
λ	Vacuum wavelength
θ	Incident angle
μ_0	Vacuum permeability
μ_r	Relative permeability
σ_g	Scaling factor for geometry
σ_ω	Scaling factor for frequency
σ_n	Scaling factor for refractive index
ϕ	Phase
φ	Phase shift
ω	Angular frequency

Latin symbols

A	WG cross-section
a	Unit cell length / period

c	Vacuum speed of light
C	Concentration
d	Land width in a grating
D_x	Component x of displacement
$\mathbf{E}$	Vectorial electric mode field
E_x	Component x of electric field
$\left\lvert\vec{E}\right\rvert$	Electric field magnitude
$\mathbf{e}_z$	Unit vector in z-direction
FF	Fill factor
FEM	Finite-element method
$\mathbf{H}$	Vectorial magnetic mode field
h	Waveguide height
K	Wavenumber of a grating
K_d	Dissociation constant
k_0	Vacuum propagation constant
l	Length
M	Diffraction order
N	Number of images in an MMI
n	Refractive index
n_g	Group refractive index
n_e	Effective refractive index
n_eg	Effective group refractive index

Δn_e	Effective refractive index change
P	Poynting vector
$\mathbf{r}$	Position vector
$S^{(\mathrm{surf})}$	Homogeneous sensitivity
$S^{(\mathrm{surf})}$	Surface sensitivity
S_sys	System sensitivity
$S_\mathrm{opt}^{(\mathrm{surf})}$	Optimized surface sensitivity
S_0	Singlet ground state
S_1	First excited singlet state
$\underline{s}$	Clarke field
T_1	Triplet state
s	Spin
t_SL	Thickness of surface layer
V	Volume
W	Pump pulse energy
$W^{(\mathrm{cell})}$	Length-related energy density
ΔW	Energy gap
W_ph	Photon energy
w	Waveguide width
Z_0	Free-space wave impedance

Danksagung

Die vorliegend Dissertation entstand während meiner Zeit am Institut für Photonik und Quantenelektronik (IPQ) und am Institut für Mikrostrukturtechnik (IMT) am Karlsruher Institut für Technologie (KIT). Unterstützt wurde ich außerdem von der Karlsruhe School of Optics and Photonics (KSOP). Ich möchte mich bei allen Personen bedanken, durch deren Unterstützung diese Arbeit ermöglicht wurde.

Mein Doktorvater Prof. Christian Koos gab mir die Möglichkeit in diesem spannenden Arbeitsumfeld an einem Forschungsthema zu arbeiten, das perfekt zu mir passte. Ich möchte mich für die zahlreichen fachlichen Diskussionen bedanken, durch die ich immer neue Denkanstöße und Ideen bekam und viele Herausforderungen meistern konnte. Ganz besonders möchte ich Herrn Prof. Freude danken. Zahllose Tage und Abende saß er mit mir an meinen Veröffentlichungen und half mir unermüdlich meine teilweise noch unausgereiften Theorien und meine experimentellen Ergebnisse in eine solide und für hoffentlich alle verständliche Form zu bringen. Wenn ich wieder mit seiner doch sehr direkten Kritik kämpfen musste, wusste er gekonnt mein Gemüt mit einem Stückchen Schokolade und einem Kaffee zu erheitern. Neben der fachlichen Expertise unterstütze er mich bis zuletzt auch persönlich und mental in schwierigen Zeiten. Weiterhin danke ich Herrn Prof. Guber, den ich bei mehreren Beisitzen kennenlernen durfte, für die freundliche Betreuung als Korreferent.

Ein besonderer Dank geht an meine langjährigen Bürokollegen Sentayehu Wondimu, Sandeep Ummethalla, Sascha Mühlbrandt, Stefan Wolf, Tobias Harter, Mareike Trappen und Kira Köhnle. Ich vermisse die vielen Momente in denen wir uns einander wie kleine Kinder Streiche gespielt haben, uns in den Pausen über jedes mögliche Thema unterhalten haben oder einfach füreinander da waren, wenn jemand einen Hoch-, oder auch einen Tiefpunkt hatte. Ich kann mir keine besseren Bürokollegen vorstellen! Meinem Kollegen „von Bosch“, Johannes Milvich, verdanke ich neben intensiven fachlichen Diskussionen auch eine seit dem anhaltende Freundschaft. Sehr herzlich möchte ich mich bei meinen Kollegen am IPQ bedanken: Muhammad Billah, Matthias Blaicher, Philipp Dietrich, Christoph Füllner, Denis Ganin, Wladislaw Hartmann, Tobias Hoose, Juned Kemal, Clemens Kieninger, Kira Köhnle, Alexander Kotz, Yasar Kutuvantavida, Matthias Lauermann, Nicole Lindemann, Pablo Marin, Aleksandar Nesic, Robert Palmer, Jörg Pfeifle, Philipp Schindler, Simon Schneider, Stefan Singer, Philipp Trocha, Claudius Weimann und Yilin Xu, Heiner Zwickel. Ich habe mich als „IMTler" immer gut „im Süden" aufgehoben gefühlt, konnte viel aus anderen Fachbereichen lernen und habe mich auf jede Kaffeepause und jeden Siegerschnaps oder Aktionen, wie Grillen auf dem Dach, Schlittschuhlaufen oder gemütliche Abende in der Kneipe gefreut. Einen besonders angenehmen Start in die Promotionszeit ermöglichte mir das ehemalige Biophotonikteam: Tobias Wienhold, Uwe Bog und Sentayehu Wondimu. Danke für die Einarbeitung und die zahlreichen Kaffeepausen!

Starke Unterstützung erhielt ich immer vom IPQ Team „im Hintergrund". Florian Rupp, Oswald Speck, David Guder, Marco Hummel, Volker Bös und Martin Winkeler: Ohne euch wäre so manches nicht umsetzbar gewesen, ohne eure immer spontane Reaktion hätte so manches deutlich länger gedauert. Ihr seid die Besten! Herzlichen Dank an Bernadette Lehmann, Tatiana Gassmann, Andrea Riemensperger, Maria-Luise Koch für die administrative Hilfe. Ich bekam von euch immer die Unterstützung, die ich gebraucht habe.

Besonderen Dank an das E-Beam Team am IMT: Lothar Hahn, Marie-Kristin Nees, Anja Eberhardt und Andreas Bacher. Mit Lothar hat sich eine Freundschaft entwickelt, die bis heute anhält, auch wenn wir uns nicht mehr oft sehen. Danke für die zahlreichen Mittagspausen mit Eisschokolade und Frankfurter Kranz und dass du immer ein offenes Ohr für mich hattest. Dem Reinraum Team verdanke ich viele angenehme Stunden im Labor. Ich bekam von jeder Seite Unterstützung und habe mich am Ende fast dem Team zugehörig gefühlt. Kerstin Länge danke ich für die Unterstützung hinsichtlich der Biofunktionalisierung, Andreas Hofmann für das oft auch spontane passivieren meiner Sensoren.

Während meiner Promotionszeit durfte ich einige Studenten betreuen: Isabel Allegro, Claudia Bett, Jan Fischer, Kristina Geistert, Rike Graß, Patric Hammler, Mercedes Hildebrand, Andreas Kalkbrenner, Corinna Kaspar, Marius Kröger, Lisa Kurz, Yvonne Martinez, Ralf Rosenberger, Gregor Schindler. Ihr habt einiges zu meinen Publikationen beigetragen, die Arbeit mit euch hat mir immer viel Spaß gemacht!

Zu guter Letzt möchte ich meiner Familie danken. Mama und Papa, ihr habt mich immer bei allem, was ich angepackt habe unterstützt und ihr seid immer hinter mir gestanden. Danke für die vielen Anreize in meiner Kindheit, egal, ob Musik, Sport, Kunst, Handwerk, Technik oder Naturwissenschaften; durch euch habe ich erst angefangen zu lernen. Carmen, Larissa, Daniel und Robert euch verdanke ich viele Abende und Nachmittage, an denen wir uns austauschen konnten oder an denen wir gemütliche und spaßige Stunden verbringen konnten, wodurch ich die Arbeit auch einmal vergessen konnte. Maximilian, ich kann dir nicht genug dafür danken, dass du mich während der gesamten Zeit und darüber hinaus mit viel Geduld und Verständnis begleitet hast. Danke, dass du immer für mich da bist.

List of Publications

Journal Publications

[J1] Milvich, J.; **Kohler, D.**; Freude, W.; Koos, C., “Integrated phase-sensitive photonic sensors: a system design tutorial,” *Adv. Opt. Photonics* **13**, 684-642 (2021)

[J2] **Kohler, D.**; Schindler, G.; Hahn, L.; Milvich, J.; Hofmann, A.; Länge, K.; Freude, W. and Koos, C., “Bio-photonic sensors with integrated Si_3N_4-organic hybrid (SiNOH) lasers for point-of-care diagnostics,” *Light Sci. Appl.* **10,** 64 (2021)

[J3] **Kohler, D.**; Allegro, I.; Wondimu, S. F.; Hahn, L.; Freude, W.; Koos C., “Lasing in Si3N4-Organic Hybrid (SiNOH) waveguides,” *Opt. Express* **28**, 5085-5104 (2020)

[J4] Milvich*, J.; **Kohler*, D.**; Freude, W.; Koos, C., “Surface sensing with integrated optical waveguides: a design guideline,” *Opt. Express* **26**, 19885-19906 (2018) *These authors contributed equally to this work.

[J5] Ishitsuka, Y.; Savage, N.; Li, Y.; Bergs, A.; Grun, N.; **Kohler, D.**; Donnelly, R.; Nienhaus, G. U.; Fischer, R.; Takeshita, N., “Superresolution microscopy reveals a dynamic picture of cell polarity maintenance during directional growth,” *Science Advances* **1** (2015)

Conference Publications

[C1] **Kohler, D.**; Wondimu, S. F.; Hahn, L.; Allegro, I.; Blaicher, M.; Freude, W.; Koos, C., “Lasing in Si_3N_4-Organic Hybrid (SiNOH) Spiral Resonators,” *Conf. on Lasers and Electro-Optics (CLEO'18), San Jose, California, USA, May 13–18*, paper SM4I.6 (2018)

[C2] Milvich, J.; **Kohler, D.**; Freude, W.; Koos, C., "Mach-Zehnder Interferometer Readout for Instantaneous Sensor Calibration and Extraction of Endlessly Unwrapped Phase," *IEEE Photonics Conference (IPC2017), Orlando, Florida, USA, 1-5 October*, paper WH3.3 (2017)

[C3] Hofmann, A.; Kroeger, M.; Ungerer, M.; Wondimu, S. F.; Dietrich, P.-I.; Wienhold, T.; Lauermann, M.; **Kohler, D.**; Koos, C.; Bretthauer, G., "Dosierplattform zur Deposition von optisch aktiven Medien für Anwendungen in der Photonik," *MikroSystemTechnik-Kongress 2015, Karlsruhe, Deutschland, Oct. 26-28*, EDAS Paper-ID 1570106627 (2015)

Karlsruhe Series in Photonics & Communications, Vol. 36
Edited by Profs. C. Koos, W. Freude and S. Randel

Karlsruhe Institute of Technology (KIT)
Institute of Photonics and Quantum Electronics (IPQ)
Germany

Preserving our health and wellbeing requires reliable methods to detect harmful conditions before they cause damage to our bodies. For this purpose, easily accessible body liquids can be examined. While many test methods require lengthy processing in a laboratory environment, point-of-care diagnostics would enable a rapid on-site evaluation. Appropriate sensor concepts using photonic waveguides have been investigated previously. A common disadvantage of these sensor designs is that their realization suffers from high production cost, and that the resulting devices are difficult to handle.

In this book, a disposable waveguide-based sensor for body liquids is investigated and fabricated on a chip that is suitable for point-ofcare applications. A new class of on-chip lasers is co-integrated with the biosensor using low-cost fabrication methods. The laser is optically pumped and couples its light to the sensor waveguide. A mathematical model helps to design the biosensor for its optimal sensitivity. The data are read out with a digital camera. The viability of the waveguide-based biosensor chip is successfully demonstrated by a number of detection experiments.

About the Author

Daria Kohler was born 1987 in Stuttgart, Germany. In 2013, she received the Dipl.-Phys. (M. Sc.) degree in physics from Karlsruhe Institute of Technology (KIT). In 2022, the KIT Department of Electrical Engineering and Information Technology awarded her the Dr.-Ing. (Ph. D.) degree. Her research focuses on on-chip laser sources and integrated sensors for point-of-care diagnostics.

ISSN 1865-1100
ISBN 978-3-7315-1228-8

Gedruckt auf FSC-zertifiziertem Papier

ISBN 978-3-7315-1228-8
9 783731 512288